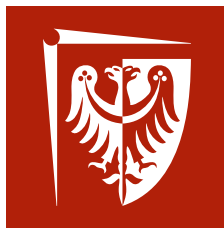

Electronic and magnetic properties of low-dimensional strongly correlated multiorbital systems

Maksymilian Środa

Ph.D. thesis prepared under the supervision of
dr hab. Jacek Herbrych



Wrocław
University
of Science
and Technology

WROCLAW
JULY, 2023

ABSTRACT

This thesis aims to establish the static and dynamic properties of the multiorbital Hubbard model in low dimensions. Inspired by the 123 family of iron-based ladders, the objective is to provide a global view on the intriguing properties exhibited by various low-dimensional multiorbital compounds with strong correlations.

This goal is realized by uncovering four distinct properties of the model via numerical calculations using the density-matrix renormalization group method. First, the investigation into the magnetism of a multiorbital ladder reveals a remarkable array of exotic magnetic patterns, including blocks, block spirals, and a spin-flux state. Second, through examining the interplay between the block-spiral order and superconductivity, this thesis demonstrates the emergence of topological Majorana zero modes, facilitated by an interaction-induced topological phase transition. Third, a similar transition is observed in a two-orbital Hubbard chain at half filling, leading to the emergence of the topological Haldane phase. Fourth, by investigating spectral functions, a generic feature called the Hund band is unveiled, which coexists with the familiar Hubbard bands in multiorbital spectra. These findings are presented in the form of four articles, to which the author of this thesis actively contributed.

Overall, this thesis emphasizes the wealth of exotic phenomena in low-dimensional multiorbital systems, providing motivation for further exploration and contributing to the broader understanding of multiorbital correlated physics.

STRESZCZENIE

Niniejsza praca doktorska ma na celu określenie statycznych i dynamicznych właściwości niskowymiarowego wielopasmowego modelu Hubbarda. Chociaż główną motywacją pracy są materiały na bazie żelaza z rodziny 123, cel rozprawy jest ogólniejszy i obejmuje wnikliwą analizę intrygujących zjawisk, które mogą występować także w innych silnie skorelowanych materiałach wielopasmowych o niskowymiarowej strukturze krystalicznej.

Cel pracy został zrealizowany poprzez odkrycie czterech właściwości badanego modelu przy wykorzystaniu obliczeń numerycznych metodą grupy renormalizacji macierzy gęstości. Po pierwsze, praca przedstawia bogaty wachlarz niekonwencjonalnych faz magnetycznych wykazywanych przez układ wielopasmowy w geometrii drabiny, m.in. bloki magnetyczne, blok-spirale i tzw. stan "strumienia magnetycznego". Po drugie, niniejsza praca odkrywa, że wzajemne oddziaływanie między blokowo-spiralnym porządkiem magnetycznym a nadprzewodnictwem prowadzi do pojawienia się topologicznych modów Majorany w wyniku indukowanego przez oddziaływanie topologicznego przejścia fazowego. Po trzecie, podobne przejście fazowe jest obserwowane w dwupasmowym łańcuchu Hubbarda przy połowicznym wypełnieniu, gdzie prowadzi ono do pojawienia się topologicznej fazy Haldane'a. Po czwarte, poprzez badanie funkcji spektralnych, niniejsza praca ujawnia tzw. podpasma Hunda, które powinny powszechnie występować w widmach układów wielopasmowych obok dobrze znanych podpasm Hubbarda. Powyższe wyniki przedstawione zostały w formie czterech artykułów, które powstały przy aktywnym udziale autora niniejszej rozprawy.

Podsumowując, niniejsza praca doktorska uwydatnia bogactwo egzotycznych zjawisk w niskowymiarowych układach wielopasmowych, motywując do dalszych badań w tym obszarze i przyczyniając się do szerszego zrozumienia fizyki układów wielopasmowych z silnymi korelacjami.

CONTENTS

Abstract	i
Streszczenie	iii
List of publications	vii
1 Introduction	1
1.1 Overview of copper-based superconductors	2
1.2 Motivation, objective, and structure of the thesis	9
2 Superconducting iron-based ladders	13
2.1 Discovery of iron-based superconductivity	13
2.2 Low-dimensional crystal structure	15
2.3 Superconducting phase diagram	17
2.4 Electronic configuration and Hund's rules	21
2.5 Three-orbital Hubbard-Kanamori model	23
2.5.1 Definition of the Hamiltonian	25
2.6 Orbital-selective Mott phase	28
2.6.1 Orbital-selective Mott phase in iron-based ladders	31
2.6.2 Effective model of the orbital-selective Mott phase: the general- ized Kondo-Heisenberg Hamiltonian	32
3 Quantum magnetism of iron-based ladders: Blocks, spirals, and spin flux	37
4 Interaction-induced topological phase transition and Majorana edge states in low-dimensional orbital-selective Mott insulators	55
5 Transition to the Haldane phase driven by electron-electron correlations	79
6 Hund bands in spectra of multiorbital systems	95
7 Summary and conclusions	111
A Density-matrix renormalization group	115
Bibliography	121
Acknowledgments	135

LIST OF PUBLICATIONS

During the work on this thesis, the following articles were prepared. This thesis is based on the first four of them [O1–O4]. At the time of writing, the articles [O3,O4] are undergoing the review process.

- [O1] M. Środa, E. Dagotto, and J. Herbrych, Quantum magnetism of iron-based ladders: Blocks, spirals, and spin flux, *Phys. Rev. B* **104**, 045128 (2021).
- [O2] J. Herbrych, M. Środa, G. Alvarez, M. Mierzejewski, and E. Dagotto, Interaction-induced topological phase transition and Majorana edge states in low-dimensional orbital-selective Mott insulators, *Nat. Commun.* **12**, 2955 (2021).
- [O3] A. Jażdżewska, M. Mierzejewski, M. Środa, A. Nocera, G. Alvarez, E. Dagotto, and J. Herbrych, Transition to the Haldane phase driven by electron-electron correlations, [arXiv:2304.11154](https://arxiv.org/abs/2304.11154) (2023), submitted to *Nat. Commun.*
- [O4] M. Środa, J. Mravlje, G. Alvarez, E. Dagotto, and J. Herbrych, Hund bands in spectra of multiorbital systems, [arXiv:2210.11209](https://arxiv.org/abs/2210.11209) (2022), submitted to *Phys. Rev. B*.
- [O5] M. Mierzejewski, M. Środa, J. Herbrych, and P. Prelovšek, Resistivity and its fluctuations in disordered many-body systems: From chains to planes, *Phys. Rev. B* **102**, 161111(R) (2020)

Author's contribution

The author of this thesis, under the guidance of the Ph.D. supervisor and with input from collaborators, completed the comprehensive preparation of the works [O1] and [O4]. All the necessary tasks, for instance, conducting numerical simulations, analyzing data, creating figures, and writing the manuscript, were successfully carried out by the author. The only exception are the dynamical mean-field theory calculations in the work [O4], which were performed by Dr. Jernej Mravlje.

Regarding the work [O2], the author rederived analytical predictions for the non-local spectral functions as a means of independent validation of the proposed conclusions. Additionally, the author conducted a numerical analysis of the spin structure factor in the ladder geometry. Due to the structure of the paper, the ladder geometry analyses were subsequently included as Supplementary Information in the article.

In the case of the work [O3], the author independently benchmarked the calculations of the string order parameter, which played a crucial role in identifying the Haldane phase. To this end, the author designed their own code based on the ITensor library [Fishman *et al.*, *SciPost Phys. Codebases* **4** (2022)].

INTRODUCTION

Modern condensed matter physics celebrates the concept of emergence, the idea that “More is different” [1] and that not all properties of a complex system can be directly predicted from the knowledge of its constituents. This is what makes condensed matter research exciting. There are always new phenomena lurking behind the corner, waiting for empirical discovery, be it in the lab or in a computer simulation. P. W. Anderson, a Nobel laureate and legend in the field, argues [1] that emergence makes condensed matter as fundamental as elementary particle physics, whose laws it obeys.

Emergence is embodied by *strongly correlated systems* [2,3], in which it is driven by the interactions between the constituents. In these systems, the constituent particles, most often the electrons, cannot be treated as independent anymore. The interaction glues them together, correlates them with each other, and entirely transforms their behavior. Such interacting electrons can develop long-range order (magnetic systems), they can get over a thousand times heavier than in the vacuum (heavy-fermion compounds [4,5]), or they can form an incompressible liquid with fractionalized quasiparticles (fractional quantum Hall systems [6]). Of course, this is not an exhaustive list, nor is such a list feasible. As new degrees of freedom are added, the possibility for exotic phenomena grows even further. This is precisely the topic of the present thesis: What new properties emerge when strong correlations meet multiorbital degrees of freedom, as happens, for instance, in iron-based materials?

As exciting as strongly correlated systems are, our understanding of their properties is still very poor. There is no universal, analytical or numerical, approach that fits all aspects of the problem. The reason is that in strongly correlated systems the strength of the interaction is on par with the kinetic energy. One cannot rely on perturbation theory, the workhorse of analytical many-body theory, because there is no small parameter in which one could attempt the perturbative expansion. Instead, there is a subtle competition of many energy scales, all of which need to be treated on an equal footing. Although brute-force numerics facilitates such a treatment, it quickly hits the wall. The Hilbert space of a many-body problem grows exponentially with the system size, limiting the calculations to tiny systems plagued by the uninteresting finite-size

effects. There are methods which work around this so-called exponential wall, but they have their own limitations. Density-matrix renormalization group [7,8] works best for one-dimensional systems, dynamical mean-field theory [9,10] is exact only in the limit of infinite dimensions, and quantum Monte Carlo [11–13] suffers from the infamous sign problem limiting its application in fermionic systems.

The prime example of how hard strongly correlated systems are is the phenomenon of high-critical-temperature (high- T_c) superconductivity [2,3,14–20]. Despite years of intensive work and strong technological motivation, the mechanism behind this effect is unknown. There is still no clear procedure to engineer superconductors with higher critical temperatures. The renowned condensed matter theorist M. Büttiker remarks that “it took almost 50 years for the BCS theory to appear after superconductivity was first discovered, so we should not expect a satisfactory theory of high- T_c superconductivity until at least 50 years after its discovery” [21]. We are getting dangerously close to this limit. Still, this is not a defeat. If it were not for high-temperature superconductivity, the field of strongly correlated systems would hardly reach its today’s popularity. Nor would this thesis be properly motivated.

Therefore, a discussion of the properties of high- T_c superconductors, focusing on the most famous cuprates, is in order. This discussion shall put the thesis into a wider context and set the ground for the later introduction to superconducting iron-based ladders (Chap. 2), which are the multiorbital systems motivating the present work.

1.1 Overview of copper-based superconductors

Historically, heavy-fermion systems were the first materials to deny the conventional Bardeen-Cooper-Schrieffer (BCS) theory of superconductivity [22]. However, their critical temperatures were low: from 2 K to 18 K in some cases. It was not until the 1986 discovery of superconductivity at ~ 30 K in copper oxide LaBaCuO [23] that the high-temperature craze began. This critical temperature shattered the previous record of 23 K [24,25], which for decades seemed unbreakable [18]. It also hit the 25–40 K mark which was believed to be the limit of the BCS paradigm [22,26]. Thus, the race began to synthesize new high- T_c compounds, measure their properties with all possible experiments, and come up with a theory. The excitement was so high that the nickname “Woodstock of Physics” was given to the session on high-temperature superconductors at the 1987 American Physical Society March Meeting [27,28]. Two thousand physicists filled the room (and the hallway), and the session lasted well into the night, finally coming to a close after 3 am. With such an intense effort, it quickly became clear that one needs to go beyond the standard BCS theory to explain the new discoveries. However, progress on the theoretical front has been rather sluggish.

Despite this, experimentalists and crystal growers continued to push the boundaries, steadily increasing the maximum attainable critical temperatures. Presently, the highest T_c ’s reach above 77 K, e.g., in the so-called YBCO compounds [29], with a record-breaking 133 K (at atmospheric pressure) achieved by HgBa₂Ca₂Cu₃O_{8+x} [30]. This is above the boiling point of nitrogen and YBCO systems have already found application in SQUID (superconducting quantum interference device) magnetometers [31,32]. The overarching motivation for further research is clear: room-temperature

superconductivity. Finding such a superconductor could revolutionize the world, addressing issues as important as climate change by improvements in energy storage and transmission.

Crystal structure and electronic configuration

The common properties of Cu-based superconductors are well illustrated by La_2CuO_4 (which superconducts when doped, lending it the name parent compound). Figure 1.1 illustrates the compound's tetragonal crystal structure. The crucial structural motif are the CuO_2 square planes, which are about 6.6 Å [16] apart and are separated by two LaO planes. The CuO_2 planes are conducting, while most of the interplane material is insulating and serves as a charge reservoir (it simply provides charge carriers). Although each Cu atom is surrounded by 6 oxygens (4 in plane and 2 above and below), the in-plane Cu-O bond is much stronger than the out-of-plane one [16]. Therefore, one treats cuprates as quasi-two-dimensional, believing that the mystery of high- T_c superconductivity is confined to the CuO_2 layer. This is expressed by Dogma I of the famous P. W. Anderson's six central dogmas for the high- T_c problem [33,34]: "All the relevant carriers of both spin and electricity reside in the CuO_2 planes". Interestingly, the majority of iron-based superconductors also crystallize in two-dimensional forms (see Chap. 2).

The electronic configurations of the elements forming La_2CuO_4 are Cu: $[\text{Ar}] 3d^{10}4s$, La: $[\text{Xe}] 5d6s^2$, and O: $[\text{He}] 2s^22p^4$. Inside the crystal, oxygen acquires two electrons, resulting in the O^{2-} valence state, whereas lanthanum loses three electrons, becoming La^{3+} . Both of these ions have a closed-shell configuration. To balance the charge, Cu must be in the Cu^{2+} state, hence it loses the 4s electron and a d electron, ending up in the $3d^9$ configuration. There is thus one hole in the d shell per copper ion, i.e., per unit cell on the plane. The Cu ion carries also a spin $\frac{1}{2}$ due to the one unpaired electron.

Naively applied band theory predicts La_2CuO_4 to be a metal due to the odd number of electrons per unit cell (which gives a partially filled band). However, band theory neglects Coulomb interactions. The d orbital, occupied by the hole, is highly localized around the nucleus [5,36,37]. This leads to a narrow bandwidth, which is comparable with the strength of the Coulomb interaction. Therefore, La_2CuO_4 is a strongly correlated material, which for one hole per unit cell (and sufficiently strong interaction) becomes a *Mott insulator*¹. Due to the repulsive interaction, the energy cost to put two holes on the same ion (hence also two electrons elsewhere) is so large that the hole motion is completely arrested. Each hole becomes effectively confined to its own unit cell and the system becomes gapped. Moreover, the insulator becomes antiferromagnetic (AFM), because when the neighboring Cu^{2+} spins are antiparallel, the interaction energy is lowered through virtual hopping (here, in the so-called superexchange mechanism). Inelastic-neutron scattering (INS) experiments confirm [38–41] that La_2CuO_4 is an insulating antiferromagnet², well described by the AFM Heisenberg model. The same holds for the majority of the cuprate family.

¹To be precise, La_2CuO_4 and other cuprates are actually charge-transfer insulators, where the charge-transfer gap (the energy difference between copper and oxygen orbitals) is smaller than the Mott gap [16,17].

²Long-range antiferromagnetic order is possible because of the weak interlayer coupling, which allows cuprates (and iron-based systems, see Chap. 2) to escape the Mermin-Wagner theorem.

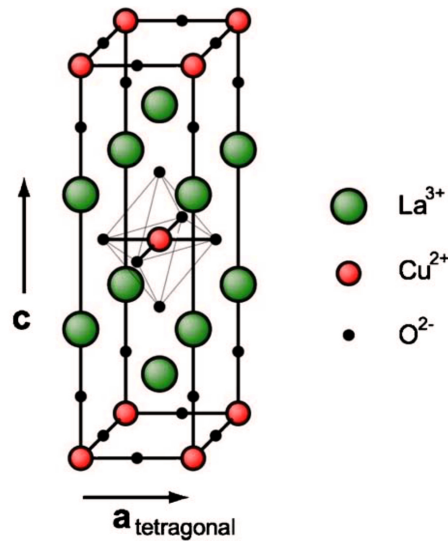


Figure 1.1: Crystal structure of cuprates on the example of La_2CuO_4 . When the space is filled with the shown tetragonal unit cell, the Cu atoms form two-dimensional layers separated by interplane La and O. Inside these CuO_2 layers, each copper atom sits on the corner of a square and the oxygen atoms sit between the coppers (in “side-centered” positions). The light gray lines mark the octahedra characteristic of the perovskite structure. REPRINTED WITH PERMISSION FROM [35]. COPYRIGHT (2006) BY THE AMERICAN PHYSICAL SOCIETY.

Superconducting phase diagram

To become superconducting, La_2CuO_4 needs to be doped. Doping is possible by substituting some of La^{3+} with Sr^{2+} , resulting in $\text{La}_{2-x}\text{Sr}_x\text{CuO}_4$. In the process, an average of x holes per unit cell are donated to the CuO_2 plane. This type of doping is aptly named hole doping (other cuprate systems can be also electron doped).

The right-hand side of Fig. 1.2 presents the temperature-doping phase diagram of a generic hole-doped cuprate, applicable also to $\text{La}_{2-x}\text{Sr}_x\text{CuO}_4$. The undoped system is an antiferromagnetic insulator with the Néel temperature $T_N \sim 300$ K [16,18]. Upon doping, the antiferromagnetic order is strongly suppressed and vanishes already at about $x \sim 0.05$. Just as antiferromagnetism vanishes, superconductivity emerges and persists in the doping range $0.05 \lesssim x \lesssim 0.27$. The $T_c(x)$ dependence encloses the superconducting phase in a peculiar dome shape, which is intrinsic to all hole-doped cuprates [18]. Importantly, the superconducting order parameter has d -wave symmetry [42,43], i.e., it changes sign for 90° rotations, unlike BCS superconductors which display isotropic s -wave symmetry. Maximal $T_c \sim 40$ K occurs at $x \sim 0.16$, which is therefore called the optimal doping.

The regime to the left of the optimal doping, $x < 0.16$, is called underdoped. Here, the normal state (above T_c) is metallic with transport properties following the temperature and frequency dependence of a Fermi liquid [45,46]. However, this regime is unlike any other metal studied before due to the appearance of a partial gap, the so-called pseudogap, reported by spectroscopy experiments. By “partial” one means that some regions in the Brillouin zone are gapped (despite the lack of superconducting long-range order [22]), while the other remain ungapped. This stands in contrast to the

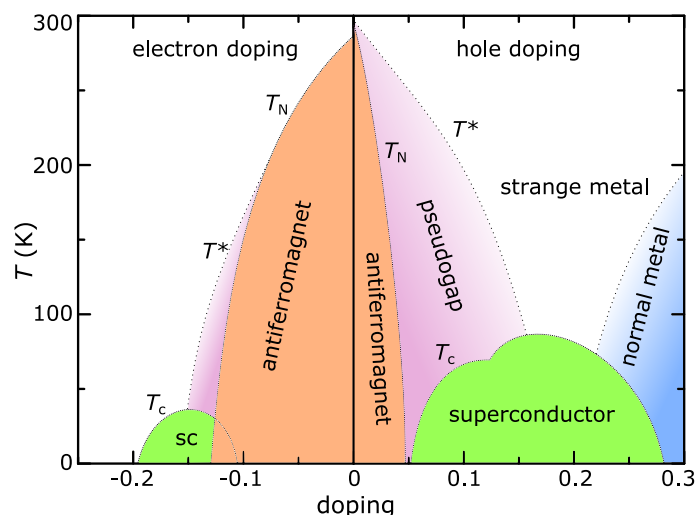


Figure 1.2: Temperature-doping phase diagram of a generic cuprate superconductor. Left and right sides correspond to electron and hole doping, respectively. Between the pseudogap, strange-metal and normal-metal regimes one expects a crossover and not a phase transition. For the hole-doped $\text{La}_{2-x}\text{Sr}_x\text{CuO}_4$, the superconducting T_c reaches a maximum of 40K, in contrast to the $\sim 100\text{K}$ marked on the diagram. Moreover, the hole doping axis should be understood as the concentration x . REPRODUCED FROM [44].

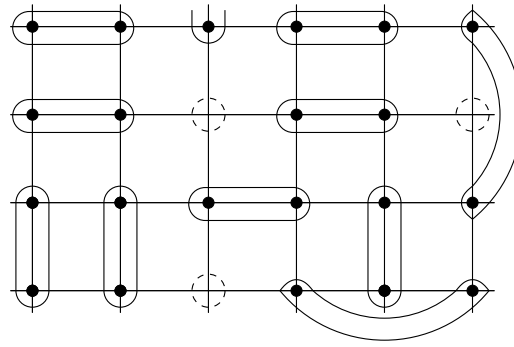
standard closed-loop Fermi surface of a normal metal. These ungapped open-ended sections of the Fermi surface bear the name Fermi arcs [47]. One view on the pseudogap regime is that of the preformed pairs [22,48]: The Cooper pairs start to form above T_c but the phase-coherent order cannot emerge unless the temperature is lowered below it. Moreover, the pseudogap regime is highly “frustrated”. There is large evidence that many types of order (stripes, charge order, orbital currents, pair-density wave etc.) compete with superconducting fluctuations [48,49].

The least understood part of the phase diagram is the “strange metal” regime. It extends for $T > T_c$ at the optimal doping. Here, the properties strongly deviate from the Fermi liquid, e.g., quasiparticles are absent, resistivity is linear in temperature T , and the Hall coefficient depends on temperature [18,48,50,51]. By contrast, the most normal part of the phase diagram appears in the overdoped regime (for $x \gg 0.16$) and is marked as “normal metal”. The system behaves here like a textbook Fermi liquid [18,22] with, e.g., the resistivity depending on temperature as T^2 .

The phase diagram shown in Fig. 1.2 highlights an important dilemma of the high- T_c problem. The superconductivity appears as an instability of the strange metal [48], or the antiferromagnet (see the next section), and not of a Fermi liquid as the BCS theory assumes. A very similar diagram will be discussed in Chap. 2 for the case of superconducting iron-based ladders, whose properties motivate this thesis.

Pairing and magnetism

One of the most widely discussed candidates for the pairing glue of cuprates is the spin-fluctuation mechanism [20,52]. A quick look on Fig. 1.2 explains why: the proximity of the superconducting and antiferromagnetic phases is rather suggestive. One



$$r \text{---} r' = \frac{|\uparrow_r \downarrow_{r'}\rangle - |\downarrow_r \uparrow_{r'}\rangle}{\sqrt{2}}$$

Figure 1.3: A single resonating valence bond (RVB) configuration formed by singlet pairs of electrons and a fraction x of doped holes. The full many-body ground state is a superposition of such configurations. REPRODUCED WITH PERMISSION FROM [57]. COPYRIGHT (2004) IOP PUBLISHING. ALL RIGHTS RESERVED.

advantage of this mechanism is that it generically produces the correct d -wave pairing symmetry [22,42]. Moreover, the conventional electron-phonon pairing mechanism is rather convincingly ruled out by, e.g., the absence of the isotope effect [22] (T_c appears to be independent of the mass of the lattice ions). Still, the spin-fluctuation ideas do not depart too far from the BCS theory, but rather try to salvage it. The hope is that one can get away with treating the normal state as a Fermi liquid but changing the source of the attraction from phonons to spins.

An alternative perspective embraces Mottness [53]. It rests on the idea that physics of high- T_c superconductors is the physics of doped Mott insulators. One should thus drop the tenets of conventional metal physics, including the Fermi liquid [54]. The main advocate for this strong-correlation point of view was P. W. Anderson himself [55]. In 1987, Anderson proposed the resonating valence bond (RVB) liquid state [56,57] as an explanation of pairing in cuprates. This state (Fig. 1.3) is a superposition (hence “resonating”) of all possible tilings of the lattice with spins bound in singlets (i.e., “valence bonds”). Upon doping, the singlets become itinerant and develop into the superconducting Cooper pairs. The pairing is thus generated by the antiferromagnetic superexchange of the original Mott insulator [57]. It should be noted, however, that there is no definitive evidence that the RVB state is realized in any cuprate [53]. Nonetheless, modern experiments [58] do indicate that the superexchange magnetic interaction plays a significant role in pair formation.

Although the RVB theory did not solve the high- T_c puzzle, Anderson’s thinking in terms of strongly correlated spins and holes became a paradigm for the entire field. Be it spin-fluctuation, superexchange, or some other pairing mechanism, there is now no doubt that magnetism and high- T_c superconductivity are intimately related (Anderson’s Dogma II [33,34]). This view is also relevant for the superconducting iron-based ladders, and the investigation of their magnetism is one of the primary contributions of this thesis (Chap. 3).

Single-band Hubbard model

According to Anderson [54,56], and largely accepted nowadays, the minimal model of cuprate physics is the single-band Hubbard model. But which band does it describe? In the crystal environment, the degenerate $3d$ orbitals of Cu^{2+} are split. The $3d_{x^2-y^2}$ orbital becomes the highest in energy, hence it “catches” the $3d^9$ hole, becoming singly occupied. Due to its shape, the $3d_{x^2-y^2}$ orbital strongly hybridizes with the fully occupied $2p_\sigma$ orbitals of the neighboring oxygens. This hybridization³ produces bonding and antibonding $2p_\sigma-3d_{x^2-y^2}$ bands. The antibonding one is pushed to higher energies, thus keeping the Cu hole and crossing the Fermi level. In this way, the antibonding band becomes the partially-filled single band of the Hubbard model [36,54,59]. See Fig. 1.4 for a schematic summarizing this process.

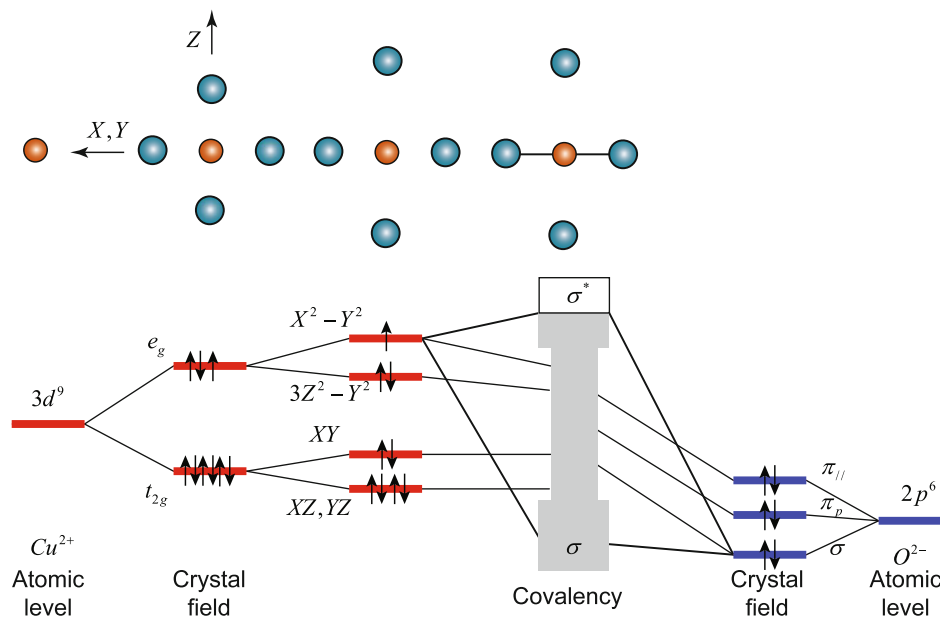


Figure 1.4: Bonding in the CuO_2 plane. The left (red) and right (blue) atomic levels correspond to Cu and O, respectively. The bonding can be understood through the following stages, progressing from left to middle: (i) atomic Cu^{2+} levels, (ii) crystal-field splitting, (iii) distortion of the apical oxygens from the perfect octahedron, (iv) Cu-O hybridization. σ^* marks the resulting antibonding $2p_\sigma-3d_{x^2-y^2}$ band. The X , Y arrows mark the in-plane direction, whereas Z marks the out-of-plane direction. Note the typographical error in the label of one of the e_g states, which should read as $3Z^2 - R^2$. USED WITH PERMISSION OF SPRINGER, FROM [60]; PERMISSION CONVEYED THROUGH COPYRIGHT CLEARANCE CENTER, INC. SIMILAR FIGURE WAS ORIGINALLY PUBLISHED IN IBM JOURNAL OF RESEARCH AND DEVELOPMENT [61].

³This hybridization is explicitly included in a three-band model, consisting of one Cu $3d_{x^2-y^2}$ and two O $2p_x, 2p_y$ orbitals. Some believe that this is the actual minimal model of cuprates. See, e.g., [16, 36] for an extended discussion of the one- and three-band models. Importantly, the possibility for a three-band description does not mean that cuprates are multiorbital. In cuprates, the orbitals belong to different atoms, hence the three-band model does not include the atomic Hund exchange, the main driver of multiorbital physics. In genuine multiorbital systems, studied in this thesis, the transition metal itself has an electronic configuration with many active orbitals.

The Hamiltonian reads

$$H = -t \sum_{ij\sigma} c_{i\sigma}^\dagger c_{j\sigma} + U \sum_i n_{i\uparrow} n_{i\downarrow}. \quad (1.1)$$

Here, $c_{i\sigma}^\dagger$ ($c_{i\sigma}$) creates (annihilates) an electron with spin $\sigma \in \{\uparrow, \downarrow\}$ at site i . $n_{i\sigma} = c_{i\sigma}^\dagger c_{i\sigma}$ is the electron density operator. For cuprates, the sum over ij is restricted to the nearest neighbors in the square lattice, modeling the CuO_2 plane. t is the hopping amplitude and $U > 0$ is the on-site Coulomb repulsion. The filling (electron density) is defined as $n = N/L$, with N being the total number of electrons and L the total number of lattice sites. The half filling $n = 1$ is equivalent to $x = 0$, i.e., an undoped cuprate, such as La_2CuO_4 . In Chap. 2, this model will be extended to the case of (low-dimensional) multiorbital systems, which are the subject of this thesis.

The essence of the Hubbard model is to capture the tight-binding characteristic of narrow d orbitals. The addition of U incorporates strong-correlation effects and ensures that the undoped phase of cuprates is correctly reproduced. That is, for $n = 1$, a sizable U opens a so-called Mott gap at the Fermi level, between the well-known lower and upper Hubbard bands, and the system becomes an AFM insulator. Specifically, for $n = 1$ and $U \gg t$, the low-energy description of Eq. (1.1) is the simple Heisenberg Hamiltonian $J \sum_{ij} \mathbf{S}_i \cdot \mathbf{S}_j$ with the AFM (super)exchange $J = 4t^2/U$. In principle, long-range part of the Coulomb interaction should also be present in Eq. (1.1), but it is assumed to be negligible due to screening effects [16,36]. Although the single-band description misses the charge-transfer character of cuprates, one can treat U as an effective parameter inducing a Mott gap of the same magnitude as the actual charge-transfer gap [16]. In such a case, the lower Hubbard band can be thought of as the “oxygen” band of the real material.

Despite its apparent simplicity, the Hamiltonian (1.1) captures much of the normal-state properties of cuprates. These properties include, but are not limited to, antiferromagnetism (and its vanishing upon doping), nematic correlations, d -wave pairing correlations, stripes, pseudogap physics, and the existence of many competing states separated by small energy scales. See Refs. [16,20,49,62–64] for a review of these results.

The long-standing problem is whether the Hubbard model captures the *long-range* superconducting order of cuprates. This question has been waiting for a satisfactory answer for over 30 years. Interestingly, there is some answer, but in the wrong limit—the weak coupling, $U/t \rightarrow 0$. In this regime, controlled perturbation-theory analyses do find a d -wave superconducting ground state upon doping [65–68]. This provides a proof of concept that the Hubbard model can generate the correct d -wave superconductivity. But, of course, cuprates occupy a different parameter space. They exhibit moderate to large interactions, $U/t \sim 6$ –8, and, here, the situation changes. Perturbation theory no longer applies, so the alternative are large-scale numerical calculations using, primarily, the density-matrix renormalization group and various flavors of quantum Monte Carlo. In the recent years, new insight has flown from such studies. Refs. [69,70] claim that the Hubbard model, as written in Eq. (1.1), *does not* display long-range superconductivity in the ground state for the physically important parameters. There is, however, a tendency for short-range d -wave pairing. The acceptance of these bold conclusions seems to be slowly growing across the community, as expressed, e.g., in the recent review [64]. Assuming that these results are reliable, one

needs to look for extensions of the Hubbard model to find superconductivity. The most common extension is the addition of the next-nearest-neighbor hopping t' . Some argue that it is actually necessary in the single-band description [71]. Upon the addition of t' , Refs. [72,73] do find quasi-long-range⁴ superconducting correlations in the Hubbard model. Similar results are reported [74,76,77] when t' is added to the t - J model, which is the effective description of the Hubbard model at strong coupling [78–80].

At this point, one cannot conclusively say that the (extended) Hubbard model captures the cuprate superconductivity. Nevertheless, the recent developments rekindle the hope that computational study of model Hamiltonians will help resolve the high- T_c problem.

1.2 Motivation, objective, and structure of the thesis

The preceding discussion used cuprate superconductivity as an illustrative example to introduce the fundamental principles of strongly correlated physics. This led us smoothly into the topic of this thesis, situating it within a broader context. However, this thesis does not study cuprates; rather, it is motivated by the discovery of high-temperature superconductivity in iron-based systems. A more comprehensive discussion of their properties is deferred to Chap. 2, while here I summarize the key points that motivate this thesis.

The discovery of iron-based superconductivity was a huge breakthrough for the field of strongly correlated physics. The existence of a new material platform restored hope for a universal explanation for the mechanism of superconductivity. Indeed, iron-based superconductors share many characteristics of their cuprate counterparts. For example, they have similar temperature-doping phase diagrams, with antiferromagnetism in close proximity to superconductivity [20]. However, unlike cuprates, iron-based systems are characterized by a multiorbital Fermi surface, as will be discussed at length in Chap. 2. The interplay between these additional multiorbital degrees of freedom and strong correlations induces new phenomena beyond what is possible in cuprates. Importantly, these phenomena are not restricted to the superconducting phase, but arise already in the normal state. An in-depth understanding of these new effects, even without directly addressing the superconducting state, is a necessary prerequisite to resolve the issue of iron-based superconductivity, and maybe also shed some light on the copper-based superconductors. This is the overarching problem to which the present thesis contributes. Specifically, this thesis identifies four novel multiorbital phenomena: the exotic magnetism of the iron-based ladders, its topological properties (Majorana modes), the Haldane phase in two-orbital chains, and the Hund bands (a generic spectral feature of multiorbital systems). These phenomena are predominantly revealed in the context of a specific family of iron-based compounds.

Most studies of iron-based systems focused on layered compounds, e.g., pnictides LaOFeAs, BaFe₂As₂, and chalcogenides FeSe, FeTe [20]. These compounds pos-

⁴These calculations employ the density-matrix renormalization group method, which models the two-dimensional geometry by an elongated cylinder. In such a geometry, the true long-range order is impossible and is represented by power-law quasi-long-range correlations [74,75].

sess crystal structures that are similar to the canonical cuprates, with Fe ions forming two-dimensional planes. However, similar to cuprates, iron-based materials also exist in distinct reduced forms, referred to as *low-dimensional*. For instance, there is a prominent family of quasi-one-dimensional two-leg ladders, known as the 123 family, with the chemical formula AFe_2X_3 ($A = \text{Ba, K, Rb, Cs, Tl}$ metals, $X = \text{S, Se, Te}$ chalcogens). Recent studies have revealed intriguing properties of these ladders, such as pressure-induced superconductivity [81–84], nontrivial magnetism [85–88], and also other characteristic properties of iron-based systems, e.g., orbital selectivity [85,89–91]. There are also iron-based compounds which have a reported (or predicted) chain-like structure [92–103]. These materials are far less explored than their higher-dimensional counterparts, especially from the theoretical perspective. The main reason for this is precisely the low dimensionality. The dynamical mean-field theory (DMFT), the workhorse in the study of multiorbital systems, is unsuitable to one-dimensional geometry. In fact, all mean-field approaches suffer from this problem, including also, e.g., the Hartree-Fock or slave-spin methods. Moreover, even in high-dimensional systems, DMFT does not account for the *spatial* many-body correlations. Similarly, the density-functional theory calculations only approximately incorporate the correlation effects. This means that long-distance properties, such as magnetism, might be underestimated in the current theoretical works on multiorbital systems. In contrast, experimental studies consistently highlight the significance of magnetism, particularly in the low-dimensional 123 compounds, where unexpected orders were discovered [85–88]. Taking these considerations into account, it is reasonable to anticipate that a multiorbital system in a ladder or chain geometry, such as the 123 family, harbors a rich array of unanticipated phenomena still waiting to be unveiled. Consequently, it becomes necessary for theory to delve into the fundamental physics of this context, not necessarily by fixating on specific compounds or the superconducting properties, but rather by exploring the fascinating new physics and providing guidance and inspiration for future experiments.

Objective

In this thesis, I thus aim to establish the static and dynamic (energy-resolved) properties of the *low-dimensional* multiorbital Hubbard model. For this purpose, the 123 family of iron-based ladders serves as a crucial motivation and a starting point to explore realistic parameter regimes of the model. However, rather than reproducing the properties of particular compounds in an *ab initio* manner, I focus on the general principles governing low-dimensional multiorbital materials with strong correlations. By doing so, I intend to broaden the applicability of my research beyond the 123 ladders and other currently synthesized materials.

To achieve my goal, I embrace the low dimensionality and base my calculations on the powerful density-matrix renormalization group method. This method performs best precisely when the dimensionality is lowered to a ladder or a chain, and it fully incorporates the many-body correlations, both short- and long-range (see the discussion in Sec. 2.5). This allows me to accurately describe the magnetic, topological and electronic properties. The magnetic properties, as it turns out, play a significant role in the physics of the low-dimensional multiorbital Hubbard model. Not only are they rich and interesting in their own right, but they also drive an interaction-induced topo-

logical phase transition, in which Majorana modes emerge. Interestingly, the potential for intriguing topological effects extends beyond Majorana physics, as a similar interaction-induced topological phase transition in different parameter regimes gives rise to the Haldane phase. Furthermore, the single-particle spectra of multiorbital systems reveal an unexpected spectral feature driven only by the Hund's coupling. This feature, dubbed the Hund band, turns out to be generic and is not restricted to the low dimensionality.

Structure

This thesis consists of a collection of four articles [O1–O4] that I coauthored during my doctoral course. To enhance readability, I included an introductory chapter on iron-based ladders, and supplemented each article with a concise introduction discussing its results and its specific context. Specifically, the thesis has the following structure.

Chapter 2 presents essential information on iron-based superconductors, paralleling the above discussion on cuprates, and focusing mostly on the 123 family of iron-based ladders. The idea is not to be exhaustive, which would be a formidable task, but rather to provide basic facts, motivation, and knowledge base relevant to this thesis. The chapter begins by briefly addressing the historical context of iron-based superconductivity. Subsequently, the chapter delves into key aspects such as the crystal structure, with emphasis on the low-dimensional nature of the 123 family, and the superconducting phase diagram. Next, it explores the electronic configuration and Hund's rules, leading to the derivation of the three-orbital Hubbard-Kanamori model. Lastly, the chapter examines the orbital-selective Mott phase, its presence in iron-based ladders, and the corresponding generalized Kondo-Heisenberg Hamiltonian.

Chapter 3 begins the discussion of the original findings by examining the magnetism of the orbital-selective Mott phase in the ladder geometry, as relevant to the 123 family. The main result is the doping n vs interaction U magnetic phase diagram, revealing robust magnetic patterns including blocks, block spirals, incommensurate antiferromagnetism, phase separation, and a quantum spin-flux state.

Chapter 4 explores the interplay between the block-spiral order and superconductivity. It reveals that placing a multiorbital chain within the orbital-selective Mott phase in proximity to an s -wave superconductor facilitates an interaction-induced topological phase transition. The transition manifests itself as the simultaneous development of spiral spin order, spin-triplet pairing amplitudes, and the emergence of Majorana zero modes at the edges of the system.

Chapter 5 focuses on a different parameter regime and explores the behavior of the two-orbital Hubbard chain at half filling. Here, another sharp and interaction-driven topological phase transition is revealed, this time into the Haldane phase. Remarkably, this transition occurs at relatively modest values of the Hubbard repulsion U , prior to the formation of fully developed magnetic moments. These findings thus extend the concept of Haldane phases to the realm of delocalized electrons.

In Chapter 6, the focus shifts to the spectral properties of the multiorbital Hubbard model. This chapter identifies a generic spectral feature of multiorbital systems, the Hund band, with energy exclusively determined by the Hund's coupling J_H and independent of the interaction strength U . Extensive calculations confirm the generality

of these findings beyond the 123 ladders, pointing to applicability in any multiorbital system with significant Hund's coupling and charge fluctuations.

The thesis concludes with Chapter 7, which provides a summary, discusses conclusions, and explores future directions. Additionally, Appendix A aids the readers by providing essential knowledge on the inner workings of the density-matrix renormalization group algorithm.

SUPERCONDUCTING IRON-BASED LADDERS

This chapter comprises an introduction to the selected properties of iron-based superconductors. This discussion parallels the discussion on copper-based materials given in Sec. 1.1. The aim is not to be exhaustive, but rather lay down the basic knowledge relevant to the context of this thesis. Therefore, the layered iron-based compounds are only briefly touched upon, and the focus lies on the low-dimensional compounds, the so-called 123 ladders. This thesis is concerned precisely with the properties of the low-dimensional multiorbital Hubbard model realized in these ladders or similar systems.

The chapter opens with a brief historical perspective on iron-based superconductivity. Next, the crystal structure and the superconducting phase diagrams are described, with the focus shifting to the low-dimensional 123 family. Then, the discussion moves to the multiorbital electronic configuration, the associated Hund's rules, and the resulting microscopic model, the three-orbital Hubbard-Kanamori Hamiltonian. Finally, the chapter ends with a description of the orbital-selective Mott phase, its relevancy to the ladder materials, and its effective model.

In this chapter and hereafter, the terms *iron-based compounds* or *iron-based materials* refer to materials which either exhibit high-temperature superconductivity themselves, or their properties are close to their superconducting counterparts. Moreover, the term *low-dimensional* denotes dimensionality below two dimensions, i.e., a ladder or a chain.

2.1 Discovery of iron-based superconductivity

In 2008, physicists got a new set of toys—the iron-based high-temperature superconductors. Although a range of superconducting materials containing iron was known earlier, their critical temperatures were rather low, $T_c \sim 2 - 8$ K [104]. The first superconducting iron pnictide LaFePO also had an unremarkable T_c of about 5 K [105]. Iron

is simply not your first pick when looking for a potential high- T_c superconductor. This is why in 2008 physicists were taken by surprise with the discovery of superconductivity at 26 K in F-doped iron pnictide LaFeAsO [106]. A wave of excitement swept throughout the field, similar to the one when cuprates emerged, with the press dubbing it the “new iron age” [107]. Preprints were appearing on arXiv at a blistering rate of 2.5 per day [108]. By subjecting LaFeAsO_{1-x}F_x to a high pressure of 4 GPa, the record critical temperature was quickly increased to 43 K [109]. This validated the claim of achieving “high-temperature” superconductivity. Subsequently, entire classes of new iron-based superconductors were identified. The most prominent being the 1111 family (e.g., the original F-doped LaFeAsO), the 122 family (e.g., K-doped BaFe₂As₂ [110]), the 111 family (e.g., LiFeAs [111]) or the iron chalcogenide 11 family (e.g., FeSe [112]). For a wider perspective, see, e.g., [20,104].

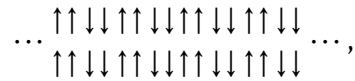
The current record T_c stands at 55 – 56 K in bulk systems, such as SmFeAsO_{0.85} [113] or Sr_{0.5}Sm_{0.5}FeAsF [114], and at about 40 – 65 K (or possibly even above 100 K [115]) in monolayer FeSe deposited on SrTiO₃ [116]. These values rank iron-based systems just behind cuprates when it comes to the highest recorded T_c 's¹. This is one link between the iron- and copper-based systems. The other important link is the structure: Fe atoms in iron-based systems are arranged into stacked square-lattice planes, similarly to Cu in cuprates. Moreover, the phase diagrams are captivatingly similar, with superconductivity in iron-based systems also arising after magnetism of the parent compound is suppressed by doping or pressure. Due to this and similar premises, it is widely believed that phonons are unlikely to be responsible for the iron-based superconductivity, with some type of magnetic mechanism being the typical alternative [20,104,118]. These shared properties make the iron-based systems a true counterpart of the cuprates. With this in mind, one needs to be aware that there are also important differences. For instance, the parent state of iron-based systems is typically a (bad) metal and not an insulator [52,119]. Furthermore, the iron-based materials need to be described with a *multiorbital* Hubbard model, and not a single-orbital one, as will become clear below. Reconciling the differences and painting a coherent picture of iron- and copper-based superconductivity requires much more work despite the initial explosion of knowledge. Especially that the iron-based superconductors are rather young compared to the more mature cuprates.

In the context of this thesis, the most important development happened in 2015, when superconductivity at 14 K and 11 GPa was discovered in BaFe₂S₃ iron-based ladder [81]. This was the first report of an iron-based superconductor without the layered square-lattice motif, but with a low-dimensional double-chain (ladder) motif instead². Superconducting ladders were already known in the context of cuprates, e.g., (La, Sr, Ca)₁₄Cu₂₄O₄₁ [120–124], which, interestingly, also need high pressure for the stabilization of the superconducting phase. Therefore, this new finding established another connection between iron- and copper-based materials. Subsequent experiment on BaFe₂S₃ confirmed the emergence of superconductivity and reported higher critical temperature 24 K, at a similar pressure 11.6 GPa [82]. Later, superconductivity was

¹At the time of writing, there appeared a new preprint [117] that reports bulk superconductivity with T_c of 80 K in the nickelate compound La₃Ni₂O₇. This finding might overthrow iron-based systems and place nickelates as the second-best to cuprates.

²See Sec. 2.2 for a description of the crystal structure.

found at 11 K and 10.2–15 GPa in BaFe_2Se_3 [83], where S was replaced by Se. In this way, the 123 series of compounds joined the privileged label of iron-based superconductors, with the ladder structure as the defining characteristic. Other isomorphic members include, e.g., $(\text{K}, \text{Rb}, \text{Cs}, \text{Tl})\text{Fe}_2\text{S}_3$, $(\text{K}, \text{Rb}, \text{Cs})\text{Fe}_2\text{Se}_3$, and $(\text{Rb}, \text{Cs}, \text{Ba})\text{Fe}_2\text{Te}_3$ [89,125–131], whose similarity to $\text{BaFe}_2(\text{S}, \text{Se})_3$ points to their potential superconductivity. Crucially, the 123 family not only shares the main properties of the layered iron-based compounds, but it also puts its own twist on the physics. For instance, while the layered compounds are usually metallic in the parent state, the ladders are insulating, with metallicity emerging only after the pressure is increased [81–84,132]. Furthermore, in ladders, the magnetism seems to be a bigger player than in the layered systems. This is evidenced, e.g., by the emergence of the block-magnetic state



which forms on the long iron ladders within the crystal structure of BaFe_2Se_3 [85–89] (see the original results in Chap. 3 for more detailed sketches and a theoretical description). In this context, the low dimensionality is especially important because it enhances the quantum effects, which are responsible for such frustrated behaviors. This in turn requires special theoretical treatment, one that does not miss the short- and long-range quantum correlations and goes beyond the usual mean-field approaches to multiorbital systems. The main topic of the present thesis is precisely an accurate theoretical modelling of the magnetism and seeking for hitherto undiscovered novel properties of the low-dimensional multiorbital systems. With the superconductivity in iron-based ladders discovered only recently, there is still much to be understood, even with respect to the normal-state properties.

The remainder of this chapter shall focus mostly on characterizing these 123 ladders from the point of view of their crystal and electronic structure, and the multi-orbital physics. In addition, it shall discuss what theoretical models and techniques should be applied to understand them. The original results predicting the novel properties which might be realized in the 123 ladders (or other low-dimensional multi-orbital materials) are presented in Chaps. 3–6.

2.2 Low-dimensional crystal structure

The fundamental motif in the crystal structure of iron-based superconductors is the FeX_4 tetrahedron, where X represents a pnictogen (e.g., As) or a chalcogen (e.g., Se). Figure 2.1 shows the crystal structures of several layered iron-based systems. In each of them, the FeX_4 tetrahedra are joined by edges, forming the Fe_2X_2 layers. In this way, the Fe atoms are arranged into a square lattice, while the X atoms sit at the centers of the Fe squares, protruding above and below the Fe lattice. Thus, the whole Fe_2X_2 layer acquires a corrugated shape. The simplest possible arrangement of such layers is realized in $\text{Fe}(\text{Se}, \text{Te})$, which is basically just a stack of them. Other compounds contain also (mostly insulating) spacer layers, whose composition and structure differentiates the various families. Crucially, the Fe_2X_2 planes are metallic and are believed to host all the interesting physics [119], particularly the supercurrent flow [108]. There is thus a

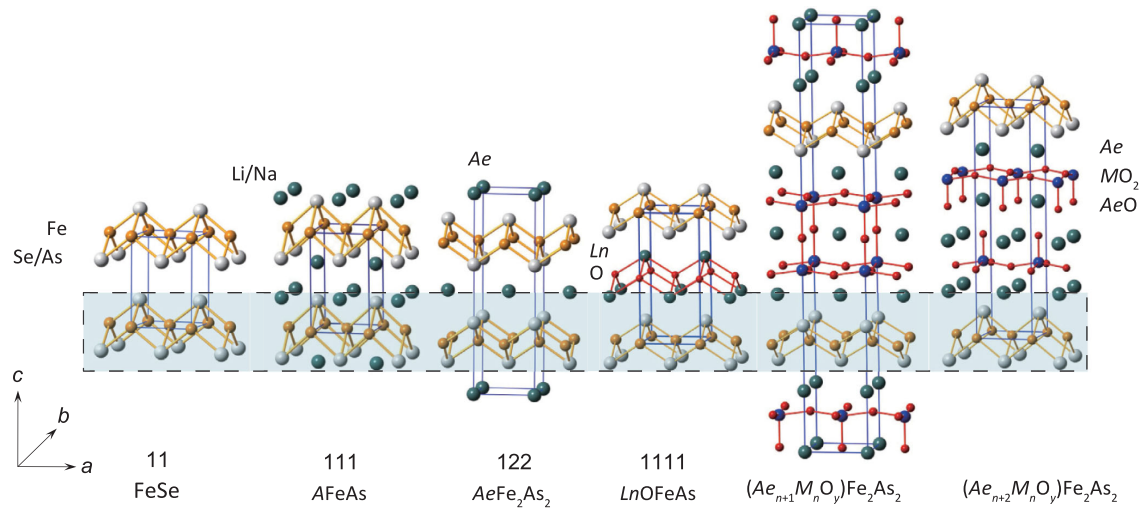


Figure 2.1: The crystal structures of several families of iron-based superconductors. A, Ae, Ln, and M stand for alkali, alkaline-earth, lanthanide, and transition metal atoms, respectively. The common structural motif, the Fe_2X_2 layer, is highlighted across all structures. Note also that each Fe atom is coordinated by 4 pnictogens/chalcogens in a tetrahedral arrangement. REPRODUCED FROM [133].

compelling similarity between the structures of the iron- and copper-based superconductors (see Chap. 1).

The structure of the low-dimensional 123 family is closely related to that of the layered compounds. For this class, the general chemical formula reads AFe_2X_3 , where $\text{A} = \text{Ba}, \text{K}, \text{Rb}, \text{Cs}, \text{Tl}$ are metals (alkaline-earth or alkali, except for Tl), and $\text{X} = \text{S}, \text{Se}, \text{Te}$ are chalcogens. Here, the Fe_2X_2 planes are “cut” into long two-leg ladders. Every third Fe atom of the plane is removed, resulting in Fe_2X_3 double chains (Fig. 2.2), which keep the substructure of the edge-sharing FeX_4 tetrahedra. These double chains run along one crystallographic axis, giving the compounds their quasi-one-dimensional (quasi-1D) character. The A atoms act as spacers between the ladders, resulting in the

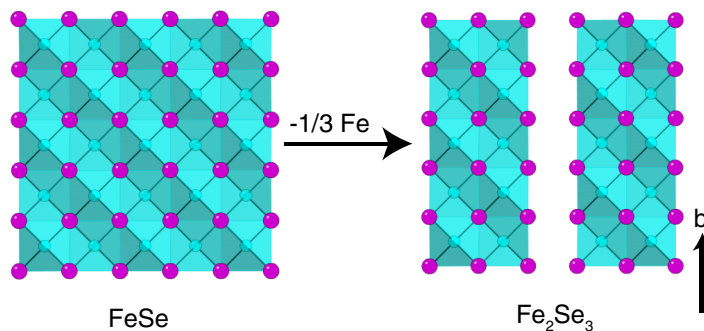


Figure 2.2: Schematic showing how the structures of layered and ladder compounds are related on the example of $\text{X} = \text{Se}$. The ladder is created by removing every third Fe atom from the layer. Purple circles mark Se atoms and cyan circles mark Fe atoms.

REPRINTED WITH PERMISSION FROM [119,134]. COPYRIGHT (2011) BY THE AMERICAN PHYSICAL SOCIETY.

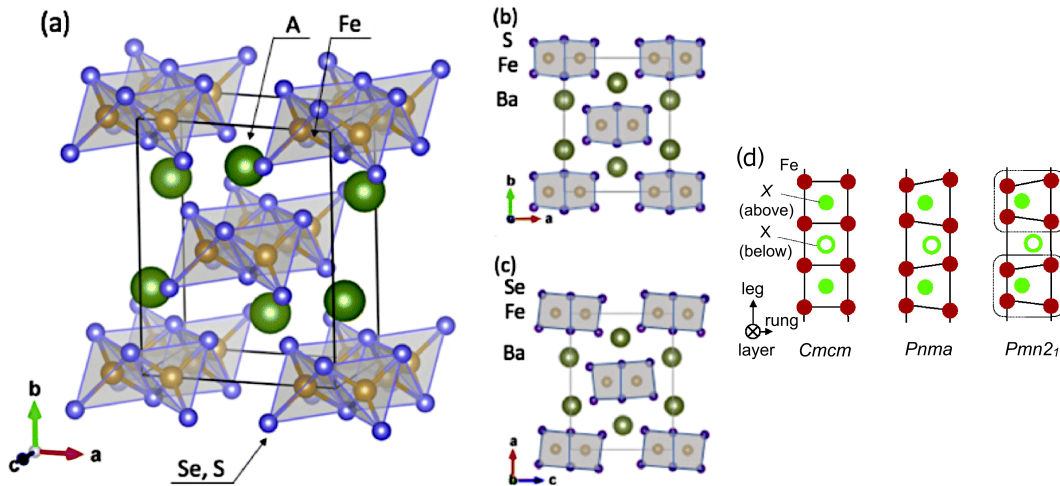


Figure 2.3: (a) Crystal structure exhibited by the 123 family of iron-based ladders. A = Ba, K, Rb, Cs, Tl are metals. The fundamental Fe(S, Se, Te)₄ tetrahedra are highlighted in gray. (b), (c) View along the ladder direction for: (b) BaFe₂S₃ with the space group *Cmcm* and (c) BaFe₂Se₃ with the space group *Pnma*. (d) Ladder structure for each orthorhombic space group *Cmcm*, *Pnma*, *Pmn*₂₁. Here, X = S, Se, Te. PANELS (A)-(C) TAKEN FROM [135] AND REPRODUCED WITH PERMISSION FROM SPRINGER NATURE. PANEL (D) REPRINTED WITH PERMISSION FROM [132]; COPYRIGHT (2020) BY THE AMERICAN PHYSICAL SOCIETY.

three-dimensional geometry displayed in Fig. 2.3. This three-dimensional structure is orthorhombic, with the most common space group being *Cmcm* [132,135], shown in Fig. 2.3(b). An exception is BaFe₂Se₃, where the ladders are tilted with respect to (w.r.t.) each other, leading to the space group *Pnma* [Fig. 2.3(c),(d)] or possibly even the noncentrosymmetric *Pmn*₂₁ [Fig. 2.3(d)], according to more recent experiments [136,137]. However, increased pressure or temperature drive BaFe₂Se₃ into the higher-symmetry and more stable structure *Cmcm* [86,132,138,139].

Finally, there are also iron-based compounds that were reported or predicted to possess a chain-like structure [92–103]. For example, the structure of BaFe₂Se₄ [97] closely resembles that of BaFe₂Se₃, but with ladders replaced by single chains (also separated by Ba atoms). However, the iron atoms in these chain compounds often exhibit a distinct valence state, setting them apart from the two-dimensional or ladder superconductors with the Fe²⁺ valence (see Sec. 2.4). Moreover, there are no reports of superconductivity in the chain compounds. Nonetheless, studying these materials offers valuable insights, and many of the findings from this thesis should be applicable to these systems as well.

2.3 Superconducting phase diagram

The generic phase diagram of a (layered) iron-based superconductor can be discussed on the example of BaFe₂As₂. Figure 2.4(a) shows the temperature-doping phase diagram compiled from several experimental studies. At a glance, this diagram is very similar to that of a typical cuprate (see Chap. 1), which captivated the interest of physicists since the initial 2008 discovery. The parent compound initially exhibits an antiferro-

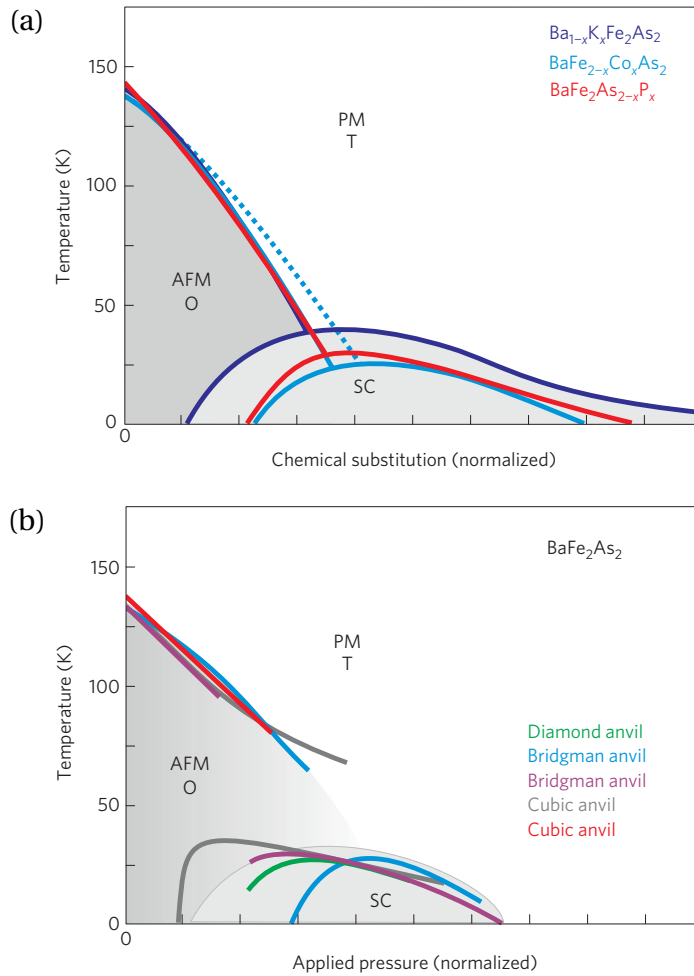


Figure 2.4: (a) Chemical-substitution (doping) phase diagram of BaFe_2As_2 , shown for K, Co, and P substitutions. To facilitate simple comparison between different experimental results, the chemical-substitution axis is normalized to collapse the lines marking the transition to the antiferromagnet (AFM). PM, SC stand for the paramagnetic and the superconducting phases, respectively. The dotted line marks the structural transition between tetragonal (T) and orthorhombic (O) phases. (b) Pressure phase diagram of BaFe_2As_2 for various techniques (diamond anvil cell, Bridgman anvil cell, cubic anvil cell). The pressure axis is normalized similarly as in (a). Here, the structural transition is coincident with the paramagnet to antiferromagnet transition. TAKEN FROM [140] AND REPRODUCED WITH PERMISSION FROM SPRINGER NATURE. REFER TO THE CITED WORK FOR REFERENCES TO THE EXPERIMENTAL RESULTS FROM WHICH THE PHASE DIAGRAMS WERE CONSTRUCTED.

magnetic (or spin-density-wave) non-superconducting state at low temperatures and goes superconducting only after the magnetism is suppressed. Also, the shape of the superconducting dome resembles that of cuprates closely. Moreover, there is a possibility for coexistence of magnetic, superconducting and orthorhombic orders in some parts of the phase diagram [20,140], which again brings to mind the many competing states encountered in cuprates.

The differences with respect to cuprates lie in the details. For instance, here, the antiferromagnetic phase is a (bad) metal instead of an insulator [110,141]. The anti-

ferromagnetism is not of a standard Néel type [ordering vector $\mathbf{q} = (\pi, \pi)$] but rather of a striped pattern [$\mathbf{q} = (\pi, 0)$]. That is, the moments are oriented antiferromagnetically along one direction and ferromagnetically along the other [20,52,140]. Moreover, the striped antiferromagnetic phase emerges upon a transition to an orthorhombic structure, while the paramagnetic phase is tetragonal (and so is most of the superconducting phase) [142]. Another interesting feature is that the tetragonal-to-orthorhombic structural transition can occur separately from the paramagnetic-to-antiferromagnetic transition [Fig. 2.4(a)]. The region in between the two transitions is called the electronically-driven nematic phase [118,143,144]. Here, one finds a substantial breaking of the discrete C_4 rotational symmetry in the orbital degree of freedom (beyond the effect of structural distortion), without the breaking of the translational symmetry³. The normal-state properties above the superconducting T_c are also interesting, with prominent orbital selectivity linked to the correlations driven by the Hund's physics [118,144]. Finally, the pairing symmetry of iron-based superconductors is not d -wave as in cuprates. Instead, current evidence suggests the s^\pm -wave symmetry, where the gap remains almost isotropic, but acquires different signs (phases) on the electron and hole pockets of the Fermi surface [118]. The pairing mechanism in iron-based superconductors is not well understood, as in cuprates, and remains the subject of intensive study [20,145].

It is instructive to note that Fig. 2.4(a) compares not only the electron- (Co) and hole- (K) doping of BaFe_2As_2 , but also the isovalent doping by P. The latter does not add or remove carriers, but introduces “chemical pressure” due to the different ionic radii of P and As [146]. From Fig. 2.4(a), it is clear that such an effect also suppresses antiferromagnetism in favor of superconductivity, and it produces analogous diagram as charge doping. This raises the question whether a direct application of physical pressure would also yield superconductivity. The answer is affirmative, as evidenced by Fig. 2.4(b), which shows the pressure-temperature phase diagram of BaFe_2As_2 .

Pressure is also the control parameter responsible for the emergence of superconductivity in the low-dimensional 123 family. Figure 2.5 shows the pressure-temperature phase diagram for the BaFe_2S_3 and BaFe_2Se_3 iron-based ladders. The general features clearly agree with the phase diagram of the layered compounds. Again, by suppressing the antiferromagnetism of the parent compound, one “uncovers” the superconducting dome. However, there are some interesting differences. For example, the parent state of $\text{BaFe}_2(\text{S}, \text{Se})_3$ exhibits a more insulating behavior, being an antiferromagnetic Mott insulator or possibly an orbital-selective Mott state (see Sec. 2.6.1). This means that the ladder systems are more correlated than their layered counterparts, agreeing well with the intuition that quantum effects are enhanced in low dimensions. In this respect, Ref. [91] shows that the density-functional theory gives a metal at ambient pressure and the insulating behavior sets in only after the correlations are included (within the dynamical mean-field theory).

Due to the insulating parent state, superconductivity in Fe ladders emerges only after an insulator-metal transition takes place, and, in fact, immediately after it occurs [82,83]. Here, the effect of pressure in driving the insulator-metal transition is usu-

³This feature explains the name of this phase, which follows from the field of liquid crystals. In a nematic liquid crystal, the molecules are arranged randomly (thus keeping the translational invariance), but they orient themselves along a preferred direction (thus breaking the rotational symmetry) [143].

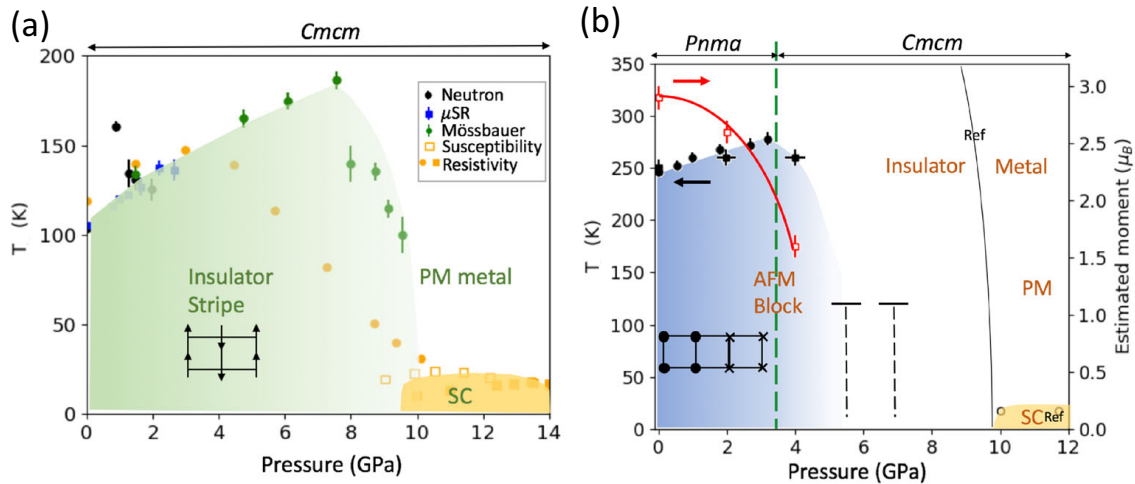


Figure 2.5: Pressure vs temperature phase diagrams for (a) BaFe_2S_3 and (b) BaFe_2Se_3 iron-based ladders. AFM, PM, SC denote the antiferromagnetic, paramagnetic, and superconducting phases, respectively. (a) The Néel temperature as a function of pressure was obtained from several studies employing different techniques (neutron diffraction, muon spin spectroscopy μSR , Mössbauer spectroscopy, resistivity measurements; see the legend). (b) The antiferromagnetic transition temperature is represented by black symbols on the left axis, with the μSR and neutron diffraction results indicated by filled circles and triangles, respectively. The estimated ordered moment is represented by red symbols on the right axis. The green dashed line marks the structural transition at 3.7 GPa. The horizontal bars at 5.5 and 6.8 GPa indicate the lowest measured temperature 120 K, at which block-type short-range magnetic correlations were observed, while the dashed lines running below indicate the upper limit for the onset of the long-range order. The open circles near the SC dome denote the critical temperature T_c , while the black solid line marks the insulator-metal transition. TAKEN FROM [135] AND REPRODUCED WITH PERMISSION FROM SPRINGER NATURE. REFER TO THE CITED WORK FOR REFERENCES TO THE EXPERIMENTAL RESULTS FROM WHICH THE PHASE DIAGRAMS WERE CONSTRUCTED.

ally attributed to broadening of the electronic bandwidth, the so-called bandwidth-controlled Mott transition [81,82,91,147]. However, an alternative view is offered by *ab initio* calculations of $(\text{Ba}, \text{K})\text{Fe}_2\text{S}_3$ [148]. These calculations suggest that pressure can lead to *self*-doping of electrons into the iron network by inducing an additional electron transfer from S to Fe without chemical substitution. This fits nicely with model calculations which find that lightly doped BaFe_2S_3 develops a tendency to superconducting pair formation [149,150]. Importantly, the proximity of the insulator-metal and superconducting transitions highlights the significance of electronic correlations for inducing superconductivity in these systems [132,135]. Accordingly, it was suggested that the antiferromagnetic fluctuations are the driving force behind superconductivity in the 123 materials [83,84,130,135]. Another interesting feature of Figs. 2.5(a) and 2.5(b) is the initial increase of the Néel temperature with pressure. This is not observed in the layered compounds and was interpreted to indicate strong magnetoelastic coupling [86,135].

Finally, the 123 ladders display unexpected magnetic orders. While BaFe_2S_3 shows the stripe-like magnetism⁴, common to layered compounds, BaFe_2Se_3 displays an exotic block-magnetic pattern of $\begin{array}{cccc} \uparrow\uparrow\downarrow\downarrow & \uparrow\uparrow\downarrow\downarrow \\ \uparrow\uparrow\downarrow\downarrow & \uparrow\uparrow\downarrow\downarrow \end{array}$. Surprisingly, the block pattern survives well above the structural *Pnma*-to-*Cmcm* transition at 3.7 GPa [84,86], indicating that its origin is not simply structural but may lie in the electronic and orbital degrees of freedom. Interestingly, *ab initio* calculations find that only at elevated 12 GPa block magnetism should finally give way to the standard stripe magnetism [84]. This coincides with the superconducting dome, suggesting that superconductivity in BaFe_2Se_3 might be related to the competition between the block and stripe states [84]. However, a more recent experiment [151] reports that the transition from the block to stripe magnetism actually occurs at 3 – 4 GPa, i.e., at the same pressure as the structural *Pnma*-to-*Cmcm* transition. The work [151] then proposes that the stripe magnetism is the universal precursor of superconductivity in 123 ladders. This challenges the earlier interpretation and motivates further work to reconcile these conflicting results. A thorough exploration of exotic magnetism in multiorbital ladders is one of the main achievements of this thesis. See Chap. 3 for a discussion of magnetism in iron-based systems and the original results.

2.4 Electronic configuration and Hund's rules

The generic electronic configuration of Fe in an iron-based system can be described on the example of BaFe_2S_3 . The configurations of the individual elements are as follows: Fe: $[\text{Ar}] 3d^6 4s^2$, Ba: $[\text{Xe}] 6s^2$, S: $[\text{Ne}] 3s^2 3p^4$. Inside the crystal, sulfur acquires two electrons, becoming S^{2-} , whereas barium loses two electrons, becoming Ba^{2+} . Both of these ions have a closed-shell configuration. To balance the charge, Fe needs to be in the Fe^{2+} state, hence it loses two 4s electrons and ends up in the $3d^6$ configuration. There are thus 6 valence electrons distributed over 5 orbitals on each Fe^{2+} ion. Such a situation is encountered in most iron-based superconductors [118,142]. This is clearly different from the cuprates, where Cu^{2+} has a configuration $3d^9$, i.e., all orbitals are filled except one, leading to a single-orbital model (see Chap. 1). By contrast, iron-based systems are intrinsically *multiorbital*—the Fe atom itself has a configuration with several active orbitals⁵. Indeed, experiments and *ab initio* calculations confirm that there are multiple bands at the Fermi level which originate in the $3d$ orbitals of Fe [118,144,152–158]. These bands have a two- [153–155] or one-dimensional-like dispersion [91,130,131,159], agreeing with the notion that the (super)current flows in the Fe_2X_2 planes or the Fe_2X_3 ladders, respectively. The multiorbital nature of iron-based systems is crucial, as it brings forth a captivating richness of phenomena that surpasses that of cuprates. This sparked heightened interest in studying multiorbital models within the condensed-matter community. The present thesis serves as a testa-

⁴Here, the spins are aligned antiferromagnetically along the legs and ferromagnetically along the rungs of the ladder, $\begin{array}{cccc} \uparrow\uparrow\downarrow\downarrow & \uparrow\uparrow\downarrow\downarrow \\ \uparrow\uparrow\downarrow\downarrow & \uparrow\uparrow\downarrow\downarrow \end{array}$.

⁵Throughout the thesis, the term *multiorbital* is used to distinguish precisely this: systems where the transition metal itself has an electronic configuration with several active orbitals. In such systems, the Hund's rules play a crucial role in determining the physics. By contrast, the term *multiband* could refer, e.g., to a system with two inequivalent atoms in the unit cell. See a relevant footnote in the discussion of the single-band Hubbard model in Chap. 1.

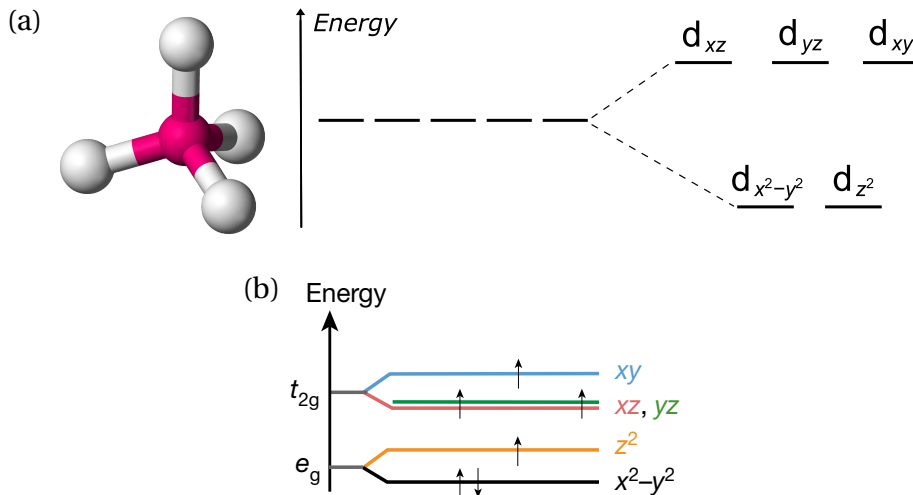


Figure 2.6: (a) Tetrahedral coordination of an isolated Fe^{2+} ion (magenta) by X ligands (white). The result is the crystal-field splitting of the $3d$ orbitals of Fe^{2+} into the t_{2g} manifold (higher in energy) and the e_g manifold (lower in energy). (b) Additional splitting of the t_{2g} and e_g manifolds due to typical distortions of the FeX_4 tetrahedron. The arrows mark the high-spin electron configuration over the $3d$ orbitals. PANEL (A) ADAPTED FROM [160,161]. PANEL (B) TAKEN FROM [118] AND REPRODUCED WITH PERMISSION FROM SPRINGER NATURE.

ment to this sentiment, as the effects unveiled in Chaps. 3–6 would not be possible in a single-orbital setting.

In iron-based systems, the Fe atoms are tetrahedrally coordinated by pnictogens or chalcogens, as marked in Fig. 2.3(a). The crystal field due to the tetrahedral coordination splits the $3d$ levels of Fe into two manifolds. These are the t_{2g} manifold of d_{xz} , d_{yz} , d_{xy} orbitals and the e_g manifold of $d_{x^2-y^2}$, d_{z^2} orbitals; see Fig. 2.6(a) for a graphical representation. Further distortion of the FeX_4 tetrahedron leads to additional splittings within the manifolds, resulting in the hierarchy of orbitals shown in Fig. 2.6(b). The electrons are distributed among the orbitals so as to form the high-spin state, which is common in the tetrahedral complex [162,163]. This high-spin state is a manifestation of the well-known atomic Hund’s rules⁶. They assert the ground-state configuration for a multielectron shell of an isolated atom or ion in terms of the quantum numbers S , L , J .

The three Hund’s rules read:

1. First, maximize the total spin S .
2. Then, for a given S , maximize the total angular momentum L .
3. Finally, favor the total angular momentum $J = |L - S|$ for a less-than-half-filled shell, and favor $J = L + S$ for a more-than-half-filled shell.

⁶For an isolated ion in free space, the Hund’s rules apply directly. However, in a crystal, the interactions behind the Hund’s rules compete with the crystal field [162,164]. This competition decides whether it is more beneficial to (i) first pair up electrons in low-energy orbitals and then maximize spin only in the higher-energy orbitals (if the crystal-field splitting is large), or (ii) avoid pairing at all costs and maximize spin across all nondegenerate orbitals (if the crystal-field splitting is small). The tetrahedral complexes fall into the second scenario.

These rules are conventionally ascribed to the minimization of the local Coulomb repulsion. For instance, for two electrons, the first rule favors the $S = 1$ state over the $S = 0$ one, since the former has an antisymmetric spatial part of the wave function where the electrons are further apart. The energy gain thus follows from the intra-atomic exchange⁷. Colloquially, the first rule is called the “bus-seat rule”: the orbitals are initially filled one-by-one with electrons of parallel spin before any double occupation occurs. Clearly, the configuration of Fig. 2.6(b) conforms to this rule and maximizes S . The third rule is due to the spin-orbit coupling, which, albeit interesting, is not the subject of the present thesis.

The first and the second Hund’s rules are the key ingredients for the physics of the multiorbital systems. They provide a new route to induce strong correlations also away from a metal-insulator Mott transition [165,166], leading to the correlated metallic state dubbed the *Hund’s metal* [165,167,168] (see Chap. 6 for a longer discussion). These rules are also essential to the original results reported in this thesis. Further discussion of Hund’s rules is left for the next section, where they will become apparent within a model Hamiltonian. Chapters 3–6 shall present my original results for which the Hund’s physics plays the key role.

2.5 Three-orbital Hubbard-Kanamori model

As discussed above, the electronic configuration of iron-based systems is multiorbital. The valence electrons originate from the $3d^6$ orbitals of Fe^{2+} . Therefore, in principle, one should incorporate all 5 $3d$ orbitals in the theoretical models, and fill these orbitals with 6 electrons. This was done, for example, using the mean-field Hartree-Fock [103,169–171], density functional theory (DFT) [84,130,131,148,170,172,173], and slave-spin mean-field [37,168,174,175] analyses. These methods can be useful to investigate some gross effects, or even the specific electronic and structural properties (in the case of the DFT), but they incorporate the electronic correlations in a limited manner. As such, they cannot elucidate the more subtle features of the quantum phases, particularly in the low-dimensional 123 ladders, in which quantum effects are enhanced (see Sec. 2.3). A common choice in modelling correlated multiorbital systems is the dynamical mean-field theory (DMFT) [9,10,165], which accurately treats the local quantum fluctuations. However, this is insufficient for the quasi-one-dimensional systems, where also spatial correlations are essential. A proper description of both local and spatial correlations necessitates the use of a more sophisticated method, such as the density-matrix renormalization group (DMRG). Nevertheless, already for the DMFT, the accurate treatment of 5 correlated orbitals is a challenge, and this challenge becomes even more formidable within the DMRG. To address this limitation and preserve the precise treatment of correlations, it is necessary to explore alternative approaches that reduce the number of orbitals without compromising the essential physics.

One such approach is the utilization of a *three-orbital* model of the t_{2g} orbitals (d_{xz} , d_{yz} , d_{xy}). This model was shown to accurately capture the physics of iron-based compounds, on the example of pnictides [156,176]. An illustrative, but simplistic, ar-

⁷However, there are other important contributions; see, e.g., [165] and references therein.

gument justifying the choice of three orbitals is based on the tetrahedral crystal-field splittings [Fig. 2.6(b)]. The t_{2g} and e_g manifolds are separated in energy, hence only one of them should cross the Fermi level. It is, however, not obvious that this would be the t_{2g} manifold, and one cannot forget that, e.g., orbital hybridization complicates this picture. Thus, the more robust evidence for this model comes from the band-structure calculations and photoemission experiments, which find that the d_{xz} , d_{yz} , d_{xy} orbitals indeed dominate at the Fermi level; see [118,144,156,158] and references therein. Another important issue in constructing the reduced model is the choice of the electronic density. Taking the high-spin state of the $3d^6$ electrons [Fig. 2.6(b)], the t_{2g} manifold should be half-filled with 3 electrons on 3 orbitals. On the other hand, if one were to fill the $3d$ orbitals from the bottom up, disregarding the Hund's rule, the t_{2g} manifold should host only 2 electrons (on the d_{xz} , d_{yz} orbitals). Both of these possibilities turn out to be unsatisfactory. Instead, Ref. [156] argues that the appropriate density is actually above half filling, i.e., 4 electrons on 3 orbitals. For this density, the three-orbital model accurately reproduces the behavior of the 6-electron Fe^{2+} valence state in pnictides [156,176,177]. For example, the Fermi surface from the local density approximation is reproduced well [156,177]. In addition, more recent works successfully applied this density to three-orbital models of chalcogenide chains⁸ with Fe^{2+} valence [93,96,101,102].

In the case of the iron-based *ladders*, recent band-structure calculations suggest that the admixture of the $d_{x^2-y^2}$ and/or d_{z^2} orbitals is substantial near the Fermi level [91,130,131]. However, a three-orbital model had already been successful in capturing the physics of the ladder materials [178–180]. In particular, such a model was used to predict [178] and confirm [179] the neutron-scattering result on BaFe_2Se_3 [85]. The same model was also used to qualitatively reproduce the spectra of resonant inelastic x-ray scattering on BaFe_2Se_3 [180]. In both of these cases, the model was applied in a more phenomenological approach, meaning that it was not derived from *ab initio* calculations but instead drew inspiration from the above considerations for pnictides [156,178]. Nonetheless, its success in addressing the experiments *a posteriori* justifies its use. The following subsection provides a more detailed description of this three-orbital model.

The reader should be aware that the aim of this thesis is not to describe a specific compound, but rather to provide a global view on the properties of the 123 ladders through the lens of the multiorbital Hubbard model. To take it even further, the 123 ladders are, in fact, used only as a motivation and a starting point to explore the low-dimensional multiorbital systems with strong correlations. It is only natural that the approach is phenomenological, with an approximate choice of the parameters, as the focus is on the underlying physics and not on the mundane details of the band structures etc. Accordingly, in Sec. 2.6, even the three-orbital model will be reduced to its “bare-bones” variant. This new version will, however, still retain the key physics, and even allow one to better appreciate it. The refinement of the properties found in this work to a particular compound would be the next logical step, which is left for future investigations.

⁸The iron-based chains received less attention than ladders due to the lack of experimental reports of superconductivity. Moreover, the conventional knowledge says that long-range superconductivity should be impossible in a truly one-dimensional system.

2.5.1 Definition of the Hamiltonian

The original parametrization of the Coulomb interactions within a $3d$ shell is due to Kanamori [181]. The resulting (three-orbital) Hubbard-Kanamori Hamiltonian [165] reads

$$H = H_{\text{kin}} + H_{\text{int}}, \quad (2.1)$$

$$H_{\text{kin}} = - \sum_{ij\sigma\gamma\gamma'} t_{\gamma\gamma'} c_{i\sigma\gamma}^\dagger c_{j\sigma\gamma'} + \sum_{i\gamma} \Delta_\gamma n_{i\gamma}, \quad (2.2)$$

$$H_{\text{int}} = U \sum_{i\gamma} n_{i\uparrow\gamma} n_{i\downarrow\gamma} + (U' - J_{\text{H}}/2) \sum_{i,\gamma<\gamma'} n_{i\gamma} n_{i\gamma'} - 2J_{\text{H}} \sum_{i,\gamma<\gamma'} \mathbf{S}_{i\gamma} \cdot \mathbf{S}_{i\gamma'} + J_{\text{H}} \sum_{i,\gamma<\gamma'} \left(P_{i\gamma}^\dagger P_{i\gamma'} + \text{H.c.} \right), \quad (2.3)$$

where the full Hamiltonian H was separated into the kinetic and interaction parts, H_{kin} , H_{int} , respectively. Here, $c_{i\sigma\gamma}^\dagger$ ($c_{i\sigma\gamma}$) creates (annihilates) an electron with spin $\sigma = \{\uparrow, \downarrow\}$ at orbital $\gamma = \{0, 1, 2\}$ of site i . For the 123 ladders, the three orbitals γ can be imagined as belonging to the t_{2g} manifold⁹. In H_{kin} , $t_{\gamma\gamma'}$ denotes the hopping matrix elements, Δ_γ denotes the crystal-field splitting, and $n_{i\gamma} = \sum_\sigma n_{i\sigma\gamma} = \sum_\sigma c_{i\sigma\gamma}^\dagger c_{i\sigma\gamma}$ is the electron density at (i, γ) . The total density (filling) of the system is denoted by $n = N/L$ where N is the total number of electrons and L the number of lattice sites. Importantly, individual ladders are relatively well isolated from one another within the three-dimensional crystal structure. Hence, it suffices to consider only one double-chain lattice of Fe atoms, i.e., the sum over ij in Eq. (2.2) can be restricted to the nearest neighbors in the so-called quasi-1D ladder geometry ($\cdots \square \square \square \square \square \square \cdots$). Indeed, density-functional-theory calculations predict one-dimensional-like electronic dispersion in the ladder compounds [91,130,131,159]. To reduce the computational effort, some model studies even choose the simpler chain geometry, which should still capture the main physics. Nevertheless, one of the main results of this thesis, Chap. 3, relies on using the proper ladder geometry and also identifies for which regimes the chain approximation should be accurate.

The interaction part H_{int} introduces the effects of strong correlations, crucial to correctly capture the physics of the 123 ladders (see Sec. 2.3). The first term in H_{int} is the standard intraorbital Hubbard repulsion $U > 0$, the second is the interorbital repulsion $U' - J_{\text{H}}/2$, the third is the ferromagnetic Hund exchange J_{H} (which couples spins $\mathbf{S}_{i\gamma}$ on different orbitals γ), and the fourth is the interorbital pair hopping ($P_{i\gamma} = c_{i\uparrow\gamma} c_{i\downarrow\gamma}$). Each term of the Hamiltonian is graphically represented in Fig. 2.7. All the interaction terms follow directly from the matrix elements of the fundamental $1/r$ Coulomb interaction; see [37,181–184] for a discussion on how they arise. The rotational symmetry is imposed by the condition $U' = U - 2J_{\text{H}}$ [165]. The Hund coupling J_{H} is usually fixed to $J_{\text{H}} = U/4$, a value widely accepted to be experimentally relevant for iron-based materials [176,185,186]. The original results of this thesis are mostly

⁹The parametrization of the interactions in Eq. (2.3) is actually exact only in cubic symmetry and when the t_{2g} or e_g manifolds are considered separately [165,175]. In practice, however, this form of the Hamiltonian is a common approximation for any multiorbital system with any number of orbitals, e.g., for the full five-orbital $3d$ shell [37,175].

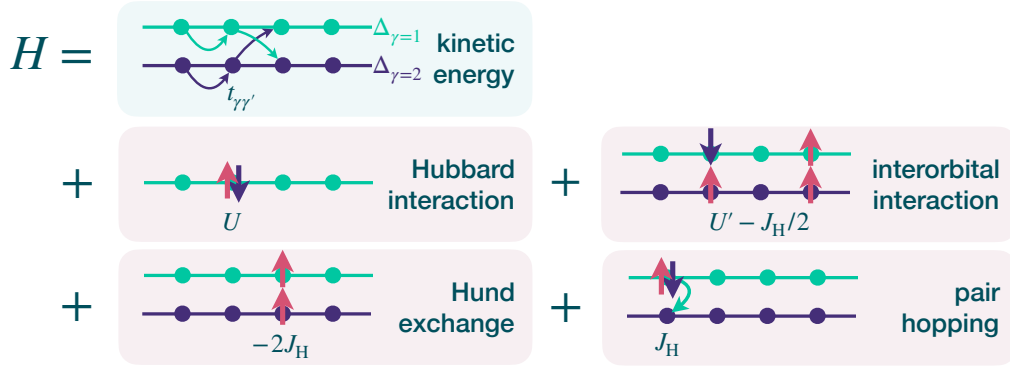


Figure 2.7: Graphical representation of the Hamiltonian (2.1). For clarity, only two orbitals are shown (as parallel lines with green and indigo dots) and the geometry is simplified from a ladder to a chain. The kinetic part H_{kin} is shaded in green, while the interacting part H_{int} in red.

obtained by varying U and n . Intuitively, this could be viewed as changing the pressure and doping the system, respectively. The kinetic-energy parameters are fixed and are discussed briefly below and also in the appropriate Chaps. 3–6. Importantly, the Hamiltonian (2.1) is useful not only to study the iron-based compounds, but also other multiorbital systems, e.g., ruthenates, iridates, etc. [165]. Often, this model is simply referred to as the “multiorbital Hubbard model”.

The key difference in the above Hubbard Hamiltonian w.r.t. the single-orbital version (1.1) is the addition of the Hund coupling J_H . But does Eq. (2.3) actually enforce the Hund’s rules discussed in Sec. 2.4? This can be checked through a simple exercise. One can rearrange the interaction terms so that the interorbital term differentiates between antiparallel and parallel spins, $U' \sum_{i,\gamma \neq \gamma'} n_{i\uparrow\gamma} n_{i\downarrow\gamma'} + (U' - J_H) \sum_{i\sigma,\gamma < \gamma'} n_{i\sigma\gamma} n_{i\sigma\gamma'}$ [165]. This form shows that a configuration of parallel spins in different orbitals is energetically favored over antiparallel spins (and also over double occupancies, since $U' < U$). This agrees with the conventional understanding that the Hund’s rules originate in the minimization of the local Coulomb repulsion. Next, to see where the quantum numbers S and L come into play, one needs to rewrite H_{int} using the local electron number, spin, and orbital angular momentum operators. These operators read, respectively,

$$\hat{n} = \sum_{\sigma\gamma} c_{\sigma\gamma}^\dagger c_{\sigma\gamma}, \quad \mathbf{S} = \frac{1}{2} \sum_{\sigma\sigma'\gamma} c_{\sigma\gamma}^\dagger \boldsymbol{\sigma}_{\sigma\sigma'} c_{\sigma'\gamma}, \quad \mathbf{L} = \sum_{\sigma\gamma\gamma'} c_{\sigma\gamma}^\dagger \boldsymbol{\ell}_{\gamma\gamma'} c_{\sigma\gamma'}, \quad (2.4)$$

where $\boldsymbol{\sigma}_{\sigma\sigma'}$ is a vector of the Pauli matrices, $\ell_{\gamma'\gamma''}^\gamma = -i\epsilon_{\gamma\gamma'\gamma''}$ are the generators of rotations, and the site index i was suppressed for simplicity. Using the above, one finds that [165,184]

$$H_{\text{int}} = (U - 3J_H) \frac{\hat{n}(\hat{n} - 1)}{2} - 2J_H \mathbf{S}^2 - \frac{J_H}{2} \mathbf{L}^2 + \frac{5}{2} J_H \hat{n}. \quad (2.5)$$

This form of the local interaction clearly shows that maximizing first S then L reduces the energy and is favored in the local state, enforcing the Hund’s rules. Although from the point of view of atomic physics the Hund’s rules are a textbook concept, they reveal

a surprising capacity to drive entirely new physics when applied to strongly correlated lattice systems. This thesis showcases the best and most novel examples of that in Chaps. 3–6, where original results are presented. In contrast, Section 2.6 discusses a more established concept in Hund’s physics, the orbital-selective Mott phase.

The specific kinetic-energy parameters used in the model (2.1) (and derived models) will be specified explicitly when numerical results are discussed, i.e., in Sec. 2.6.2 and in Chaps. 3–6. Here, it is useful to stress that for the 123 ladders these parameters are chosen phenomenologically, using pnictides as a guide, and originate in the works [178–180]. This approach aims to emphasize the generic physics of Eq. (2.1) in low dimensions and not the specifics of a given compound. The noninteracting band structure roughly reflects the generic crystal-field splitting expected within the t_{2g} manifold of the distorted tetrahedra forming the 123 ladder compound; compare Fig. 2.6(b) and the inset of Fig. 2.10(c). The electronic density used is $n = 4$ electrons on 3 orbitals. This is the density argued above as appropriate to model the Fe^{2+} valence state in a three-orbital model. Note that the integer density $n = 4$ allows for the emergence of a Mott insulator at large U [178,187]. Therefore, this choice of density can capture the insulating behavior of the 123 ladders at ambient pressures (see Fig. 2.5). Furthermore, for $n = 4$, also the selective localization of some of the orbitals, the orbital-selective Mott phase, is possible for slightly decreased U . This phase was argued to be the actual parent state of the 123 ladders either at ambient [85,180] or increased pressure¹⁰ [90,91]; see Sec. 2.6.1 for further discussion. Therefore, a three-orbital Hubbard model at $n = 4$ seems to cover a major part of the physics of the ladders, and, indeed, this was found to be true in previous investigations [178–180]. In this thesis, also different n shall be explored in order to find new physics which could be realized upon doping. The discussion of the orbital-selective Mott phase and its relevancy for the normal state of ladders will be continued in Sec. 2.6.

In this thesis, the ground states of the Hamiltonians are studied predominantly via the density-matrix renormalization group method. As pointed out several times already, this is the only method that enables an accurate treatment of a strongly correlated multiorbital systems in one dimension. Mean-field methods are inappropriate, as they miss the quantum fluctuations crucial in reduced dimensionality. In particular, the dynamical mean-field theory captures only the local and not the spatial correlations responsible for the development of magnetism and topological properties (studied in Chaps. 3–5). In principle, the exact-diagonalization method could be used, as it is capable of capturing all the correlation effects. However, the exponential growth of the Hilbert space strongly limits the accessible system sizes, especially in the multiorbital setting. For the three-orbital model, already the dimension of the on-site Hilbert space is huge, $4^3 = 64$, hence the total dimension for L sites scales as 64^L . The maximum reachable size with Lanczos exact diagonalization is thus $L \sim 4$. Such a cluster size is too small for reliable investigation of long-range properties (e.g., magnetism) and it cannot capture the shape of the ladder. Therefore, the DMRG method is the only viable choice. It fulfills all the criteria: (i) it incorporates all correlation effects, (ii) it performs best precisely in one dimension, (iii) it allows for reaching system sizes of the order of $L \sim 50$ or more, (iv) it is based on a general entanglement-based ansatz

¹⁰Consistently, increased pressure means decreased U in the model situation (or increased electronic bandwidth).

and does not involve any uncontrolled approximations. This method was essential to discover the exotic correlation-driven quantum phases of my original results (e.g., the block-spiral and spin-flux magnetism in Chap. 3, or the interaction-induced topological phases in Chaps. 4 and 5). To avoid obstructing the discussion of physics, a description of the DMRG method is located in Appendix A. The reader will learn there both the inner workings of the DMRG algorithm and compelling arguments showcasing how it effectively fulfills the above criteria.

Finally, one should be aware that, even for the DMRG, the calculations of a three-orbital model are extremely expensive. This means that accurate simulations of three-orbital systems are mostly restricted to the chain geometry, with ladders being largely out of reach. This is why the previous studies of the 123 family actually used the simplified chain geometry [178–180]. In contrast, in Chap. 3, this thesis explicitly investigates the ladder geometry. The objective is twofold: to determine the regimes or conditions where the chain approximation holds and to reveal novel phases inaccessible in the chain system. To facilitate accurate calculations in the ladder geometry, a simplified “two-orbital” model is employed in this thesis, designed to faithfully reproduce the orbital-selective Mott phase observed in the three-orbital case. The subsequent section provides a detailed description of this phase and the derivation of the effective model. Notably, the simplified model not only streamlines computations but also enhances the understanding and appreciation of the fundamental physics.

2.6 Orbital-selective Mott phase

Orbital selectivity, or orbital differentiation, is a common trend across the families of iron-based systems [118,144,158,165]. This concept highlights that despite the different $3d$ orbitals share the same interactions, their degree of correlation can vary. This is manifested, e.g., by orbital-selective mass enhancements [174] or bandwidth renormalizations [144], shown to be quite universal via extensive surveys of experimental results (see, e.g., [144,175] and references therein). In particular, it was found that out of the three dominant orbitals d_{xz} , d_{yz} , d_{xy} , the last one, d_{xy} , is usually the most correlated [144]. The simultaneous presence of weakly and strongly correlated electrons might explain several inconsistencies in experimental reports on iron-based compounds [37,175]. This ties into a heated debate on whether Fe-based superconductors are strongly or weakly correlated materials and establishes a perspective that they are actually both simultaneously. Finally, orbital selectivity is directly relevant for the superconducting properties, at least for FeSe, in which experiments discovered orbital-selective quasiparticles [188] and pairing [189].

Orbital selectivity has its roots in the effects that lift the orbital degeneracy, i.e., crystal fields and/or inequivalent bandwidths. However, it would not be that robust if it were not for the Hund’s coupling [165,174,190–192]. The Hund’s coupling, in the presence of the interaction U , acts as an orbital decoupler by suppressing *interorbital* charge fluctuations¹¹. As a result, the degree of correlation of each orbital is deter-

¹¹This reads as a paradox: something called Hund’s “coupling” actually “decouples” the orbitals. But note that the decoupling refers to the charge fluctuations which become independent, while the spins between the orbitals are coupled (or correlated) in that they maximize the on-site spin S .

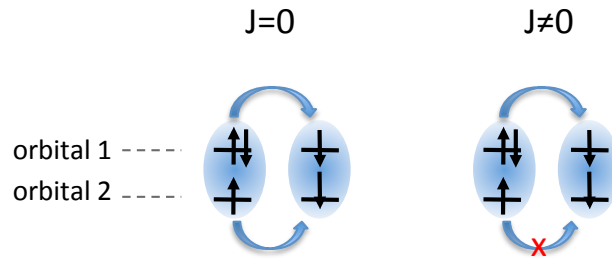


Figure 2.8: A toy example of the orbital-decoupling effect of Hund's coupling. This figure uses the notation $J \equiv J_H$. Consider a half-filled two-orbital system, in which a charge excitation was created on orbital 1. In the absence of Hund's coupling ($J_H = 0$, left), the charge excitation can delocalize in two ways. It can either hop within its own orbital (top arrow), or it can also gain kinetic energy due to hopping of another particle within orbital 2 (bottom arrow). Both processes cost the same energy: they produce equivalent final states on the right lattice site, while the final states of the left lattice site, $|\text{orbital 1, orbital 2}\rangle = |\downarrow, \uparrow\rangle, |\uparrow\downarrow, 0\rangle$, are degenerate for $J_H = 0$. For $J_H \neq 0$, on the other hand, one can easily check using Eq. (2.3) that the latter states are no longer degenerate. The final state $|\uparrow\downarrow, 0\rangle$ will cost more energy than the alternative state $|\downarrow, \uparrow\rangle$. Hence, the bottom process is suppressed, and the charge excitation delocalizes only within its own orbital. The orbitals are effectively decoupled. REPRODUCED FROM [168].

mined by its individual filling, bandwidth, band structure etc. For a simple example of how this comes about, see Fig. 2.8 and its caption, whereas a more thorough explanation of the orbital-decoupling mechanism is given in Ref. [192].

The culmination of orbital selectivity is the orbital-selective Mott phase (OSMP) [165,190,193–195]. In this phase, a subset of orbitals becomes Mott-insulating, while the others remain metallic. This is, of course, driven by the above orbital decoupling effect of the Hund's coupling [191,192], which allows the different orbitals to have such a contrasting response to the same interactions U . The resulting metal-insulator mixture leads to unusual properties, e.g., it is a non-Fermi liquid [165,190,191], and it exhibits exotic magnetism beyond simple ferro- or antiferromagnetic patterns [178,196]. Crucially, this thesis contributes to the discovery of new magnetic structures in the OSMP in the ladder geometry (see Chap. 3).

There are a few different scenarios in which the OSMP can arise [165,175,190]. As mentioned above, the orbital degeneracy needs to be lifted, hence OSMP arises, e.g., in systems where orbitals have different bandwidths [194,195] or are split in energy by the crystal-field splittings [190,191]. Here, it is instructive to discuss the latter case, as outlined in Ref. [190]. Figure 2.9 shows the U vs J_H phase diagram of the three-orbital Hubbard model (2.1) at filling $n = 4$ but in infinite dimensions¹². The kinetic-energy parameters are chosen so that the orbitals are of equal bandwidths, but one of them is split off to higher energies. By tuning the splitting, one may reduce the population

¹²While in Sec. 2.5.1, the three-orbital model was discussed from the perspective of the low-dimensional ladders, here, it is applied to a general high-dimensional multiorbital system. Such systems were the ones for which the mechanism of the OSMP was first elucidated, hence the discussion of such results is appropriate here. The particular choice of infinite dimensions is convenient for the mean-field methods, e.g., the slave-spin mean-field technique and the dynamical mean-field theory.

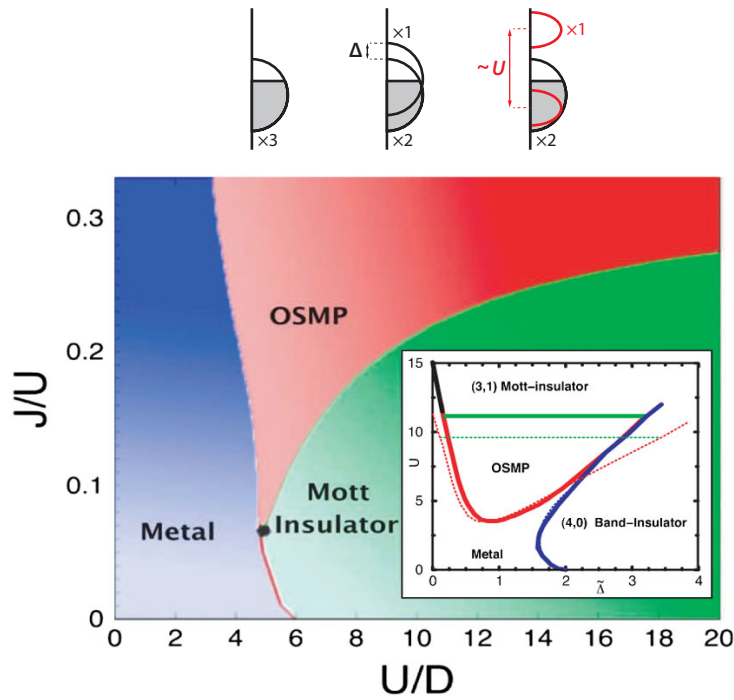


Figure 2.9: Phase diagram of a three-orbital Hubbard model at filling $n = 4$, as a function of the interaction strength U/D and the Hund's coupling J_H/U . The figure uses the label $J \equiv J_H$. D is the half-bandwidth of the assumed semicircular density of states, corresponding to a system in infinite dimensions, convenient for mean-field methods. The crystal field breaks the threefold degeneracy in a way that the upper orbital becomes half-filled while the lower two orbitals are still degenerate and host three electrons in total. The presence of J_H stabilizes an orbital-selective Mott phase (OSMP), where a gap opens in the half-filled orbital (sketched at the top). The phase diagram was obtained within the slave-spin mean-field approach and corroborated with the dynamical-mean field theory. Inset: phase diagram as a function of U and the crystal field $\tilde{\Delta}$ at fixed $J_H/U = 0.25$. SKETCH AT THE TOP USED WITH PERMISSION OF ANNUAL REVIEWS, INC., FROM [165]; PERMISSION CONVEYED THROUGH COPYRIGHT CLEARANCE CENTER, INC. PHASE DIAGRAM AT THE BOTTOM REPRINTED WITH PERMISSION FROM [190]; COPYRIGHT (2009) BY THE AMERICAN PHYSICAL SOCIETY.

of the shifted orbital, until it becomes exactly half-filled. The remaining 3 electrons are then shared by the lower two degenerate orbitals. In this case, one expects that there exists a value of the interaction U that is enough to localize the half-filled orbital, but is too small to localize the other two orbitals, which have a larger kinetic energy due to the degeneracy and have a fractional filling ~ 1.5 . Indeed, this is possible, leading to a robust region of the OSMP, as seen in Fig. 2.9. However, it is required that J_H is large enough to suppress the interorbital fluctuations and decouple the orbitals. Otherwise, particularly for $J_H = 0$, the system simply undergoes a complete full Mott localization upon increasing U . This scenario clearly highlights the key role of J_H in inducing the OSMP [191]. Crucially, while this simplified example assumed that the crystal field tunes one orbital exactly to half filling, this is not actually a requirement. The OSMP is in fact stable across a range of crystal fields, as demonstrated in the inset of Figure 2.9. Ref. [190] also highlights that the OSMP is quite robust w.r.t. doping.

Furthermore, it is expected that the OSMP can withstand small degeneracy lifting in the lower orbitals and weak orbital hybridization, as long as Hund's coupling is the dominant energy scale that quenches the interorbital fluctuations [37,184]. Despite that, it was suggested that orbital hybridization might ultimately disrupt the OSMP at low temperatures (in particular at $T = 0$), transforming it into a very heavy Fermi liquid [165], in which strongly and weakly correlated electrons coexist in the conduction bands [37]. This issue, however, remains unresolved and is subject to ongoing investigation [197–200].

A similar phase diagram to Fig. 2.9 will be presented in Sec. 2.6.2 for a different three-orbital model relevant to the 123 iron-based ladders. There, the density-matrix renormalization group calculations will be discussed which suggest that the OSMP is stable. Within the specific model, one of the orbitals will have narrower bandwidth than the others, along with the energy offset, making it more susceptible to localization. Subsequently, the model will be simplified to a “bare-bones” description of the OSMP, retaining only the key degrees of freedom. Before discussing that further, it is valuable to first establish the presence of the OSMP in the Fe-based ladders based on experimental findings.

2.6.1 Orbital-selective Mott phase in iron-based ladders

Several experimental works point to the orbital-selective Mott phase (OSMP) as the potential parent state of the 123 ladders [85,89,90,201–203]. For example, the experimental work [90] argues that the OSMP is the “true” parent state of superconductivity at *higher* pressures. This perspective is supported by recent *ab initio* investigations [91,204], combining density-functional theory and dynamical mean-field theory (DFT+DMFT) methods. These studies report the presence of complete Mott insulator at ambient pressure in $\text{BaFe}_2(\text{S, Se})_3$, with an orbital-selective Mott phase manifesting at higher pressures. For BaFe_2Se_3 , Ref. [91] faithfully reproduces the experimental resistivity-vs-temperature curve at 12.7 GPa, which is the pressure at which superconductivity emerges (see the phase diagram, Fig. 2.5). Thus, this result recognizes the OSMP as the high-pressure normal state of the 123 ladders, above the superconducting T_c .

An alternative, or complementary, conclusion can be drawn from calculations using the density-matrix renormalization group method [178–180]. These calculations also invoked the OSMP, but to address the experimental results for *ambient* pressure. Using a phenomenological three-orbital Hubbard model (Sec. 2.5), the DMRG simulations predicted [178] and confirmed [179] the neutron-scattering result on BaFe_2Se_3 [85], and also qualitatively reproduced [180] the spectra of resonant inelastic x-ray scattering on the same compound [202]. Note that the assumption of the OSMP at ambient pressure is still consistent with the experimental reports of the insulating behavior. The DMRG studies report the presence of a small pseudogap even in the, in principle, metallic OSMP [180], and this gap aligns with the activation energy of resistivity, 0.13 – 0.18 eV, reported experimentally for BaFe_2Se_3 [88,205].

The above discussion highlights the undeniable significance of the OSMP in understanding the behavior of the 123 ladders. Whether it exists in the high-pressure regime, ambient-pressure regime, or both, its impact on the system's properties is evi-

dent. Moreover, exploring the properties of the OSMP offers valuable insights not only for explaining the experimental results but is also of interest in its own right, especially in low dimensions. This shall become clear from the original results of Chaps. 3 and 4.

2.6.2 Effective model of the orbital-selective Mott phase: the generalized Kondo-Heisenberg Hamiltonian

As discussed in Sec. 2.5.1, performing calculations within the three-orbital Hubbard model can be computationally demanding, particularly in the ladder geometry. Therefore, it becomes necessary to employ a simplified version of the model. Depending on the problem at hand, this thesis employs either the original three-orbital Hubbard model utilized in the aforementioned DMRG studies [178–180] or its streamlined version. Since the simpler model is specifically tailored to capture the OSMP, it is useful to first explore how the OSMP arises in the full three-orbital setting studied via DMRG.

Figure 2.10(a) shows the U vs J_H phase diagram of the three-orbital Hubbard model (2.1) on a chain geometry for filling $n = 4$ [178,180]. The kinetic-energy parameters are phenomenologically chosen to model the physics of the 123 ladders. They are explicitly given in the figure’s caption, whereas the resulting noninteracting bandwidth is shown in the inset of Fig. 2.10(c). The key result is the emergence of the OSMP, which is established once the value of J_H surpasses a threshold determined by the crystal-field splittings. Note the striking similarity between the diagram Fig. 2.10(a) and Fig. 2.9, despite the different dimensionalities and different methods used. Here, the OSMP encompasses the regime with $J_H/U \sim 0.25$ and intermediate U/W , which is considered to be realistic for actual materials [176,185,186]. Crucially, in the OSMP, one orbital $\gamma = 2$ (also labeled c) opens a gap, while the other two orbitals are apparently metallic, albeit with a small pseudogap¹³; see the density of states in Fig. 2.10(b). The OSMP is also characterized by interesting magnetism, which is further studied in Chap. 3.

It is interesting to zoom in on the properties that helped in identifying the above OSMP. Figure 2.10(c) displays the orbital occupancies $\langle n_\gamma \rangle$ vs U/W for the typical value $J_H/U = 0.25$. In the metallic regime at small U , the occupancies $\langle n_\gamma \rangle$ gradually evolve from the noninteracting limit. Interestingly, at a critical U/W , the occupancy of the $\gamma = 2$ orbital “locks” at 1 for a wide range of interactions, while the other two orbitals have occupancies ~ 1.5 . The obtained results are robust w.r.t. variations in the system size, supporting the existence of an OSMP, which persists until a second critical value of U/W is reached, marking the transition to the Mott-insulator regime. Moreover, within the OSMP, a robust magnetic moment develops, as shown in Fig. 2.10(d). This moment reaches the maximum possible value $\langle \mathbf{S}^2 \rangle \simeq 2$ already at an intermediate $U/W \sim 1$. This is usually a feature of an insulator, whereas, here, the system still remains (bad) metallic.

The OSMP in the three-orbital chain is also stable w.r.t. doping. In Fig. 2.11(a), one observes that upon doping the occupancies of the itinerant orbitals increase linearly, while the occupancy of the localized orbital is unaffected and stays locked to 1. Fig. 2.11(b), on the other hand, shows the *intraorbital* charge fluctuations, which are

¹³Despite the presence of the small pseudogap, the orbitals $\gamma = 0, 1$ are hereafter called metallic or itinerant.

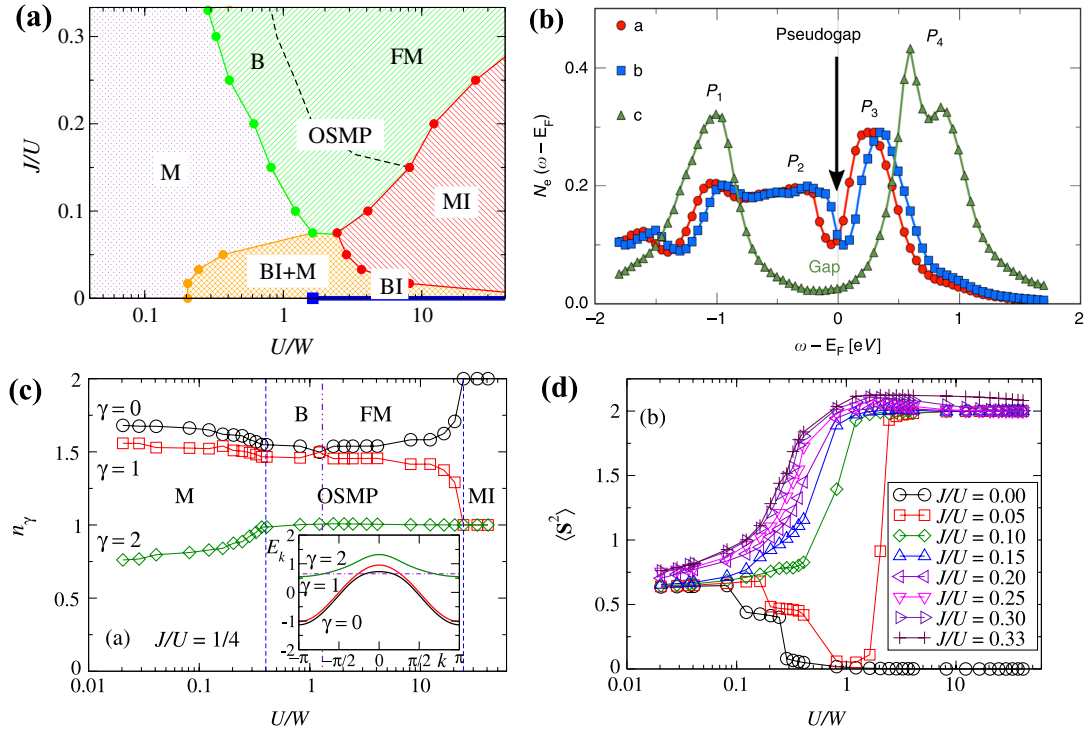


Figure 2.10: Orbital-selective Mott phase studied via DMRG for the three-orbital Hubbard model (2.1) applied to 123 ladders. To facilitate DMRG calculations for three orbitals, the geometry is reduced from the ladder to a chain. The parameters are phenomenological and follow from [178–180]; see Sec. 2.5 for an exhaustive discussion. Explicitly, in eV units, $t_{00} = t_{11} = -0.5$, $t_{22} = -0.15$, with a small hybridization $t_{02} = t_{12} = 0.1$, $t_{01} = 0$ ($t_{\gamma\gamma'}$ is symmetric). The crystal-field splittings are $\Delta_0 = -0.1$, $\Delta_1 = 0$, $\Delta_2 = 0.8$. The resulting noninteracting band structure is shown in the inset of panel (c), where the dashed line marks the Fermi level at $n = 4$ (the density chosen here to model the Fe^{2+} valence). The orbitals $\gamma = 0, 1, 2$ can be attributed to the realistic d_{xz} , d_{yz} , d_{xy} orbitals, respectively; compare the band structure and the crystal-field splitting shown in Fig. 2.6(b). The bandwidth, $W = 2.45$ eV, is used as the energy unit. Note that the same kinetic-energy parameters are used in some of the original results of Chaps. 3–6. In this figure, $J \equiv J_H$. **(a)** Phase diagram as a function of the interaction strength U/W and the Hund’s coupling J_H/U . The labels stand for: a metal (M), a band insulator (BI), a metallic state resembling the BI state (BI+M), Mott insulator (MI). Within the OSMP, one distinguishes block-magnetic (B) and ferromagnetic (FM) states; see Chap. 3 for an investigation of magnetism. **(b)** The density of states within the OSMP ($U/W = 0.8$, $J_H/U = 0.25$). Here, the orbitals are labeled as $\gamma = a, b, c$, corresponding to $\gamma = 0, 1, 2$, respectively. The numbered P labels are irrelevant for the present discussion. **(c)** Average occupancy $n_\gamma \equiv \langle n_\gamma \rangle$ of each orbital vs the interaction U/W at Hund coupling $J_H/U = 0.25$ **(d)** Average local magnetic moment $\langle S^2 \rangle$ vs the interaction U/W for various Hund couplings J_H/U . PANELS (A), (C), (D) REPRINTED WITH PERMISSION FROM [178]; COPYRIGHT (2014) BY THE AMERICAN PHYSICAL SOCIETY. PANEL (B) ADAPTED FROM [180].

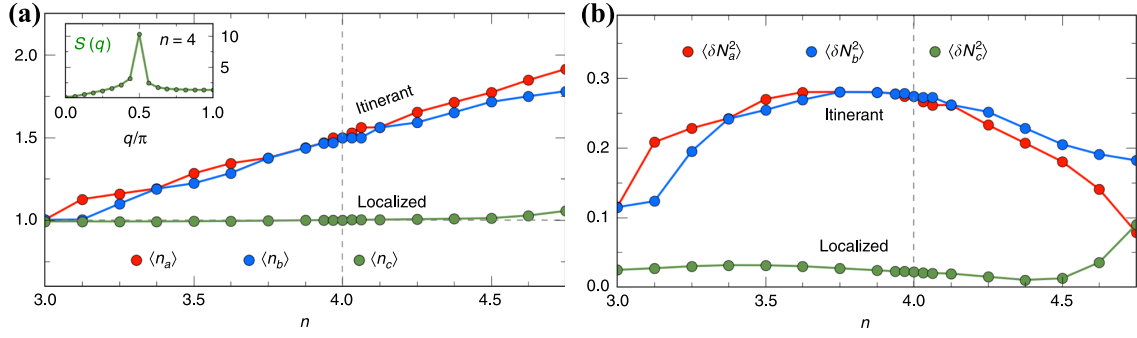


Figure 2.11: Stability of the OSMP with respect to doping for the same model as in Fig. 2.10. The interactions are $U/W = 0.8$, $J_H/U = 0.25$. Here, the orbitals are labeled as $\gamma = a, b, c$, corresponding to $\gamma = 0, 1, 2$ on Fig. 2.10. (a) Average occupancy $\langle n_\gamma \rangle$ of each orbital vs total filling n . The inset shows the total static spin structure factor, which is irrelevant for the present discussion, but shall be addressed in Chap. 3. (b) Average charge fluctuations $\langle \delta N_\gamma^2 \rangle = \langle n_\gamma^2 \rangle - \langle n_\gamma \rangle^2$ for each orbital vs the total filling n . ADAPTED FROM [180].

vanishing in the localized orbital, while substantial in the itinerant ones, and this situation is again unaffected by doping. In summary, the DMRG data confirms the emergence of the OSMP with both local and spatial correlation effects included, with the presence of the magnetic order (see Chap. 3), and even with small interorbital hybridization. As expected, the OSMP is gradually suppressed as J_H/U decreases [Fig. 2.10(a)]. At small interaction strengths U/W , this suppression arises due to competition with the crystal-field splitting that promotes the metallic and band-insulating states. On the other hand, at large interaction strengths U/W , the suppression occurs as a result of competition with the Mott-insulating state.

The above properties of the OSMP enable the derivation of an effective model [196,206]. The derivation starts with the observation that the two itinerant orbitals are very close to degeneracy; see the inset of Fig. 2.10(c). Therefore, when the occupancy of the localized orbital is locked to 1, the other two orbitals behave very similarly w.r.t. several different observables [Fig. 2.10(c) and Fig. 2.11]. They also have nearly identical occupancies ~ 1.5 . To reduce the number of degree of freedoms, the idea is thus to simply drop one of the orbitals and consider a two-orbital model¹⁴. The rationale is that the essential characteristics of the OSMP should be primarily determined by the inherent coexistence of the localized and metallic orbitals, rather than the details and the precise number of the orbitals. Still, this is just an educated guess, which, however, turns out to be a good one. It was shown that the two-orbital model correctly reproduces both the static [196,207] and dynamic [206] properties of the OSMP found in the three-orbital chains.

The next step in the derivation is the observation that the reduced two-orbital model within the OSMP still contains degrees of freedom unnecessary for a low-energy

¹⁴This two-orbital model keeps the orbitals $\gamma = 1, 2$ of the three-orbital model parametrized in Fig. 2.10. In the two-orbital case, also the interorbital hybridization was neglected, as it was found that it does not affect the physics appreciably [196]. However, the values of the hopping amplitudes and the crystal-field splittings were retained.

description. That is, similarly as the single-orbital Hubbard model reduces to the spin-only Heisenberg model for large U and half filling, here, one can eliminate the charge degrees of freedom on the localized orbital. The result would be a model that retains one itinerant orbital, described by the standard Hubbard model and one localized orbital, described by the Heisenberg model. Crucially, the two subsystems should be coupled via the Hund's coupling. Rigorously, to arrive at such a model from the full two-orbital Hamiltonian, one needs to use the Schrieffer-Wolff transformation [208].

The specific Schrieffer-Wolff procedure is outlined in the Supplemental Material of Ref. [196]. Here, only the final result is provided, dubbed the generalized Kondo-Heisenberg (gKH) Hamiltonian,

$$H_K = -t_{11} \sum_{ij\sigma} c_{i\sigma}^\dagger c_{j\sigma} + U \sum_i n_{i\uparrow 1} n_{i\downarrow 1} + K \sum_{ij} \mathbf{S}_{i2} \cdot \mathbf{S}_{j2} - 2J_H \sum_i \mathbf{S}_{i1} \cdot \mathbf{S}_{i2}. \quad (2.6)$$

Figure 2.12 shows a graphical representation of the Hamiltonian. In the above, the notation is kept consistent with Eq. (2.1). The subscripts $\gamma = 1, 2$ mark the itinerant and localized orbitals¹⁵, respectively. $K = 4t_{22}^2/U$ is the Heisenberg-like exchange between spins on the localized orbital. For the 123 ladders, the sums over ij are restricted to the nearest-neighbors in the ladder (or chain) geometry. The electronic density of the gKH model n_K is obtained from the original density n by subtracting the occupancy of the localized orbital, i.e., $n_K = n - 1$. Alternatively, one can also choose $n_K = 3 - n$, due to the particle-hole symmetry of Eq. (2.6). Importantly, for $J_H/U = 0.25$, the description (2.6) is valid even at what might be considered a not too large $U/W \sim 0.8$ [196]. This is because from the point of view of the narrow orbital $\gamma = 2$, such a value of the interaction is already quite large; note the wide gap in Fig. 2.10(b). The interested reader is referred to [196,206,207] (and their Supplemental Materials) for a thorough comparison of different properties between the gKH, the two- and the three-orbital Hamiltonians.

From the physical point of view, the effective Hamiltonian (2.6) reveals that the OSMP naturally favors exotic magnetism. This magnetism follows from the competition between the superexchange mechanism, known from Hubbard-like models, and

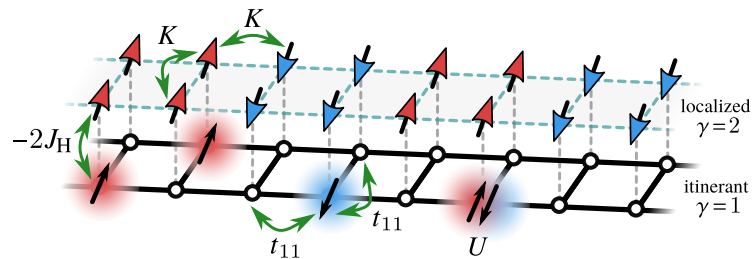


Figure 2.12: Graphical representation of the generalized Kondo-Heisenberg Hamiltonian, Eq. (2.6). SIMILAR FIGURE WAS PUBLISHED IN [O1].

¹⁵Phenomenologically, the itinerant orbital can be attributed to one of the d_{xz}, d_{yz} orbitals, while the localized to d_{xy} . This is consistent with the *ab initio* study on BaFe_2Se_3 [91].

the double-exchange mechanism, known from Kondo lattice models, which generates a unique form of frustration [207]. The exploration of the magnetism in the ladder geometry is the topic of the original results of the next chapter, Chap. 3. On the other hand, Chap. 4 shows how this magnetism leads to the emergence of topological Majorana modes.

From a different, say “technical”, point of view, an important feature of the Hamiltonian (2.6) is its relatively modest Hilbert space dimension, 8^L . Although still more challenging than the single-orbital Hubbard model with 4^L , it is much less complex than the two-orbital model with 16^L , let alone the three-orbital model with its vast 64^L -dimensional space. This property allows for an accurate treatment of the gKH model using the DMRG method on relatively large clusters of size $L \sim 50 - 70$, enabling precise calculations for sizable ladders such as 2×36 . Additionally, even the exact-diagonalization methods can be employed here, reaching usable clusters of size $L \sim 12 - 16$. Finally, note that the DMRG method’s applicability in the ladder geometry is slightly compromised due to the increased entanglement compared to the truly one-dimensional chains. Without the application of the gKH model, the computational cost of simulating a multiorbital ladder would be prohibitively high. Hence, the gKH model plays a pivotal role in the results presented in this thesis, being utilized in most of the original works (Chaps. 3, 4, 6), and being particularly essential for the results of Chap. 3.

QUANTUM MAGNETISM OF IRON-BASED LADDERS: BLOCKS, SPIRALS, AND SPIN FLUX

Having outlined the essential background, in this chapter, I present the first of my original works [O1]. This work explores the magnetic properties of multiorbital systems, setting the stage for the later investigation of electronic and topological effects.

My main achievement here is charting the doping n vs interaction U magnetic phase diagram of the generalized Kondo-Heisenberg model. This model is relevant to the description of the 123 ladders (see Sec. 2.5 and, particularly, Sec. 2.6.2). While previous studies primarily focused on the simpler chain geometry [196,207], I explicitly construct the phase diagram in the ladder configuration. The diagram reveals that the rich magnetic patterns of the orbital-selective Mott phase (OSMP), such as blocks and spirals, remain surprisingly robust as the dimensionality is increased from a chain to a ladder. This establishes a closer connection between the theory, the experiment, and the real materials. Crucially, I also reveal that the ladder supports phases absent in its chain counterpart. For example, I discover incommensurate antiferromagnetism, a robust regime of phase separation (discussed recently in Refs. [209,210]), and a novel quantum spin-flux state (possibly relevant to the results of Ref. [211]). To enhance the reader's understanding and appreciation of these findings, I will now more broadly discuss the previous investigations into magnetism in iron-based systems.

As discussed in Chap. 2, most iron-based materials are magnetically ordered in the parent state, with the typical pattern being the stripe antiferromagnetism [ordering vector $\mathbf{q} = (\pi, 0)$]. However, the magnetic patterns, as realized, for instance, in pnictides, can go beyond the stripes. Perturbations, including pressure, doping, and isovalent chemical substitution, have the potential to induce previously undiscovered forms of magnetism [118]. For example, electron-doping of BaFe_2As_2 with Co replaces the commensurate stripe order with an incommensurate spin-density wave [212]. Instead, hole-doping of the same compound leads to double- \mathbf{q} (or, equivalently, C_4) magnetic

phases [213]. These phases are superpositions of patterns with two different stripe ordering vectors \mathbf{q} , allowing to preserve the tetragonal C_4 symmetry [118,213,214]. There are two realizations of such phases [118,214]. One is the charge-spin density wave, with a nonuniform magnetization that vanishes at even sites and is staggered along the odd sites (realized in hole-doped SrFe_2As_2 [213]). The other is the spin-vortex crystal, characterized by noncollinear (but coplanar) magnetization forming spin vortices that are staggered across the plaquettes (realized in electron-doped $\text{CaKFe}_4\text{As}_4$ [215]).

Unexpected magnetic orders arise also in iron chalcogenides. For instance, in FeTe , a double-stripe magnetic order is observed [216–218]. Unlike the typical single-stripe pattern, this order features double stripes of parallel spins within each Fe layer. Upon doping the compound with additional Fe, resulting in Fe_{1+x}Te , the double-stripe order transforms into an incommensurate (yet collinear) spin-density wave and, with further doping, into noncollinear helical order [219]. In the family of the 245 compounds, e.g., $(\text{K}, \text{Rb})_2\text{Fe}_4\text{Se}_5$, a so-called block-magnetic order emerges, stabilized in the presence of ordered $\sqrt{5} \times \sqrt{5}$ iron vacancies [220–224]. This magnetic order consists of ferromagnetically aligned 2×2 blocks, separated by the vacancies, and antiferromagnetically coupled from block to block. Additionally, in compounds like $\text{K}_x\text{Fe}_{2-y}\text{Se}_2$, phase separation between magnetic iron-vacancy and superconducting regions was observed at nanometer scales (see [119] and references therein).

The chalcogenide ladders of the 123 family inherit the tendency to rich magnetism of their higher-dimensional cousins. Although the standard $(\pi, 0)$ -stripe magnetism remains the most common, there are notable exceptions. For instance, BaFe_2Se_3 exhibits the block magnetism [85–89], similar to $(\text{K}, \text{Rb})_2\text{Fe}_4\text{Se}_5$, but without the need for iron vacancies. Here, the pattern is composed of 2×2 ferromagnetic blocks, ordered along the ladder in a staggered fashion, $\begin{array}{cccc} \uparrow\uparrow & \downarrow\downarrow & \uparrow\uparrow & \downarrow\downarrow \\ \uparrow\uparrow & \downarrow\downarrow & \uparrow\uparrow & \downarrow\downarrow \end{array}$. In the case of CsFe_2Se_3 , recent measurements report some type of incommensurate order to be present [211].

Within the theory department, the magnetic states of the 123 ladders were studied via the Hartree-Fock [170] and density-functional theory [84,130,131,148,173] analyses. Although these methods can answer which magnetic order minimizes the energy, they cannot reliably discover previously unanticipated orders. Moreover, they only approximately capture the crucial electronic correlations. This can lead to overlooking some subtle frustration effects, thus missing the microscopic mechanism behind the origin of a particular magnetic tendency. To mitigate this problem, complementary studies relied on the density-matrix renormalization group method [178,179,196,207]. However, these studies focused on the simplified chain geometry and not the true ladder configuration. Although such an approximation is reasonable, as the ladders are quasi-one-dimensional systems where intrachain coupling should be the most relevant, taking into account the proper ladder geometry permits more orders to emerge. This is clearly found in the original results below. Additionally, these results determine the regimes where the chain approximation holds, e.g., in the block or block-spiral phases. The subsequent Chaps. 4–6 shall leverage that and employ the computationally less demanding chain geometry, which is sufficient for the concepts discussed there.

With the above perspective in mind, it becomes evident that exploring magnetism in correlated multiorbital models in the ladder geometry is a timely task. This is particularly significant due to the prevailing notion that magnetism is important for high- T_c superconductivity (see Chaps. 1 and 2).


Quantum magnetism of iron-based ladders: Blocks, spirals, and spin flux

Maksymilian Środa¹, Elbio Dagotto^{2,3}, and Jacek Herbrych¹

¹*Department of Theoretical Physics, Faculty of Fundamental Problems of Technology, Wrocław University of Science and Technology, 50-370 Wrocław, Poland*

²*Department of Physics and Astronomy, University of Tennessee, Knoxville, Tennessee 37996, USA*

³*Materials Science and Technology Division, Oak Ridge National Laboratory, Oak Ridge, Tennessee 37831, USA*

 (Received 10 May 2021; revised 1 July 2021; accepted 1 July 2021; published 16 July 2021)

Motivated by increasing experimental evidence of exotic magnetism in low-dimensional iron-based materials, we present a comprehensive theoretical analysis of magnetic states of the multiorbital Hubbard ladder in the orbital-selective Mott phase (OSMP). The model we used is relevant for iron-based compounds of the $A\text{Fe}_2X_3$ family (where $A = \text{Cs, Rb, Ba, K}$ are alkali metals and $X = \text{S, Se}$ are chalcogenides). To reduce computational effort, and obtain almost exact numerical results in the ladder geometry, we utilize a low-energy description of the Hubbard model in the OSMP—the generalized Kondo-Heisenberg Hamiltonian. Our main result is the doping vs interaction magnetic phase diagram. We reproduce the experimental findings on the $A\text{Fe}_2X_3$ materials, especially the exotic block magnetism of BaFe_2Se_3 (antiferromagnetically coupled 2×2 ferromagnetic islands of the $\uparrow\uparrow\downarrow\downarrow$ form). As in recent studies of the chain geometry, we also unveil block magnetism beyond the 2×2 pattern (with block sizes varying as a function of the electron doping) and also an interaction-induced frustrated block-spiral state (a spiral order of rigidly rotating ferromagnetic islands). Moreover, we predict new phases beyond the one-dimensional system: a robust regime of phase separation close to half filling, incommensurate antiferromagnetism for weak interaction, and a quantum spin-flux phase of staggered plaquette spin currents at intermediate doping. Finally, exploiting the bonding/antibonding band occupations, we provide an intuitive physical picture giving insight into the structure of the phase diagram.

DOI: [10.1103/PhysRevB.104.045128](https://doi.org/10.1103/PhysRevB.104.045128)

I. INTRODUCTION

The lattice geometry plays an important role in quantum many-body systems, especially if the problem is reduced to one (1D) or two (2D) dimensions. For example, the crossover from 1D chains to 2D planes of the spin-1/2 Heisenberg model shows that the system behaves fundamentally differently if one considers an even or odd number of coupled chains [1]. Consequently, in the last three decades, there was a tremendous effort devoted to understanding the physics of quantum ladders, i.e., the systems at the crossroads between 1D and 2D worlds. Furthermore, while unbiased analytical or numerical calculations are often not possible in 2D, the 1D chains and quasi-1D ladders—due to the possibility of an accurate treatment via quasixact numerical simulations—have become a playground for condensed-matter physicists to test various theoretical scenarios.

The interest in the physics of the ladder systems goes beyond a toy model investigation. There are many materials whose lattice structure is of the ladder geometry. The unique interplay between theory and experiment in low-dimensional systems allows for an in-depth understanding of various complex phenomena. For example, within cuprates the so-called *telephone-number* two-leg ladder compounds $(\text{La, Sr, Ca})_{14}\text{Cu}_{24}\text{O}_{41}$ were extensively studied motivated by the presence of pressure-induced high-critical-temperature superconductivity [2–4]. Interestingly, the latter was

numerically predicted [5,6], showing the power of theoretical investigation of low-dimensional systems. Another series of cuprate materials, $\text{Sr}_x\text{Cu}_y\text{O}_z$, allows one to study the differences between various lattice geometries, from chains (Sr_2CuO_3), through two- (SrCu_2O_3) and three-leg ($\text{Sr}_2\text{Cu}_2\text{O}_5$) ladders, to 2D planes (SrCuO_2). The first of these compounds is one of the best realizations of a 1D system, with the intrachain exchange integral being four orders of magnitude larger than the interchain one [7]. Despite that the hole doping necessary for superconductivity is hard to achieve, the next two exhibit a large contribution of magnons [8,9] to the thermal conductivity, in agreement [10,11] with the thermal current being a constant of motion of 1D quantum spin systems.

Iron-based ladders are far less explored, especially from the theoretical perspective. Recent experimental investigations have shown that the two-leg ladder materials from the so-called 123 family, i.e., $A\text{Fe}_2X_3$ where A are alkali metals and X chalcogenides, become superconducting under pressure [12–14], as in the Cu-based equivalents. Canonical $(\pi, 0)$ order, i.e., staggered antiferromagnetic (AFM) ordering along the legs and ferromagnetic (FM) along the rungs, was identified in $(\text{Ba, K})\text{Fe}_2\text{S}_3$ [15] and $(\text{Cs, Rb})\text{Fe}_2\text{Se}_3$ [16–18]. More recent measurements on CsFe_2Se_3 [19] suggest that an incommensurate order emerges in this compound instead of the AFM.

Interestingly, the magnetic orders identified in $A\text{Fe}_2X_3$ ladders display more variety than those found in cuprates. In a

series of experiments on the BaFe_2Se_3 compound, an exotic block-magnetic order was reported, with the spins forming FM islands which are then AFM coupled $\uparrow\uparrow\downarrow\downarrow\uparrow\uparrow\downarrow\downarrow$ (on the ladder this takes the form of 2×2 FM blocks which are AFM coupled). This unusual magnetic state was identified with the help of inelastic neutron scattering (INS) [20], x-ray [21] and neutron powder diffraction [21–23], and muon spin relaxation [21]. Remarkably, yet again, the block-magnetic order was predicted by numerical calculations [24]. It can be argued that the spin arrangement of the BaFe_2Se_3 ladder is a low-dimensional equivalent of the magnetic state found in 2D iron-based systems, i.e., the double stripe or staggered dimer ordering found in FeSe [25], the $\sqrt{5} \times \sqrt{5}$ iron vacancies ordering in $(\text{K}, \text{Rb})_{0.8}\text{Fe}_{1.6}\text{Se}_2$ [26–29], or the blocklike magnetism found in the family of 245 iron-based superconductors $(\text{K}, \text{Rb})_2\text{Fe}_4\text{Se}_5$ [30,31]. Also, similar block magnetism was predicted in a 1D iron selenide compound Na_2FeSe_2 [32].

The theoretical analysis of iron-based systems is a challenging task due to their multiorbital nature. While the single-orbital Hubbard model is often sufficient to describe the Cu-based parent compounds (with the charge density close to one electron per site), the Fe-based materials need (in principle) five orbitals filled with six electrons; i.e., they have to be described by the multiorbital Hubbard model with intra- and interorbital interactions treated on an equal footing. As a consequence, exact-diagonalization many-body calculations are challenging to achieve due to the exponential growth of the Hilbert space of the Hamiltonian— $\dim(\mathcal{H}) = 4^{\Gamma L}$ with Γ the number of active orbitals and L the number of sites in the system. In order to study the physics of such systems, we must rely on some form of approximations. For example, the full five-orbital Hubbard model was investigated via the mean-field Hartree-Fock analysis [33–36], revealing a complex filling-Hund/Hubbard interaction magnetic phase diagram with many competing phases. Many of such phases were also confirmed by density functional theory [34,37–42]. Moreover, the electronic properties of the multiorbital Hubbard model were extensively investigated via the dynamical mean-field theory [43–45], especially the orbital-selective Mott phase (OSMP), namely the possibility of the localization of a fraction of the conduction electrons (on one or more orbitals) [46–49]. The latter phase is regarded as a promising candidate for the parent state of iron-based superconductors [50–53] and, most relevantly, of the 123-family ladders [18,47,49,54–56].

Despite their value, the aforementioned theoretical approaches are limited in that they cannot properly incorporate the effects of quantum fluctuations over long distances. This issue is particularly important for low-dimensional systems, where it is well known that quantum fluctuations must be treated accurately, thereby requiring full many-body calculations. In order to facilitate the latter, an alternative route has to be taken, such as decreasing the number of considered orbitals. For instance, it was shown [57] that the three-orbital Hubbard model can accurately describe the physics of iron-based materials. In the latter, the e_g orbitals ($d_{x^2-y^2}$ and d_{z^2}) are far enough from the Fermi level to be neglected, rendering only the t_{2g} orbitals (d_{xy} , d_{xz} , d_{yz}) active. Importantly, the three-orbital model was used to predict [24,58] and confirm

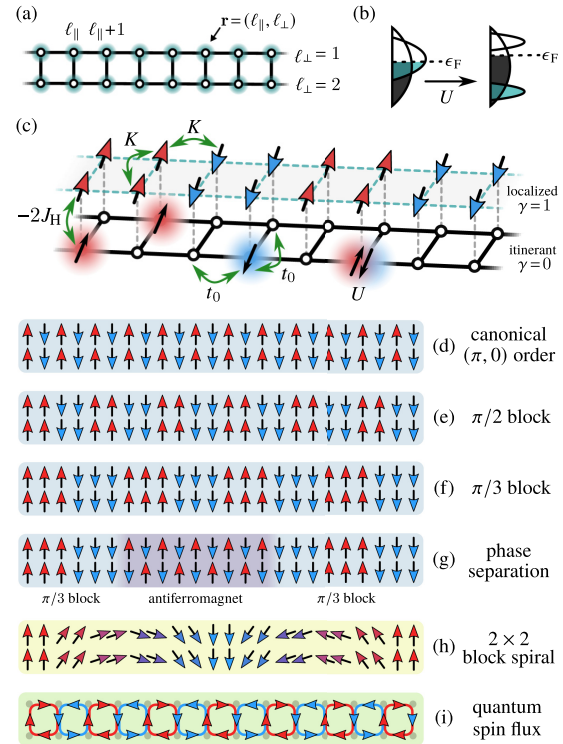


FIG. 1. Schematic representation of (a) the ladder geometry, (b) density of states in the orbital-selective Mott phase, (c) the generalized Kondo-Heisenberg model, (d)–(i) the unveiled exotic magnetic orders.

[59] the INS result on BaFe_2Se_3 [20] related to the block-magnetic order, while also tracing its origin to the presence of the OSMP. Nevertheless, it should be noted that accurate many-body simulations of three-orbital systems are mostly restricted to the chain geometry, with ladders being largely out of reach. Recently, it was realized that one may further reduce the number of degrees of freedom captured within minimal models by noting that the d_{yz} and d_{xz} orbitals are close to being degenerate in tetragonal systems of the 123 family [49,54]. As a result, two-orbital models were designed, which, within the OSMP, were found to correctly reproduce both the static [60,61] and dynamic [62] properties of the three-orbital chains.

In this work, we use such a minimal approach to go beyond the chain geometry—bridging the gap between theory and experiment—and perform a comprehensive analysis of the magnetic phases within the OSMP of a multiorbital Hubbard ladder. To facilitate numerically exact many-body calculations, we focus on a two-orbital model, which we further map onto an accurate low-energy description, the generalized Kondo-Heisenberg Hamiltonian. We unveil a rich variety of exotic magnetic phases [see Figs. 1(d)–1(i) for sketches], summarized in our *central result*: the doping vs interaction magnetic phase diagram. In particular, we reproduce the

experimental finding on BaFe_2Se_3 , i.e., the $\uparrow\uparrow\downarrow\downarrow$ block phase, and predict the possibility of experimentally realizing larger blocks, e.g., $\uparrow\uparrow\downarrow\downarrow\downarrow\downarrow$, by doping this or related compounds. Furthermore, we report a highly unusual block-spiral state (with the blocks rigidly rotating throughout the system), discovered first using a chain geometry [61], and predict this spiral to be stable also on the experimentally relevant ladder. Surprisingly, we reveal that the ladder supports also phases absent in its chain counterpart. For example, in the vicinity of half filling, we discover incommensurate AFM order as well as a robust regime of phase separation (relating our effort to previous works on cuprates and manganites, respectively). Last but not least, we report the emergence of a novel quantum spin flux state at intermediate doping, with staggered spin currents circulating around 2×2 plaquettes. Our magnetic phase survey is supplemented by an intuitive physical picture involving the bonding/antibonding ladder bands, which explains the observed magnetic tendencies and generalizes our conclusions to models with more orbitals.

The paper is organized as follows. In Sec. II, we introduce the two-orbital Hubbard ladder relevant for the AFe_2X_3 compounds and simplify this formalism into the generalized Kondo-Heisenberg Hamiltonian. Then, we describe the computational method used to solve the many-body problem. In Sec. III, we present the main result: the doping vs interaction magnetic phase diagram. Each reported phase is discussed in detail within three subsections III A, III B, III C, addressing the cases of large, low, and intermediate doping, respectively. Finally, in Sec. IV, we give a summary and draw conclusions. In the Appendix, we discuss additional details regarding the computational accuracy.

II. MODEL AND METHOD

We aim to establish the magnetic properties, within the OSMP, of a two-orbital Hubbard model on a two-leg ladder. In the generic SU(2)-symmetric form, the Hamiltonian reads

$$\begin{aligned}
 H_{\text{H}} = & \sum_{\gamma(\mathbf{r}\mathbf{m})\sigma} t_{\gamma} c_{\gamma\mathbf{r}\sigma}^{\dagger} c_{\gamma\mathbf{m}\sigma} + \sum_{\gamma\mathbf{r}} \Delta_{\gamma} n_{\gamma\mathbf{r}} \\
 & + U \sum_{\gamma\mathbf{r}} n_{\gamma\mathbf{r}\uparrow} n_{\gamma\mathbf{r}\downarrow} + (U - 5J_{\text{H}}/2) \sum_{\mathbf{r}} n_{0\mathbf{r}} n_{1\mathbf{r}} \\
 & - 2J_{\text{H}} \sum_{\mathbf{r}} \mathbf{S}_{0\mathbf{r}} \cdot \mathbf{S}_{1\mathbf{r}} + J_{\text{H}} \sum_{\mathbf{r}} (P_{0\mathbf{r}}^{\dagger} P_{1\mathbf{r}} + \text{H.c.}). \quad (1)
 \end{aligned}$$

Here, $c_{\gamma\mathbf{r}\sigma}^{\dagger}$ ($c_{\gamma\mathbf{r}\sigma}$) creates (annihilates) an electron with spin $\sigma = \{\uparrow, \downarrow\}$ at orbital $\gamma = \{0, 1\}$ of site $\mathbf{r} = (\ell_{\parallel}, \ell_{\perp})$, where $\ell_{\parallel} = \{1, \dots, L_{\parallel}\}$ and $\ell_{\perp} = \{1, 2\}$ enumerate the sites in directions parallel and perpendicular to the legs, respectively. The total number of sites is $L = 2 \times L_{\parallel}$. The $(\mathbf{r}\mathbf{m})$ brackets indicate summation over nearest-neighbor (NN) sites in the ladder geometry [see the sketch in Fig. 1(a)]. The first two terms of the Hamiltonian constitute the kinetic energy part, with t_{γ} denoting the hopping matrix elements, Δ_{γ} denoting the crystal-field splitting, and $n_{\gamma\mathbf{r}} = \sum_{\sigma} n_{\gamma\mathbf{r}\sigma} = \sum_{\sigma} c_{\gamma\mathbf{r}\sigma}^{\dagger} c_{\gamma\mathbf{r}\sigma}$ being the total electron density at (γ, \mathbf{r}) . The remaining four terms form the interaction part: the first is the standard intra-orbital Hubbard repulsion $U > 0$, the second is the interorbital repulsion $U - 5J_{\text{H}}/2$, the third is the ferromagnetic Hund

exchange J_{H} (which couples spins $\mathbf{S}_{\gamma\mathbf{r}}$ on different orbitals γ), and the fourth is the interorbital pair hopping ($P_{\gamma\mathbf{r}} = c_{\gamma\mathbf{r}\uparrow} c_{\gamma\mathbf{r}\downarrow}$). Note that all the interaction terms follow directly from the matrix elements of the fundamental $1/r$ Coulomb interaction [63–65].

We adopt the following set of hopping amplitudes (eV units): $t_0 = 0.5$ and $t_1 = 0.15$. The interorbital hybridization is neglected, as it was shown that a realistically small hybridization leaves the overall physics unaffected [60]. Moreover, here, we choose equal hoppings along the legs and the rungs, i.e., $t_{\gamma}^{\parallel} = t_{\gamma}^{\perp} = t_{\gamma}$, although density-functional theory [34] and spin-wave theory [20] analyses suggest that this is only an approximation for real materials. Nevertheless, below we shall argue that such a choice does not compromise the generality of our results. The crystal-field splittings are assumed as (eV units) $\Delta_0 = 0$, $\Delta_1 = 1.6$, where the latter is taken large enough to energetically separate the two orbitals. The rationale behind the above values of t_{γ} and Δ_{γ} is to reproduce the essential feature of the band structure of the 123-family materials—the coexistence of nondegenerate wide and narrow orbitals [24,34,43,46,56,57]—and, in this sense, these values are generic. The total kinetic-energy bandwidth $W = 3.55$ eV is here the energy unit throughout the paper. To further reduce the number of free parameters in the model, we also fix the Hund exchange to $J_{\text{H}} = U/4$, a value widely accepted to be experimentally relevant for iron-based materials [66–70]. Finally, we note that our choice of model parameters ensures that for a wide region of electronic fillings, $2 < n_{\text{H}} < 3$, and Hubbard interaction strengths, $U \gtrsim W$, the ground state is in the OSMP [60,62], where the narrow ($\gamma = 1$) orbital undergoes Mott localization while the wide ($\gamma = 0$) orbital remains itinerant [see Fig. 1(b)]. In the following, we shall vary both n_{H} and U to produce a rich variety of magnetic phases [see Figs. 1(d)–1(i)].

The selective localization implies that the charge degrees of freedom in the narrow orbital are essentially frozen out and should no longer play a role in low-energy processes. Let us consider the single-particle spectral function of the two-orbital Hubbard ladder (1) defined as

$$\begin{aligned}
 A_{\gamma}(\mathbf{q}, \omega) = & -\frac{1}{\pi\sqrt{L}} \sum_{\mathbf{r}} e^{i\mathbf{q}(\mathbf{r}-\mathbf{c})} \text{Im} \left\langle c_{\gamma\mathbf{r}}^{\dagger} \frac{1}{\omega^{+} + (H - \epsilon_{\text{GS}})} c_{\gamma\mathbf{c}} \right\rangle \\
 & -\frac{1}{\pi\sqrt{L}} \sum_{\mathbf{r}} e^{i\mathbf{q}(\mathbf{r}-\mathbf{c})} \text{Im} \left\langle c_{\gamma\mathbf{r}} \frac{1}{\omega^{+} - (H - \epsilon_{\text{GS}})} c_{\gamma\mathbf{c}}^{\dagger} \right\rangle. \quad (2)
 \end{aligned}$$

where $c_{\gamma\mathbf{r}}^{\dagger} = \sum_{\sigma} c_{\gamma\mathbf{r}\sigma}^{\dagger}$, $\mathbf{c} = (L_{\parallel}/2, 1)$, $\mathbf{q} = (q_{\parallel}, q_{\perp})$, $\omega^{\pm} = \omega + i\eta$, and $\langle \cdot \rangle \equiv \langle \text{GS} | \cdot | \text{GS} \rangle$ with $|\text{GS}\rangle$ being the ground-state vector with energy ϵ_{GS} . In Fig. 2, as an example we show the case of $A_{\gamma}(\mathbf{q}, \omega)$ for $\gamma = 0, 1$, $n_{\text{H}} = 2.75$, and $U/W = 1$. Several conclusions can be drawn from the results. (i) The interaction U heavily modifies the dispersion relation which in the $U \rightarrow 0$ limit would have a simple cosine form (see also the discussion in the next section). (ii) As expected in the OSMP regime, already at $U/W \simeq 1$ the electrons at the $\gamma = 1$ orbital localize, which can be deduced from the flat (momentum-independent) spectral function $A_1(\mathbf{q}, \omega)$. The two modes of the latter, separated by a wide charge gap, resemble the lower and upper Hubbard subbands of a Mott insulator. Similar

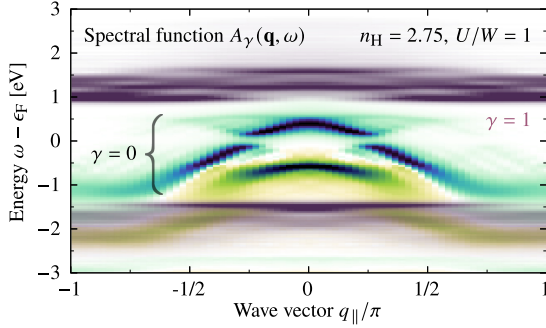


FIG. 2. Single-particle spectral function $A_\gamma(\mathbf{q}, \omega)$ of the two-orbital Hubbard model (1) in the vicinity of the Fermi level ϵ_F . The itinerant ($\gamma = 0$) orbital is presented as blue-green color, whereas the localized ($\gamma = 1$) as dark purple. Both $q_\perp = 0, \pi$ components of each orbital are displayed. The frequency resolution was chosen to be $\Delta\omega = 0.02$ eV with the broadening $\eta = 2\Delta\omega$. The results were obtained for a ladder of $L = 72$ sites, filling $n_H = 2.75$, and interaction $U/W = 1$.

properties of the OSMP were also identified in 1D systems [61,62].

The charge gap of the localized orbital is robust enough to result in vanishing charge fluctuations already for $U \simeq W$. Correspondingly, the double occupancy of the latter orbital can be traced out via the standard Schrieffer-Wolff transformation [71], leaving only the spin degrees of freedom active. Such a procedure results [60] in the generalized Kondo-Heisenberg (gKH) Hamiltonian

$$H_K = t_0 \sum_{(\mathbf{r}\mathbf{m})\sigma} c_{0\mathbf{r}\sigma}^\dagger c_{0\mathbf{m}\sigma} + U \sum_{\mathbf{r}} n_{0\mathbf{r}\uparrow} n_{0\mathbf{r}\downarrow} + K \sum_{(\mathbf{r}\mathbf{m})} \mathbf{S}_{1\mathbf{r}} \cdot \mathbf{S}_{1\mathbf{m}} - 2J_H \sum_{\mathbf{r}} \mathbf{S}_{0\mathbf{r}} \cdot \mathbf{S}_{1\mathbf{r}}, \quad (3)$$

where $K = 4t_0^2/U$ is a Heisenberg-like exchange between the localized $\gamma = 1$ spins. See Fig. 1(c) for a graphical representation of the Hamiltonian. The electronic filling n_K of the gKH model is obtained from the original filling n_H by subtracting the occupancy of the $\gamma = 1$ orbital, i.e., $n_K = n_H - 1$. However, it is noteworthy that due to the particle-hole symmetry of (3), one could equivalently choose $n_K = 3 - n_H$. The effective description (3) reveals that the OSMP naturally favors exotic magnetism due to the coexistence of itinerant electrons and well-developed local magnetic moments. In particular, within the OSMP, the Hund exchange induces a remarkably complex correlated behavior where the total on-site magnetic moment (\mathbf{S}_r^z) ($\mathbf{S}_r = \sum_\gamma \mathbf{S}_{\gamma r}$) is completely maximized [24,58,60] as in an insulator, despite the system remaining metallic.

Previous comparisons between models (1) and (3) concluded that the latter not only qualitatively but also quantitatively reproduces both the static [60,61] and dynamic [62] properties of the former (provided that the system is in the OSMP). Accordingly, hereafter, in our numerical calculations, we exclusively use the model (3), utilizing its considerably smaller Hilbert space to perform extensive simulations with feasible computational cost. The many-body ground state

(temperature $T = 0$) of the system is studied via the density matrix renormalization group (DMRG) method within the single-center site approach [72,73]. Throughout the DMRG procedure, we typically keep up to $M = 1200$ states and perform 20–30 full sweeps in the finite-size algorithm, maintaining the truncation error below 10^{-6} . We focus on the subspace with zero total spin projection and a fixed particle number N , which sets the filling $n_K = N/L$. Open boundary conditions are assumed. All results are obtained using the DMRG++ computer program developed at Oak Ridge National Laboratory [73,74], and the input scripts are available online [75]. Additional details regarding the computational accuracy are discussed in the Appendix.

The key observables used to identify the magnetic orders are the total spin-spin correlation function ($\mathbf{S}_r \cdot \mathbf{S}_m$) (viewed as a function of distance or on NN bonds) and its Fourier transform—the spin structure factor, defined as $S(\mathbf{q}) = \langle \mathbf{S}_q \cdot \mathbf{S}_{-\mathbf{q}} \rangle$, where $\mathbf{S}_q = (1/\sqrt{L}) \sum_r \exp(i\mathbf{q}r) \mathbf{S}_r$. These two quantities, albeit very useful, cannot distinguish between all possible magnetic orders. Therefore, we supplement our analysis with the chirality correlation function, which is explicitly defined in the next section. Note that the exotic magnetic patterns we observe are not static (as would be the case for a combination of domain walls or a spin density wave), but exhibit significant quantum fluctuations. For example, in the case of the block pattern $\uparrow\uparrow\downarrow\downarrow$ (whose extended version we report), exact diagonalization studies confirm [59] that the many-body ground state is in at least 50% of the singlet form $|\uparrow\uparrow\downarrow\downarrow\rangle - |\downarrow\downarrow\uparrow\uparrow\rangle$. Accordingly, the individual magnetic blocks should be considered as regions with strong FM correlations, as opposed to domains with finite magnetization.

III. RESULTS

To better understand the general structure of the magnetic phase diagram reported below, it is instructive to recall the properties of a noninteracting ($U = 0$) ladder system. In such a case, the Hamiltonian (3) retains only the kinetic-energy term which can be easily diagonalized by first introducing the bonding and antibonding (symmetric and antisymmetric, respectively) combinations of the rung states and then Fourier transforming along the leg direction (here, we assume periodic boundary conditions). In the general case of unequal leg and rung hoppings, one obtains the dispersion relation $\epsilon(\mathbf{q}) = 2t_0^\parallel \cos(q_\parallel) + t_0^\perp \cos(q_\perp)$, consisting of two bands (bonding $q_\perp = 0$ and antibonding $q_\perp = \pi$) separated by the energy $2t_0^\perp$ [see Fig. 3(a)]. The respective fillings are denoted by n_K^b, n_K^a . Since these bands can host at most $2L_\parallel$ electrons, the maximum possible filling is $\max\{n_K^b\} = \max\{n_K^a\} = 1$, and thus $n_K^b, n_K^a \in [0, 1]$, consistent with the relation $n_K = n_K^b + n_K^a$. Note that this dispersion corresponds only to the $\gamma = 0$ orbital, as the $\gamma = 1$ orbital is completely localized within the model (3). To avoid any confusion, hereafter, we reserve the term *band* to denote the latter bonding/antibonding bands and not the underlying orbitals.

Owing to the band structure, the behavior of the ladder system is nontrivial even in the noninteracting case. The Fermi level ϵ_F can cross either one or both bands [see the sketches in Fig. 3(c)], giving rise to qualitatively different Fermi “surfaces” with two ($\pm k_F^b$) or four ($\pm k_F^b, \pm k_F^a$) Fermi

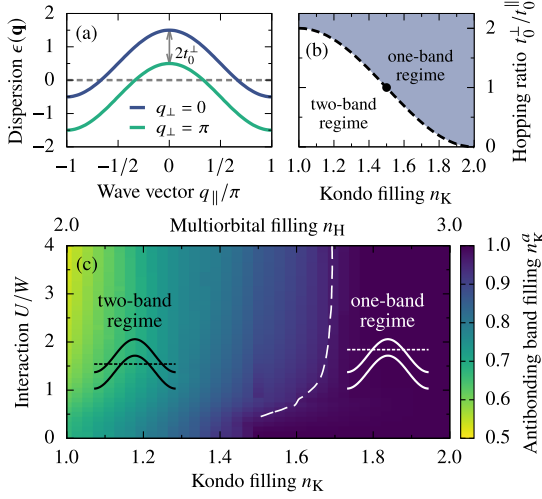


FIG. 3. Properties of the band structure. (a) Noninteracting ($U = 0$) band structure of (3) for $t_0^{\perp} = t_0^{\parallel}$. The dispersion concerns only the itinerant $\gamma = 0$ orbital, as the $\gamma = 1$ orbital is completely localized. The dashed line marks the Fermi level ϵ_F at half filling, $n_K = 1$. (b) n_K - t_0^{\perp} phase diagram of the noninteracting ladder. The dashed line marks the point where the Fermi level touches the tip of the antibonding ($q_{\perp} = \pi$) band, while the dot marks the phase boundary between the one- and two-band regimes for $t_0^{\perp} = t_0^{\parallel}$. (c) DMRG results for the antibonding band filling n_K^a vs the interaction U and the total filling n_K at fixed $t_0^{\perp} = t_0^{\parallel}$. The plot is composed of 37×40 data points obtained for the generalized Kondo-Heisenberg ladder of $L = 72$ sites. The sketches show the one-band ($n_K^a \simeq 1$) and two-band (both bands fractionally occupied) regimes. The dashed line is a contour at $n_K^a \simeq 1$.

points, respectively. Whenever convenient, we will use the abbreviated notation $\mathbf{k}_F = \{k_F^b, k_F^a\}$ to collectively refer to both wave vectors. To tune between the one- and two-band regimes, one may use both the filling n_K (to shift the Fermi level) and/or the rung hopping t_0^{\perp} (to vary the band separation). This is summarized in the n_K - t_0^{\perp} phase diagram [76], Fig. 3(b), where one clearly recognizes the complementary role of the two parameters in deciding whether one or two bands are fractionally occupied.

The picture of one- and two-band regimes can be extended also beyond the $U = 0$ case. Here, although finite U inevitably renormalizes the band fillings, the latter retain their physical meaning and can be calculated in a straightforward manner. In Fig. 3(c), we show the antibonding band filling n_K^a (with $n_K^a = n_K - n_K^b$) as a function of the total filling n_K and the interaction strength U at fixed $t_0^{\perp} = t_0^{\parallel}$. We observe that there exists a robust region where $n_K^a \simeq 1$; i.e., the antibonding band is completely filled. This condition provides a convenient definition of the one-band regime for a general $U \neq 0$. Starting from $U = 0$, the boundary between the one- and two-band regimes occurs at three-quarter filling $n_K = 1.5$ [in agreement with Fig. 3(b)] and shifts rightward with increasing U . Notably, although the width of the one-band regime decreases with

the interaction, it does not vanish up to the largest considered $U/W = 4$.

The significance of the above discussion lies in the fact that the block magnetism of the gKH chain was shown to be controlled by the Fermi wave vector of the itinerant orbital [60], even though $U \simeq W$. In the following, we shall see that this insight remains meaningful also on the ladder, where the distinct Fermi surfaces of the one- and two-band regimes will necessarily come into play. In particular, we are already in a position to argue that the main influence of varying t_0^{\perp} on the magnetic properties of our system should come precisely from tuning between the one- and two-band regimes. Consider first the one-band regime. Here, as long as t_0^{\perp} is varied in a range that will not push the system into the two-band regime, there is only one Fermi wave vector k_F^{\perp} available, whose position does not depend on t_0^{\perp} . This suggests that the magnetism, which depends on the Fermi wave vector, shall remain mostly unaffected. At a few points within the one-band regime, we checked (not shown) that this indeed holds true, at least for a modest perturbation of the $t_0^{\perp}/t_0^{\parallel}$ ratio (since one expects that for $t_0^{\perp} \gg t_0^{\parallel}$ the system will behave as uncoupled rung dimers and our argument will eventually break). In the two-band regime, the situation becomes more complicated, as here varying t_0^{\perp} at a fixed filling n_K does change the values of \mathbf{k}_F . Nevertheless, judging by Fig. 3(b), it is reasonable to assume that the latter change of Fermi wave vectors—and the resulting impact on magnetism—will be complementary to that achievable by tuning n_K at fixed t_0^{\perp} . In that sense, although in the following we fix $t_0^{\perp} = t_0^{\parallel}$, we do not expect a qualitatively different magnetic phase diagram for other $t_0^{\perp}/t_0^{\parallel}$ ratios, but rather a similar diagram with renormalized magnetic phase boundaries, originating in the renormalization of the one- and two-band regimes. Finally, let us stress that it is the one-band regime where we reproduce the experimentally reported block magnetism, and clearly this is the regime which is least affected by the perturbation of t_0^{\perp} .

The *central result* of this work, shown in Fig. 4, is the n_K - U magnetic phase diagram of the gKH model on a ladder geometry, relevant for the low-dimensional 123-family iron-based superconductors within the OSMP. The details on each reported magnetic phase are provided in the following three sections: Sec. III A discusses the one-band regime, i.e., $n_K \gtrsim 1.6$, whereas Secs. III B and III C discuss the two-band regime at low ($n_K \lesssim 1.3$) and intermediate fillings ($n_K \sim 1.5$), respectively. Here, let us first focus on a few generic phases. (i) For all considered electronic fillings n_K , the system is a paramagnet at small values of the interaction strength $U/W \lesssim 0.5$. Note that in this regime our effective description (3) only approximately depicts the behavior of the full multiorbital Hubbard model. This stems from the fact that the latter is not yet within the OSMP and the magnetic moments $\langle \mathbf{S}_i^z \rangle$ are not yet fully developed. (ii) In the other extreme, when $U \gg W$, the system is a ferromagnet for all noninteger fillings, $1 < n_K < 2$, due to the dominance of the double-exchange mechanism (favored by a large value of the Hund exchange J_H). This phase is also present at moderate interaction strength $U \simeq W$ in the proximity of $n_K = 2$. (iii) For special values of the electron density $n_K = 1$ and $n_K = 2$, i.e., at half filling and in the case of a band insulator, respectively, the usual (π, π) (staggered along the legs and rungs) AFM order develops.

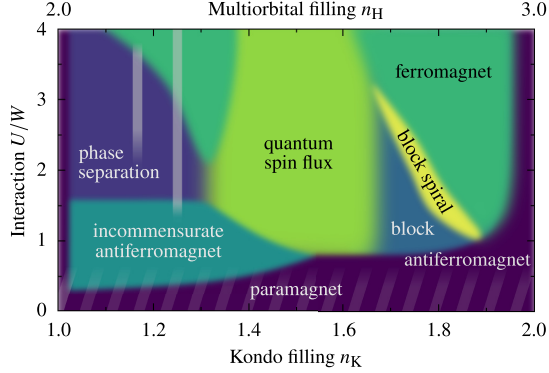


FIG. 4. Schematic n_K - U magnetic phase diagram of the generalized Kondo-Heisenberg ladder of $L = 72$ sites. The vertical lines within the phase-separation regime mark special fillings $n_K = 1.17, 1.25$, where perfect block order is recovered (see the discussion in Sec. III B). The phase diagram was inferred from extensive DMRG calculations performed at 37×40 data points uniformly distributed over the range of the plot. The phase boundaries are necessarily approximate as they cannot be exactly determined from finite-size calculations.

A. Block and block-spiral magnetism (one-band regime)

As follows from Fig. 3(c), the spatially isotropic ($t_0^\perp = t_0^\parallel$) system is in the one-band regime for $n_K \gtrsim 1.6$. In the rest of this subsection, we shall argue that this is the most experimentally relevant region hosting the block-magnetic phase found in BaFe_2Se_3 . It is important to note that the filling n_K of the OSMP effective model (3) does not correspond to the electronic density of the real materials or to the full five-orbital Hubbard model. However, as we will argue below, it is the position of the Fermi wave vectors \mathbf{k}_F that is crucial for the magnetism within the block phase (as well as strongly influences the behavior of the other phases, even in the two-band regime). This remains true also beyond the noninteracting $U \rightarrow 0$ limit where the \mathbf{k}_F become, in principle, a nontrivial function of the electronic density. As a consequence, we believe that our findings are generic provided that the multi-orbital system is in the OSMP and has similar values of the Fermi points \mathbf{k}_F , irrespective of the precise densities necessary to attain them or the number of active orbitals.

Previous efforts [24,59,60] showed that the magnetic order of the $\uparrow\uparrow\downarrow\downarrow$ form can be stabilized on the chain lattice in the $U \sim O(W)$ region of the phase diagram. In such a case, the block magnetism follows twice the Fermi wave vector of the noninteracting limit $2k_F = \pi(2 - n_K)$ (recall that we work above half filling, $n_K > 1$). On the ladder geometry, in the one-band regime, the latter is given by $2k_F^b = \pi(2 - 2n_K^b)$, where the additional factor of 2 arises due to $\max\{n_K^b\} = 1$. Our results shown in Fig. 5 support that the latter predicts also the block-magnetic order of the two-leg ladder for $U/W \simeq 1 \rightarrow 2$. Namely, in Fig. 5(a), we present the spin-spin correlation function $\langle S_{L_{\parallel/2,1}} \cdot S_{\mathbf{r}} \rangle$ between the sites on the same or different legs (lines and symbols, respectively). Clearly, both correlation functions lie on top of each other and exhibit a characteristic stiplike pattern. This indicates that the

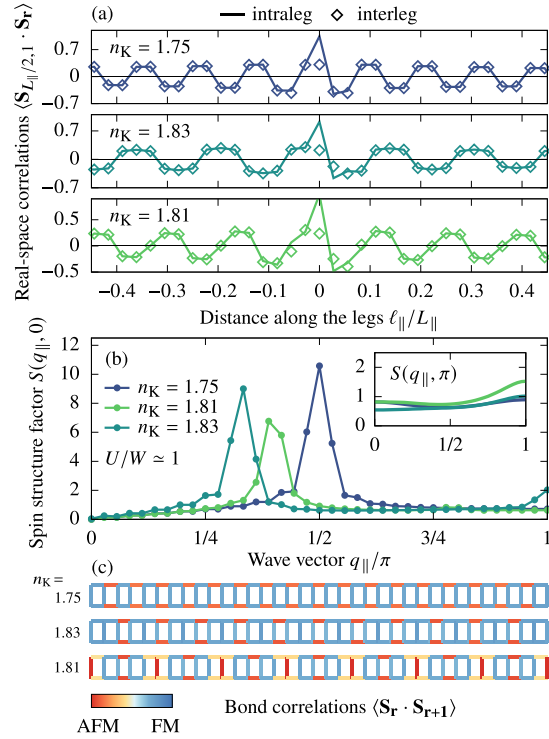


FIG. 5. Block-magnetic order. (a) Spin-spin correlations $\langle S_{L_{\parallel/2,1}} \cdot S_{\mathbf{r}} \rangle$ as a function of distance with $\mathbf{r} = (\ell_{\parallel}, 1)$ (intraleg) or $\mathbf{r} = (\ell_{\parallel}, 2)$ (interleg). Top to bottom: $\pi/2$ block ($n_K = 1.75$, $U/W = 1$), $\pi/3$ block ($n_K = 1.83$, $U/W = 1.1$), mixed block ($n_K = 1.81$, $U/W = 1$). (b) Spin structure factor $S(\mathbf{q})$ being the Fourier transform of the correlations shown in (a). (c) Bond correlations $\langle S_{\mathbf{r}} \cdot S_{\mathbf{r}+1} \rangle$ corresponding to (a) and (b). $\mathbf{1}$ connects the nearest-neighbor sites on the ladder. All results were obtained for a generalized Kondo-Heisenberg ladder of $L = 72$ sites.

spins are arranged in, e.g., AFM-coupled 2×2 FM blocks for $n_K = 1.75$ [sketched in Fig. 1(e)], i.e., the so-called $\pi/2$ -block pattern $\uparrow\uparrow\downarrow\downarrow$. This unusual magnetic order can be also identified via the spin structure factor $S(\mathbf{q})$; see Fig. 5(b). Here, the bonding component $S(q_{\parallel}, 0)$ (along the legs) has a well-pronounced maximum at $(2k_F^b, 0)$ for all considered fillings n_K . On the other hand, the antibonding component $S(q_{\parallel}, \pi)$ has only a weak momentum dependence. We again stress that the observed alternating FM block patterns are inferred from the spin-spin correlations and not the static magnetization $\langle S_z^i \rangle$.

On our finite lattice of $L = 72$ sites, the largest perfect (i.e., AFM-coupled FM) block that we have stabilized is of 3×2 size, the so-called $\pi/3$ block $\uparrow\uparrow\downarrow\downarrow\downarrow$ [sketched in Fig. 1(f)], present at $n_K = 1.83$. However, it was shown [60] that a small spin anisotropy can be used to stabilize even larger FM islands, possibly accessible here using larger L . The block nature of the correlations can be also seen in the NN bond correlations $\langle S_{\mathbf{r}} \cdot S_{\mathbf{r}+1} \rangle$ shown in Fig. 5(c) (here, $\mathbf{1}$ connects

the NN sites on the ladder geometry). Interestingly, the block-magnetic order is not restricted to perfect blocks of the same size, as those above, but can also involve complicated patterns of differently sized blocks. This is the case of $n_K = 1.81$, for which the real-space and bond correlation functions indicate a repeating motif of a large 5×2 magnetic unit cell, within which smaller blocks can be nevertheless still discerned. The unusual periodicity of the latter pattern leads to a strong maximum in $S(q_{\parallel}, 0)$ at $q_{\parallel}/\pi \simeq 0.4$, in agreement with the $2k_F^b$ prediction. This finding is consistent with the analysis of the block-magnetic orders in 1D systems [60,62]. There, the perfect block order can be found for $2k_F = \pi/m$ with $m \in \mathbb{Z}$. On the other hand, for $2k_F \neq \pi/m$, complex block patterns are stabilized. It is important to note that these are not phase-separated regions but true complicated spin arrangements in an overall spatially isotropic system (see also the discussion in the next section).

As already discussed, for $U \gg W$, the system orders ferromagnetically due to the double-exchange mechanism dominating for large Hund exchange J_H . Furthermore, it was recently shown in 1D systems [61] that between the block and the FM phases another order exists: the frustrated block-spiral state. In Fig. 6(a), we show the evolution of the spin structure factor $S(\mathbf{q})$ starting from the block phase at $U/W = 1$, for the important special case of $n_K = 1.75$, i.e., the $\pi/2$ block of $\uparrow\uparrow\downarrow\downarrow$ form. Upon increasing U , the maximum of $S(q_{\parallel}, 0)$ smoothly interpolates from $q_{\parallel} = \pi/2$ toward $q_{\parallel} \rightarrow 0$, taking incommensurate values in between. However, the real-space correlations [shown in Fig. 6(b)] reveal that this order differs significantly from a “simple” block pattern. To gain an understanding of this behavior, let us focus on the chirality correlation function along the legs, i.e., $\langle \kappa_r \cdot \kappa_m \rangle$ with

$$\kappa_r = \mathbf{S}_r \times \mathbf{S}_{r+1}. \quad (4)$$

Here, $\mathbf{1}$ connects NN sites along the legs (in Sec. III C we shall generalize it to involve also NN sites along the rungs). Since the above operator is proportional to the angle ϕ between NN spins, $\kappa_r \propto \sin(\phi)$, it is evident that if NN bond correlations are of FM ($\phi = 0$) or AFM ($\phi = \pi$) kind, the operator vanishes. On the other hand, if NN spins are rotated by $0 < \phi < \pi$, the $\langle \kappa_r \cdot \kappa_m \rangle$ correlation can detect the spiral order. In Fig. 6(c), we present the spatially resolved $\langle \kappa_{L_{\parallel}/2, 1} \cdot \kappa_r \rangle$ vs the interaction strength U for $n_K = 1.75$. As expected, in the block phase ($U/W = 1$) the chirality correlation function vanishes. In this phase, spin correlations are alternating between FM and AFM [see Figs. 5(c) and 6(b)]. Surprisingly, at $U/W \simeq 2$, $\langle \kappa_r \cdot \kappa_m \rangle$ takes finite values even at distances as long as $L_{\parallel}/2$, and exhibits a zigzag-like decaying pattern. Such behavior continues until $U/W \simeq 2.6$, when the system enters the FM phase with $\phi = 0$.

The above behavior was identified [61] as the block-spiral phase: upon increasing the strength of the Hubbard interaction U , the FM islands of the block phase start to rigidly rotate with respect to each other. The zigzag (small-large) pattern reflects the fact that within the $\langle \kappa_r \cdot \kappa_m \rangle$ correlation the κ_r operators act between the blocks (large value) or within the block (small value). Here, we establish that such a phase is also stable on the ladder geometry, where—in the particular case of the $\pi/2$ block at $n_K = 1.75$ —all four spins of the block start to rotate

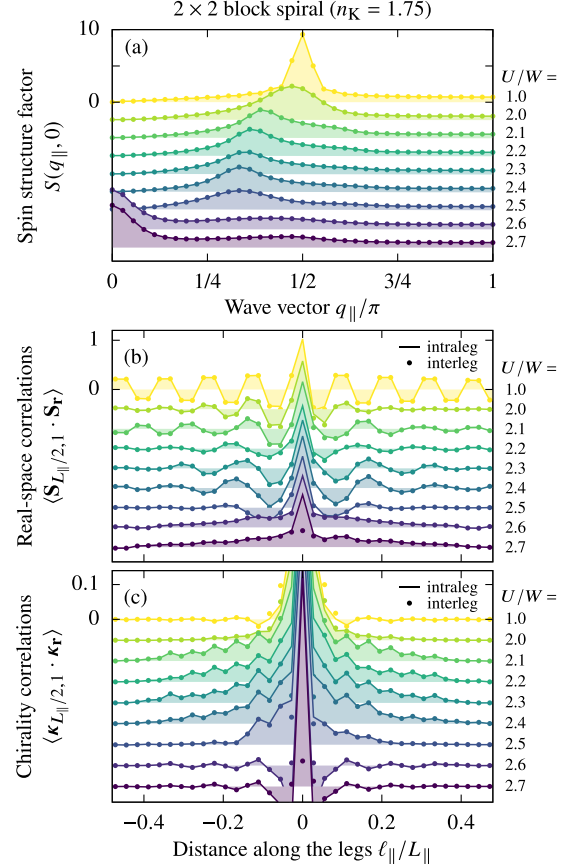


FIG. 6. Block-spiral magnetic order. (a) Interaction U evolution of the spin structure factor $S(q_{\parallel}, 0)$ for the 2×2 block spiral ($n_K = 1.75$). (b) Spin-spin correlations $\langle \mathbf{S}_{L_{\parallel}/2, 1} \cdot \mathbf{S}_r \rangle$ as a function of distance corresponding to (a). (c) Chirality correlations $\langle \kappa_{L_{\parallel}/2, 1} \cdot \kappa_r \rangle$ as a function of distance corresponding to (a). In (a) and (b), both the intraleg [$\mathbf{r} = (\ell_{\parallel}, 1)$] and interleg [$\mathbf{r} = (\ell_{\parallel}, 2)$] components are presented (as lines and symbols, respectively). All results were obtained for a generalized Kondo-Heisenberg ladder of $L = 72$ sites.

$\uparrow\uparrow\uparrow\uparrow\rightarrow\rightarrow\rightarrow\rightarrow\downarrow\downarrow\downarrow\downarrow$ [see also the sketch in Fig. 1(h)]. As marked on the phase diagram, Fig. 4, the block spiral is not restricted to $n_K = 1.75$, but develops also for the other block patterns at different n_K . The unique block modulation of our spiral is expected to be visible also in the Fourier decomposition, i.e., in the spin structure factor $S(\mathbf{q})$. In Fig. 7(a), we present a zoom-in plot of $S(\mathbf{q})$ for the 2×2 block spiral. Apart from the standard strong peak at $q_{\parallel} \simeq \pi/3$ related to the spiral’s pitch, there is an additional weaker peak at $q_{\parallel} \simeq \pi - \pi/3$, which is precisely the fingerprint of the block structure persisting during the spiral rotation [61]. In the same plot, Fig. 7(a), we point out that the perfect blocks with $2k_F^b = \pi/m$ also exhibit a unique secondary Fourier peak inherent to their steplike structure [61,62].

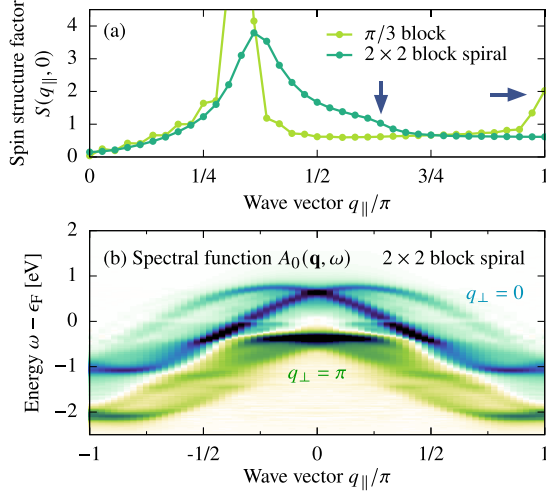


FIG. 7. Special features of the block-spiral phase. (a) Secondary Fourier mode (arrows) being a fingerprint of the block and block-spiral order. Shown are the representative cases of $\pi/3$ block ($n_K = 1.83$, $U/W = 1.1$) and 2×2 block spiral ($n_K = 1.75$, $U/W = 2.2$). (b) Spectral function of the itinerant orbital $A_0(\mathbf{q}, \omega)$ corresponding to the 2×2 block spiral of (a). The frequency resolution was chosen to be $\Delta\omega = 0.02$ eV with the broadening $\eta = 2\Delta\omega$. All results were obtained for a generalized Kondo-Heisenberg ladder of $L = 72$ sites.

Finally, let us briefly comment on another unique feature of the block-spiral phase which can be observed in the behavior of the itinerant orbital $\gamma = 0$. Since the OSMP system is in an overall metallic state, the spiral-like arrangement of the spins heavily modifies the single-particle spectral function $A_0(\mathbf{q}, \omega)$, Eq. (2). In Fig. 7(b), we present the bonding ($q_\perp = 0$) and antibonding ($q_\perp = \pi$) components of $A_0(\mathbf{q}, \omega)$ near the Fermi level ϵ_F (evaluated within the gKH model). Both components develop an additional two branches which can be associated with parity-breaking quasiparticles; i.e., $q_\parallel \rightarrow -q_\parallel$ changes the character (branch) of the particles. We want to note that this phase was proposed [19] as a possible magnetic order of the CsFe_2Se_3 ladder compound. Furthermore, a superconducting OSMP system with the parity-breaking quasiparticles was recently predicted [77] to exhibit nontrivial topological properties with Majorana modes emerging at the edges of the system. We refer the interested reader to Refs. [61] and [77] for details of this exotic phase.

B. Incommensurate antiferromagnet and phase separation (two-band regime at low doping)

We now move to discuss the two-band regime. Here, we find that the four-point Fermi surface makes this regime host qualitatively different magnetic phases than those present in the one-band case. Based on the magnetic phases found, we will split this region into two parts: low and intermediate doping. The latter will be discussed in the next section.

In Fig. 8(a), we show the spin structure factor $S(\mathbf{q})$ for an intermediate interaction strength $U/W = 1$ and a range

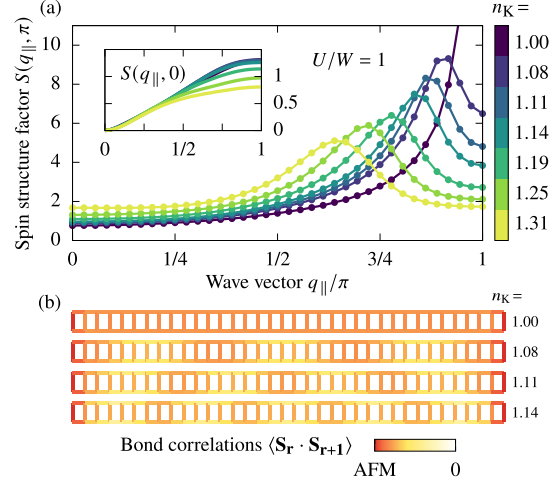


FIG. 8. Incommensurate antiferromagnet. (a) The filling n_K evolution of the spin structure factor $S(\mathbf{q})$ within the two-band regime at $U/W = 1$. The main panel (inset) shows the antibonding $S(q_\parallel, \pi)$ [bonding $S(q_\parallel, 0)$] component. (b) The filling n_K evolution of the bond correlations $\langle \mathbf{S}_r \cdot \mathbf{S}_{r+1} \rangle$ corresponding to the structure factors shown in (a). $\mathbf{1}$ connects the nearest-neighbor sites on the ladder. Note the evident amplitude modulation of the AFM correlations. All results were obtained for a generalized Kondo-Heisenberg ladder of $L = 72$ sites.

of fillings $1 < n_K < 1.3$ in the vicinity of half filling. Here, in contrast to the block phase of the one-band regime, the antibonding component $S(q_\parallel, \pi)$ (main panel) exhibits a well-defined maximum and dominates the bonding part $S(q_\parallel, 0)$ (inset), indicating that the rungs are predominantly AFM coupled. As expected, the half-filled ($n_K = 1$) system is a two-orbital Mott insulator with a (π, π) AFM order. Upon doping, the $S(q_\parallel, \pi)$ maximum shifts to smaller wave vectors. In contrast to the one-band regime, here, the latter maximum does not correspond to magnetic blocks, as clearly evidenced by the bond correlations [Fig. 8(b)] which do not show any alternating FM/AFM pattern. Instead, for all n_K in this region, the bond correlations are AFM with an additional amplitude modulation. Clearly, it is the periodicity of the latter modulation that is responsible for shifting the $S(q_\parallel, \pi)$ peak away from (π, π) . Moreover, the evolution of the $S(q_\parallel, \pi)$ peak also follows the (noninteracting) Fermi wave vectors \mathbf{k}_F of the itinerant orbital. Being deep in the two-band regime, both Fermi wave vectors play a role and the maximum occurs at $(k_F^b + k_F^a, \pi) \simeq (2\pi - \pi n_K, \pi)$, a result recognized already on a single-orbital Hubbard ladder [76]. Indeed, this type of exponentially decaying (short-range) incommensurate AFM is not an exclusively multiorbital feature, but relates to the long-standing problem of charge stripes, studied extensively in the doped single-orbital Hubbard model beyond 1D [76,78–84], as relevant in the context of cuprate high- T_c superconductors [85–87]. These stripes are a combination of codirectional charge-density waves and modulated AFM correlations (or spin-density waves in the case of a symmetry-broken state), wherein the region of maximum

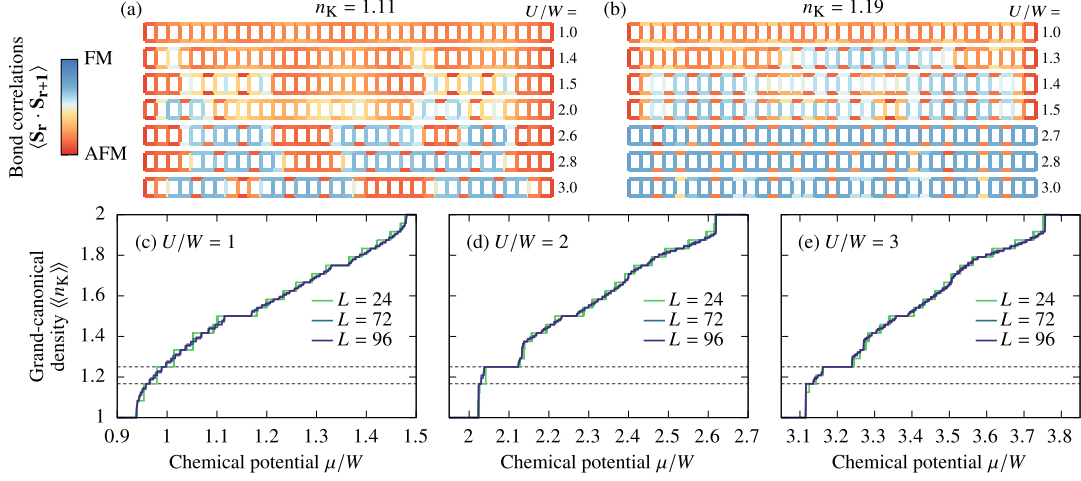


FIG. 9. Phase separation. (a), (b) Bond correlations $\langle \mathbf{S}_r \cdot \mathbf{S}_{r+1} \rangle$ for two fillings (a) $n_K = 1.11 \in [1, 1.17]$, (b) $n_K = 1.19 \in [1.17, 1.25]$ lying within the intervals of unstable densities. **1** connects the nearest-neighbor sites on the ladder and the system size is $L = 72$ sites. (c)–(e) Grand-canonical electron density $\langle n_K \rangle$ vs μ for different values of the interaction $U/W = 1, 2, 3$ and three system sizes $L = 24, 72, 96$. The horizontal lines mark $\langle n_K \rangle = 1.17$ ($\pi/3$ block) and $\langle n_K \rangle = 1.25$ ($\pi/2$ block). All results were obtained for a generalized Kondo-Heisenberg ladder.

charge density coincides with a domain wall in the AFM [82]. In other words, the AFM correlations experience a π -phase shift across each charge-density peak, explaining the incommensurate tendencies [78,81]. We checked (not shown) that the spin correlations of Fig. 8 are indeed accompanied by striped charge-density waves and exhibit the appropriate phase shift. For completeness, we also verified that the chirality correlation $\langle \kappa_r \cdot \kappa_m \rangle$ is zero in this phase. Finally, let us comment that incommensurate AFM was also reported before in the context of the multiorbital Hubbard model [88,89].

Intuitively, the single-orbital behavior is recovered in the above since in the vicinity of half filling the double-exchange mechanism requires larger Hund exchange J_H to fully develop. Correspondingly, upon increasing U (hence also increasing $J_H = U/4$), we find that the double exchange starts to play an important role. The bond correlations change drastically: the incommensurate AFM is lost in favor of the returning block formation tendencies; see Figs. 9(a) and 9(b). At special fillings $n_K = 1.17, 1.25$, the system again develops $\pi/3$ -block $\uparrow\uparrow\uparrow\downarrow\downarrow\downarrow$ and $\pi/2$ -block $\uparrow\uparrow\downarrow\downarrow$ orders, respectively. However, in contrast to the block phase of the one-band regime—where at arbitrary fillings n_K also other (more complicated) block-magnetic patterns emerged—here, the system coexists in spatially separated regions of the $\pi/3$ -block ($n_K = 1.17$), $\pi/2$ -block ($n_K = 1.25$), and the π -AFM ($n_K = 1$) correlations instead. For example, at $n_K = 1.11 \in [1, 1.17]$ the system is divided into regions with AFM and $\pi/3$ -block-like correlations for all presented values of U [Fig. 9(a)]. The closer the density is to $n_K = 1.17$, the more the $\pi/3$ -block regions grow at the cost of the AFM regions, and vice versa when moving closer to $n_K = 1$. At $n_K = 1.19 \in [1.17, 1.25]$, on the other hand, the system shows first AFM- $\pi/2$ separation for $U/W \simeq 1.3$, and then a $\pi/3$ - $\pi/2$ separation for $U/W \simeq 2.7$ [Fig. 9(b)]. Such irregular local correlations are

also reflected in an irregular behavior of the structure factor $S(\mathbf{q})$ which does not show any pronounced maximum or shows maxima that appear at seemingly random wave vectors for different values of U .

In order to truly identify the above behavior as phase separation, one usually analyzes whether the compressibility acquires negative values, which signals the system being unstable [90,91]. However, this can be troublesome, as it involves the evaluation of a second-order derivative, which is highly prone to the smallest numerical errors. Therefore, we opt to use another observable—we investigate the $\langle n_K \rangle$ vs μ curves, where $\langle n_K \rangle$ is the (grand-canonical) electron density at a given chemical potential μ . If $\langle n_K \rangle(\mu)$ exhibits a discontinuity, then there are densities that cannot be stabilized, irrespective of the value of μ . For calculations within the canonical ensemble, as performed here, this means that if the system is initialized with a density in the unstable interval, it will spontaneously separate into two regions of different densities [90–92], i.e., the behavior implied by Figs. 9(a) and 9(b).

Although, in principle, $\langle n_K \rangle(\mu)$ needs to be calculated in the grand-canonical ensemble, it is possible to obtain it from the fixed-density DMRG results by searching for the particle number N that minimizes the expectation value $\langle H_K - \mu \hat{N} \rangle = \epsilon_{GS}(N, L) - \mu N$ at each μ [90,93], where \hat{N} is the total particle number operator and $\epsilon_{GS}(N, L)$ is the ground-state energy for a fixed density $n_K = N/L$. In this way, we are able to study large system sizes, as presented in Figs. 9(c)–9(e), enabling us to distinguish a true discontinuity from one being a finite-size effect. One may observe that for $U/W = 1$ and the smallest size $L = 24$ [Fig. 9(c)], the $\langle n_K \rangle(\mu)$ curve is manifestly discrete. However, this discreteness disappears for larger sizes $L = 72, 96$, where the $\langle n_K \rangle(\mu)$ curves collapse and become smooth. This is the standard nonseparated

behavior. Contrarily, for $U/W = 2$ [Fig. 9(d)], there are several clear discontinuities at $1 < \langle n_K \rangle \lesssim 1.4$, which persist despite the increasing system size. In particular, there is a discontinuity between $\langle n_K \rangle = 1$ and $\langle n_K \rangle = 1.17$ (AFM- $\pi/3$ separation), and another between $\langle n_K \rangle = 1.17$ and $\langle n_K \rangle = 1.25$ ($\pi/3$ - $\pi/2$ separation), in perfect agreement with the bond correlation results [Figs. 9(a) and 9(b)]. Figure 9(e) leads to the same conclusions, but for $U/W = 3$. Therefore, we conclude that a clear tendency to phase-separate exists in our model for relatively low fillings n_K , close to half filling.

Finally, from Figs. 9(c)–9(e) it also follows that the phase separation is absent in the one-band regime; in particular, even the complicated block patterns [e.g., the one shown in Fig. 5(c) at $n_K = 1.81$] are robust uniform phases with no phase separation. Curiously, here, in the two-band regime, the blocks with complicated unit cells are in fact entirely absent, as we only see phase separation between AFM, $\pi/3$, and $\pi/2$ blocks. It is possible that larger system sizes would need to be accessed to find separation between the blocks with unusual periodicities. We do, however, find the signatures of block spirals at the special points $n_K = 1.17, 1.25$, which appear before FM for excessively large values of U . We have also checked (not shown) that phase separation is not present in the chain geometry. This is consistent with the picture that the chain can approximate the ladder well but only in the one-band regime, while the two-band regime cannot be captured (as the Fermi surface is closer to 2D). It is also worth noting that phase separation tendencies were reported experimentally in a layered iron superconductor $K_{0.8}Fe_{1.6}Se_2$ [94], albeit they concern separation between magnetic and nonmagnetic regions of different lattice constants.

C. Spin flux (two-band regime at intermediate doping)

Let us now describe the last region of our phase diagram—the two-band regime at intermediate doping, i.e., in the vicinity of three-quarter filling $n_K \sim 1.5$. We find this region to behave surprisingly very differently from the low-doping case, despite the same (noninteracting) Fermi surface. We shall attribute this difference to the strong renormalization of the Fermi surface due to the simultaneous competition of all energy scales at this intermediate parameter regime.

In the inset of Fig. 10(a), we present the spin structure factor $S(\mathbf{q})$ at $n_K = 1.5$ and at an intermediate interaction strength $U/W = 1$. We observe a dominant maximum in the bonding component $S(q_{\parallel}, 0)$ at wave vector $(\pi, 0)$ and a rather structureless antibonding part $S(q_{\parallel}, \pi)$. This result corresponds to the case of FM rungs and AFM legs, $\uparrow\downarrow\uparrow\downarrow$, i.e., the canonical magnetic order found experimentally in several iron-based ladders (see the introduction) and also widely believed to be the parent state of 2D iron-based superconductors [25,95]. Surprisingly, with increasing U , we find that this order is suppressed (albeit does not vanish) in favor of a maximum in the antibonding $S(q_{\parallel}, \pi)$ developing at $(0, \pi)$ [main panel of Fig. 10(a)]. Similar behavior was recently reported in Ref. [89], which studied the pairing-related properties of the two-leg ladder $BaFe_2S_3$. Figure 10(b) shows that this behavior is not restricted to $n_K = 1.5$, but occurs consistently at other fillings in the entire $1.3 \lesssim n_K \lesssim 1.6$ interval and also in a wider range of interactions $1 \lesssim U/W \lesssim 4$. The dominant

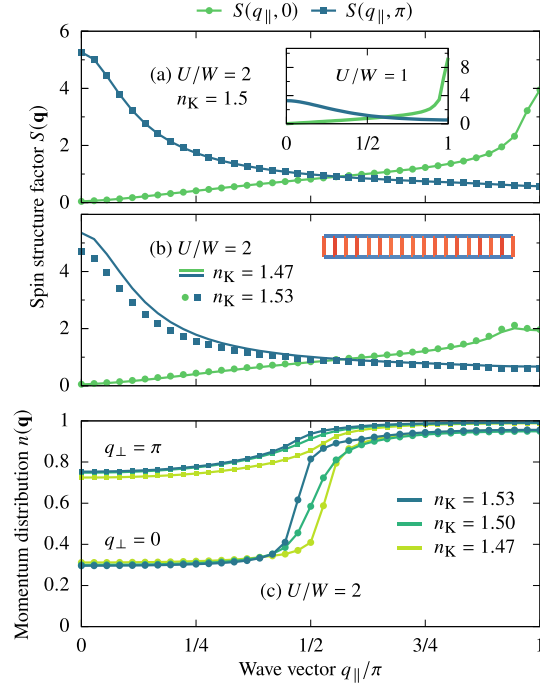


FIG. 10. Spin structure factor and momentum distribution function in the spin-flux region. (a) Spin structure factor $S(\mathbf{q})$ at $n_K = 1.5$ and $U/W = 1$ (inset), $U/W = 2$ (main panel). (b) The same as in (a) but at $n_K = 1.47$ (lines), $n_K = 1.53$ (symbols), and $U/W = 2$. The inset shows the bond correlations $(\mathbf{S}_r \cdot \mathbf{S}_{r+1})$ corresponding to $n_K = 1.47$. Here, red (blue) color marks AFM (FM) bonds and **1** connects the nearest-neighbor sites on the ladder. (c) Momentum distribution function $n(\mathbf{q})$ at $n_K = 1.47, 1.5, 1.53$ and $U/W = 2$. All results were obtained for a generalized Kondo-Heisenberg ladder of $L = 72$ sites.

peak at $(0, \pi)$ leads to the bond correlations taking now the form of AFM rungs and FM legs [inset of Fig. 10(b)].

Although in the bond correlations there is no discernible pattern related to the weak $S(q_{\parallel}, 0)$ features present in both Figs. 10(a) and 10(b), further analysis offers a useful insight. In particular, from Fig. 10(b) it follows that the structure factor $S(\mathbf{q})$ behaves identically at both $n_K = 1.47$ and $n_K = 1.53$, pointing to a symmetry around the $n_K = 1.5$ point, quite unexpected in the two-band regime. Crucially, here, we are in fact at the crossroads between the one- and two-band regimes, as the latter is enforced solely due to the finite interaction U [Fig. 3(c)]. In the noninteracting case, we would have two Fermi wave vectors for $n_K < 1.5$, but only one for $n_K > 1.5$, meaning that neither the noninteracting $2k_F^b$ prediction from Sec. III A nor the $k_F^b + k_F^a$ prediction from Sec. III B can be meaningfully applied to the apparent symmetry in the structure factors.

To elucidate this issue, we investigate the momentum distribution function defined as $n(\mathbf{q}) = \langle n_{0\mathbf{q}} \rangle = \langle \sum_{\sigma} c_{0\mathbf{q}\sigma}^{\dagger} c_{0\mathbf{q}\sigma} \rangle$, where $c_{0\mathbf{q}\sigma}^{\dagger} = (1/\sqrt{L}) \sum_{\mathbf{r}} \exp(i\mathbf{q}\mathbf{r}) c_{0\mathbf{r}\sigma}^{\dagger}$. The results are

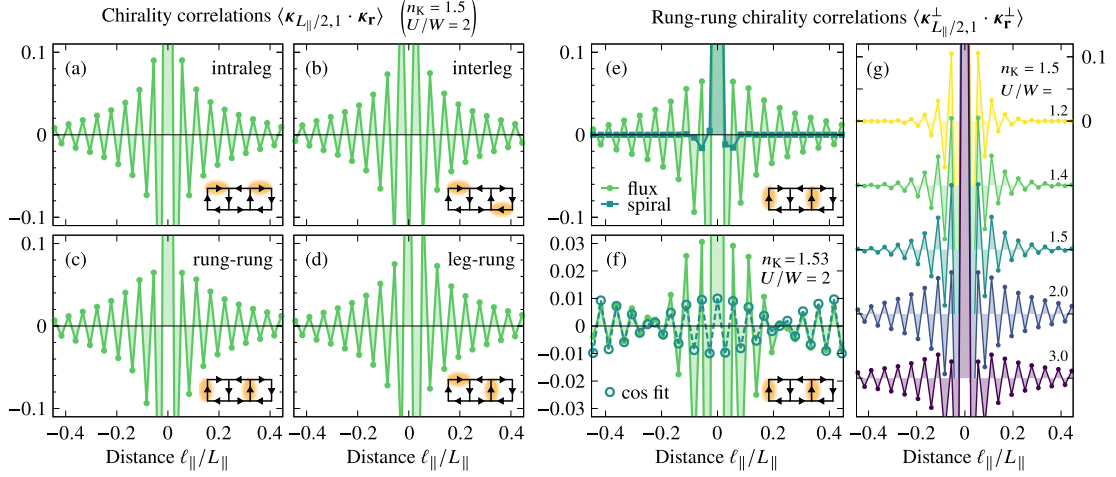


FIG. 11. Spin flux. (a)–(d) Chirality correlations $\langle \kappa_{L_{\parallel}/2,1} \cdot \kappa_{\mathbf{r}} \rangle$ at $n_K = 1.5$, $U/W = 2$ as a function of distance. Shown are all possible components: (a) intraleg, (b) interleg, (c) rung-rung, (d) leg-rung. The sketches show the proposed magnetic order and also highlight the bonds which are involved in the calculation. (e) Comparison of the distance-dependent rung-rung chirality $\langle \kappa_{L_{\parallel}/2,1}^{\perp} \cdot \kappa_{\mathbf{r}}^{\perp} \rangle$ between the flux ($n_K = 1.5$, $U/W = 2$) and the 2×2 block spiral ($n_K = 1.75$, $U/W = 2.2$). (f) Rung-rung chirality in the flux phase with $n_K = 1.53$, $U/W = 2$. The dark symbols correspond to $\cos(2\tilde{k}_F^b \ell_{\parallel})$ fit using the effective Fermi wave vector \tilde{k}_F^b obtained from Fig. 10(c). (g) Interaction U evolution of the rung-rung chirality for the spin flux with $n_K = 1.5$. All results were obtained for a generalized Kondo-Heisenberg ladder of $L = 72$ sites.

presented in Fig. 10(c) for the three fillings $n_K = 1.47, 1.5, 1.53$ and the interaction $U/W = 2$. One immediately notices that the momentum distribution of the antibonding band ($q_{\perp} = \pi$) is highly renormalized with respect to the $U = 0$ case, where it would be a step function centered at k_F^a . Here, it is strongly flattened instead, and its shape seems to be weakly dependent on the filling n_K . The bonding band ($q_{\perp} = 0$), on the other hand, acts as though it was the only one being filled: Adding (removing) particles shifts its effective Fermi wave vector \tilde{k}_F^b [taken here as the inflection point of $n(q_{\parallel}, 0)$], and the function $n(q_{\parallel}, 0)$ appears relatively sharp despite the large interaction U . Remarkably, the weak peak in $S(q_{\parallel}, 0)$ corresponds to $(2\tilde{k}_F^b, 0)$, explaining why the structure factors at the two fillings $n_K = 1.47, 1.53$ are identical [Fig. 10(b)]. This is precisely due to the symmetric behavior of $n(q_{\parallel}, 0)$ around the $n_K = 1.5$ point. Therefore, although both bands are fractionally filled, as follows from both Figs. 3(c) and 10(c), the interaction U promotes an emergent one-band behavior. This stands in contrast to the low-doping case (deep within the two-band regime), where such a behavior is absent.

The strong $(0, \pi)$ peak and the bond correlations with FM legs and AFM rungs suggest that this order could be a ladder analog of 2D patterns argued [25] to be relevant for the layered compounds Fe(Se,Te). However, the analysis of chirality correlations offers a different interpretation. In Fig. 11(a), we present the intraleg chirality correlation function $\langle \kappa_{\mathbf{r}} \cdot \kappa_{\mathbf{m}} \rangle$ at $n_K = 1.5$ and $U/W = 2.0$. Remarkably, we observe significant and slowly decaying chirality correlations, indicating that the spins are noncollinear. This is quite unexpected considering the commensurate structure factors shown in Fig. 10(a). Moreover, the chirality displays an intriguing staggered pattern, which is present not only in the intraleg

correlations but also in the interleg case [Fig. 11(b)], and the highly nontrivial rung-rung and leg-rung cases [Figs. 11(c)–11(d)]. It is hard to imagine a (quantum) spin ordering which would lead to all the chirality correlation functions simultaneously showing the same staggered pattern. The solution to this conundrum can be found by noticing that the z component of the chirality correlation function is in fact equal to the spin-current correlation function, $\kappa_{\mathbf{r}}^z = S_{\mathbf{r}}^x S_{\mathbf{r}+1}^y - S_{\mathbf{r}}^y S_{\mathbf{r}+1}^x = i/2 (S_{\mathbf{r}}^+ S_{\mathbf{r}+1}^- - S_{\mathbf{r}}^- S_{\mathbf{r}+1}^+)$. Indeed, we checked that the z component has a significant contribution to the presented chirality values. Therefore, we propose that the system realizes a novel quantum spin-flux phase, wherein the spin currents circulate around 2×2 plaquettes and are staggered from plaquette to plaquette [see the sketches in Figs. 11(a)–11(d) and 1(i)], with no net current flow.

Since all the chirality functions behave in the same manner, in the following we discuss only the representative rung-rung case $\langle \kappa_{\mathbf{r}}^{\perp} \cdot \kappa_{\mathbf{m}}^{\perp} \rangle$, which corresponds to spin currents flowing along the rungs. In Fig. 11(e), we compare the spin flux to the other chiral phase of our model—the block spiral. Clearly, in the latter the rung-rung (and also leg-rung) chirality vanishes, highlighting that it is indeed unique to the flux. Moreover, this unique chirality is not restricted to the $n_K = 1.5$ filling, but appears also for $n_K \neq 1.5$ in the entire regime being discussed in this section, i.e., for $1.3 \lesssim n_K \lesssim 1.6$ and $1 \lesssim U/W \lesssim 4$. Variation of the filling introduces an additional modulation of the staggered pattern, as shown in Fig. 11(f) for $n_K = 1.53$. Furthermore, the latter modulation is controlled by the effective Fermi wave vector \tilde{k}_F^b , i.e., $\langle \kappa_{\mathbf{r}}^{\perp} \cdot \kappa_{\mathbf{r}+\mathbf{d}}^{\perp} \rangle \propto \cos(2\tilde{k}_F^b d)$ [96]. This “hidden” periodicity—which is readily seen in the chirality correlations but not in the real-space spin correlations—elucidates the origin of the $(2\tilde{k}_F^b, 0)$ maximum

we earlier noted in $S(q_{\parallel}, 0)$, which accompanies the strong $(0, \pi)$ peak [Figs. 10(a)–10(b)]. In particular, at $n_K = 1.5$, we have $(2k_F^{\parallel}, 0) = (\pi, 0)$. This understanding is consistent with the results for the 2D FM Kondo lattice of classical spins, where the similar-weight structure factor maxima at $(\pi, 0)$ and $(0, \pi)$ were recognized as the hallmark of the spin flux [97–99]. The latter spin configuration cannot be specified by only one wave vector [97]. In our case, the spin-flux phase emerges within a fully quantum model and, moreover, it is promoted by the interaction U , as follows from Fig. 11(g). Consistently, the structure factor peak at $(0, \pi)$ [Fig. 10(a)] acquires significant weight only when the staggered chirality correlations are well developed. From this perspective, we treat the canonical $(\pi, 0)$ order of AFM legs and FM rungs, $\uparrow\downarrow\uparrow\downarrow$, present at $U/W = 1$ [inset of Fig. 10(a)], as an underdeveloped flux, rather than a separate phase, and we do not mark it individually on the phase diagram, Fig. 4.

IV. CONCLUSIONS

To summarize, using an accurate computational technique we have studied the magnetic phase diagram of the two-leg multiorbital ladder in the orbital-selective Mott phase. Although our effective model, the generalized Kondo-Heisenberg Hamiltonian, describes the electron densities of the iron-based systems in an approximate manner, it properly captures the symmetric and antisymmetric bands (bonding and antibonding, respectively). The latter are crucial to a proper description of the magnetic order.

The magnetic phase diagram of the ladder OSMP is dominated by tendencies to form magnetic blocks of various shapes and sizes. At large fillings, $n_K \gtrsim 1.6$, where the antibonding band ($q_{\perp} = \pi$) is fully filled and only the bonding band ($q_{\perp} = 0$) carries the Fermi wave vectors, the system develops perfect blocks of $\uparrow\uparrow\downarrow\downarrow$ form at $U \sim W$. Increasing the strength of the interaction U leads to the uniform rotation of the blocks, i.e., to the formation of the exotic block-spiral phase with nontrivial properties. In the opposite limit, close to half filling $n_K \sim 1$, the four Fermi wave vectors present in two bands drive the system toward phase separation with (predominantly) $\pi/2$ and $\pi/3$ blocks. Finally, when $n_K \sim 1.5$, the ladder system develops a quantum spin flux originating in the competing energy scales inherent to the OSMP. This phase can be naively viewed as staggered spin currents circulating within 2×2 plaquettes (however, no plaquette carries net current due to its quantum nature in a finite system).

Our phase diagram indicates that the magnetism of iron-based ladders, due to the presence of charge, spin, and orbital degrees of freedom, combines phenomena known from cuprates with those found in manganites [100,101]. Namely, at small interaction U and close to half filling $n_K \sim 1$, we have found the striped incommensurate antiferromagnetism—the challenging and still not fully understood magnetic order relevant for 2D cuprate superconductors. On the other hand, increasing the interaction strength U , one can find the phase-separated region known from the manganites. Most importantly, our results indicate that the family of iron-based AFe_2X_3 compounds lies within the one-band regime, where the block and block-spiral orders can be found (also experimentally). We believe that our comprehensive study

provides motivation and theoretical guidance for crystal growers and experimentalists to discover new iron-based ladder compounds that may display the highly unusual magnetic properties reported here.

ACKNOWLEDGMENTS

We acknowledge fruitful discussions with M. M. Maška, M.Ś. and J.H. acknowledge grant support by the Polish National Agency for Academic Exchange (NAWA) under Contract No. PPN/PPO/2018/1/00035 and by the National Science Centre (NCN), Poland, via Project No. 2019/35/B/ST3/01207. E.D. was supported by the U.S. Department of Energy (DOE), Office of Science, Basic Energy Sciences (BES), Materials Sciences and Engineering Division. Calculations have been carried out using resources provided by Wrocław Centre for Networking and Supercomputing.

APPENDIX: COMPUTATIONAL ACCURACY REGARDING THE SU(2) SYMMETRY

It is well-known that within DMRG implementations which exploit only the U(1) spin symmetry, and not the full SU(2) symmetry, it is possible to converge to a state with finite local magnetization $\langle S_i^z \rangle$, even though a finite system cannot break the SU(2) symmetry. This effect is more pronounced in simulations beyond 1D and is a recurring issue in the studies of 2D Hubbard and t - J models [79,80,83,102,103]. Although here we discuss a two-leg ladder, its two-orbital nature makes it effectively a four-leg problem, and in some cases our DMRG indeed ends up in a state with nonvanishing $\langle S_i^z \rangle$. This issue can be mitigated by drastically increasing the number of states kept [79,83,103], but then the already demanding computational effort would quickly become prohibitively expensive. Still, where feasible, we did verify that increasing M in our DMRG procedure does drive $\langle S_i^z \rangle$ to zero, while preserving the spin-spin correlations and introducing a minimal adjustment of the ground-state energy. Moreover, sometimes a slight perturbation of the model parameters (e.g., changing U by as little as 5%) was enough to tip the algorithm toward a final state which respects the SU(2) symmetry, but appears otherwise unchanged with respect to other quantities. These observations suggest that the finite $\langle S_i^z \rangle$ arises because the DMRG selects a subset of states (with a particular direction of the order parameter) from the macroscopic superposition present within the true ground state [79,104]. Since the states in the latter superposition are expected to be (nearly) degenerate, the difference in the final energy is minimal, making it hard to completely converge. Nonetheless, such a spurious “partial” symmetry breaking within the final state should not lead to a misrepresentation of the magnetic order existing in our system, nor should it affect the behavior of itinerant carriers doped into those states (see the discussion in Ref. [79]). We therefore conclude that the occasional presence of finite $\langle S_i^z \rangle$ is insignificant for our study and does not invalidate our results. That being said, the nondecaying nature of the static magnetization can make the maxima in $S(\mathbf{q})$ appear excessively sharp. To avoid the misinterpretation of $S(\mathbf{q})$, while plotting the latter we discard the fictitious spin-density

contribution; i.e., we define $\langle \mathbf{S}_r \cdot \mathbf{S}_m \rangle \equiv \langle \mathbf{S}_r \cdot \mathbf{S}_m \rangle - \langle S_r^z \rangle \langle S_m^z \rangle$. The fact that this does not reduce $\langle \mathbf{S}_r \cdot \mathbf{S}_m \rangle$ to zero confirms that our ground state retains most, if not all, quantum fluctuations on top of the artificial magnetization.

The issue described above is especially troublesome in the intermediate-doping ($n_K \sim 1.5$) region discussed in Sec. III C, which seems to be the most demanding for the DMRG method. There, all the energy scales are simultaneously at

play, making it hard to fully stabilize the system within current computational limitations. As a consequence, a more detailed analysis focusing solely on the latter region is called for, involving also a systematic study of the t_0^\perp influence, which is however beyond the scope of the present, more general, survey of the magnetic phases. Our already interesting findings reported here provide motivation for such a more in-depth study of the intermediate-doping region in the near future.

- [1] E. Dagotto and T. M. Rice, *Science* **271**, 618 (1996).
- [2] M. Uehara, T. Nagata, J. Akimitsu, H. Takahashi, N. Môri, and K. Kinoshita, *J. Phys. Soc. Jpn.* **65**, 2764 (1996).
- [3] N. Motoyama, H. Eisaki, S. Uchida, N. Takeshita, N. Môri, T. Nakanishi, and H. Takahashi, *Europhys. Lett.* **58**, 758 (2002).
- [4] S. Maekawa, *Science* **273**, 1515 (1996).
- [5] E. Dagotto, J. Riera, and D. Scalapino, *Phys. Rev. B* **45**, 5744 (1992).
- [6] T. M. Rice, S. Gopalan, M. Sigrist, and F. C. Zhang, *J. Low Temp. Phys.* **95**, 299 (1995).
- [7] N. Motoyama, H. Eisaki, and S. Uchida, *Phys. Rev. Lett.* **76**, 3212 (1996).
- [8] N. Hlubek, P. Ribeiro, R. Saint-Martin, A. Revcolevschi, G. Roth, G. Behr, B. Büchner, and C. Hess, *Phys. Rev. B* **81**, 020405(R) (2010).
- [9] C. Hess, *Phys. Rep.* **811**, 1 (2019).
- [10] R. Steinigeweg, J. Herbrych, X. Zotos, and W. Brenig, *Phys. Rev. Lett.* **116**, 017202 (2016).
- [11] C. Karrasch, D. M. Kennes, and F. Heidrich-Meisner, *Phys. Rev. B* **91**, 115130 (2015).
- [12] H. Takahashi, A. Sugimoto, Y. Nambu, T. Yamauchi, Y. Hirata, T. Kawakami, M. Avdeev, K. Matsubayashi, C. Du, F. Kawashima, H. Soeda, S. Nakano, Y. Uwatoko, Y. Ueda, T. J. Sato, and K. Ohgushi, *Nat. Mater.* **14**, 1008 (2015).
- [13] J. Ying, H. Lei, C. Petrovic, Y. Xiao, and V. V. Struzhkin, *Phys. Rev. B* **95**, 241109(R) (2017).
- [14] S. Wu, B. A. Frandsen, M. Wang, M. Yi, and R. Birgeneau, *J. Supercond. Nov. Magn.* **33**, 143 (2019).
- [15] M. Wang, S. J. Jin, M. Yi, Y. Song, H. C. Jiang, W. L. Zhang, H. L. Sun, H. Q. Luo, A. D. Christianson, E. Bourret-Courchesne, D. H. Lee, D.-X. Yao, and R. J. Birgeneau, *Phys. Rev. B* **95**, 060502(R) (2017).
- [16] T. Hawaii, Y. Nambu, K. Ohgushi, F. Du, Y. Hirata, M. Avdeev, Y. Uwatoko, Y. Sekine, H. Fukazawa, J. Ma, S. Chi, Y. Ueda, H. Yoshizawa, and T. J. Sato, *Phys. Rev. B* **91**, 184416 (2015).
- [17] M. Wang, M. Yi, S. Jin, H. Jiang, Y. Song, H. Luo, A. D. Christianson, C. de la Cruz, E. Bourret-Courchesne, D.-X. Yao, D. H. Lee, and R. J. Birgeneau, *Phys. Rev. B* **94**, 041111(R) (2016).
- [18] S. Chi, Y. Uwatoko, H. Cao, Y. Hirata, K. Hashizume, T. Aoyama, and K. Ohgushi, *Phys. Rev. Lett.* **117**, 047003 (2016).
- [19] M. Murase, K. Okada, Y. Kobayashi, Y. Hirata, K. Hashizume, T. Aoyama, K. Ohgushi, and M. Itoh, *Phys. Rev. B* **102**, 014433 (2020).
- [20] M. Mourigal, S. Wu, M. B. Stone, J. R. Neilson, J. M. Caron, T. M. McQueen, and C. L. Broholm, *Phys. Rev. Lett.* **115**, 047401 (2015).
- [21] S. Wu, J. Yin, T. Smart, A. Acharya, C. L. Bull, N. P. Funnell, T. R. Forrest, G. Simutis, R. Khasanov, S. K. Lewin, M. Wang, B. A. Frandsen, R. Jeanloz, and R. J. Birgeneau, *Phys. Rev. B* **100**, 214511 (2019).
- [22] J. M. Caron, J. R. Neilson, D. C. Miller, A. Llobet, and T. M. McQueen, *Phys. Rev. B* **84**, 180409(R) (2011).
- [23] Y. Nambu, K. Ohgushi, S. Suzuki, F. Du, M. Avdeev, Y. Uwatoko, K. Munakata, H. Fukazawa, S. Chi, Y. Ueda, and T. J. Sato, *Phys. Rev. B* **85**, 064413 (2012).
- [24] J. Rincón, A. Moreo, G. Alvarez, and E. Dagotto, *Phys. Rev. Lett.* **112**, 106405 (2014).
- [25] J. K. Glasbrenner, I. I. Mazin, H. O. Jeschke, P. J. Hirschfeld, R. M. Fernandes, and R. Valentí, *Nat. Phys.* **11**, 953 (2015).
- [26] M. Wang, C. Fang, D.-X. Yao, G. T. Tan, L. W. Harriger, Y. Song, T. Netherton, C. Zhang, M. Wang, M. B. Stone, W. Tian, J. Hu, and P. Dai, *Nat. Commun.* **2**, 580 (2015).
- [27] B. Wei, Q.-Z. Huang, G.-F. Chen, D.-M. Wang, J.-B. He, and Y.-M. Qiu, *Chin. Phys. Lett.* **28**, 086104 (2011).
- [28] Y.-Z. You, H. Yao, and D.-H. Lee, *Phys. Rev. B* **84**, 020406(R) (2011).
- [29] R. Yu, P. Goswami, and Q. Si, *Phys. Rev. B* **84**, 094451 (2011).
- [30] J. Guo, S. Jin, G. Wang, S. Wang, K. Zhu, T. Zhou, M. He, and X. Chen, *Phys. Rev. B* **82**, 180520(R) (2010).
- [31] F. Ye, S. Chi, W. Bao, X. F. Wang, J. J. Ying, X. H. Chen, H. D. Wang, C. H. Dong, and M. Fang, *Phys. Rev. Lett.* **107**, 137003 (2011).
- [32] B. Pandey, L.-F. Lin, R. Soni, N. Kaushal, J. Herbrych, G. Alvarez, and E. Dagotto, *Phys. Rev. B* **102**, 035149 (2020).
- [33] Q. Luo, A. Nicholson, J. Riera, D.-X. Yao, A. Moreo, and E. Dagotto, *Phys. Rev. B* **84**, 140506(R) (2011).
- [34] Q. Luo, A. Nicholson, J. Rincón, S. Liang, J. Riera, G. Alvarez, L. Wang, W. Ku, G. D. Samolyuk, A. Moreo, and E. Dagotto, *Phys. Rev. B* **87**, 024404 (2013).
- [35] Q. Luo, K. Foyevtsova, G. D. Samolyuk, F. Reboredo, and E. Dagotto, *Phys. Rev. B* **90**, 035128 (2014).
- [36] Q. Luo and E. Dagotto, *Phys. Rev. B* **89**, 045115 (2014).
- [37] W.-G. Yin, C.-H. Lin, and W. Ku, *Phys. Rev. B* **86**, 081106(R) (2012).
- [38] S. Dong, J.-M. Liu, and E. Dagotto, *Phys. Rev. Lett.* **113**, 187204 (2014).
- [39] Y. Zhang, L. Lin, J.-J. Zhang, E. Dagotto, and S. Dong, *Phys. Rev. B* **95**, 115154 (2017).
- [40] Y. Zhang, L.-F. Lin, J.-J. Zhang, E. Dagotto, and S. Dong, *Phys. Rev. B* **97**, 045119 (2018).
- [41] Y. Zhang, L.-F. Lin, A. Moreo, S. Dong, and E. Dagotto, *Phys. Rev. B* **100**, 184419 (2019).
- [42] Y. Zhang, L.-F. Lin, A. Moreo, S. Dong, and E. Dagotto, *Phys. Rev. B* **101**, 144417 (2020).

- [43] L. de' Medici, S. R. Hassan, M. Capone, and X. Dai, *Phys. Rev. Lett.* **102**, 126401 (2009).
- [44] A. Georges, L. de' Medici, and J. Mravlje, *Annu. Rev. Condens. Matter Phys.* **4**, 137 (2013).
- [45] A. Isidori, M. Berović, L. Fanfarillo, L. de' Medici, M. Fabrizio, and M. Capone, *Phys. Rev. Lett.* **122**, 186401 (2019).
- [46] M. Yi, Y. Zhang, Z.-X. Shen, and D. Lu., *npj Quant. Mater.* **2**, 57 (2017).
- [47] J. M. Caron, J. R. Neilson, D. C. Miller, K. Arpino, A. Llobet, and T. M. McQueen, *Phys. Rev. B* **85**, 180405(R) (2012).
- [48] T. Yamauchi, Y. Hirata, Y. Ueda, and K. Ohgushi, *Phys. Rev. Lett.* **115**, 246402 (2015).
- [49] L. Craco and S. Leoni, *Phys. Rev. B* **101**, 245133 (2020).
- [50] M. Yi, D. H. Lu, R. Yu, S. C. Riggs, J.-H. Chu, B. Lv, Z. K. Liu, M. Lu, Y.-T. Cui, M. Hashimoto, S.-K. Mo, Z. Hussain, C. W. Chu, I. R. Fisher, Q. Si, and Z.-X. Shen, *Phys. Rev. Lett.* **110**, 067003 (2013).
- [51] F. Hardy, A. E. Böhrer, D. Aoki, P. Burger, T. Wolf, P. Schweiss, R. Heid, P. Adelmann, Y. X. Yao, G. Kotliar, J. Schmalian, and C. Meingast, *Phys. Rev. Lett.* **111**, 027002 (2013).
- [52] M. Yi, Z.-K. Liu, Y. Zhang, R. Yu, J.-X. Zhu, J. J. Lee, R. G. Moore, F. T. Schmitt, W. Li, S. C. Riggs, J.-H. Chu, B. Lv, J. Hu, M. Hashimoto, S.-K. Mo, Z. Hussain, Z. Q. Mao, C. W. Chu, I. R. Fisher, Q. Si *et al.*, *Nat. Commun.* **6**, 7777 (2015).
- [53] J.-X. Zhu, R. Yu, H. Wang, L. L. Zhao, M. D. Jones, J. Dai, E. Abrahams, E. Morosan, M. Fang, and Q. Si, *Phys. Rev. Lett.* **104**, 216405 (2010).
- [54] K. Takubo, Y. Yokoyama, H. Wadati, S. Iwasaki, T. Mizokawa, T. Boyko, R. Sutarto, F. He, K. Hashizume, S. Imaizumi, T. Aoyama, Y. Imai, and K. Ohgushi, *Phys. Rev. B* **96**, 115157 (2017).
- [55] P. Materne, W. Bi, J. Zhao, M. Y. Hu, M. L. Amigó, S. Seiro, S. Aswartham, B. Büchner, and E. E. Alp, *Phys. Rev. B* **99**, 020505(R) (2019).
- [56] N. D. Patel, A. Nocera, G. Alvarez, A. Moreo, S. Johnston, and E. Dagotto, *Commun. Phys.* **2**, 64 (2019).
- [57] M. Daghofer, A. Nicholson, A. Moreo, and E. Dagotto, *Phys. Rev. B* **81**, 014511 (2010).
- [58] J. Rincón, A. Moreo, G. Alvarez, and E. Dagotto, *Phys. Rev. B* **90**, 241105(R) (2014).
- [59] J. Herbrych, N. Kaushal, A. Nocera, G. Alvarez, A. Moreo, and E. Dagotto, *Nat. Commun.* **9**, 3736 (2018).
- [60] J. Herbrych, J. Heverhagen, N. D. Patel, G. Alvarez, M. Daghofer, A. Moreo, and E. Dagotto, *Phys. Rev. Lett.* **123**, 027203 (2019).
- [61] J. Herbrych, J. Heverhagen, G. Alvarez, M. Daghofer, A. Moreo, and E. Dagotto, *Proc. Natl. Acad. Sci. U.S.A.* **117**, 16226 (2020).
- [62] J. Herbrych, G. Alvarez, A. Moreo, and E. Dagotto, *Phys. Rev. B* **102**, 115134 (2020).
- [63] J. Kanamori, *Prog. Theor. Phys.* **30**, 275 (1963).
- [64] A. M. Oleś, *Phys. Rev. B* **28**, 327 (1983).
- [65] E. Dagotto, T. Hotta, and A. Moreo, *Phys. Rep.* **344**, 1 (2001).
- [66] K. Haule and G. Kotliar, *New J. Phys.* **11**, 025021 (2009).
- [67] Z. P. Yin, K. Haule, and G. Kotliar, *Nat. Mater.* **10**, 932 (2011).
- [68] J. Ferber, K. Foyevtsova, R. Valentí, and H. O. Jeschke, *Phys. Rev. B* **85**, 094505 (2012).
- [69] Q. Luo, G. Martins, D.-X. Yao, M. Daghofer, R. Yu, A. Moreo, and E. Dagotto, *Phys. Rev. B* **82**, 104508 (2010).
- [70] P. Dai, J. Hu, and E. Dagotto, *Nat. Phys.* **8**, 709 (2012).
- [71] J. R. Schrieffer and P. A. Wolff, *Phys. Rev.* **149**, 491 (1966).
- [72] S. R. White, *Phys. Rev. B* **72**, 180403(R) (2005).
- [73] G. Alvarez, *Comput. Phys. Commun.* **180**, 1572 (2009).
- [74] See <https://g1257.github.io/dmrgPlusPlus>.
- [75] See <https://bitbucket.org/herbrychjacek/corrwro>.
- [76] R. M. Noack, S. R. White, and D. J. Scalapino, *Physica C* **270**, 281 (1996).
- [77] J. Herbrych, M. Środa, G. Alvarez, M. Mierzejewski, and E. Dagotto, *Nat. Commun.* **12**, 2955 (2021).
- [78] G. B. Martins, C. Gazza, J. C. Xavier, A. Feiguin, and E. Dagotto, *Phys. Rev. Lett.* **84**, 5844 (2000).
- [79] S. R. White and D. J. Scalapino, *Phys. Rev. Lett.* **91**, 136403 (2003).
- [80] G. Hager, G. Wellein, E. Jeckelmann, and H. Fehske, *Phys. Rev. B* **71**, 075108 (2005).
- [81] G. Ehlers, S. R. White, and R. M. Noack, *Phys. Rev. B* **95**, 125125 (2017).
- [82] B.-X. Zheng, C.-M. Chung, P. Corboz, G. Ehlers, M.-P. Qin, R. M. Noack, H. Shi, S. R. White, S. Zhang, and G. K.-L. Chan, *Science* **358**, 1155 (2017).
- [83] H.-C. Jiang and T. P. Devereaux, *Science* **365**, 1424 (2019).
- [84] M. Qin, C.-M. Chung, H. Shi, E. Vitali, C. Hubig, U. Schollwöck, S. R. White, and S. Zhang (Simons Collaboration on the Many-Electron Problem), *Phys. Rev. X* **10**, 031016 (2020).
- [85] J. M. Tranquada, B. J. Sternlieb, J. D. Axe, Y. Nakamura, and S. Uchida, *Nature (London)* **375**, 561 (1995).
- [86] J. M. Tranquada, J. D. Axe, N. Ichikawa, Y. Nakamura, S. Uchida, and B. Nachumi, *Phys. Rev. B* **54**, 7489 (1996).
- [87] J. M. Tranquada, J. D. Axe, N. Ichikawa, A. R. Moodenbaugh, Y. Nakamura, and S. Uchida, *Phys. Rev. Lett.* **78**, 338 (1997).
- [88] N. D. Patel, A. Nocera, G. Alvarez, A. Moreo, and E. Dagotto, *Phys. Rev. B* **96**, 024520 (2017).
- [89] B. Pandey, R. Soni, L.-F. Lin, G. Alvarez, and E. Dagotto, *Phys. Rev. B* **103**, 214513 (2021).
- [90] E. Dagotto, S. Yunoki, A. L. Malvezzi, A. Moreo, J. Hu, S. Capponi, D. Poilblanc, and N. Furukawa, *Phys. Rev. B* **58**, 6414 (1998).
- [91] E. Dagotto, *Nanoscale Phase Separation and Colossal Magnetoresistance: The Physics of Manganites and Related Compounds*, Springer Series in Solid-State Sciences (Springer, Berlin, 2003).
- [92] S. Yunoki, J. Hu, A. L. Malvezzi, A. Moreo, N. Furukawa, and E. Dagotto, *Phys. Rev. Lett.* **80**, 845 (1998).
- [93] D. R. Neuber, M. Daghofer, H. G. Evertz, W. von der Linden, and R. M. Noack, *Phys. Rev. B* **73**, 014401 (2006).
- [94] A. Ricci, N. Poccia, G. Campi, B. Joseph, G. Arrighetti, L. Barba, M. Reynolds, M. Burghammer, H. Takeya, Y. Mizuguchi, Y. Takano, M. Colapietro, N. L. Saini, and A. Bianconi, *Phys. Rev. B* **84**, 060511(R) (2011).
- [95] A. Kreisel, P. J. Hirschfeld, and B. M. Andersen, *Symmetry* **12**, 1402 (2020).
- [96] J. O. Fjærestad, J. B. Marston, and U. Schollwöck, *Ann. Phys. (NY)* **321**, 894 (2006).
- [97] M. Yamanaka, W. Koshibae, and S. Maekawa, *Phys. Rev. Lett.* **81**, 5604 (1998).
- [98] D. F. Agterberg and S. Yunoki, *Phys. Rev. B* **62**, 13816 (2000).

- [99] H. Aliaga, B. Normand, K. Hallberg, M. Avignon, and B. Alascio, *Phys. Rev. B* **64**, 024422 (2001).
- [100] J. Riera, K. Hallberg, and E. Dagotto, *Phys. Rev. Lett.* **79**, 713 (1997).
- [101] T. Hotta, M. Moraghebi, A. Feiguin, A. Moreo, S. Yunoki, and E. Dagotto, *Phys. Rev. Lett.* **90**, 247203 (2003).
- [102] S. R. White and D. J. Scalapino, *Phys. Rev. Lett.* **80**, 1272 (1998).
- [103] Y.-F. Jiang, J. Zaanen, T. P. Devereaux, and H.-C. Jiang, *Phys. Rev. Research* **2**, 033073 (2020).
- [104] E. Stoudenmire and S. R. White, *Annu. Rev. Condens. Matter Phys.* **3**, 111 (2012).

INTERACTION-INDUCED TOPOLOGICAL PHASE TRANSITION AND MAJORANA EDGE STATES IN LOW-DIMENSIONAL ORBITAL-SELECTIVE MOTT INSULATORS

Previous chapter discovered a wealth of rich magnetic phases within the OSMP of a multiorbital ladder. One prominent magnetic order is the noncollinear block-spiral state, characterized by magnetic blocks that rigidly rotate along the ladder. Building upon these findings, this chapter presents the original research [O2], revealing that the interplay between the block-spiral order and superconductivity induces topological properties.

The key result is the discovery of an interaction-induced topological phase transition upon placing a generalized Kondo-Heisenberg chain (Sec. 2.6.2) in proximity to an *s*-wave superconductor. To reduce computational effort, hereafter, the chain geometry is used in place of the ladder, an approximation validated by my calculations of the spin structure factor. The topological transition manifests itself as the emergence of mutually correlated edge modes, the Majorana zero modes. Their presence is indicated by peaks in the local density of states, the sudden growth of entanglement throughout the system, and the appearance of spin-triplet pairing amplitudes. Crucially, the topological phase transition is driven by the change in magnetic properties: the spiral emerges together with the Majorana modes at a critical interaction U . To confirm that the edge states are indeed of Majorana origin, I independently cross-checked the analytical predictions for the nonlocal spectral functions, which were then verified numerically. This work proposes the 123 iron ladders as a potential platform to host Majorana states, which are of relevancy to quantum computing. For the convenience of the reader, a brief discussion now follows that enhances the appreciation of these findings.

The concept of Majorana fermions originates in elementary particle physics. It denominates a real-valued solution to the Dirac equation, that is, a particle which

is its own antiparticle [225]. To date, no experiment has conclusively reported such a particle. However, an intriguing manifestation of this concept emerges in the field of condensed-matter physics. Specifically, after the seminal works of A. Kitaev [226,227], the condensed-matter community put a tremendous effort to realize a particular flavor of Majoranas, the so-called *Majorana zero modes* (MZM). These are in-gap states at zero excitation energy (i.e., at the Fermi level) bound to a defect in a topological superconductor (a kind of “spinless” superconductor that realizes topological phases [228]). In one dimension (1D), MZM end up on the system’s edges, whereas in two dimensions (2D) they form, e.g., inside vortex cores [228].

The interest in MZM stems from their potential for achieving fault-tolerant quantum computing [227]. The key principles are as follows. Two unpaired MZM, e.g., at the ends of a 1D topological superconductor, constitute a single fermion, which can be in an empty or occupied state. The latter two states are degenerate and can be used to define a qubit¹. Crucially, quantum information encoded in this qubit is stored non-locally due to the spatial separation between the MZM. This property makes the information resilient against decoherence caused by local noise [230]. In order to alter the fermionic state, a disturbance must act nonlocally and coherently on both MZM, an unlikely scenario in any environment [228]. Furthermore, the gap between the MZM and the rest of the spectrum shields the qubit against hybridization with higher-energy nontopological excited states, which could corrupt the stored information [231]. These two properties are the crux of *topological protection*. Once the noise-resistant qubit is realized, the next step is to manipulate it in a topologically-protected manner in order to perform quantum computation. Here, the non-Abelian statistics of the MZM comes into play [230,231]. An MZM is neither a fermion nor a boson but rather a non-Abelian anyon. This property allows for so-called braiding operations, in which adiabatically exchanging the positions of the MZM implements unitary transformations within the degenerate ground-state manifold. By braiding, one can thus implement quantum gates and perform topologically-protected quantum computations. One caveat is that not every gate can be realized in this manner. Therefore, a topological quantum computer would still need to incorporate some “unprotected” operations [228,231]. However, in principle, these unprotected operations should be less susceptible to errors compared to their counterparts in nontopological platforms [231]. As such, a topological quantum computer emerges as a promising possibility in the race for reliable quantum computation.

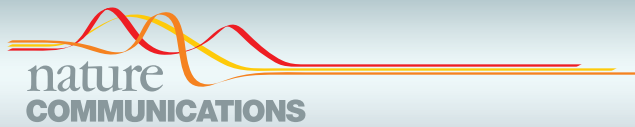
There are several routes to realize Majorana zero modes in the condensed-matter setting [228,230]. In 1D, which is relevant to the original results presented below, all of these approaches involve engineering the conditions elucidated in the prototypical Kitaev chain, namely, spinless-fermion behavior combined with spin-triplet (*p*-wave) superconductivity [226,228,230,232]. To achieve this, one prepares a so-called heterostructure, i.e., an intentional arrangement of multiple distinct materials, such as superconductors, semiconductors, etc. One such popular setup is the semiconducting quantum wire with strong spin-orbit coupling, subjected to a uniform magnetic field, and proximitized to a conventional *s*-wave superconductor [233,234]. The first two ingredients alter the band structure of the wire to achieve the desired “spinless” behavior,

¹To be precise, four MZM are actually necessary for a single qubit due to the selection rules dictated by parity symmetry [229].

while also enabling the third ingredient, the proximity-induced superconductivity, to become effectively p -wave [230]. See Ref. [232] for a discussion showing that the effective low-energy Hamiltonian of this setup takes the form of the Kitaev chain. An alternative configuration consists of a chain of magnetic adatoms deposited on an s -wave superconductor [235–243]. Crucially, the adatoms are assumed to have a classical noncollinear *spiral* spin texture, which has an equivalent effect on the band structure as the combination of the spin-orbit coupling and the uniform magnetic field. This equivalence can be shown rigorously via a gauge transformation [244], and one can also show here that the effective low-energy Hamiltonian is the Kitaev chain [235]. Both the semiconducting-wire [245–252] and the magnetic-adatom setups [253–259] were experimentally realized in numerous works. Despite such a tremendous experimental effort, an unambiguous report of MZM that demonstrates their topological properties is still missing.

Recently, topological properties have gained experimental relevance in the context of 2D iron-based superconductors [260–265]. Notably, scanning tunneling microscope measurements on the surface of $\text{FeTe}_{1-x}\text{Se}_x$ have revealed the presence of both zero-energy bound states and higher-energy discrete levels within vortex cores [260,262,263]. These zero-energy bound states manifest as zero-bias peaks in conductivity, which do not split when moving away from a vortex center for a wide range of magnetic fields. This lends strong support to their identification as MZM. Moreover, in the same material, there is evidence for linearly dispersing Majorana modes that propagate along crystalline domain walls [264]. These findings hold great promise due to the unique nature of this iron-based platform. In contrast to the setups discussed above, this particular platform does not necessitate any heterostructure engineering. It is a single material where topologically nontrivial bands and (high- T_c) superconductivity naturally emerge, providing all the necessary ingredients for MZM [263].

The work presented below establishes the iron-based ladders of the 123 family as another promising platform for MZM. As discussed above, a spiral magnetic order plus s -wave superconductivity has proven to be a reliable recipe for generating MZM. Nevertheless, only a handful of studies focusing on magnetic-adatom configurations [258,259] have effectively achieved the desired spiral spin texture within the adatom chain. The majority of these experiments, however, have predominantly realized a conventional ferromagnetic pattern instead, which is comparatively easier to stabilize but still necessitates the presence of spin-orbit coupling provided by the superconducting substrate [253,266]. On the other hand, it seems reasonable that a multiorbital ladder within OSMP has the potential to embody a quantum variant of this recipe, where the spiral order arises spontaneously from intricate interactions (see Chap. 3) and the superconductivity can either be an intrinsic property of the material itself, rendering the platform self-contained, or be induced by the usual proximity effect. By assuming proximity-induced superconductivity, the following work confirms this hypothesis and establishes the emergence of the MZM through an interaction-induced topological phase transition. Notably, the proposed multiorbital framework could offer a solution to mitigate the experimental challenges.



ARTICLE

<https://doi.org/10.1038/s41467-021-23261-2>

OPEN

Interaction-induced topological phase transition and Majorana edge states in low-dimensional orbital-selective Mott insulators

J. Herbrych ^{1✉}, M. Środa ¹, G. Alvarez ², M. Mierzejewski ¹ & E. Dagotto ^{3,4}

Topological phases of matter are among the most intriguing research directions in Condensed Matter Physics. It is known that superconductivity induced on a topological insulator's surface can lead to exotic Majorana modes, the main ingredient of many proposed quantum computation schemes. In this context, the iron-based high critical temperature superconductors are a promising platform to host such an exotic phenomenon in real condensed-matter compounds. The Coulomb interaction is commonly believed to be vital for the magnetic and superconducting properties of these systems. This work bridges these two perspectives and shows that the Coulomb interaction can also drive a canonical superconductor with orbital degrees of freedom into the topological state. Namely, we show that above a critical value of the Hubbard interaction the system simultaneously develops spiral spin order, a highly unusual triplet amplitude in superconductivity, and, remarkably, Majorana fermions at the edges of the system.

¹Department of Theoretical Physics, Faculty of Fundamental Problems of Technology, Wrocław University of Science and Technology, Wrocław, Poland.

²Computational Sciences and Engineering Division and Center for Nanophase Materials Sciences, Oak Ridge National Laboratory, Oak Ridge, TN, USA.

³Department of Physics and Astronomy, University of Tennessee, Knoxville, TN, USA. ⁴Materials Science and Technology Division, Oak Ridge National Laboratory, Oak Ridge, TN, USA. ✉email: jacek.herbrych@pwr.edu.pl

Topologically protected Majorana fermions—the elusive particles which are their own antiparticles—are exciting because of their potential importance in fault-resistant quantum computation. From the experimental perspective, heterostructure-based setups were proposed as the main candidates to host the Majorana zero-energy modes (MZM). For example, the topologically protected gapless surface states of topological insulators can be promoted to MZM by the proximity-induced pairing caused by an underlying superconducting (SC) substrate¹. However, the large spin-orbit coupling required to split the doubly degenerated bands due to the electronic spins, renders such a setup hard to engineer. Another group of proposals utilizes magnetic atoms (e.g., Gd, Cr, or Fe) arranged in a chain structure on a BCS superconductor^{2–12}. These important efforts have shown that creating MZM in real condensed-matter compounds is challenging and only rare examples are currently available.

Interestingly, a series of recent works have shown that doped high critical temperature iron-based superconductor Fe(Se,Te) can host MZM^{13–17}. Although the electron–electron interaction is believed to be relevant for the pairing, its role in the stabilization of MZM is unknown. In fact, in most theoretical proposals to realize MZM, these zero-energy modes are a consequence of specific features in the non-interacting band structure, with the electron–electron interaction playing only a secondary role (and often even destabilizing the MZM)^{18,19}. By contrast, here we will show that a SC system with orbital degrees of freedom can be driven into a topologically nontrivial phase hosting MZM via increasing Hubbard interactions; see illustrative sketch in Fig. 1a. We will focus on a generic model with coexisting wide and narrow energy bands, relevant to low-dimensional iron-based materials²⁰. It was previously shown^{21–23} that the multi-orbital Hubbard model can accurately capture static and dynamical properties of iron selenides, especially the block-magnetic order²⁴ of the 123 family AFe₂X₃ of iron-based ladders (with A alkali metals and X chalcogenides). For example, the three- and two-

orbital Hubbard model on a one-dimensional (1D) lattice^{23,25} successfully reproduces the inelastic neutron scattering spin spectrum, with nontrivial optical and acoustic modes. The aforementioned models exhibit^{21,26} the orbital-selective Mott phase (OSMP), with coexistent Mott-localized electrons in one orbital and itinerant electrons in the remaining orbitals. The system is then in an exotic state with simultaneously metallic and insulating properties. Furthermore, the localized orbitals have vanishing charge fluctuations, simplifying the description²⁶ into an OSMP effective model, i.e. the generalized Kondo–Heisenberg model (gKH)

$$H_{\text{gKH}} = t_i \sum_{\ell, \sigma} \left(c_{\ell, \sigma}^\dagger c_{\ell+1, \sigma} + \text{H.c.} \right) + U \sum_{\ell} n_{\ell, \uparrow} n_{\ell, \downarrow} + \mu \sum_{\ell, \sigma} n_{\ell, \sigma} - 2J_{\text{H}} \sum_{\ell} \mathbf{S}_{\ell} \cdot \mathbf{s}_{\ell} + K \sum_{\ell} \mathbf{S}_{\ell} \cdot \mathbf{S}_{\ell+1}. \quad (1)$$

The first three terms in the above Hamiltonian describe the itinerant electrons: $c_{\ell, \sigma}^\dagger$ ($c_{\ell, \sigma}$) creates (destroys) an electron with spin projection $\sigma = \{\uparrow, \downarrow\}$ at site $\ell = \{1, \dots, L\}$, t_i is their hopping amplitude, U is the repulsive Hubbard interaction, and $\mu = \epsilon_{\text{F}}$ is the Fermi energy set by the density of itinerant electrons $\bar{n} = \sum_{\ell} (n_{\ell, \uparrow} + n_{\ell, \downarrow}) / L$.

The double occupancy of the localized orbital can be eliminated by the Schrieffer–Wolff transformation and the remaining degrees of freedom, the localized spins \mathbf{S}_{ℓ} in the above model, interact with one another via a Heisenberg term with spin-exchange $K = 4t_i^2 / U$ [t_i is the hopping amplitude within the localized band]. Finally, J_{H} stands for the on-site interorbital Hund interaction, coupling the spins of the localized and itinerant electrons, \mathbf{S}_{ℓ} and \mathbf{s}_{ℓ} , respectively. Figure 1b contains a sketch of the model. Here, we consider a 1D lattice and use $t_i = 0.5$ [eV] and $t_l = 0.15$ [eV], with kinetic energy bandwidth $W = 2.1$ [eV] as a unit of energy²⁷. Furthermore, to reduce the number of parameters in the model, we set $J_{\text{H}} / U = 1/4$, a value widely used when modeling iron superconductors. Systems with open boundary

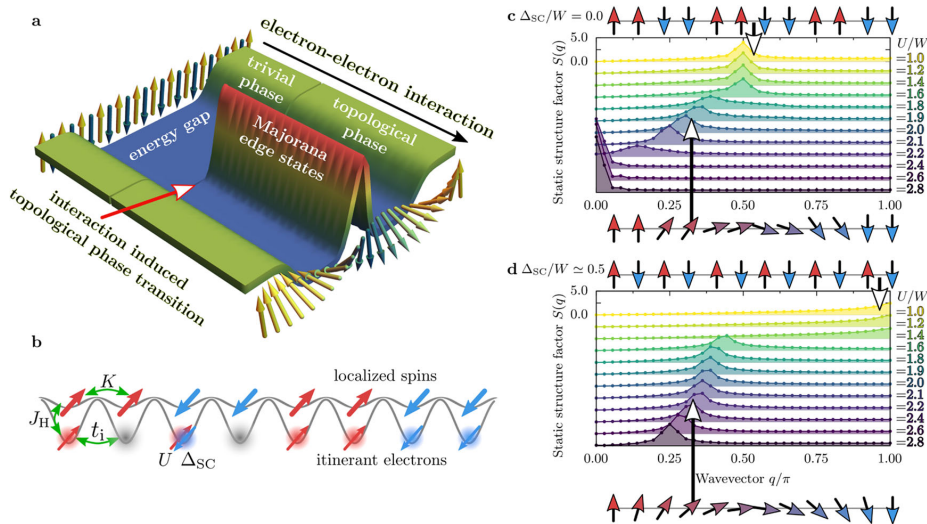


Fig. 1 Orbital-selective Mott phase and Majoranas. **a** Sketch of the chain edge density-of-states as a function of the electron–electron Hubbard interaction strength. Magnetic orders (depicted by arrows) in the trivial and the topological superconducting (SC) phases are also presented. **b** Schematic representation of the generalized Kondo–Heisenberg model studied here, with localized and itinerant electrons and simultaneously active Hubbard U and superconducting Δ_{SC} couplings. **c** and **d** Interaction U dependence of the static structure factor $S(q)$ for **c** $\Delta_{\text{SC}} = 0$, **d** $\Delta_{\text{SC}} / W \approx 0.5$ (calculated for $L = 36$ and $\bar{n} = 0.5$).

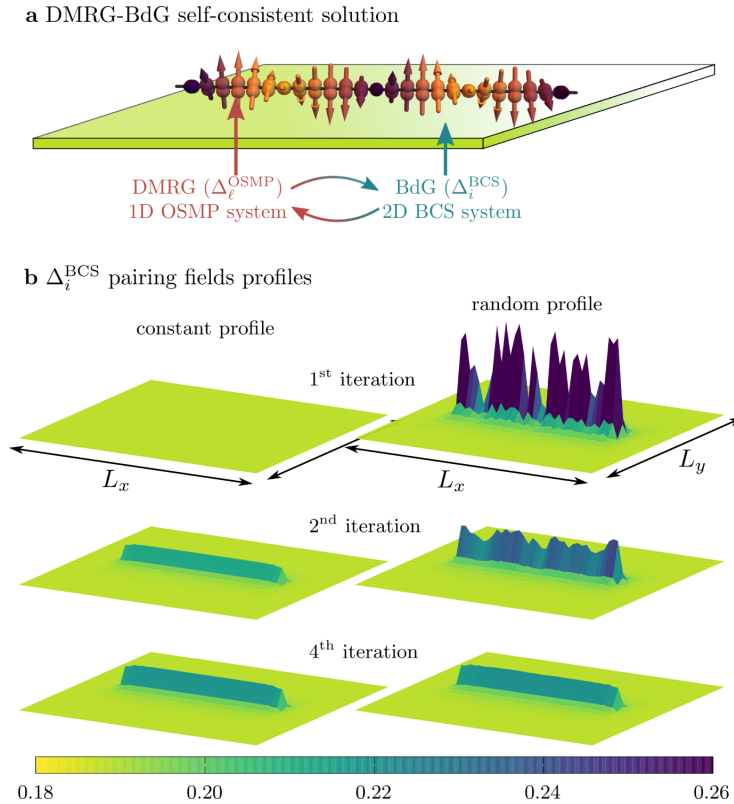


Fig. 2 BdG self-consistent solution. **a** Sketch of the hybrid DMRG-BdG algorithm. The OSMP chain is placed in the middle of a 2D BCS superconductor and coupled to it via the pairing field amplitudes present in both systems. **b** Iteration dependence of the Δ_i^{BCS} profiles for the case with the OSMP chain placed in the middle. The left (right) column depicts results initialized without (with random) pairing fields in the 1D OSMP system (calculated for $U/W = 2$). See the “Methods” sections for details.

conditions are studied via the density-matrix renormalization group (DMRG) method (see the “Methods” section).

The key ingredient in systems expected to host the MZM is the presence of an SC gap, modeled typically by an s -wave pairing field. Such a term represents the proximity effect²⁹ induced on the magnetic system by an external s -wave superconductor. However, it should be noted that the SC proximity effect has to be considered with utmost care. For example, recent experimental investigations³⁰ showed that although the interface between Nb (BCS s -wave SC) and Bi_2Se_3 film (topological metal) leads to induced SC order, the same setup with $(\text{Bi}_{1-x}\text{Sb}_x)_2\text{Se}_3$ (another topological insulator) displays massive suppression of proximity pairing. On the other hand, in the class of systems studied here (low-dimensional OSMP iron-based materials), the pairing tendencies could arise from the intrinsic superconductivity of BaFe_2S_3 and BaFe_2Se_3 under pressure^{31–33} or doping^{22,34}.

In order to keep our discussion general, we will make minimal assumptions on the SC state, and consider only the simplest on-site pairing. The reader should consider it either as the intrinsic pairing tendencies of the iron-based SC material or as the pairing field induced by the proximity to an s -wave SC substrate, e.g., Pb or Nb. Independently of its origin, the SC in the 1D OSMP system studied here must be investigated beyond the 1D lattice since the quantum fluctuations would inevitably destroy any long-range order. Therefore, let us first consider the OSMP chain placed atop the center of a two-dimensional (2D) BCS

superconductor (see Fig. 2a for a sketch) and the total system described by the Hamiltonian

$$H_{\text{tot}} = H_{\text{gKH}} + H_{\text{BCS}} - V \sum_{(\ell, \ell')} (c_{\ell, \uparrow}^\dagger c_{\ell', \downarrow}^\dagger a_{\ell, \downarrow} a_{\ell', \uparrow} + \text{H.c.}) \quad (2)$$

Here, ℓ represents the single site within the 2D BCS system H_{BCS} which is closest to the site ℓ in the OSMP chain, and $a_{i, \sigma}, a_{i, \sigma}^\dagger$ stand for fermionic operators within the BCS superconductor (see the “Methods” section). The interaction between the subsystems [last term in Eq. (2)] is studied within the BCS-like decoupling scheme, where we introduce the pairing amplitudes $\Delta_\ell^{\text{BCS}} = \langle a_{\ell, \downarrow} a_{\ell, \uparrow} \rangle$ and $\Delta_\ell^{\text{OSMP}} = \langle c_{\ell, \downarrow} c_{\ell, \uparrow} \rangle$ for the BCS superconductor and the OSMP chain, respectively. In order to fully take into account the many-body nature of the OSMP system, we have developed a hybrid algorithm, the details of which are given in the “Methods” section. In summary: we iteratively solve the OSMP chain and the BCS system by means of the DMRG and the Bogoliubov–de Gennes (BdG) equations, respectively. This back-and-forth computational setup is costly but important to gain confidence in our result.

We monitor the landscapes of pairing fields in both systems and exemplary results are presented in Fig. 2b (for more results see Supplementary Note 1). Initially, only the BCS system has finite, spatially uniform, pairing amplitudes Δ_ℓ^{BCS} (left column in Fig. 2b), which are then used in the DMRG procedure applied to

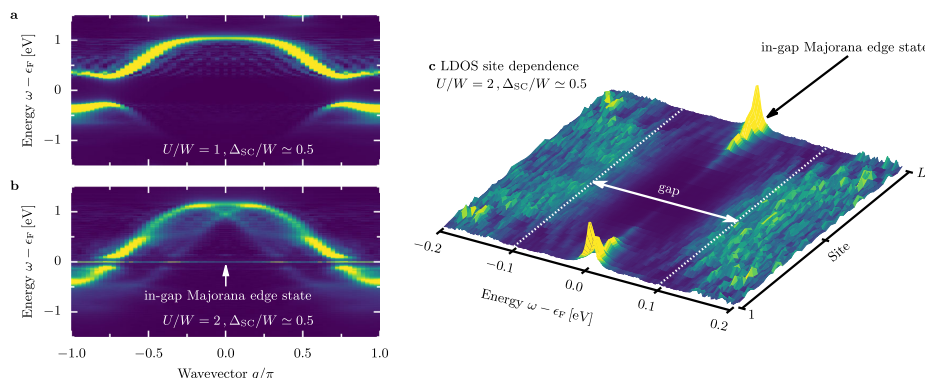


Fig. 3 Spectral functions. Effect of the finite pairing field $\Delta_{SC}/W \simeq 0.5$ on the single-particle spectral function $A(q, \omega)$ for **a** $U/W = 1$ and **b** $U/W = 2$ calculated for $L = 36$, $\bar{n} = 0.5$, and $\delta\omega = 0.02$ [eV]. Majorana zero-energy modes are indicated in **b**. **c** Local density-of-states (LDOS) in the in-gap frequency region ($\delta\omega = 0.002$ [eV]) vs. chain site index. The sharp LDOS peaks at the edges represent Majorana edge states, while the bulk of the system exhibits gapped behavior.

the OSMP Hamiltonian

$$H = H_{\text{gKH}} + \sum_{\ell} \Delta_{\ell} \left(c_{\ell, \uparrow}^{\dagger} c_{\ell, \downarrow}^{\dagger} + \text{H.c.} \right), \quad (3)$$

where $\Delta_{\ell} = -V\Delta_{\ell}^{\text{BCS}}$. Next, the $\Delta_{\ell}^{\text{OSMP}}$ set is calculated from DMRG and returned to the BdG equations relevant for the BCS system. The procedure is repeated until convergence is established. The results presented in Fig. 2b show that already after ~ 4 iterations the landscape of $\Delta_{\ell}^{\text{BCS}}$ stabilizes to an interaction U -dependent value. We found that the resulting amplitude $\Delta_{\ell} = -V\Delta_{\ell}^{\text{BCS}}$ is almost uniform within the OSMP chain. Furthermore, we have also confirmed that using extended s -wave pairing (creating pairs on nearest-neighbor sites) does not influence our conclusions. Therefore, in the remainder of the paper, we use spatially uniform $\Delta_{\ell} = \Delta_{SC}$ in Eq. (3). Also, in order to emphasize the role of interaction, in the main text, we fix the pairing field to $\Delta_{SC}/W \simeq 0.5$. The detailed Δ_{SC} -dependence of our findings is discussed in Supplementary Note 1.

Results

Magnetism of OSMP. Previous work has shown that the OSMP (with $\Delta_{SC} = 0$) has a rich magnetic phase diagram²⁶. (i) At small U the system is paramagnetic. (ii) At $\bar{n} = 1$ and $\bar{n} = 0$ standard antiferromagnetic (AFM) order develops, $\uparrow\downarrow\uparrow\downarrow$, with total on-site magnetic moment $\langle S^2 \rangle = S(S+1) = 2$ and $3/4$, respectively. (iii) For $0 < \bar{n} < 1$ and $U \gg W$ the system is a ferromagnet (FM) $\uparrow\uparrow\uparrow$. Interestingly, in the always challenging intermediate interaction regime $U \sim \mathcal{O}(W)$ the AFM- and FM-tendencies (arising from superexchange and double-exchange, respectively) compete and drive the system towards novel magnetic phases unique to multi-orbital systems. (iv) For $U \sim W$, the system develops a so-called block-magnetic order, consisting of FM blocks that are AFM coupled, e.g. $\uparrow\uparrow\downarrow\downarrow$, as sketched in Fig. 1c. The block size appears controlled by the Fermi vector k_F , i.e., the propagation wavevector of the block-magnetism is given by $q_{\text{max}} = 2k_F$ (with $2k_F = \pi\bar{n}$ for the chain lattice geometry). In this work, we choose $\bar{n} = 0.5$ (adjusted via the chemical potential μ), as the relevant density for BaFe_2Se_3 $\pi/2$ -block magnetic order²⁴. Then, the latter order can be identified via the peak position of the static structure factor $S(q) = \langle \mathbf{T}_{-q} \cdot \mathbf{T}_q \rangle$ at $q_{\text{max}} = \pi/2$ or via a finite dimer order parameter $D_{\pi/2} = \sum_{\ell} (-1)^{\ell} \langle \mathbf{T}_{\ell} \cdot \mathbf{T}_{\ell+1} \rangle / L$, where we introduced the Fourier transform $\mathbf{T}_q = \sum_{\ell} \exp(iq\ell) \mathbf{T}_{\ell} / \sqrt{L}$ of the total spin operator $\mathbf{T}_{\ell} = \mathbf{S}_{\ell} + \mathbf{s}_{\ell}$. In Fig. 1c $S(q)$ is shown at

moderate interaction: at $U/W < 1.6$ it displays a maximum at $q_{\text{max}} = \pi/2$, consistent with $\uparrow\uparrow\downarrow\downarrow$ the order.

Remarkably, it has been shown recently²⁷ that there exists an additional unexpected phase in between the block- and FM-ordering. Namely, upon increasing the interaction ($1.6 < U/W < 2.4$), the maximum of $S(q)$ in Fig. 1c shifts towards incommensurate wavevectors (while for $U/W > 2.4$ the system is a ferromagnet). This incommensurate region reflects a novel magnetic spiral where the magnetic islands maintain their ferromagnetic character (with $D_{\pi/2} \neq 0$) but start to rigidly rotate, forming a so-called block-spiral (see sketch Fig. 1c). The latter can be identified by a large value²⁷ of the long-range chirality correlation function $\langle \kappa_{\ell} \cdot \kappa_m \rangle$ where $\kappa_{\ell} = \mathbf{T}_{\ell} \times \mathbf{T}_{\ell+N}$ and N is the block size. It is important to note that the spiral magnetic order appears without any direct frustration in the Hamiltonian (1), but rather is a consequence of hidden frustration caused by competing energy scales in the OSMP regime. Finally, it should be noted that the block-spiral OSMP state is not limited to 1D chains. In Supplementary Note 2, we show similar investigations for the ladder geometry and find rigidly rotating 2×2 FM islands. These results are consistent with recent nuclear magnetic resonance measurements on the CsFe_2Se_3 ladder compound which reported the system's incommensurate ordering³⁵.

Interestingly, an interaction-induced spiral order is also present when SC pairing is included in the model, as evident from Fig. 1d. However, the spiral mutates from block- to canonical-type with $D_{\pi/2} = 0$ (see the sketch in Fig. 1d), indicating unusual back-and-forth feedback between magnetism and superconductivity. As discussed below, the pairing optimizes the spiral profile to properly create the Majoranas. The competition between many energy scales (Hubbard interaction, Hund exchange, and SC pairing) leads to novel phenomena: an interaction-induced topological phase transition into a many-body state with MZM, unconventional SC, and canonical spiral.

Majorana fermions. Figure 3 shows the effect of $\Delta_{SC}/W \simeq 0.5$ on the single-particle spectral function $A(q, \omega)$ (see the “Methods” section) for the two crucial phases in our study, the block-collinear and block-spiral magnetic orders ($U/W = 1$ and $U/W = 2$, respectively). As expected, in both cases, a finite SC gap opens at the Fermi level ϵ_F (~ 0.5 [eV] for $U/W = 1$ and ~ 0.1 [eV] for $U/W = 2$). Remarkably, in the block-spiral phase, an additional prominent feature appears: a sharply localized mode inside the gap at ϵ_F , displayed in Fig. 3b. Such an in-gap mode is a

characteristic feature of a topological state, namely the bulk of the system is gapped, while the edge of the system contains the in-gap modes. To confirm this picture, in Fig. 3c, we present a high-resolution frequency data of the real-space local density-of-states (LDOS; see the “Methods” section) near the Fermi energy ϵ_F . As expected, for the topologically nontrivial phase, the zero energy modes are indeed confined to the system’s edges. It is important to note that this phenomenon is absent for weaker interaction $U/W = 1$. Furthermore, one cannot deduce this behavior from the $U \rightarrow \infty$ or $J_H \rightarrow \infty$ limits, where the system has predominantly collinear AFM or FM ordering, leading again to a trivial SC behavior. However, as shown below, at moderate U the competing energy scales present in the OSMP lead to the topological phase transition controlled by the electron–electron interaction.

Let us now identify the induced topological state. The size dependence of the LDOS presented in Fig. 3c reveals zero-energy edge modes, namely peaks at frequency $\omega \simeq \epsilon_F$ localized at the edges of the chain with open ends. While such modes are a characteristic property of the MZM, finding peaks in the LDOS alone is insufficient information for unambiguous identification. To demonstrate that the gKH model with superconductivity indeed hosts Majorana modes, we have numerically checked three distinct features of the MZM:

- (i) Since the Majorana particles are their own antiparticles, the spectral weight of the localized modes should be built on an equal footing from the electron and hole components. Figure 4a shows that this is indeed the case.
- (ii) The total spectral weight present in the localized modes can be rigorously derived from the assumption of the MZM’s existence (see the “Methods” section), and it should be equal to 0.5. Integrating our DMRG results in Fig. 3c over a narrow energy window and adding over the first few edge sites gives $\simeq 0.47$, very close to the analytical prediction. Note that the Majoranas are not strictly localized at one edge site $\ell \in \{1, L\}$, as evident from Fig. 4a. Instead, the MZM is exponentially decaying over a few sites (see

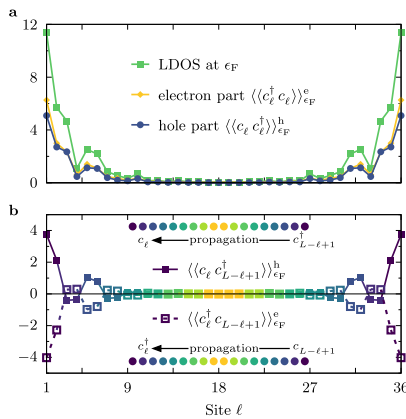


Fig. 4 Correlation functions of Majorana fermions. **a** Site ℓ dependence of the local density-of-states (LDOS) at the Fermi level ($\omega = \epsilon_F$) together with its hole ($\langle\langle c_\ell c_\ell^\dagger \rangle\rangle_{\epsilon_F}^h$) and electron ($\langle\langle c_\ell^\dagger c_\ell \rangle\rangle_{\epsilon_F}^e$) contributions. **b** Site dependence of the centrosymmetric spectral function ($\langle\langle c_\ell c_{L-\ell+1}^\dagger \rangle\rangle_{\epsilon_F}^h$ and $\langle\langle c_\ell^\dagger c_{L-\ell+1} \rangle\rangle_{\epsilon_F}^e$). Sketches represent the calculated process: the probability of creating the electron on one end of the system (site ℓ) and a hole at the opposite end (site $L - \ell + 1$), or vice-versa, at given energy ω . The pairs of sites where the spectral function is evaluated are represented by the same colors. All results were calculated for $L = 36$, $U/W = 2$, $\Delta_{SC}/W \simeq 0.5$, and $\bar{n} = 0.5$.

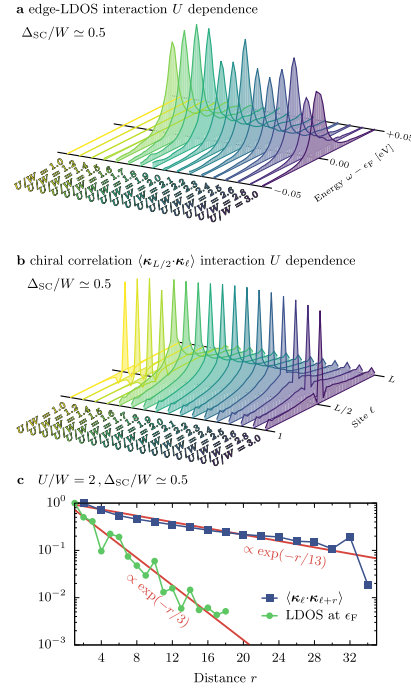


Fig. 5 Interaction dependence of the MZM. Dependence on the Hubbard interaction U of **a** the edge-LDOS at site $\ell = 1$ (near the Fermi level ϵ_F) and **b** the chirality correlation function $\langle\kappa_{L/2}, \kappa_\ell\rangle$. All results calculated for $\Delta_{SC}/W \simeq 0.5$, $\bar{n} = 0.5$, $L = 36$. **c** Spatial decay of the local density-of-states at the Fermi level (LDOS at ϵ_F) and the chirality correlation function $\langle\kappa_\ell \cdot \kappa_{\ell+r}\rangle$ for $U/W = 2$. Red solid lines indicate exponential decay $\exp(-r/l_a)$ with $l_{MZM} = 3$ and $l_s = 15$, for the MZM and the spiral order, respectively.

Fig. 5c), and we must add the spectral weight accordingly (separately for the left and right edges).

- (iii) The MZM located at the opposite edges of the system form one fermionic state, namely the edge MZM is correlated with one another over large distances. To show such behavior, consider the hole- and electron-like centrosymmetric spectral functions, $\langle\langle c_\ell c_{L-\ell+1}^\dagger \rangle\rangle_\omega^h$ and $\langle\langle c_\ell^\dagger c_{L-\ell+1} \rangle\rangle_\omega^e$, respectively. These functions represent the probability amplitude of creating an electron on one end and a hole at the opposite end (or vice-versa) at a given energy ω (see the “Methods” section for detailed definitions and Supplementary Note 3 for further discussion). Figure 4b shows $\langle\langle c_\ell c_{L-\ell+1}^\dagger \rangle\rangle_\omega^h$ and $\langle\langle c_\ell^\dagger c_{L-\ell+1} \rangle\rangle_\omega^e$ at the Fermi level $\omega = \epsilon_F$, namely in the region where the MZM should be present. As expected, the bulk of the system behaves fundamentally different from the edges. In the former, crudely when $L/2 \lesssim \ell \lesssim 3L/4$, the aforementioned spectral functions vanish reflecting the gapped (bulk) spectrum with lack of states at the Fermi level. However, at the boundaries ($\ell \ll L/2$ and $\ell \gg L/2$) the values of the centrosymmetric spectral functions are large, with a maximum at the edges $\ell \in \{1, L\}$. The long-range (across the system) correlations of the edge states strongly support their topological nature.

Finally, let us discuss the physical mechanism causing the onset of MZM. In Fig. 5a we present the Hubbard U interaction dependence of the edge-LDOS ($\ell = 1$) in the vicinity of the Fermi

level, $\omega \sim \epsilon_F$. It is evident from the presented results that the edge-LDOS acquires a finite value quite abruptly for $U > U_c \simeq 1.5$. To further clarify this matter, let us return to the magnetic states in the OSMP regime. Figure 5b shows the chirality correlation function $\langle \kappa_{l/2} \cdot \kappa_\ell \rangle$ (with $\kappa_\ell = \mathbf{T}_\ell \times \mathbf{T}_{\ell+1}$) for increasing value of the Hubbard U strength. We observe a sudden appearance of the chirality correlation exactly at U_c , a behavior similar to that of the edge LDOS. Interestingly, in the system without the pairing field, $\Delta_{SC} = 0$, at a similar value of $U \simeq 1.6$ the system enters the block-spiral phase with rigidly rotating FM islands. However, in our setup, the tendencies of OSMP to create magnetic blocks²⁶ are highly suppressed by empty and doubly occupied sites favored by the finite pairing field Δ_{SC} . As a consequence, the block-spiral order is reshaped to a canonical type of spiral without dimers $D_{\pi/2} = 0$. This behavior is similar to the MZM observed when combining s -wave SC with a classical magnetic moment heterostructure^{2,4–6}. In the latter, the Ruderman–Kittel–Kasuya–Yosida (RKKY) mechanism stabilizes a classical long-range spiral with $2k_F$ pitch (where $k_F \propto \bar{n}$ is the Fermi wavevector). Within the OSMP, however, the pitch is, on the other hand, controlled by the interaction U (at fixed \bar{n}), as evident from the results presented in Fig. 1b, c.

Furthermore, analysis of the chirality correlation function $\langle \kappa_\ell \cdot \kappa_{\ell+r} \rangle$ indicates that the spiral order decays with the distance r (see Fig. 5c), as expected in a 1D quantum system. Note, however, that the MZM decay length scale, l_{MZM} , and that of the spiral, l_s , differ substantially. The Majoranas are predominantly localized at the system edges, thus yielding a short localization length $l_{MZM} \simeq 3$. The spiral, although still decaying exponentially, has a robust correlation length $l_s \simeq 13$, of the same magnitude as the $\Delta_{SC} = 0$ result²⁷. Then, for large but finite chains the overlap between the edge modes is negligible while the magnetic correlations on the distance L are still large enough to promote triplet pairing and the Majorana modes. In addition, we have observed that smaller values of Δ_{SC} than considered here also produce the MZM. However, since the Majoranas have an edge localization length inversely proportional to Δ_{SC} , reducing the latter leads to overlaps between the left and right Majorana states in our finite systems^{28,36}, thus distorting the physics we study. After exploration, $\Delta_{SC}/W \simeq 0.5$ was considered an appropriate compromise to address qualitatively the effects of our focus given our practical technical constraints within DMRG (see Supplementary Note 4 for details).

Conceptually, it is important to note that the interaction-induced spiral at $U/W = 2$ is not merely frozen when Δ_{SC} increases. Specifically, the characteristics²⁷ of the chirality correlation function $\langle \kappa_i \cdot \kappa_j \rangle$ qualitatively differ between the trivial ($\Delta_{SC} = 0$) and topological phases ($\Delta_{SC} \neq 0$): increasing Δ_{SC} suppresses the dimer order and leads to a transformation from block spiral to a standard canonical spiral with $D_{\pi/2} = 0$ in the topologically nontrivial phase. As a consequence, the proximity to a superconductor influences on the magnetic order to optimize the spin pattern needed for MZM. Surprisingly, Δ_{SC} influences on the collinear spin order as well. In fact, at $U/W = 1$, before spirals are induced, the proximity to superconductivity changes the block spin order into a more canonical staggered spin order to optimize the energy (see Fig. 3b). This is a remarkable, and unexpected, back-and-forth positive feedback between degrees of freedom that eventually causes the stabilization of the MZM.

Discussion

Our main findings are summarized in Fig. 6: upon increasing the strength of the Hubbard interaction U within the OSMP with added SC pairing field, the system undergoes a topological phase transition. The latter can be detected as the appearance of edge modes which are mutually correlated in a finite system. This

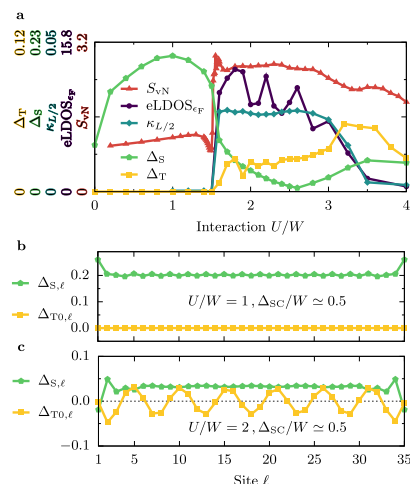


Fig. 6 Phase diagram. **a** Hubbard interaction U dependence of the (i) von Neumann entanglement entropy S_{vN} , (ii) edge local density-of-states at the Fermi level (eLDOS $_{eF}$), (iii) the value of chirality correlation function at distance $L/2$ (i.e. $\langle \kappa_{L/4} \cdot \kappa_{3L/4} \rangle$), as well as (iv) nonlocal singlet Δ_S and triplet Δ_T pairing amplitudes. See text for details. All results were calculated for $L = 36$, $\Delta_{SC}/W \simeq 0.5$, and $\bar{n} = 0.5$. **b**, **c** Spatial dependence of the singlet and triplet SC amplitudes, $\Delta_{S,\ell}$ and $\Delta_{T0,\ell}$, respectively (see the “Methods” section for details), with **b** the trivial phase ($U/W = 1$, $\Delta_{SC}/W \simeq 0.5$) and **c** the topological phase ($U/W = 2$, $\Delta_{SC}/W \simeq 0.5$). In the latter, the oscillations of the triplet component are related to the pitch of the underlying spiral magnetic order.

turn leads to, e.g., the sudden increase of the entanglement, as measured by the von Neumann entanglement entropy S_{vN} (see the “Methods” section). The transition is driven by the change in the magnetic properties of the system, namely by inducing a finite chirality visible in the correlation function $\langle \kappa_\ell \cdot \kappa_m \rangle$. The above results are consistent with the appearance of the MZM at the topological transition. It should be noted that the presence of those MZM implies unconventional p -wave superconductivity⁸. As a consequence, for our description to be consistent, the topological phase transition ought to be accompanied by the onset of triplet SC amplitudes Δ_T . To test this nontrivial effect, we monitored the latter, together with the singlet SC amplitude Δ_S (related to a nonlocal s -wave SC; see the “Methods” section for detailed definitions). As is evident from the results in Fig. 6, for $U < U_c$ we observe only the singlet component Δ_S canonical for an s -wave SC, while for $U \geq U_c$ the triplet amplitude Δ_T develops a robust finite value. It is important to stress that $\Delta_T \neq 0$ is an emergent phenomenon, induced by the correlations present within the OSMP, and is not assumed at the level of the model (we use a trivial on-site s -wave pairing field as input).

In summary, we have shown that the many competing energy scales induced by the correlation effects present in SC multi-orbital systems within OSMP lead to a topological phase transition. Differently from the other proposed MZM candidate setups, our scheme does not require frozen classical magnetic moments or, equivalently, FM ordering in the presence of the Rashba spin-orbit coupling³. All ingredients necessary to host Majorana fermions appear as a consequence of the quantum effects induced by the electron–electron interaction. The pairing field can be induced by the proximity effect with a BCS superconductor, or it could be an intrinsic property of some iron superconductors under pressure or doping. It is important to note that the

coexistence of SC and nontrivial magnetic properties is mostly impossible in single-orbital systems. Here, the OSMP provides a unique platform in which this constraint is lifted by, on the one hand, spatially separating such phenomena, and, on the other hand, strongly correlating them with each other. Furthermore, our proposal allows to study the effect of quantum fluctuations on the MZM modes. There are only a few candidate materials that may exhibit the behavior found here. The block-magnetism (a precursor of the block-spiral phase) was recently argued to be relevant for the chain compound $\text{Na}_2\text{Fe}_2\text{Se}_3$ ³⁷, and was already experimentally found in the BaFe_2Se_3 ladder²⁴. Incommensurate order was reported in CsFe_2Se_3 ³⁵. Also, the OSMP^{38–40} and superconductivity^{31–33} proved to be important for other compounds from the 123 family of iron-based ladders.

Our findings provide also a new perspective to the recent reports of topological superconductivity and Majorana fermions found in two-dimensional compounds $\text{Fe}(\text{Se},\text{Te})$ ^{13–17}. Since orbital-selective features were observed in clean FeSe ^{41,42}, it is reasonable to assume that OSMP is also relevant for doped $\text{Fe}(\text{Se},\text{Te})$ ⁴³. Regarding magnetism, the ordering of FeSe was mainly studied within the classical long-range Heisenberg model⁴⁴, where block-like structures (e.g., double stripe or staggered dimers) dominate the phase diagram for realistic values of the system parameters. Note that the effective spin model of the block-spiral phase studied here was also argued to be long-ranged²⁷. The aforementioned phases of FeSe are typically neighboring (or are even degenerate with) the frustrated spiral-like magnetic orders⁴⁴, also consistent with the OSMP magnetic phase diagram²⁶. In view of our results, the following rationale could be used to explain the behavior of the above materials: the competing energy scales present in multi-orbital iron-based compounds, induced by changes in the Hubbard interaction due to chemical substitution or pressure, lead to exotic magnetic spin textures. The latter, together with the SC tendencies, lead to topologically nontrivial phases exhibiting the MZM^{45,46}. Also, similar reasoning can be applied to the heavy-fermion metal UTe_2 . It was recently shown that this material displays spin-triplet superconductivity⁴⁷ together with incommensurate magnetism⁴⁸.

Methods

DMRG method. The Hamiltonians and observables discussed here were studied using the density matrix renormalization group (DMRG) method^{49,50} within the single-center site approach⁵¹, where the dynamical correlation functions are evaluated via the dynamical-DMRG^{52,53}, i.e., calculating spectral functions directly in frequency space with the correction-vector method using Krylov decomposition⁵³. We have kept up to $M = 1200$ states during the DMRG procedures, allowing us to accurately simulate system sizes up to $L = 48$ and $L = 60$ with truncation errors $\sim 10^{-8}$ and $\sim 10^{-6}$, respectively.

We have used the DMRG++ computer program developed at Oak Ridge National Laboratory (<https://github.com/dmrgPlusPlus/>). The input scripts for the DMRG++ package to reproduce our results can be found at <https://bitbucket.org/herbrychjacek/corrwro/> and also on the DMRG++ package webpage.

Hybrid DMRG-BdG algorithm. We consider a 2D, s -wave, BCS superconductor at half-filling,

$$H_{\text{BCS}} = -t_{\text{BCS}} \sum_{(i,j),\sigma} a_{i,\sigma}^\dagger a_{j,\sigma} - V_{\text{BCS}} \sum_r \left(\Delta_r^{\text{BCS}} a_{r,\uparrow}^\dagger a_{r,\downarrow}^\dagger + \text{H.c.} \right). \quad (4)$$

Here $\langle i,j \rangle$ denotes summation over nearest-neighbor sites of a square lattice and $a_{i,\sigma}^\dagger$ ($a_{i,\sigma}$) creates (destroys) an electron with spin projection $\sigma = \{\uparrow, \downarrow\}$ at site i . The BCS system is coupled to the OSMP chain, as described by the last term of Hamiltonian (2) in the main text. At the BCS level, the latter term emerges as an additional (external) pairing field to the OSMP region

$$H_V = -V \sum_r \left(\Delta_r^{\text{OSMP}} a_{r,\uparrow}^\dagger a_{r,\downarrow}^\dagger + \text{H.c.} \right). \quad (5)$$

Here, the summation is restricted to the sites of the BCS system which are coupled to the OSMP chain. In numerical calculations, we set the hopping integral $t_{\text{BCS}} = 2$ [eV], fix the system size to $L_x = 54$ and $L_y = 27$ (with 1D OSMP system coupled to the $\ell' = 14$ row of sites), use the BCS attractive potential $V_{\text{BCS}}/t_{\text{BCS}} = 2$ and the

coupling strength $V/t_{\text{BCS}} = 2$. Although we assume periodic boundary conditions for the BCS system, the translational invariance is broken by the coupling to the OSMP chain.

Our procedure consists of two alternating steps:

1. **BdG calculations:** In the first step, we assume an initial set $\Delta_\ell^{\text{OSMP}}$ and diagonalize the Hamiltonian $H_{\text{BCS}} + H_V$, as defined in Eqs. (4) and (5). To this end, we use the standard BdG equations at zero temperature. They yield self-consistent results for the pairing amplitude, $\Delta_i^{\text{BCS}} = (a_{i,\downarrow} a_{i,\uparrow})$, for all sites i within the BCS system. From among the latter results, we single out the amplitudes $\Delta_{\ell'}^{\text{BCS}}$ on the sites $i = \ell'$ which are coupled to the OSMP chain.
2. **DMRG calculations:** The OSMP system within Eq. (3) is evaluated using the DMRG approach. The spatially dependent amplitudes $\Delta_\ell^{\text{OSMP}}$ are calculated providing a new set of external fields for the subsequent BdG calculations.

The above procedure is repeated iteratively until we obtain converged results. In the main text (see Fig. 2) we presented results of the above algorithm starting from $\Delta_\ell^{\text{OSMP}} = 0$. However, the procedure can also start from arbitrary pairing fields $\Delta_\ell^{\text{OSMP}}$ in the first step. The right column of Fig. 2b depicts results obtained using a random initial profile $\Delta_\ell^{\text{OSMP}} \in [0, 1]$. It is evident from the presented results that the converged result is independent of the initial configuration (at least for the couplings studied here). See Supplementary Note 1 for further discussion and additional results.

Spectral functions. Let us define the site-resolved frequency (ω)-dependent electron (e) and hole (h) correlation functions

$$\langle\langle A_\ell B_m \rangle\rangle_\omega^{\text{e,h}} = -\frac{1}{\pi} \text{Im} \langle \text{gs} | A_\ell \frac{1}{\omega \mp (H - \epsilon_0)} B_m | \text{gs} \rangle, \quad (6)$$

where the signs + and – should be taken for $\langle\langle \dots \rangle\rangle_\omega^{\text{e}}$ and $\langle\langle \dots \rangle\rangle_\omega^{\text{h}}$, respectively. Here, $|\text{gs}\rangle$ is the ground-state, ϵ_0 the ground-state energy, and $\omega^\mp = \omega + i\eta$ with η a Lorentzian-like broadening. For all results presented here, we choose $\eta = 2\delta\omega$, with $\delta\omega/W = 0.001$ (unless stated otherwise).

The single-particle spectral functions $A(q, \omega) = A^{\text{e}}(q, \omega) + A^{\text{h}}(q, \omega)$, where A^{e} (A^{h}) represent the electron (hole) part of the spectrum, have a standard definition,

$$\begin{aligned} A^{\text{h}}(q, \omega) &= \sum_\ell e^{-i\ell(\ell-L/2)} \langle\langle c_\ell c_{L/2}^\dagger \rangle\rangle_\omega^{\text{h}}, \\ A^{\text{e}}(q, \omega) &= \sum_\ell e^{+i\ell(\ell-L/2)} \langle\langle c_\ell^\dagger c_{L/2} \rangle\rangle_\omega^{\text{e}}, \end{aligned} \quad (7)$$

with $c_\ell = \sum_\sigma c_{\ell,\sigma}$. Finally, the LDOS is defined as

$$\text{LDOS}(\ell, \omega) = \langle\langle c_\ell c_\ell^\dagger \rangle\rangle_\omega^{\text{h}} + \langle\langle c_\ell^\dagger c_\ell \rangle\rangle_\omega^{\text{e}}. \quad (8)$$

Spectral functions of Majorana edge-states. For simplicity, in this section, we suppress the spin index σ and assume that the lattice index j contains all local quantum numbers. The many-body Hamiltonian is originally expressed in terms of fermionic operators $c_j^{(\uparrow)}$, but it may be equivalently rewritten using the Majorana fermions (not to be confused with the MZM):

$$\gamma_{2j-1} = c_j + c_j^\dagger, \quad \gamma_{2j} = -i(c_j - c_j^\dagger), \quad (9)$$

where $\gamma_j^\dagger = \gamma_j$ and $\{\gamma_i, \gamma_j\} = 2\delta_{ij}$. The latter anticommutation relation is invariant under orthogonal transformations, thus we can rotate the Majorana fermions arbitrarily with

$$\Gamma_a = \sum_j \hat{V}_{aj} \gamma_j, \quad (10)$$

where \hat{V} are real, orthogonal matrices $\hat{V}^\top \hat{V} = \hat{V} \hat{V}^\top = 1$. If the system hosts a pair of Majorana edge modes, Γ_L and Γ_R , then we can find a transformation \hat{V} such that the following Hamiltonian captures the low-energy physics

$$H \simeq i \frac{\epsilon}{2} \Gamma_L \Gamma_R + H'. \quad (11)$$

It is important to note that H' does not contribute to the in-gap states. It contains all Majorana operators, Γ_a , other than the MZM (Γ_L and Γ_R). The first term in Eq. (11) arises from the overlap of the MZM in a finite system, while in the thermodynamic limit $\epsilon \rightarrow 0$ both Γ_L and Γ_R become strictly the zero modes. While the ground state properties obtained from the zero temperature DMRG do not allow us to formally construct the transformation \hat{V} , we demonstrate below that the computed local and non-local spectral functions are fully consistent with the MZM. In fact, we are not aware of any other scenario that could explain the spectral functions reported in this work.

Let us investigate the retarded Green's functions

$$\begin{aligned} G^h(c_j, c_i^\dagger) &= -i \int_0^\infty dt e^{i\omega t} \langle \text{gs} | c_j(t) c_i^\dagger | \text{gs} \rangle, \\ G^c(c_j, c_i^\dagger) &= -i \int_0^\infty dt e^{i\omega t} \langle \text{gs} | c_j^\dagger c_i(t) | \text{gs} \rangle, \end{aligned} \quad (12)$$

which are related to the already introduced spectral functions

$$\begin{aligned} \langle (c_j c_i^\dagger) \rangle_\omega^h &= -\frac{1}{\pi} \text{Im} G^h(c_j, c_i^\dagger), \\ \langle (c_j^\dagger c_i) \rangle_\omega^c &= -\frac{1}{\pi} \text{Im} G^c(c_j, c_i^\dagger). \end{aligned} \quad (13)$$

Using the transformations (9) and (10) one may express $G^{c,h}(c_j, c_i^\dagger)$ as a linear combination of the Green's functions defined in terms of the Majorana fermions $G^{c,h}(\Gamma_a, \Gamma_b)$. However, the only contributions to the in-gap spectral functions come from the zero-modes, i.e., from $a, b \in \{L, R\}$, and the corresponding functions can be obtained directly from the effective Hamiltonian (11),

$$\begin{aligned} G^h(\Gamma_L, \Gamma_L) &= G^h(\Gamma_R, \Gamma_R) = \frac{1}{\omega - |\epsilon| + i\eta}, \\ G^c(\Gamma_L, \Gamma_L) &= G^c(\Gamma_R, \Gamma_R) = \frac{1}{\omega + |\epsilon| + i\eta}. \end{aligned} \quad (14)$$

The Green's functions determine the in-gap peak in the left part of the system

$$G^\alpha(c_j, c_i^\dagger) = \frac{V_{L,2j}^2 + V_{L,2j-1}^2}{4} G^\alpha(\Gamma_L, \Gamma_L), \quad (15)$$

with $\alpha \in \{e, h\}$, and a similar expression holds for the peak on its right side. Utilizing the orthogonality of \hat{V} , one may explicitly sum up the Green's functions over the lattice sites

$$\sum_j G^\alpha(c_j, c_i^\dagger) = \frac{1}{4} G^\alpha(\Gamma_L, \Gamma_L), \quad (16)$$

where the sum over j contains few sites at the edge of the system due to the exponential decay of the \hat{V} elements. The result Eq. (16) explains why the total spectral weights originating from $\sum_j G^\alpha$ equal 1/4, while the total spectral weights of the peaks in LDOS equal 1/2. A similar discussion of the nonlocal centrosymmetric spectral functions $\langle (c_\ell c_{L-\ell+1}^\dagger) \rangle_{\epsilon_\ell}^h$ and $\langle (c_\ell^\dagger c_{L-\ell+1}) \rangle_{\epsilon_\ell}^c$ can be found in Supplementary Note 3.

Von Neumann entanglement entropy. $S_{\text{vN}}(\ell)$ measures entanglement between two subsystems containing, respectively, ℓ and $L-\ell$ sites, and can be easily calculated within DMRG via the reduced density matrix ρ_b , i.e., $S_{\text{vN}}(\ell) = -\text{Tr} \rho_b \ln \rho_b$. The results presented in Fig. 6 depict the system divided into two equal halves, $\ell = L/2$. The full spatial dependence of $S_{\text{vN}}(\ell)$ is presented in Supplementary Note 5.

SC amplitudes. The s -wave and p -wave SC can be detected with singlet Δ_S and triplet Δ_T amplitudes, respectively, defined as

$$\begin{aligned} \Delta_S &= \sum_{\ell=L/4}^{3L/4} |\Delta_{S,\ell}|, \\ \Delta_T &= \sum_{\ell=L/4}^{3L/4} (|\Delta_{T0,\ell}| + |\Delta_{T1,\ell}| + |\Delta_{T2,\ell}|), \end{aligned} \quad (17)$$

with

$$\begin{aligned} \Delta_{S,\ell} &= \langle c_{\ell,\uparrow}^\dagger c_{\ell+1,\downarrow}^\dagger - c_{\ell,\downarrow}^\dagger c_{\ell+1,\uparrow}^\dagger \rangle, \\ \Delta_{T0,\ell} &= \langle c_{\ell,\uparrow}^\dagger c_{\ell+1,\downarrow}^\dagger + c_{\ell,\downarrow}^\dagger c_{\ell+1,\uparrow}^\dagger \rangle, \\ \Delta_{T1,\ell} &= \langle c_{\ell,\uparrow}^\dagger c_{\ell+1,\uparrow}^\dagger \rangle, \quad \Delta_{T2,\ell} = \langle c_{\ell,\downarrow}^\dagger c_{\ell+1,\downarrow}^\dagger \rangle. \end{aligned} \quad (18)$$

Data availability

The data that support the findings of this study are available from the corresponding author upon request.

Received: 27 October 2020; Accepted: 21 April 2021;

Published online: 19 May 2021

References

- Elliott, S. R. & Franz, M. Colloquium: Majorana fermions in nuclear, particle, and solid-state physics. *Rev. Mod. Phys.* **87**, 137 (2015).
- Nadj-Perge, S., Drozdov, I. K., Bernevig, B. A. & Yazdani, A. Proposal for realizing Majorana fermions in chains of magnetic atoms on a superconductor. *Phys. Rev. B* **88**, 020407(R) (2013).
- Braunecker, B., Japaridze, G. I., Klinovaja, J. & Loss, D. Spin-selective Peierls transition in interacting one-dimensional conductors with spin-orbit interaction. *Phys. Rev. B* **82**, 045127 (2010).
- Braunecker, B. & Simon, P. Interplay between classical magnetic moments and superconductivity in quantum one-dimensional conductors: toward a self-sustained topological Majorana phase. *Phys. Rev. Lett.* **111**, 147202 (2013).
- Klinovaja, J., Stano, P., Yazdani, A. & Loss, D. Topological superconductivity and Majorana Fermions in RKKY systems. *Phys. Rev. Lett.* **111**, 186805 (2013).
- Vazifeh, M. M. & Franz, M. Self-organized topological state with Majorana fermions. *Phys. Rev. Lett.* **111**, 206802 (2013).
- Nadj-Perge, S. et al. Observation of Majorana fermions in ferromagnetic atomic chains on a superconductor. *Science* **346**, 602 (2014).
- Pawlak, R., Hoffman, S., Klinovaja, J., Loss, D. & Meyer, E. Majorana fermions in magnetic chains. *Prog. Part. Nucl. Phys.* **107**, 1 (2014).
- Steinbrecher, M. et al. Non-collinear spin states in bottom-up fabricated atomic chains. *Nat. Commun.* **9**, 2853 (2018).
- Jack, B. et al. Observation of a Majorana zero mode in a topologically protected edge channel. *Science* **364**, 1255 (2019).
- Kim, H. et al. Toward tailoring Majorana bound states in artificially constructed magnetic atom chains on elemental superconductors. *Sci. Adv.* **11**, aar5251 (2018).
- Palacio-Morales, A. et al. Atomic-scale interface engineering of Majorana edge modes in a 2D magnet-superconductor hybrid system. *Sci. Adv.* **5**, eaav6600 (2019).
- Wang, D. et al. Evidence for Majorana bound states in an iron-based superconductor. *Science* **362**, 333 (2018).
- Zhang, P. et al. Observation of topological superconductivity on the surface of an iron-based superconductor. *Science* **360**, 182 (2018).
- Machida, T. et al. Zero-energy vortex bound state in the superconducting topological surface state of Fe(Se,Te). *Nat. Mater.* **18**, 811 (2019).
- Wang, Z. et al. Evidence for dispersing 1D Majorana channels in an iron-based superconductor. *Science* **367**, 104 (2020).
- Chen, C. et al. Atomic line defects and zero-energy end states in monolayer Fe(Te,Se) high-temperature superconductors. *Nat. Phys.* **16**, 536 (2020).
- Thomale, R., Rachel, S. & Schmitteckert, P. Tunneling spectra simulation of interacting Majorana wires. *Phys. Rev. B* **88**, 161103(R) (2013).
- Rahmani, A., Zhu, X., Franz, M. & Affleck, I. Phase diagram of the interacting Majorana Chain Model. *Phys. Rev. B* **92**, 235123 (2015).
- Daghofer, M., Nicholson, A., Moreo, A. & Dagotto, E. Three orbital model for the iron-based superconductors. *Phys. Rev. B* **81**, 014511 (2010).
- Rincón, J., Moreo, A., Alvarez, G. & Dagotto, E. Exotic magnetic order in the orbital-selective Mott regime of multiorbital systems. *Phys. Rev. Lett.* **112**, 106405 (2014).
- Patel, N. D. et al. Magnetic properties and pairing tendencies of the iron-based superconducting ladder BaFe₂S₅: combined ab initio and density matrix renormalization group study. *Phys. Rev. B* **94**, 075119 (2016).
- Herbrych, J. et al. Spin dynamics of the block orbital-selective Mott phase. *Nat. Commun.* **9**, 3736 (2018).
- Mourigal, M. et al. Block magnetic excitations in the orbital selective Mott insulator BaFe₂Se₃. *Phys. Rev. Lett.* **115**, 047401 (2015).
- Herbrych, J., Alvarez, G., Moreo, A. & Dagotto, E. Block orbital-selective Mott insulators: a spin excitation analysis. *Phys. Rev. B* **102**, 115134 (2020).
- Herbrych, J. et al. Novel magnetic block states in low-dimensional iron-based superconductors. *Phys. Rev. Lett.* **123**, 027203 (2019).
- Herbrych, J. et al. Block-spiral magnetism: an exotic type of frustrated order. *Proc. Natl Acad. Sci. USA* **117**, 16226 (2020).
- Kitaev, A. Y. Unpaired Majorana fermions in quantum wires. *Phys. -Usp.* **44**, 131 (2001).
- van Wees, B. J. & Takayanagi, H. The superconducting proximity effect in semiconductor-superconductor systems: ballistic transport, low dimensionality and sample specific properties. In *Mesoscopic Electron Transport. NATO ASI Series (Series E: Applied Sciences)*, Vol. 345 (eds Sohn, L. H., Kouwenhoven, L. P. & Schön, G.) (Springer, 1997).
- Hevlyack, J. et al. Massive suppression of proximity pairing in topological (Bi_{1-x}Sb_x)₂Te₃ films on niobium. *Phys. Rev. Lett.* **124**, 236402 (2020).
- Takahashi, H. et al. Pressure-induced superconductivity in the iron-based ladder material BaFe₂S₅. *Nat. Mater.* **14**, 1008 (2015).
- Yamauchi, T., Hirata, Y., Ueda, Y. & Ohgushi, K. Pressure-induced Mott transition followed by a 24-K superconducting phase in BaFe₂S₅. *Phys. Rev. Lett.* **115**, 246402 (2015).
- Ying, J., Lei, H., Petrovic, C., Xiao, Y. & Struzhkin, V. V. Interplay of magnetism and superconductivity in the compressed Fe-ladder compound BaFe₂Se₃. *Phys. Rev. B* **95**, 241109(R) (2017).
- Patel, N. D., Nocera, A., Alvarez, G., Moreo, A. & Dagotto, E. Pairing tendencies in a two-orbital Hubbard model in one dimension. *Phys. Rev. B* **96**, 024520 (2017).

35. Murase, M. et al. Successive magnetic transitions and spin structure in the two-leg ladder compound CsFe_2Se_3 observed by ^{133}Cs and ^{77}Se NMR. *Phys. Rev. B* **102**, 014433 (2020).
36. Stanescu, T. D., Lutchyn, R. M. & DasSarma, S. Dimensional crossover in spin-orbit-coupled semiconductor nanowires with induced superconducting pairing. *Phys. Rev. B* **87**, 094518 (2013).
37. Pandey, B. et al. Prediction of exotic magnetic states in the alkali-metal quasi-one-dimensional iron selenide compound Na_2FeSe_2 . *Phys. Rev. B* **102**, 035149 (2020).
38. Caron, J. M. et al. Orbital-selective magnetism in the spin-ladder iron selenides $\text{Ba}_{1-x}\text{K}_x\text{Fe}_2\text{Se}_3$. *Phys. Rev. B* **85**, 180405 (2012).
39. Ootsuki, D. et al. Coexistence of localized and itinerant electrons in BaFe_2X_3 ($\text{X}=\text{S}$ and Se) revealed by photoemission spectroscopy. *Phys. Rev. B* **91**, 014505 (2015).
40. Craco, L. & Leoni, S. Pressure-induced orbital-selective metal from the Mott insulator BaFe_2Se_3 . *Phys. Rev. B* **101**, 245133 (2020).
41. Yu, R., Zhu, J.-X. & Si, Q. Orbital selectivity enhanced by nematic order in FeSe . *Phys. Rev. Lett.* **121**, 227003 (2018).
42. Kostin, A. et al. Imaging orbital-selective quasiparticles in the Hundas metal state of FeSe . *Nat. Mater.* **17**, 869 (2018).
43. Jiang, Q. et al. Nematic fluctuations in an orbital selective superconductor $\text{Fe}_{1-x}\text{Te}_{1-x}\text{Se}_x$. Preprint at *arXiv* <https://arxiv.org/abs/2006.15887> (2020).
44. Glasbrenner, J. K. et al. Effect of magnetic frustration on nematicity and superconductivity in iron chalcogenides. *Nat. Phys.* **11**, 953 (2014).
45. Nakosai, S., Tanaka, Y. & Nagaosa, N. Two-dimensional p -wave superconducting states with magnetic moments on a conventional s -wave superconductor. *Phys. Rev. B* **88**, 180503(R) (2013).
46. Steffensen, D., Andersen, B. M. & Kotetes, P. Majorana zero modes in magnetic texture vortices. Preprint at *arXiv* <https://arxiv.org/abs/2008.10626> (2020).
47. Jiao, L. et al. Chiral superconductivity in heavy-fermion metal UTe_2 . *Nature* **579**, 523 (2020).
48. Duan, C. et al. Incommensurate spin fluctuations in the spin-triplet superconductor candidate UTe_2 . *Phys. Rev. Lett.* **125**, 237003 (2020).
49. White, S. R. Density matrix formulation for quantum renormalization groups. *Phys. Rev. Lett.* **69**, 2863 (1992).
50. Schollwöck, U. The density-matrix renormalization group. *Rev. Mod. Phys.* **77**, 259 (2005).
51. White, S. R. Density matrix renormalization group algorithms with a single center site. *Phys. Rev. B* **72**, 180403 (2005).
52. Jeckelmann, E. Dynamical density-matrix renormalization-group method. *Phys. Rev. B* **66**, 045114 (2002).
53. Nocera, A. & Alvarez, G. Spectral functions with the density matrix renormalization group: Krylov-space approach for correction vectors. *Phys. Rev. E* **94**, 053308 (2016).

Acknowledgements

J. Herbrich and M. Środa acknowledge support by the Polish National Agency for Academic Exchange (NAWA) under contract PPN/PPO/2018/1/00035, and together with M. Mierzejewski, by the National Science Centre (NCN), Poland via project 2019/

35/B/ST3/01207. The work of G. Alvarez was supported by the Scientific Discovery through Advanced Computing (SciDAC) program funded by the US DOE, Office of Science, Advanced Scientific Computer Research and Basic Energy Sciences, Division of Materials Science and Engineering. The development of the DMRG++ code by G. Alvarez was conducted at the Center for Nanophase Materials Science, sponsored by the Scientific User Facilities Division, BES, DOE, under contract with UT-Battelle. E. Dagotto was supported by the US Department of Energy (DOE), Office of Science, Basic Energy Sciences (BES), Materials Sciences and Engineering Division. A part of the calculations was carried out using resources provided by the Wrocław Centre for Networking and Supercomputing.

Author contributions

J.H., M.M., and E.D. planned the project. G.A. developed the DMRG++ computer program. J.H. and M.Ś. performed the numerical simulations. J.H., M.Ś., M.M., and E.D. wrote the manuscript. All co-authors provided comments on the paper.

Competing interests

The authors declare no competing interests.

Additional information

Supplementary information The online version contains supplementary material available at <https://doi.org/10.1038/s41467-021-23261-2>.

Correspondence and requests for materials should be addressed to J.H.

Peer review information *Nature Communications* thanks the anonymous reviewer(s) for their contribution to the peer review of this work.

Reprints and permission information is available at <http://www.nature.com/reprints>

Publisher's note Springer Nature remains neutral with regard to jurisdictional claims in published maps and institutional affiliations.



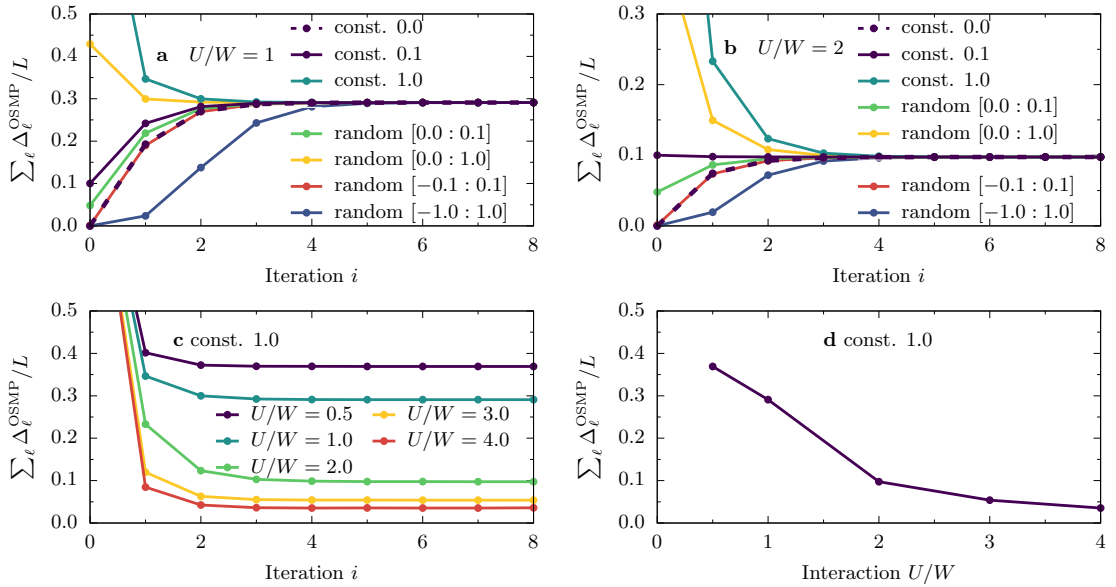
Open Access This article is licensed under a Creative Commons Attribution 4.0 International License, which permits use, sharing, adaptation, distribution and reproduction in any medium or format, as long as you give appropriate credit to the original author(s) and the source, provide a link to the Creative Commons license, and indicate if changes were made. The images or other third party material in this article are included in the article's Creative Commons license, unless indicated otherwise in a credit line to the material. If material is not included in the article's Creative Commons license and your intended use is not permitted by statutory regulation or exceeds the permitted use, you will need to obtain permission directly from the copyright holder. To view a copy of this license, visit <http://creativecommons.org/licenses/by/4.0/>.

© The Author(s) 2021

Supplementary Note 1. Stability of the hybrid BdG-DMRG algorithm

In the main text, we have presented how the spatial profiles of the pairing fields (PF) in the BCS system Δ_i^{BCS} converge in subsequent steps of the iteration procedure. Here, as supplementary information, we will discuss the convergence of PF $\Delta_\ell^{\text{OSMP}}$ obtained for the 1D OSMP system. Furthermore, we will test the stability of the introduced procedure and demonstrate that the obtained results are independent of the initial choice of the PF.

From the results presented in the main text, it is evident that the PF converge to almost uniform (spatially independent) values within the 1D OSMP system. Consequently, to simplify the presentation of the results, we will discuss only the behaviour of the average PF, $\sum_\ell \Delta_\ell^{\text{OSMP}}/L$. In Supplementary Figure 1 we present the iteration dependence of the latter for various initial starting points. As explained in the Methods section of the main text, our DMRG-BdG algorithm can be started from arbitrary amplitudes in the 1D OSMP system. We have considered: (1) zero PF (the result discussed in the main text), (2) constant PF $\Delta_\ell^{\text{OSMP}} = 0.1$ and $\Delta_\ell^{\text{OSMP}} = 1.0$, and (3) random PF drawn from a box distribution of widths $[0.0, 0.1]$, $[0.0, 1.0]$, $[-0.1, 0.1]$, and $[-1.0, 0.1]$. Several conclusions can be obtained directly from the results for $U/W = 1$ (trivial phase, Supplementary Figure 1a) and $U/W = 2$ (topological phase, Supplementary Figure 1b): (i) For all considered cases, the converged spatial profiles are almost uniform within the OSMP chain. This is best exemplified by the results presented in the right column of Fig. 2b of the main text, where we show the convergence of the hybrid procedure for the case when iterations are initialized by random PF, i.e., $\Delta_\ell^{\text{OSMP}} \in [0, 1]$. (ii) For all considered initial PF, the results converge to the same - interaction dependent - value. This nontrivial result shows that the hybrid BdG-DMRG procedure is numerically very stable. (iii) The quick convergence of the hybrid procedure holds true for the entire range of the Coulomb repulsion considered in the present studies: see results for $\sum_\ell \Delta_\ell^{\text{OSMP}}/L$ shown in Supplementary Figure 1c and Supplementary Figure 1d.



Supplementary Figure 1. **Pairing fields within the 1D OSMP system.** **a,b** Iteration convergence of the average pairing field amplitudes $\sum_\ell \Delta_\ell^{\text{OSMP}}/L$ as obtained for **a** $U/W = 1$ and **b** $U/W = 2$, starting from various initial configuration of $\Delta_\ell^{\text{OSMP}}$. Calculated for $L = 36$, $\bar{n} = 0.5$, and $V = 4$ [eV]. All units in eV. See the Methods section of the main text for details. **c** depicts the interaction U dependence of the convergence for the case of an initial $\Delta_\ell^{\text{OSMP}} = 1$ [eV]. The asymptotic value of $\sum_\ell \Delta_\ell^{\text{OSMP}}/L$ as function of U is given in **d**.

Supplementary Note 2. Ladder geometry considerations

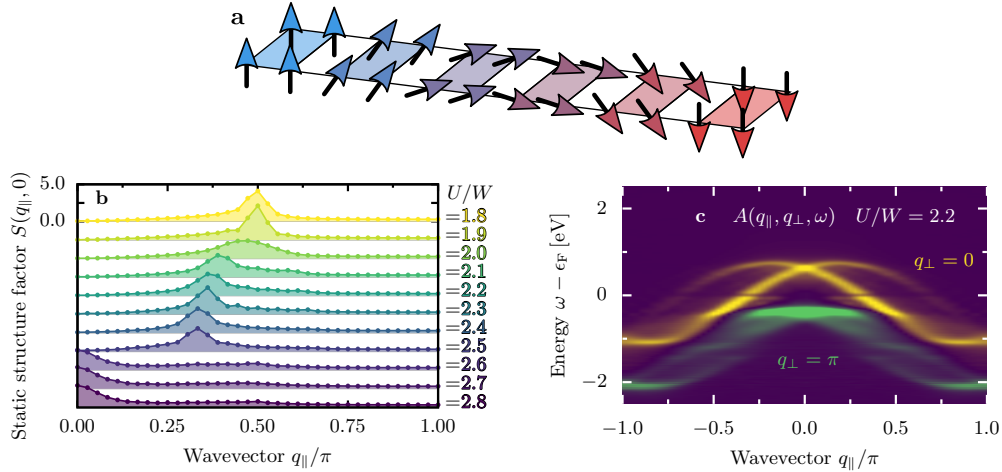
In the main text, we have shown that the generalized Kondo-Heisenberg (gKH) model on the chain geometry can support Majorana zero-energy modes (MZM) when in the presence of a superconducting (SC) pairing field Δ_{SC} . Here, we will show that the key ingredients necessary to support the MZM in the gKH model are also present in the ladder geometry, i.e. the block-spiral magnetic state (see Supplementary Figure 2a for a sketch) and single-particle spectra with parity-breaking quasi-particles. We will consider a spatially isotropic ladder with $t_{\parallel} = t_{\perp} \equiv t$, the latter hopping defined in the main text, and choose filling $\bar{n} = 1.75$, which supports block-magnetism at $U \sim W$ [1, 2]. Although accurate calculations within the grand-canonical ensemble (needed with finite pairing field $\Delta_{\text{SC}} \neq 0$) are numerically too demanding (due to the doubling of the lattice sites on the ladder of L rungs), precise canonical calculations of the static structure factor can still be performed, i.e.,

$$S(q_{\parallel}, q_{\perp}) = \sum_{\ell, \ell'} \sum_{r, r'} e^{+iq_{\perp}(r-r')} e^{+iq_{\parallel}(\ell-\ell')} \langle \mathbf{T}_{\ell, r} \cdot \mathbf{T}_{\ell', r'} \rangle, \quad (1)$$

where $\mathbf{T}_{\ell, r} = \mathbf{S}_{\ell, r} + \mathbf{s}_{\ell, r}$, and (ℓ, r) represent the leg and rung number, respectively. Our results in Supplementary Figure 2b reveal that the $S(q_{\parallel}, q_{\perp})$ lies at incommensurate values of the wavevectors, the one of the block-spiral magnetic state signatures [3]. Another feature of the latter is the existence of two cosine-like bands in the single-particle spectral (see also the discussion in the next section) $A(q_{\parallel}, q_{\perp}, \omega) = A^e(q_{\parallel}, q_{\perp}, \omega) + A^h(q_{\parallel}, q_{\perp}, \omega)$ near the Fermi level $\omega \sim \epsilon_{\text{F}}$, where

$$\begin{aligned} A^e(q_{\parallel}, q_{\perp}, \omega) &= \sum_{\ell} \sum_{r, r'} e^{+iq_{\perp}(r-r')} e^{-iq_{\parallel}(\ell-L/2)} \langle \langle c_{\ell, r} c_{L/2, r'}^{\dagger} \rangle \rangle_{\omega}^e, \\ A^h(q_{\parallel}, q_{\perp}, \omega) &= \sum_{\ell} \sum_{r, r'} e^{+iq_{\perp}(r-r')} e^{+iq_{\parallel}(\ell-L/2)} \langle \langle c_{\ell, r}^{\dagger} c_{L/2, r'} \rangle \rangle_{\omega}^h. \end{aligned} \quad (2)$$

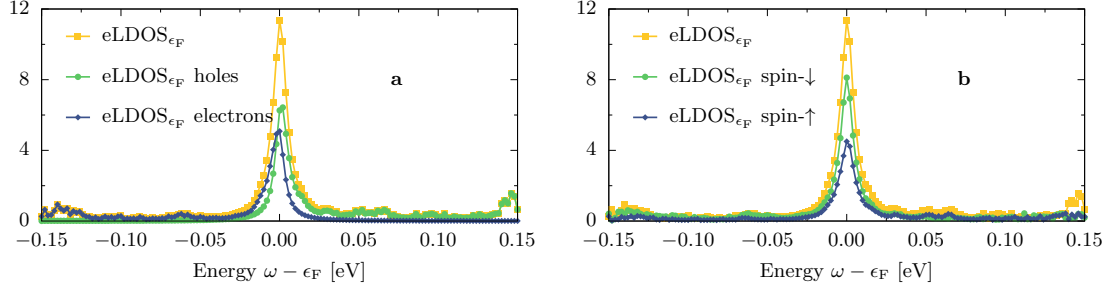
The results presented in Supplementary Figure 2c (for $L = 36$ rungs, $U/W = 2.2$, $J_{\text{H}}/U = 0.25$, and $\bar{n} = 1.75$) are consistent with this scenario and resemble the chain geometry results. Consequently, it is reasonable to assume that the influence of a finite pairing field $\Delta_{\text{SC}} \neq 0$ will lead to a topological superconducting state and the emergence of the MZM also on the ladder lattice.



Supplementary Figure 2. **Block-spiral state on the ladder geometry.** **a** Sketch of the block-spiral state on the ladder geometry. Color (shaded) area represents rigidly rotating 2×2 FM blocks. **b** Interaction dependence of the symmetric component $q_{\perp} = 0$ of the static structure factor $S(q_{\parallel}, q_{\perp} = 0)$. **c** Wavevector dependence of both components (symmetric and antisymmetric) of the single-particle spectral function $A(q_{\parallel}, q_{\perp} = 0, \omega) + A(q_{\parallel}, q_{\perp} = \pi, \omega)$ near the Fermi level in the block-spiral phase ($\eta = 2\delta\omega$ and $\delta\omega = 0.02$ [eV]). All results calculated for the gKH ladder of $L = 36$ rungs, $J_{\text{H}}/U = 0.25$, $\bar{n} = 1.75$, and $\Delta_{\text{SC}} = 0$.

Supplementary Note 3. Spectral functions

In Fig. 4 of the main text, we have shown the spatial dependence of the local density-of-states (LDOS) at the Fermi level, together with equal contributions of the electron and hole components, as expected for MZM. Here, in Supplementary Figure 3, we show that the same holds in frequency ω space. Furthermore, in the same figure we show that both spin components contribute equally (within our numerical precision).



Supplementary Figure 3. **Components of the Majorana edge states.** Frequency ω dependence of the edge-LDOS ($\ell = 1$) near the Fermi level $\omega \sim \epsilon_F$. Panel **a** depicts electron and hole contributions, while panel **b** the \downarrow - and \uparrow -spin component. Calculated for $L = 36$, $U/W = 2$, $\Delta_{SC}/W \simeq 0.5$, and $\bar{n} = 0.5$.

The same reasoning used for the LDOS in the main text can also be applied to the off-diagonal functions $G^\alpha(c_j, c_l^\dagger)$ where sites j and l belong to the left $j < L/2$ and the right $l > L/2$ portions of the system. Then, it can be shown that

$$G^\alpha(c_j, c_l^\dagger) = \frac{V_{L,2j-1}V_{R,2l-1} + V_{L,2j}V_{R,2l}}{4} G^\alpha(\Gamma_L, \Gamma_R), \\ + i \frac{V_{L,2j}V_{R,2l-1} - V_{L,2j-1}V_{R,2l}}{4} G^\alpha(\Gamma_L, \Gamma_R), \quad (3)$$

with

$$G^h(\Gamma_L, \Gamma_R) = -G^h(\Gamma_R, \Gamma_L) = \frac{i \operatorname{sgn}(\varepsilon)}{\omega - |\varepsilon| + i\eta}, \\ G^e(\Gamma_L, \Gamma_R) = -G^e(\Gamma_R, \Gamma_L) = \frac{-i \operatorname{sgn}(\varepsilon)}{\omega + |\varepsilon| + i\eta}. \quad (4)$$

Since the considered Hamiltonian is real, the spectral functions $\langle\langle c_j c_l^\dagger \rangle\rangle_\omega^h$ and $\langle\langle c_l^\dagger c_j \rangle\rangle_\omega^e$ should be real as well. Given that the weights of $\langle\langle \Gamma_L \Gamma_R \rangle\rangle_\omega^\alpha$ are purely imaginary [see Supplementary Eq. (4)], the upper line in Supplementary Eq. (3) should vanish. Indeed, for real Hamiltonians, Γ_L (and also Γ_R) contains γ_j with only even or odd j . In other words, Γ_L contains only γ_{2j} and Γ_R contains only γ_{2j-1} or *vice versa*. Without losing generality, we may choose the former possibility,

$$G^\alpha(c_j, c_l^\dagger) = i \frac{V_{L,2j}V_{R,2l-1}}{4} G^\alpha(\Gamma_L, \Gamma_R) \\ G^\alpha(c_l, c_j^\dagger) = -i \frac{V_{R,2l-1}V_{L,2j}}{4} G^\alpha(\Gamma_R, \Gamma_L) = G^\alpha(c_j, c_l^\dagger), \quad (5)$$

and obtain the spectral functions shown in Supplementary Figure 4 and Fig. 4b of the main text

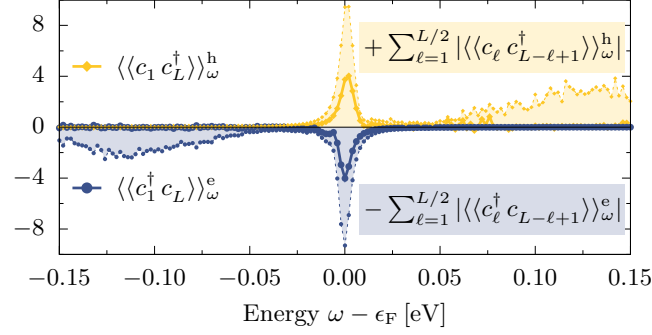
$$\langle\langle c_l c_{L-l+1}^\dagger \rangle\rangle_\omega^h = -\frac{1}{4} \left\{ \begin{array}{l} V_{L,2l}V_{R,2L-2l+1} \text{ for } l < L/2 \\ V_{L,2L-2l+2}V_{R,2l-1} \text{ for } l > L/2 \end{array} \right\} \operatorname{sgn}(\varepsilon) \delta(\omega - |\varepsilon|), \\ \langle\langle c_l^\dagger c_{L-l+1} \rangle\rangle_\omega^e = +\frac{1}{4} \left\{ \begin{array}{l} V_{L,2l}V_{R,2L-2l+1} \text{ for } l < L/2 \\ V_{L,2L-2l+2}V_{R,2l-1} \text{ for } l > L/2 \end{array} \right\} \operatorname{sgn}(\varepsilon) \delta(\omega + |\varepsilon|), \quad (6)$$

where the electron and hole contributions arise with opposite signs, as it is also visible in Supplementary Figure 4 and Fig. 4b of the main text. Finally, it is reasonable to assume that the spatial profiles of the MZMs at both

system edges are mutually symmetric, i.e., $|V_{R,2L-2l+1}| \simeq |V_{L,2l}|$. Then, comparing Eq. 15 of the main text and Supplementary Eq. (6) we obtain a mirroring of the diagonal (local) and off-diagonal spectral functions

$$\begin{aligned} |\langle\langle c_l c_{L-l+1}^\dagger \rangle\rangle_\omega^h| &\simeq |\langle\langle c_l c_l^\dagger \rangle\rangle_\omega^h|, \\ |\langle\langle c_{L-l+1}^\dagger c_l \rangle\rangle_\omega^e| &\simeq |\langle\langle c_l^\dagger c_l \rangle\rangle_\omega^e|, \end{aligned} \quad (7)$$

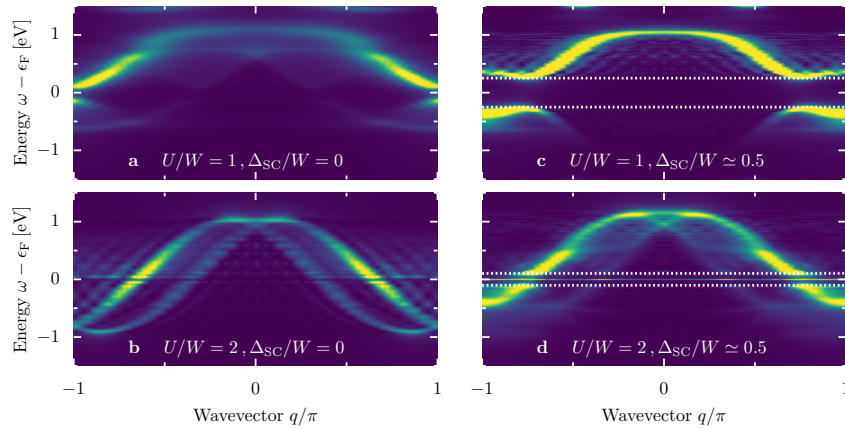
which is reasonably well reproduced by the numerical results.



Supplementary Figure 4. **Off-diagonal spectral functions.** Frequency dependence of centrosymmetric spectral functions, Supplementary Eq. (6), at the edge of the system $\ell = 1$ (solid points). We also present spatially integrated, according to Eq. 16 of the main text, spectral functions as colored area. Results shown were calculated for $L = 36$, $U/W = 2$, $\Delta_{SC}/W \simeq 0.5$, and $\bar{n} = 0.5$.

Supplementary Note 4. Parameter dependence

In this section, we will discuss the pairing field Δ_{SC} dependence of our results. Let us first focus on the single-particle spectral function $A(q, \omega)$ [see Eq. 7 of the main text]. In Supplementary Figure 5a and Supplementary Figure 5b we show $A(q, \omega)$ for systems (at electronic filling $\bar{n} = 0.5$) without pairing field $\Delta_{\text{SC}} = 0$ for two representative values of the interaction: $U/W = 1$ and $U/W = 2$, i.e., in the block-collinear and block-spiral magnetic phases. Both spectra exhibit a finite density-of-states (DOS) at the Fermi level ϵ_{F} . In the case of the block-spiral phase at $U/W = 2$, Supplementary Figure 5b, one can observe two bands of quasiparticles: left and right movers reflecting the two possible rotations of the spirals. It is obvious from these results that the quasiparticles break the parity symmetry; i.e., going from $q \rightarrow -q$ momentum changes the quasiparticle character, as expected for a spiral state. It is also worth noting that for the block-magnetic order ($U/W = 1$ and $\Delta_{\text{SC}} = 0$) one can observe [3] the V-like shape of DOS in the vicinity of ϵ_{F} . The latter indicates a semiconductor-like behaviour which was also experimentally found [4] in the 2×2 block-magnetic ladder compound BaFe_2Se_3 . This result shows our model's strength and relevance for realistic investigations of the iron-based materials from the 123 family.



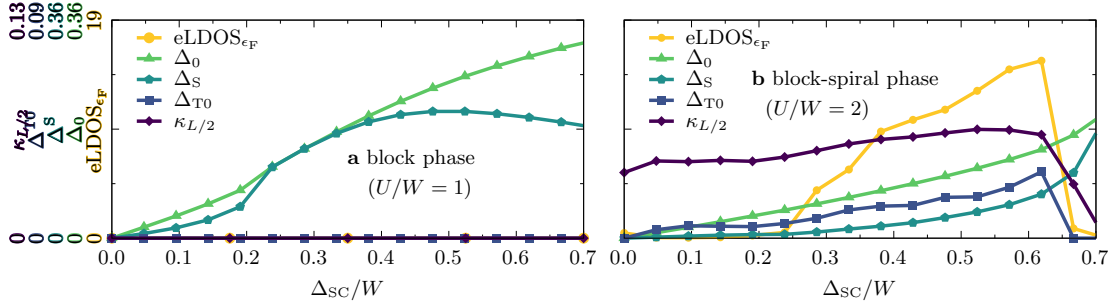
Supplementary Figure 5. **Single-particle spectra for block-collinear and block-spiral magnetism.** Single-particle spectra $A(q, \omega)$ of the gKH model using $L = 36$ sites and electronic filling $\bar{n} = 0.5$ for **a** $U/W = 1, \Delta_{\text{SC}} = 0$, **b** $U/W = 2, \Delta_{\text{SC}} = 0$, **c**, $U/W = 1, \Delta_{\text{SC}}/W \simeq 0.5$, and **d** $U/W = 2, \Delta_{\text{SC}}/W \simeq 0.5$.

The pairing field $\Delta_{\text{SC}} \neq 0$ has a striking effect on these two phases, see Supplementary Figure 5c and Supplementary Figure 5d where we present results for $\Delta_{\text{SC}}/W \simeq 0.5$. As discussed in detail in the main text, the pairing field leads to the appearance of MZM in the spiral phase ($U/W = 2$, Supplementary Figure 5d), with the flat δ -mode inside the superconducting gap. On the other hand, for the collinear block-magnetic phase ($U/W = 1$, Supplementary Figure 5c) we observe only a trivial opening of the SC gap, without any in-gap states. These results indicate that the Hubbard interaction strength U , as the main driver between the two magnetic states, plays a crucial role in the stabilization of the MZM.

In order to investigate all these aspects in more detail, in Supplementary Figure 6 we present the pairing field Δ_{SC} dependence of the quantities discussed in the main text, i.e.: (i) value of edge-LDOS at the Fermi level ϵ_{F} (eLDOS), (ii) chirality correlation function $\langle \kappa_{L/4} \cdot \kappa_{3L/4} \rangle$ at $L/2$ distance ($\kappa_{L/2}$), and (iii) amplitudes of extended (non-local) SC singlet and triplet amplitudes, Δ_{S} and Δ_{T0} , respectively [see Eq. 17 of the main text]. Furthermore, in the same figure we present the value of the on-site pairing amplitude

$$\Delta_0 = \frac{2}{L} \sum_{\ell=L/4}^{3L/4} |c_{\ell,\uparrow}^\dagger c_{\ell,\downarrow}^\dagger|. \quad (8)$$

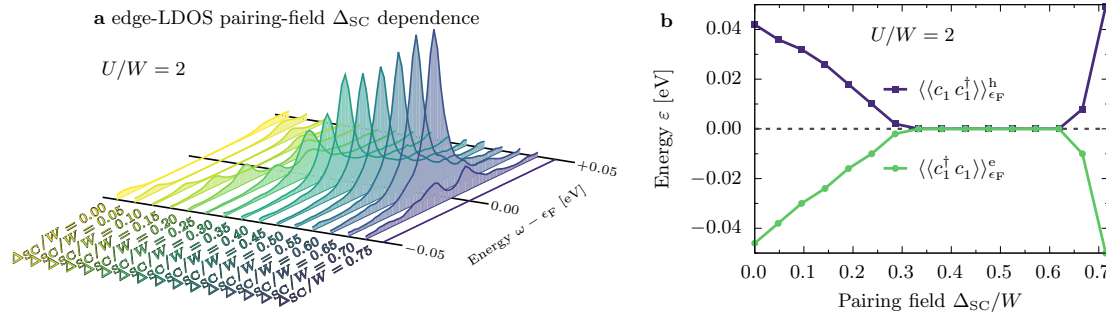
For the collinear block-magnetic phase ($U/W = 1$, Supplementary Figure 6a) we observe that the Δ_{SC} does not induce any topological phase transitions. For all considered values of the pairing field, $0 < \Delta_{\text{SC}}/W \lesssim 0.7$, the eLDOS,



Supplementary Figure 6. **Phase diagram.** Pairing field Δ_{SC} dependence of: (i) the value of edge-LDOS at the Fermi level ϵ_{F} (eLDOS), (ii) chirality correlation function $\langle \kappa_{L/4} \cdot \kappa_{3L/4} \rangle$ at $L/2$ distance ($\kappa_{L/2}$), (iii) amplitudes of local and non-local SC singlet amplitudes, Δ_0 and Δ_S , respectively, together with triplet component Δ_{T0} . Panel **a** shows results for the block-collinear magnetic phase ($U/W = 1$), while panel **b** for the block-spiral phase ($U/W = 2$). All results were calculated for $L = 36$ and $\bar{n} = 0.5$.

$\kappa_{L/2}$, and Δ_{T} are zero. Only the singlet SC amplitudes, local Δ_0 and non-local Δ_S , take a finite value. The behaviour of the $U/W = 2$ case is strikingly different (see Supplementary Figure 6b). The chirality correlation function $\kappa_{L/2}$ has a finite value already at $\Delta_{\text{SC}} = 0$, reflecting the block-spiral ordering at this interaction strength, and weakly changes till $\Delta_{\text{SC}}/W \sim 0.6$, after which it decays to zero. Simultaneously, the triplet SC amplitude Δ_{T0} increases smoothly with the pairing-field Δ_{SC} (together with singlet components Δ_0 and Δ_S). It is worth noting that this behaviour is strikingly different from the U variation presented in the main text, where we observed a sudden appearance of $\kappa_{L/2}$ and Δ_{T0} at a specific value of $U_c/W = 1.51$. Moreover, we remark again that the pairing field influences on the characteristics of the spiral, optimizing its shape from block to canonical, to better host the MZM.

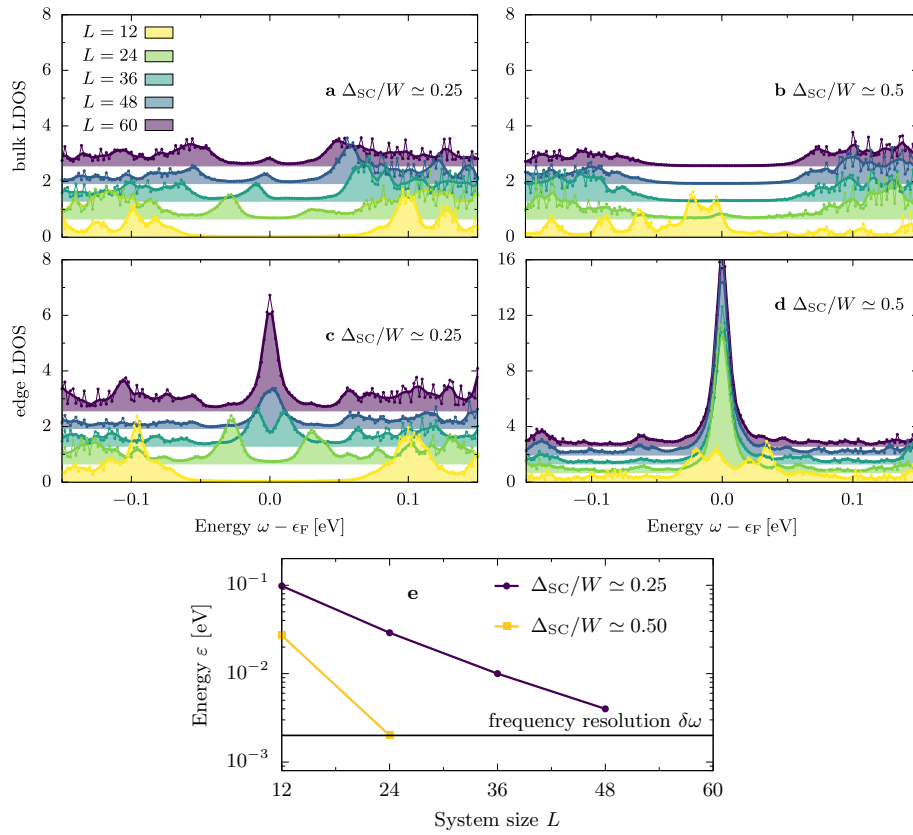
The behaviour of the edge-LDOS in the spiral phase needs special attention. As evident from the results presented in Supplementary Figure 6b, the value of the latter becomes finite for $\Delta_{\text{SC}}/W \gtrsim 0.25$ and vanishes for $\Delta_{\text{SC}}/W \sim 0.7$ (together with the already discussed $\kappa_{L/2}$ and Δ_{T0}). In order to explain the missing weight of edge LDOS for $\Delta_{\text{SC}}/W \lesssim 0.25$ let us investigate the frequency dependence of the hole $\langle \langle c_1^\dagger c_1 \rangle \rangle_{\omega}^{\text{h}}$ and electron $\langle \langle c_1^\dagger c_1 \rangle \rangle_{\omega}^{\text{e}}$ contributions to the edge-LDOS. As it is evident from the results in Supplementary Figure 7a, upon increasing Δ_{SC} the peaks in the electron- and hole-like spectral functions approach each other (Supplementary Figure 7b shows in more detail the positions of both maxima). Within the accessible frequency resolution, both peaks are easily distinguishable for $\Delta_{\text{SC}}/W \simeq 0.25$, while they merge into a single peak for $\Delta_{\text{SC}}/W > 0.3$.



Supplementary Figure 7. **Pairing field dependence of the edge local density-of-states.** **a** Frequency ω dependence of edge ($\ell = 1$) local density-of-states (LDOS) as a function of the pairing field $\Delta_{\text{SC}}/W \simeq \{0.0, 0.05, \dots, 0.7\}$, as calculated for $L = 36$, $\bar{n} = 0.5$, and $U/W = 2$. **b** Pairing field dependence of the maximum position [i.e., offset energy ϵ , see Eq. 14 of the main text] of the hole $\langle \langle c_1^\dagger c_1 \rangle \rangle_{\omega}^{\text{h}}$ and electron $\langle \langle c_1^\dagger c_1 \rangle \rangle_{\omega}^{\text{e}}$ contributions to edge-LDOS, see Eq. 8 of the main text (based on the data presented in panel **a**).

The behaviour described above is characteristic of systems hosting the MZM, i.e., despite the Majorana modes being

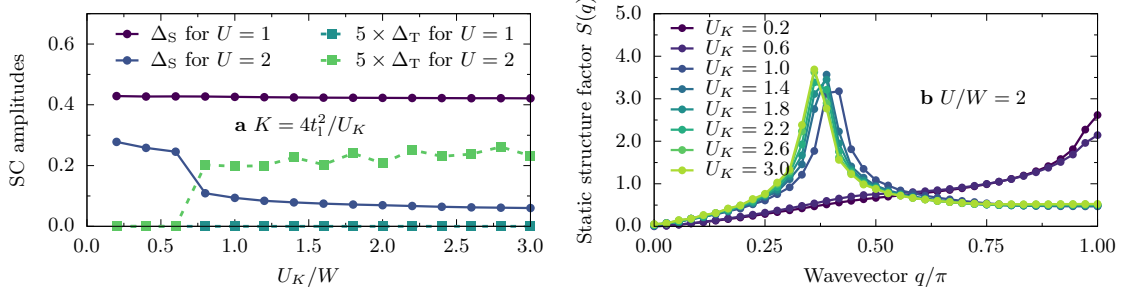
located at the opposite edges of the studied chain, they overlap in any finite- L system [5, 6]. Due to this overlap, the peaks arise at a nonzero frequency $\omega = \pm\varepsilon$, see Eq. 14 of the main text. The clear splitting in the former case allows for a systematic finite-size study, shown in Supplementary Figure 8. In order to obtain well merged Majorana modes for $\Delta_{\text{SC}}/W \simeq 0.25$, one needs to consider chains with at least $L \sim 60$ sites (see Supplementary Figure 8c), whereas systems half that size are sufficient for the case that is primarily studied in the present work, i.e., for $\Delta_{\text{SC}}/W \simeq 0.5$ (see Supplementary Figure 8d). Furthermore, it is worth noting that if the chain is too short, then the remnants of the peaks become visible also in the middle of the system, as it is visible from results for $L = 24$ in Supplementary Figure 8a and Supplementary Figure 8c. On the other hand, a clear single peak at the system's edge always coincides with a well-developed gap in the bulk, as shown in Supplementary Figure 8b and Supplementary Figure 8d. All these results consistently support the scenario that the nonzero splitting ε originates from the overlap of the edge modes. In Supplementary Figure 8e we explicitly show that ε decays exponentially with L , as expected for systems hosting the MZM [5, 6].



Supplementary Figure 8. **Finite-size analysis.** System lengths $L = \{12, 24 \dots, 60\}$ dependence of the local density-of-states **a-b** in the middle of the chain representing the bulk ($\ell = L/2$) and **c,d** at the edge ($\ell = 1$) of the system, as calculated for $U/W = 2$, **a,c** $\Delta_{\text{SC}}/W \simeq 0.25$ and **b,d** $\Delta_{\text{SC}}/W \simeq 0.5$. **e** System size L dependence of the offset energy ε [see Eq. 14 of the main text] for $\Delta_{\text{SC}}/W \simeq \{0.25, 0.5\}$ (based on the data presented in panels **c** and **d**).

Finally, we discuss the robustness of our results to modifications in the localized orbital interaction strength U_K . Within our model, the latter manifests as a change in the spin exchange integral $K = 4t_1^2/U_K$. Our results, presented in Supplementary Figure 9a, indicate that when the system is in the trivial phase, $U/W = 1$ and $\Delta_{\text{SC}}/W \simeq 0.5$, only a singlet SC amplitude is present for all considered values of $U_K/W \in [0.2, 3.0]$. For the topological phase at $U/W = 2$, the results (the presence of the triplet SC amplitude) do not depend on U_K as long as the spiral nature of magnetism is not destroyed, i.e., for $U_K/W \gtrsim 0.8$. On the other hand, when the spin exchange integral $K \propto 1/U_K$ dominates as

an energy scale, the AFM ordering of the spins becomes energetically favorable [see Supplementary Figure 9b for the analysis of static structure factor $S(q)$] and, consequently, the system goes away from the topological phase. These results highlight the importance of the competing energy scales present in the multi-orbital OSMP system.

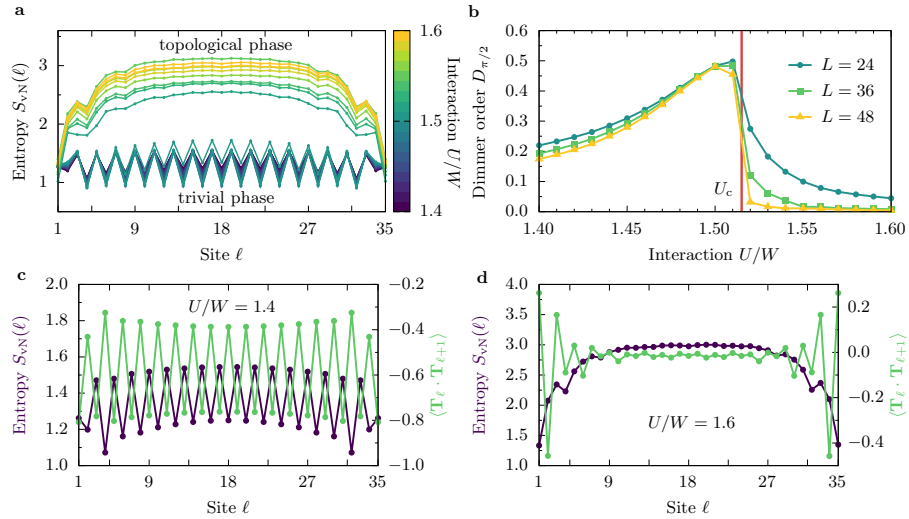


Supplementary Figure 9. **Spin exchange analysis.** **a** Dependence of the singlet Δ_S and triplet Δ_T SC amplitudes on the localized orbital interaction strength U_K , calculated for $L = 36$, $U/W = 1, 2$, $\bar{n} = 0.5$, and $\Delta_{SC}/W \simeq 0.5$. **b** Static spin structure factor $S(q)$ dependence on the localized orbital interaction strength U_K , calculated for $L = 36$, $U/W = 2$, $\bar{n} = 0.5$, and $\Delta_{SC}/W \simeq 0.5$.

Supplementary Note 5. Entropy and dimer order

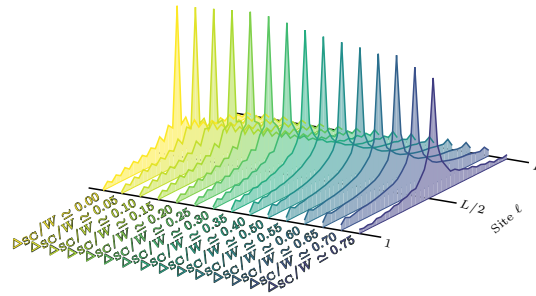
In this section, we demonstrate that the interaction-induced topological phase transition at U_c may be identified via studying the entanglement entropy. Supplementary Figure 10a shows the dependence of the von Neumann entropy $S_{\text{vN}}(\ell)$ on the subsystem size, $\ell \leq L$, in the vicinity of the transition, i.e., for $1.4 < U/W < 1.6$. Two characteristic behaviours emerge: for $U < U_c \simeq 1.51W$ $S_{\text{vN}}(\ell)$ displays an oscillatory behaviour, while for $U > U_c$ the entropy increases abruptly and becomes a smooth function of ℓ . This sudden change in the entropy behaviour signifies the interaction-induced topological phase transition and the appearance of MZM.

We also argue that the topological transition in the OSMP chain is accompanied by a rapid change of the dimer order $D_{\pi/2}$ (see Supplementary Figure 10b). In Supplementary Figures 10c and 10d we have shown the entanglement entropy, respectively for the trivial and nontrivial phases, where $S_{\text{vN}}(\ell)$ displays clear oscillations in the former case. To explain the physical origin of such oscillations we have also plotted the static spin-spin correlation function $\langle \mathbf{T}_\ell \cdot \mathbf{T}_{\ell+1} \rangle$. We can observe that the maxima of $|\langle \mathbf{T}_\ell \cdot \mathbf{T}_{\ell+1} \rangle|$ and $S_{\text{vN}}(\ell)$ coincide. Recall to calculate the entanglement entropy, we split the system into two subsystems cutting the bond between sites ℓ and $\ell + 1$. Whenever a bond with a large spin-spin correlation is cut, also the entanglement entropy is large. Therefore, we expect that the oscillatory behaviour of $S_{\text{vN}}(\ell)$ is a direct manifestation of the dimer order. Indeed, in the topological phase the spin dimerization persists only at the very edges of the system, as shown in Supplementary Figure 10d, so that the (bulk) dimer order vanishes presumably as $1/L$, see Supplementary Fig. 10b. Due to the absence of bulk dimer order, the entanglement entropy smoothly changes with ℓ , as demonstrated also in Supplementary Figure 10a.



Supplementary Figure 10. **Entropy S_{vN} and dimer order $D_{\pi/2}$.** **a** Interaction $U \in \{1.41, 1.42, \dots, 1.59, 1.60\}$ dependence of the von Neumann entanglement entropy $S_{\text{vN}}(\ell)$ of the subsystem of size ℓ . Calculated for $L = 36$, $\bar{n} = 0.5$, and $\Delta_{\text{SC}}/W \simeq 0.5$. **b** Interaction dependence of the dimer order parameter $D_{\pi/2}$ as calculated for $L = 24, 36, 38$, $\bar{n} = 0.5$, and $\Delta_{\text{SC}}/W \simeq 0.5$. **c-d** Site ℓ dependence of von Neumann entanglement entropy S_{vN} and local spin-spin correlation function $\langle \mathbf{T}_\ell \cdot \mathbf{T}_{\ell+1} \rangle$ (where $\mathbf{T}_\ell = \mathbf{S}_\ell + \mathbf{s}_\ell$ is the total on-site spin) **c** below ($U/W = 1.4$) and **d** above ($U/W = 1.6$) the topological phase transition. Results calculated for $L = 36$, $\Delta_{\text{SC}}/W \simeq 0.5$, and $\bar{n} = 0.5$.

Furthermore, the vanishing of the dimer order can also be observed in the behaviour of the chirality correlation function $\langle \boldsymbol{\kappa}_{L/2} \cdot \boldsymbol{\kappa}_\ell \rangle$ shown in Supplementary Figure 11. As expected in the $\Delta_{\text{SC}} \rightarrow 0$ limit (for which $D_{\pi/2} \neq 0$), the $\langle \boldsymbol{\kappa}_{L/2} \cdot \boldsymbol{\kappa}_\ell \rangle$ correlation displays a clear zig-zag-like pattern, reflecting the $\pi/2$ -block nature of the spiral (for details see Ref. [3]). It is evident from the presented results that the decay length of the $\boldsymbol{\kappa}$ -correlation is not affected by the pairing field strength. On the other hand, the spatial details of $\langle \boldsymbol{\kappa}_{L/2} \cdot \boldsymbol{\kappa}_\ell \rangle$ change from a zig-zag to a smooth function of distance. The latter is consistent with the $D_{\pi/2} \rightarrow 0$ result in this region.



Supplementary Figure 11. **Pairing field dependence of the spiral order.** Site dependence of the chirality correlation function $\langle \kappa_{L/2} \cdot \kappa_\ell \rangle$ as calculated for various strengths of the SC pairing fields $\Delta_{SC}/W \simeq (0.00, 0.05, \dots, 0.75)$ ($\bar{n} = 0.5$, $U/W = 2$, $L = 36$).

-
- [1] Herbrych, J. *et al.* Spin dynamics of the block orbital-selective Mott phase. *Nat. Commun.* **9**, 3736 (2018).
 - [2] Herbrych, J. *et al.* Novel Magnetic Block States in Low-Dimensional Iron-Based Superconductors. *Phys. Rev. Lett.* **123**, 027203 (2019).
 - [3] Herbrych, J. *et al.* Block-Spiral Magnetism: An Exotic Type of Frustrated Order. *Proc. Natl Acad. Sci. USA* **117**, 16226 (2020).
 - [4] Lei, H., Ryu, H., Frenkel, A. I. & Petrovic, C. Anisotropy in BaFe₂Se₃ single crystals with double chains of FeSe tetrahedra. *Phys. Rev. B* **84**, 214511 (2011).
 - [5] Stanescu, T. D. , Lutchyn, R. M. & Das Sarma, S. Dimensional crossover in spin-orbit-coupled semiconductor nanowires with induced superconducting pairing. *Phys. Rev. B* **87**, 094518 (2013).
 - [6] Rainis, D., Trifunovic, L., Klinovaja, J. & Loss, D. Towards a realistic transport modeling in a superconducting nanowire with Majorana fermions. *Phys. Rev. B* **87**, 024515 (2013).

TRANSITION TO THE HALDANE PHASE DRIVEN BY ELECTRON-ELECTRON CORRELATIONS

This chapter further explores the topological properties of low-dimensional multiorbital systems with strong correlations. While the previous chapter focused on Majorana modes in the orbital-selective Mott phase away from half filling, this chapter investigates another topological effect that occurs specifically at half filling. This effect corresponds to the well-known topological Haldane phase of the $S = 1$ Heisenberg chain. However, here, it is examined from the perspective of the two-orbital Hubbard chain. Although this work [O3] deviates slightly from the context of the 123 ladders, it remains within the scope of low-dimensional correlated multiorbital systems, maintaining its relevance to this thesis.

Here, the central finding is the identification of yet another sharp and interaction-driven topological phase transition. Namely, upon increasing the Hubbard repulsion U and Hund exchange J_H , the two-orbital Hubbard chain transitions into the Haldane phase, accompanied by the emergence of spin-1/2 edge modes. Remarkably, this transition occurs at relatively modest values of U , when the magnetic moments are not yet fully formed and the system is far from the limit of the spin-1 Heisenberg chain. Therefore, this work expands Haldane's concepts for spin chains into an uncharted territory of delocalized electrons. Furthermore, the results indicate that the topological regime can be effectively described by a valence-bond liquid state, which maintains its character even at interaction strengths on the order of the bare kinetic energy. In the scope of this work, my task was to independently implement the calculations of the string order parameter using the density-matrix renormalization group method in the matrix-product state implementation. This task served as a crucial cross-check of earlier calculations and of the proposed conclusions, giving further evidence to the Haldane character of the observed transition. Appropriately, a short discussion of the string order parameter and its relevance to the Haldane phase shall now follow.

In 1983, Haldane put forth a conjecture that the Heisenberg chain with an integer spin, in particular $S = 1$, possesses a gap and exhibits exponentially decaying correlation functions [267,268]. This conjecture challenged the prevailing expectation derived from the extensively studied spin-1/2 chain, which suggested that all spin chains are gapless and have (quasi-)long-range correlations. However, Haldane's conjecture was soon confirmed to be true and found to be linked to remarkable topological properties, laying the foundation for the tremendous interest in this field today. In recognition of his contributions, Haldane was awarded the Nobel Prize in 2016 “for theoretical discoveries of topological phase transitions and topological phases of matter” [269]. The distinct topological characteristics exhibited by the $S = 1$ Heisenberg chain are now commonly referred to as the Haldane phase.

In the aftermath of Haldane's initial work, it was discovered that although the Haldane phase has no usual (quasi-)long-range antiferromagnetic order, it has a *hidden* nonlocal long-range order [270–272]. This is markedly different from the usual classification of phases of matter, which is based on spontaneous symmetry breaking and local order parameters, e.g., magnetization. Instead, the topological nonlocal order is related to a hidden symmetry breaking. To reveal it, Kennedy and Tasaki [271,272] invoked a nonlocal unitary transformation of the spin-1 chain, upon which the hidden order manifests itself as explicit breaking of the $Z_2 \times Z_2$ symmetry in the transformed Hamiltonian. The transformed system has a fourfold degenerate set of ferromagnetic ground states, which correspond to the fourfold degeneracy of the edge modes in the original spin-1 chain [271,273]. While in the transformed form the order parameter is trivial, from the perspective of the original Hamiltonian, it is the nonlocal string order [270]

$$\mathcal{O}_s = \lim_{|m-n| \rightarrow \infty} - \left\langle S_m^z \exp \left(i\pi \sum_{k=m+1}^{n-1} S_k^z \right) S_n^z \right\rangle, \quad (5.1)$$

where $\langle \dots \rangle$ is taken in the ground state. A perfect order of this type is realized in the so-called Affleck-Kennedy-Lieb-Tasaki (AKLT) state [274,275]. This state is a simple valence-bond solid, and is well established to qualitatively capture the physics of the Haldane phase of the spin-1 chain [276,277]. While in a spin-1 system a general spin configuration has the form $|\dots, \downarrow, 0, \uparrow, \uparrow, 0, \downarrow, 0, \dots\rangle$, in every component of the AKLT wave function, one can erase the sites with $S^z = 0$ to reveal a perfect antiferromagnetic order $|\dots, \downarrow, \uparrow, \downarrow, \uparrow, \dots\rangle$ [273–275]. The parameter \mathcal{O}_s measures precisely this type of “diluted” antiferromagnetic order, interlaced by the $S^z = 0$ states. Although such an order is not perfect in the ground state of the spin-1 Heisenberg chain, the string correlation \mathcal{O}_s is robust, indicating the presence of the Haldane phase.

In the following work, the reader will discover an interesting result: the string order parameter can have robust nonzero values not only in spin chains but also in systems with delocalized electrons. Specifically, this occurs in a correlated multiorbital chain, where it signals the interaction-driven emergence of the Haldane phase. This finding is further supported by analyzing other observables, as discussed below.

Transition to the Haldane phase driven by electron-electron correlations

A. Jażdżewska,¹ M. Mierzejewski,² M. Środa,² A. Nocera,³ G. Alvarez,⁴ E. Dagotto,^{5,6} and J. Herbrych²

¹*Faculty of Physics and Astronomy, University of Wrocław, 50-383 Wrocław, Poland*

²*Institute of Theoretical Physics, Wrocław University of Science and Technology, 50-370 Wrocław, Poland*

³*Department of Physics and Astronomy and Stewart Blusson Quantum Matter Institute, University of British Columbia, Vancouver, B.C. V6T 1Z1, Canada*

⁴*Computational Sciences and Engineering Division,*

Oak Ridge National Laboratory, Oak Ridge, Tennessee 37831, USA

⁵*Department of Physics and Astronomy, University of Tennessee, Knoxville, Tennessee 37996, USA*

⁶*Materials Science and Technology Division, Oak Ridge National Laboratory, Oak Ridge, Tennessee 37831, USA*

One of the most famous quantum systems with topological properties, the spin $S = 1$ antiferromagnetic Heisenberg chain, is well-known to display exotic $S = 1/2$ edge states. However, this spin model has not been analyzed from the more general perspective of strongly correlated systems varying the electron-electron interaction strength. Here we report the numerical investigation of the emergence of the Haldane state and its edge modes in a system of interacting electrons – the two-orbital Hubbard model – with increasing repulsion strength U . We show that these interactions not only form the magnetic moments but also form a topologically nontrivial fermionic many-body ground-state with zero-energy edge states that only at very large U converge to the Haldane chain model. Specifically, upon increasing the strength of the Hubbard repulsion and Hund exchange, we identify a novel sharp transition point separating topologically trivial and nontrivial ground-states. Surprisingly, the latter appears already at rather small values of the interaction U , in a regime where the magnetic moments are *barely developed*, thus generalizing the ideas of Haldane for $S = 1$ spin Heisenberg models into previously unexplored territory involving delocalized electrons. Furthermore, our results indicate that the topological regime can be described by a liquid valence bonds state down to interaction strength of the order of the bare kinetic energy.

The precise role of the electron-electron interaction in many condensed matter systems is still under much debate. From the high critical temperature superconductivity of copper- and iron-based compounds to the magnetic properties of idealized spin models, strong correlations appear crucial for our understanding of materials physics. In parallel, topology in various compounds has been typically realized and investigated at the level of non-interacting band structures in the presence of spin-orbit coupling. However, the detailed study of the Coulomb correlation effects intertwined with topological physics has barely started and represents one of the grand challenges of present-day theoretical and experimental physics.

In particular, in one of the most famous topologically nontrivial systems, i.e., the $S = 1$ antiferromagnetic (AFM) Heisenberg model $H_S = J \sum_{\ell} \mathbf{S}_{\ell} \cdot \mathbf{S}_{\ell+1}$ on a one-dimensional (1D) lattice geometry, the spin-spin interactions are necessary to form the zero-energy edge states, which is the hallmark of topological states. In his seminal work [1, 2], Haldane showed that integer $S = 1, 2, \dots$ and half-integer $S = 1/2, 3/2, \dots$ spin systems behave fundamentally different: the latter are gapped while the former are gapless. Affleck, Kennedy, Lieb, and Tasaki (AKLT) proved [3] that the ground-state of $S = 1$ chains when generalized including biquadratic interactions, can be expressed as a valence bond state (VBS) composed of interacting $S = 1/2$ -like singlets. In this picture, the AKLT state, when defined on an open chain, has two unpaired $S = 1/2$ spins at the edges of the system forming zero-energy modes.

The existence of topologically protected edge states in $S = 1$ chains have been shown by extensive theoretical [4–9] and experimental [10–15] studies. Also, the road to the Haldane states from well-formed $S = 1/2$ spins has been studied. The AKLT VBS state initiated various investigations of ladder-like $S = 1/2$ systems where special constraints, such as ferromagnetic rung exchange or unpaired sites at the edges of overall AFM systems, lead to the topological $S = 1$ Haldane phase. Such systems are not only a playground for theoretical investigations but were also realized using cold atoms in optical lattice setups [13]. In this context, the extended Bose Hubbard model (containing nearest-neighbour interactions) can also host the Haldane phase [16, 17].

However, in real low-dimensional materials [18], the $S = 1$ moments arise due to the electron-electron correlations in a multi-orbital Hubbard model setup, which is technically challenging. Because the $S = 1/2$ moments themselves are already an effective description of some fermionic systems, such analysis is usually unjustified for many compounds. But in more refined descriptions, the Coulomb repulsion and Hund’s coupling not only cooperate but also can compete [19, 20]. Depending on their specific values, the Mott localization of electrons and the formation of well-developed spins can occur in portions of the phase diagram. As an example, in the largest family of $S = 1$ chains, the nickel-based compounds [18], the two e_g electrons of Ni^{+2} ions are necessary to form the $S = 1$

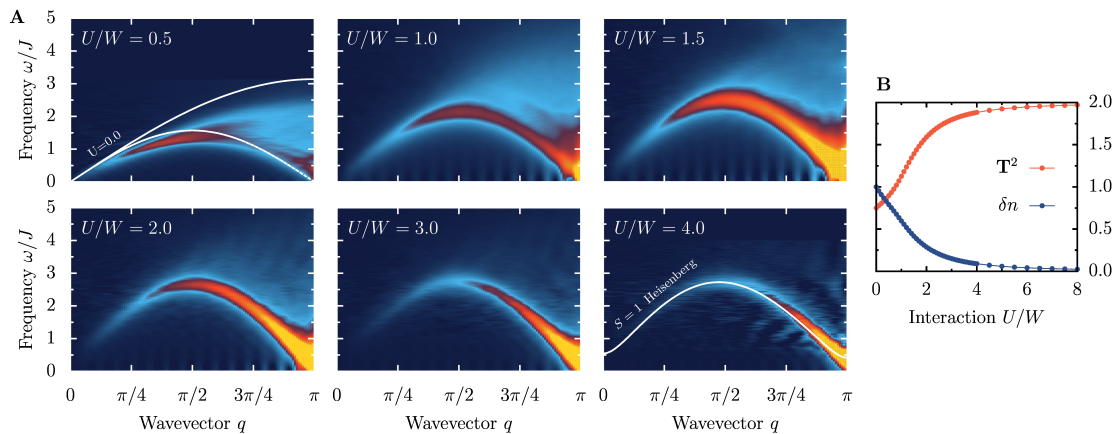


Figure 1. **Spin excitations.** **A** Evolution of the spin excitations, as measured by the dynamical spin structure factor $S(q, \omega)$, with increasing strength of electron-electron interaction U for a system of $L = 80$ sites and $J_H/U = 0.25$. The frequency scale was renormalized by the effective spin exchange $J = 2t^2/(U + J_H)$. White lines in the left top panel represent the two-spinon continuum of $U = 0$ Hubbard model, while the line in the bottom right panel depicts the magnon dispersion of the $S = 1$ Heisenberg model. In the open boundary systems considered here, the zero energy Haldane edge states are expected at $\omega = 0$. However, the latter's large intensity can blur the spectra's details. To avoid this issue, we have evaluated the spin excitations only in the bulk of the system. **B** Total magnetic moment per site $\mathbf{T}^2 = S(S + 1)$ and charge fluctuations δn vs. interaction strength U . Note \mathbf{T}^2 starts at 0.75 for noninteracting $U = 0$ electrons.

spins due to the Hund's rule that maximizes the on-site magnetic moment. For AgVP_2S_6 or $\text{Tl}_2\text{Ru}_2\text{O}_7$ the latter occurs on the t_{2g} orbitals of V^{+3} or Ru^{+4} , respectively. In all the previously mentioned compounds, the emergence of the topological states is unknown when described from the more fundamental perspective of quantum mechanically fluctuating individual mobile electrons, including electron-electron interaction.

To fully understand how the topological state in $S = 1$ chains emerges from a fermionic description, one has to focus on the effects of electron interaction within the multi-orbital systems in which Hubbard and Hund's couplings are crucial ingredients. Here we demonstrate that the latter are sufficient for the onset of the topologically nontrivial phase. Specifically, upon increasing the strength of the Coulomb repulsion, we identify a clear transition between topologically trivial and nontrivial ground-states. Our analysis unveils the threshold value of the interaction U_c where the Haldane gap opens. Although at U_c we also identify the emergence of zero-energy edge states and finite string order correlations (the signature properties of $S = 1$ Haldane phase), surprisingly, the magnetic moments are far from being fully developed, and spin excitations still resemble those in the regime of weak $U \rightarrow 0$. Consequently, we here report that the Haldane phase is not limited by having $S = 1$ moments. Specifically, its generalized existence can be shown to extend to unexpectedly small values of the interaction $U \sim W$, with W being the kinetic energy half-bandwidth.

From two-orbital to Heisenberg model. We employ the zero-temperature density-matrix renormalization group method [4, 21, 22] (DMRG) to solve the 1D two-orbital Hubbard model (2oH) at half electronic filling ($n = 2$, i.e., two particles per site; one particle per orbital) and zero total magnetization $S_{\text{tot}}^z = 0$, relevant for Ni^{+2} -based compounds. The 2oH is given by

$$\begin{aligned}
 H_H = & t \sum_{\gamma\ell\sigma} \left(c_{\gamma\ell\sigma}^\dagger c_{\gamma\ell+1\sigma} + \text{H.c.} \right) + U \sum_{\gamma\ell} n_{\gamma\ell\uparrow} n_{\gamma\ell\downarrow} \\
 & + U' \sum_{\ell} n_{0\ell} n_{1\ell} - 2J_H \sum_{\ell} \mathbf{S}_{0\ell} \cdot \mathbf{S}_{1\ell} \\
 & + J_H \sum_{\ell} \left(P_{0\ell}^\dagger P_{1\ell} + \text{H.c.} \right). \quad (1)
 \end{aligned}$$

Although challenging, the above model contains the most generic many-body interactions found in multiorbital systems: U and $U' = U - 5J_H/2$ represent the intra- and inter-orbital electron-electron Coulomb repulsion, respectively, while J_H accounts for the Hund rule, i.e., ferromagnetic exchange between spins at different orbitals; finally, $P_{0\ell}^\dagger P_{1\ell}$ with $P_{\gamma\ell}^\dagger = c_{\gamma\ell\uparrow}^\dagger c_{\gamma\ell\downarrow}^\dagger$ represents the doublon-holon exchange. We will focus on degenerate bands with $t = 0.5$ [eV], and in the following, we will use the half-bandwidth of kinetic energy as a unit, i.e., $W = 2t = 1$ [eV]. While we will mostly consider the $J_H/U = 0.25$ case, other values of Hund exchange will also be investigated [23]. Note that the $\mathbf{S}_{\gamma\ell}$ operators represent the spin-1/2 of electrons and that the above model preserves the $\text{SU}(2)$ symmetry provided that $U' = U - 5J_H/2$ and

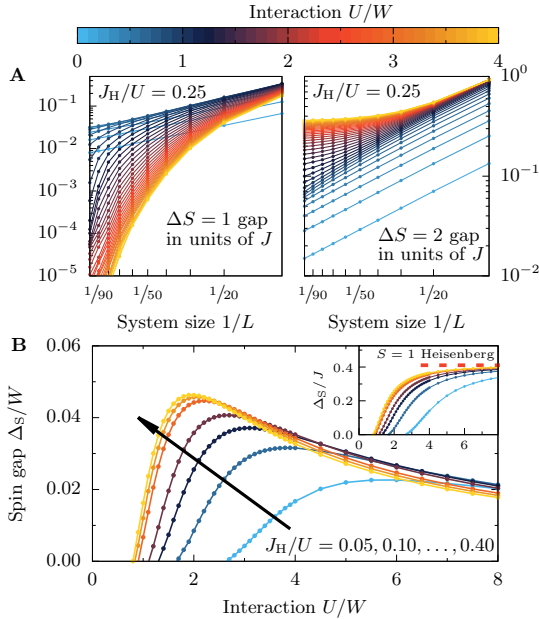


Figure 2. **Spin gaps.** **A** Finite-size scaling of $\Delta S = 1$ (left panel) and $\Delta S = 2$ (right panel) spin excitations for $J_H/U = 0.25$ and $L \in \{10, 20, \dots, 100\}$. Line color-code represents the value of the interaction U . **B** U dependence of the extrapolated magnon gaps in units of W . Top to bottom: $J_H/U = 0.05, 0.10, \dots, 0.40$. Inset depicts the same data but renormalized by the effective spin exchange J . The saturation to the Haldane gap $\Delta_S/J \simeq 0.41$ is clearly visible (red dashed line).

the doublon-holon exchange term is included.

The standard probe of spin excitations is the momentum q and energy ω resolved dynamical spin structure factor $S(q, \omega)$, which is the Fourier transform of the non-local Green's functions $\langle\langle \mathbf{T}_\ell \mathbf{T}_{\ell'} \rangle\rangle_\omega$ [23], with \mathbf{T}_ℓ as the total on-site spin $\mathbf{T}_\ell = \sum_\gamma \mathbf{S}_{\gamma\ell}$. The calculated $S(q, \omega)$ is routinely compared to inelastic neutron scattering or resonant inelastic X-ray scattering data, also in the case of $\mathcal{S} = 1$ compounds. With increasing strength of interaction U , the 2oH spectrum (Fig. 1A) develops from a continuum of $\mathcal{S} = 1/2$ -like excitations at $U = 0$ [24, 25] to the well-established magnon-like excitations [26, 27] of the $\mathcal{S} = 1$ Heisenberg model at large $U \gg W$. Renormalizing the frequency by the effective spin exchange, $J = 2t^2/(U + J_H)$ [19], yields qualitative agreement between the models at $U/W \simeq 4$. As expected, for such value of interaction U , the average total magnetic moment is almost maximized $\mathbf{T}^2 = \mathcal{S}(\mathcal{S} + 1) \simeq 2$ and the charge fluctuations $\delta n = \langle n^2 \rangle - \langle n \rangle^2$ are vanishing (Fig. 1B).

The artificial broadening needed in the dynamical-DMRG method [28, 29] prevents us from extracting accu-

rate values of the magnon gap directly from the spectrum of $S(q, \omega)$. Instead, the gaps can be obtained from the difference in ground-state energies of two magnetization sectors with different S_{tot}^z (with ΔS being the magnetization difference) at fixed electron density n . It is important to note that working on a finite-size lattice, the $\Delta S = 1$ excitations of 2oH are always gapless when extrapolated to the thermodynamic limit $L \rightarrow \infty$ (Fig. 2A). For $U \rightarrow 0$, the gapless spin excitations manifest the physics of noninteracting fermions, with an inverse-linear dependence on the system size $\mathcal{O}(1/L)$ of the gap according to Lieb-Schultz-Mattis theorem [30]. In the opposite limit of the $\mathcal{S} = 1$ Heisenberg model at $U \gg W$, the gapless $\Delta S = 1$ excitation originates in a four-fold degenerate ground-state (two-fold in the $S_{\text{tot}}^z = 0$ sector) with two $\mathcal{S} = 1/2$ edge states [27, 31]. For a finite L , the latter are split due to their overlap [32], which decays exponentially with increasing system size. See large- U data in Fig. 2A. Thus, within the open boundary condition system with edge states, the true magnon gap Δ_S can be extracted from $\Delta S = 2$ excitations [4, 33, 34]. Still, for $U \rightarrow 0$, the magnons are gapless with $\mathcal{O}(1/L)$ size dependence of the gap. On the other hand, increasing the strength of U changes the nature of the scaling. At large U , we observe a saturation to a finite value in the $L \rightarrow \infty$ limit. This saturation is to the well-known Haldane gap $\Delta_S/J \simeq 0.41$ for $U \gtrsim 4$, confirming the accuracy of our procedure. Crucially, the finite-size scaling varying U reveals a novel critical (Hund J_H dependent [23]) value of the interaction $U_c = U_c(J_H)$ where the gap opens (Fig. 2B). For example, for $J_H/U = 0.25$ the magnons become gapped at $U_c/W \simeq 0.9$.

It is worth noting that the magnon gap Δ_S opens at a value of the interaction $U = U_c$ for which the overall spin excitations are *far* from the $\mathcal{S} = 1$ Heisenberg model magnon-like spectrum. In fact, for $U/W \sim 1$, the spin excitations still visually resemble the noninteracting continuum of $\mathcal{S} = 1/2$ -like moments, though with redistributed spectral weights (Fig. 1A).

Zero-energy edge modes. As mentioned, the exponential in the system size dependence of the $\Delta S = 1$ gaps (Fig. 2A) indicates the presence of edge states. To quantify them, we analyze (Fig. 3) the zero-frequency $\omega = 0$ dynamical spin-spin correlation functions between the edge and the bulk of the system, i.e., the non-local Green's functions $(-1)^\ell \langle\langle T_\ell^z T_\ell^z \rangle\rangle_{\omega=0}$, capable of capturing zero-energy modes. Here, the $(-1)^\ell$ prefactor removes the AFM staggered pattern. At small U , the spin correlations decay exponentially with distance ℓ (Fig. 3A), as expected for a paramagnetic region. Increasing U leads to a slower, although still exponential, decay. At $U \simeq U_c$, the $\omega = 0$ correlations are approximately site-independent. Note that the latter does not originate in any long-range order because the value of spin correlations decays with the system size (see Fig. 3B and the discussion below).

Interestingly, a characteristic V-shape of correlations develops above U_c . The latter is the manifestation of

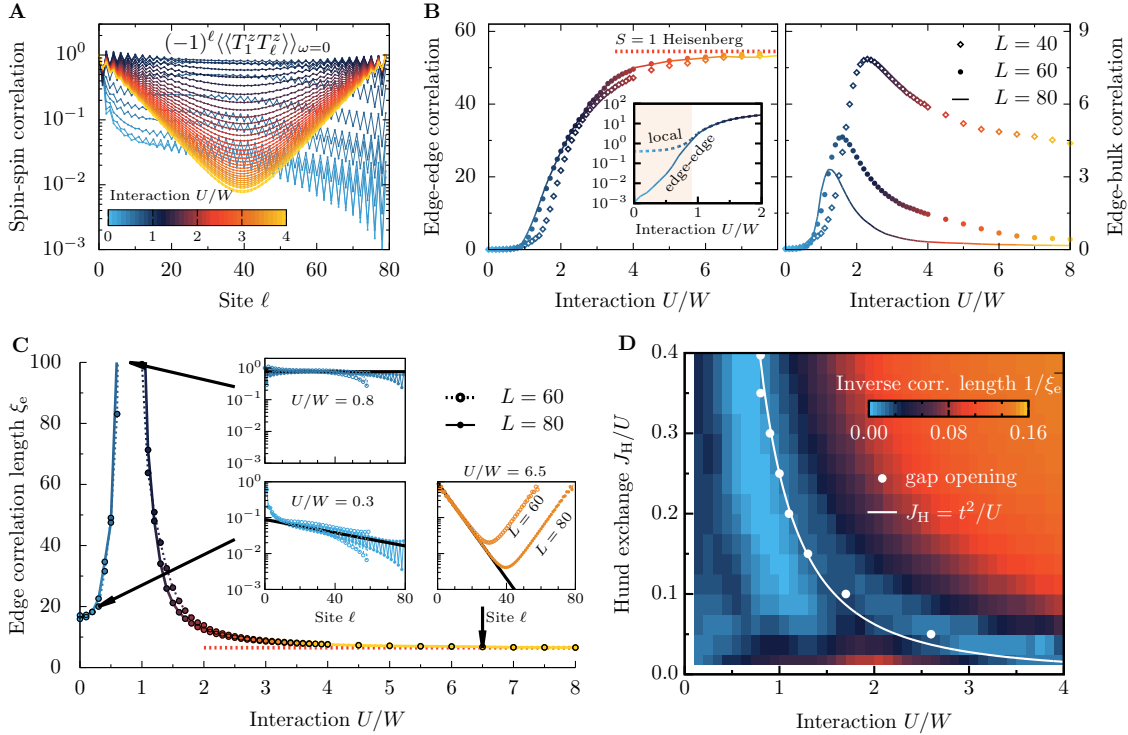


Figure 3. **Edge spin correlations.** **A** Distance ℓ dependence of the zero frequency $\omega = 0$ dynamical spin-spin correlations $(-1)^\ell \langle \langle T_1^z T_\ell^z \rangle \rangle_{\omega=0}$ for various values of interaction U (denoted by color-code). The results are normalized by the $\ell = 1$ value of the correlation function [23]. **B** Edge-edge $\langle \langle T_1^z T_\ell^z \rangle \rangle_{\omega=0}$ (left panel) and edge-bulk $\langle \langle T_1^z T_{L/2}^z \rangle \rangle_{\omega=0}$ (right panel) dynamical spin correlations vs. interaction strength U . At U_c , we observe the appearance of finite edge-edge correlations, saturating at $U \gg W$ to the value given by the $S = 1$ Heisenberg model (red dashed line). **C** Extracted, Eq. (2), edge correlation length ξ_e vs. interaction strength U . Insets depict examples of spin-spin correlations for two system sizes ($L = 60$ and $L = 80$, together with fitted exponentials $\propto \exp(-\ell/\xi_e)$). All data are calculated at $J_H/U = 0.25$. **D** Interaction U/W - Hund exchange J_H/U phase diagram on the basis of inverse edge correlation length $1/\xi_e$ for $L = 60$. White points depict U_c obtained from the spin gap Δ_S opening, while the white line represents $J_H = t^2/U$.

the edge states present at the (open) boundaries of the system [5]. In the $S = 1$ Heisenberg model, the zero-energy modes are not localized at a single edge site but decay exponentially with the correlation length $\xi_S \simeq 6.1$. The latter leads to finite (exponentially suppressed) AFM spin correlations up to half $\ell \sim L/2$ of the system. The increase of $\langle \langle T_1^z T_\ell^z \rangle \rangle_{\omega=0}$ for $\ell > L/2$ is exactly a consequence of correlated edge states: the edge-edge correlations are finite, while the edge-bulk correlations are vanishing.

To assess the development of spin-spin correlations in the 2oH system, especially the correlated edge states, we can monitor the behaviour of the edge-edge and edge-bulk (Fig. 3B) values vs. the interaction U . The former acquires a nonzero value at U_c [23] and displays small finite-size effects. On the other hand, the finite value of the edge-bulk correlations decreases with system size L

and vanishes in the $L \rightarrow \infty$ limit.

Furthermore, we can extract the interaction dependence of the edge correlation length (Fig. 3C) by fitting $\ell < L/2$ data of the 2oH to

$$(-1)^\ell \langle \langle T_1^z T_\ell^z \rangle \rangle_{\omega=0} \propto \exp(-\ell/\xi_e). \quad (2)$$

For $U/W > 4$ we reproduce $\xi_e \simeq \xi_S \simeq 6.1$, consistent with dynamical spin structure factor $S(q, \omega)$ investigations of the $S = 1$ Heisenberg model physics. Interestingly, the extracted ξ diverges at U_c . The latter reflects the site-independent correlations in this region [23].

Topological phase transition. The opening at U_c of a spin gap Δ_S , the emergence of edge-edge correlations $\langle \langle T_1^z T_\ell^z \rangle \rangle_{\omega=0}$, and the diverging edge correlation length ξ_e all consistently indicate the existence of an interaction-induced topological phase transition. The latter is between topologically trivial and nontrivial regions, with

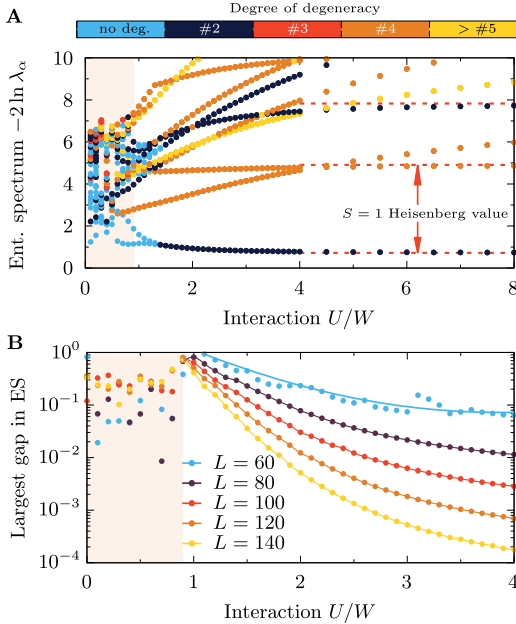


Figure 4. **Topological phase transition.** **A** Interaction U dependence of the entanglement spectrum $-2 \ln \lambda_\alpha$, obtained at $J_H/U = 0.25$ using a $L = 140$ site system partitioned in half. Color code depicts the number of occurrences of a given eigenvalue (number of degeneracies). The values for the $\mathcal{S} = 1$ Heisenberg model are also displayed (red dashed lines). **B** Analysis of the largest gap in the entanglement spectrum for various system sizes $L = 60, 80, 100, 120, 140$ [23].

the emergence of the Haldane edge states at U_c . The topological phases can be identified by investigating the entanglement spectrum of the system [35, 36], i.e., the Schmidt coefficients λ_α of left/right ($|L\rangle/|R\rangle$) decomposed ground-state $|\text{gs}\rangle = \sum_\alpha \lambda_\alpha |L\rangle_\alpha |R\rangle_\alpha$, with λ_α^2 being the eigenvalues of the reduced density matrix of the partition. In the topologically nontrivial region, all λ_α 's are evenly degenerate. Consequently, the entanglement entropy $S_{vN} = -\sum_\alpha \lambda_\alpha^2 \ln \lambda_\alpha^2$ cannot drop below the $\ln 2$ value for any cut of the system, consistent with the presence of entangled $\mathcal{S} = 1/2$ edge states. The analysis of the 2oH model indicates that this condition is fulfilled for $U \gtrsim U_c$ (Fig. 4A). Detailed investigation of the largest gap [23] in the entanglement spectrum (Fig. 4B) shows that the trivial region $U < U_c$ does not have any apparent structure in the λ_α eigenvalues. On the other hand, the largest gap decays exponentially with system size for any $U > U_c$ (though, with slower decay in the proximity of U_c) and vanishes in the thermodynamic limit $L \rightarrow \infty$.

In the context of the $\mathcal{S} = 1$ Heisenberg model, the topological Haldane phase can also be detected by study-

ing the non-local string order parameter [31, 37, 38]

$$\mathcal{O}_s(\ell) = - \left\langle A_m \exp \left(i\theta \sum_{n=m+1}^{m+\ell-1} A_n \right) A_{m+\ell} \right\rangle, \quad (3)$$

which for $\theta = \pi$ and $A_\ell = S_\ell^z$ measures the breaking of the discrete $Z_2 \times Z_2$ hidden symmetry (i.e., the dihedral group of π rotations). It is important to note that the phase $\theta = \pi$ was obtained via the valence bond state structure of the AKLT state. For a generic spin- \mathcal{S} Heisenberg model, the string order phase becomes spin-dependent $\theta = \theta(\mathcal{S})$, i.e., it has to reflect the properties of a given VBS ground-state [39–42].

In the case of the 2oH model, for $U > U_c$, the π -string order \mathcal{O}_s does not decay (Fig. 5), as expected in the $\mathcal{S} = 1$ Haldane phase. However, it is important to note that the total spin operator of 2oH, $A_\ell = T_\ell^z$, involves not only $\mathcal{S} = 1$ but also $\mathcal{S} = 1/2$ degrees of freedom and that for $U \simeq U_c$ the magnetic moment deviates strongly from $\mathcal{S} = 1$ (Fig. 1B). Nevertheless, we observe a *finite* string order all the way down to $U = U_c \sim W$ showing that this type of order can exist in a fermionic system as well, even without well defined moments. Interestingly, consistent with the topological phase transition at U_c , for $U < U_c$ the string order vanishes, and the system size dependence changes from weakly increasing with L (for $U > U_c$) to weakly decreasing with L (for $U < U_c$). The latter is consistent with the slow scaling of \mathcal{O}_s for $\mathcal{S} = 1/2$ moments [43].

Discussion and conclusion. Investigating systems on finite lattices, especially with many-body interactions incorporated, is always a challenge: are we observing a true phase transition or a very rapid crossover? Furthermore, interaction-induced transitions in one dimension are rare due to the Mermin-Wagner theorem.

The non-local character of the topological phases allows for such phenomenon even in 1D. Our numerical results indicate that the correlated one-dimensional two-orbital Hubbard model has a sharp transition at $U_c \sim W$ between a topologically trivial region and a generalized fermionic Haldane phase with edge states. Surprisingly, the magnetic moments are not yet fully developed in a vast region of the topological phase (Fig. 1B), and thus the $\mathcal{S} = 1$ Heisenberg model-like description cannot be applied directly. Actually, our analysis shows that the gapped ground-state with finite string order survives down to $U \sim W \sim \mathcal{O}(t)$. Consequently, the latter indicates that a VBS-like state, similar to the AKLT state, could be formulated [44] even with mobile fermions. It seems true despite the fact that the length scale of spin-spin correlations indicate the spatially extended character of the ground-state, although with moments small in value. Our detailed interaction U and Hund exchange J_H investigation (Fig. 3D) indicates that the $SU(2)$ symmetric system undergoes the transition at $J_H \simeq t^2/U$, and consequently a finite $U \sim W$ is necessary for the onset of the non-topological-topological phase transition in real materials.

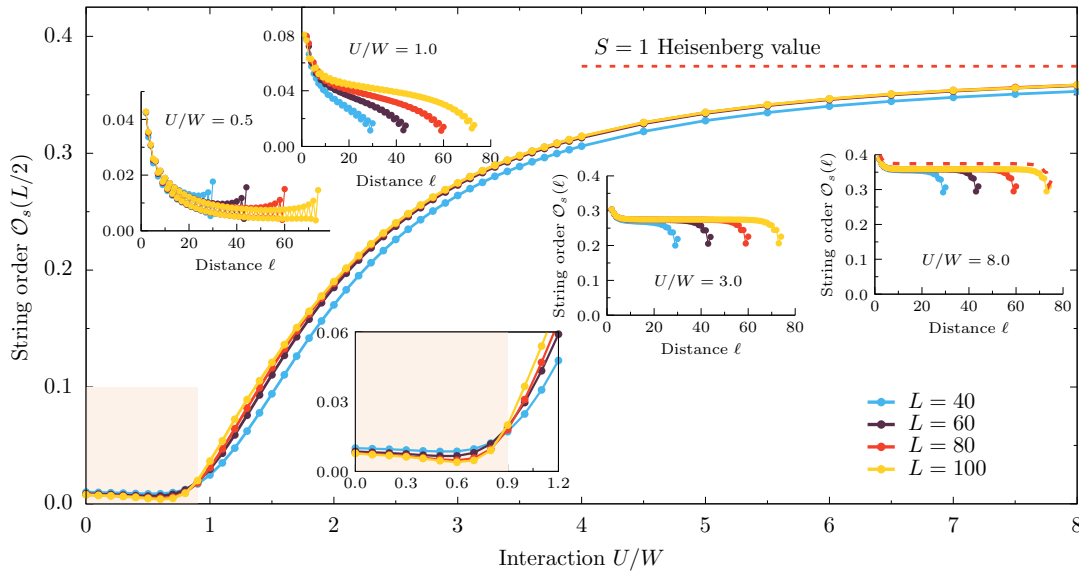


Figure 5. **String order.** Interaction U dependence of the string order parameter $\mathcal{O}_s(\ell)$ with $\theta = \pi$ phase at $\ell = L/2$ distance in the bulk ($m = L/4$). Upper insets depicts $\mathcal{O}_c(\ell)$ vs. distance ℓ for $U = 0.5, 1.0, 3.0, 8.0$ (left to right). The lower inset depicts a zoom to the proximity of the phase transition U_c , with the shaded region depicting the trivial phase. All data are evaluated at $J_H/U = 0.25$ using $L = 40, 60, 80, L = 100$ site systems.

Also, one could expect that for $J_H \gg U$ (i.e., when the system always has well developed on-site triplets formed by electrons), even small interaction will induce the Haldane phase. However, such region of parameter space is unrealistic because for $J_H/U > 0.4$ the inter-orbital interaction $U' = U - 5J_H/2$ becomes attractive $U' < 0$. It is therefore evident that setups with coupled $S = 1/2$ triplets represent, from the electron system perspective, broken spin rotation with $U' \neq U - 5J_H/2$. Previous analysis of the Haldane phase in such setups indicate its fragility with respect to charge fluctuations [6, 7]. Our results indicate that within a two-orbital setup, the Haldane phase is robust down to rather small values of the interaction U , in a regime where the magnetic moments are barely developed, thus generalizing the ideas of Haldane for $S = 1$ spin Heisenberg models into previously unexplored territory involving delocalized electrons.

ACKNOWLEDGMENTS

Funding: M.M. acknowledges support from the National Science Centre (NCN), Poland, via project 2020/37/B/ST3/00020. M.Ś. and J.H. acknowledge grant support from the National Science Centre (NCN), Poland, via project 2019/35/B/ST3/01207. A.N. ac-

knowledges support from the Max Planck-UBC-UTokyo Center for Quantum Materials and Canada First Research Excellence Fund (CFREF) Quantum Materials and Future Technologies Program of the Stewart Blusson Quantum Matter Institute (SBQMI), and the Natural Sciences and Engineering Research Council of Canada (NSERC). G.A. was partly supported by the Scientific Discovery through Advanced Computing (SciDAC) program funded by the U.S. DOE, Office of Science, Advanced Scientific Computing Research and BES, Division of Materials Sciences and Engineering. E.D. was supported by the US Department of Energy, Office of Science, Basic Energy Sciences, Materials Sciences and Engineering Division. Part of the calculations have been carried out using resources provided by Wroclaw Centre for Networking and Supercomputing. **Author contributions:** J.H. conceived the study. A.J., M.M., E.D., and J.H. planned the project. A.J., M.Ś., and J.H. performed the numerical experiments and analyzed the data. A.N. and G.A. developed and tested the simulation codes. M.M., E.D., and J.H. wrote the manuscript. All authors provided comments on the publication. **Competing interests:** The authors declare no competing interests. **Data and materials availability:** The data and the code that supports the plots within this paper and other findings of this study are available at [45] and [46].

- [1] F. D. M. Haldane, “Nonlinear Field Theory of Large-Spin Heisenberg Antiferromagnets: Semiclassically Quantized Solitons of the One-Dimensional Easy-Axis Néel State,” *Phys. Rev. Lett.* **50**, 1153 (1983).
- [2] F. D. M. Haldane, “Continuum dynamics of the 1-D Heisenberg antiferromagnet: Identification with the O(3) nonlinear sigma model,” *Phys. Lett. A* **93**, 464 (1983).
- [3] I. Affleck, T. Kennedy, E. H. Lieb, and H. Tasaki, “Rigorous results on valence-bond ground states in antiferromagnets,” *Phys. Rev. Lett.* **59**, 799 (1987).
- [4] S. R. White, “Density matrix formulation for quantum renormalization groups,” *Phys. Rev. Lett.* **69**, 2863 (1992).
- [5] S. R. White and D. A. Huse, “Numerical renormalization-group study of low-lying eigenstates of the antiferromagnetic $S = 1$ Heisenberg chain,” *Phys. Rev. B* **48**, 3844 (1993).
- [6] F. Anfuso and A. Rosch, “Fragility of string orders,” *Phys. Rev. B* **76**, 085124 (2007).
- [7] S. Moudgalya and F. Pollmann, “Fragility of symmetry-protected topological order on a Hubbard ladder,” *Phys. Rev. B* **91**, 155128 (2015).
- [8] T. Jolicoeur and O. Golinelli, “Physics of integer-spin antiferromagnetic chains: Haldane gaps and edge states,” *C. R. Chimie* **22**, 445 (2019).
- [9] E. H. Kim, G. Fáth, J. Sólyom, and D. J. Scalapino, “Phase transitions between topologically distinct gapped phases in isotropic spin ladders,” *Phys. Rev. B* **62**, 14965 (2000).
- [10] I. A. Zaliznyak, S.-H. Lee, and S. V. Petrov, “Continuum in the Spin-Excitation Spectrum of a Haldane Chain Observed by Neutron Scattering in CsNiCl₃,” *Phys. Rev. Lett.* **87**, 017202 (2001).
- [11] M. Kenzelmann, R. A. Cowley, W. J. L. Buyers, Z. Tun, R. Coldea, and M. Enderle, “Properties of Haldane excitations and multiparticle states in the antiferromagnetic spin-1 chain compound CsNiCl₃,” *Phys. Rev. B* **66**, 024407 (2002).
- [12] M. Kenzelmann, G. Xu, I. A. Zaliznyak, C. Broholm, J. F. DiTusa, G. Aeppli, T. Ito, K. Oka, and H. Takagi, “Structure of End States for a Haldane Spin Chain,” *Phys. Rev. Lett.* **90**, 087202 (2003).
- [13] P. Sompet, S. Hirthe, D. Bourgund, T. Chalopin, J. Bibo, J. Koepsell, P. Bojović, R. Verresen, F. Pollmann, G. Salomon, C. Gross, T. A. Hilker, and I. Bloch, “Realizing the symmetry-protected Haldane phase in Fermi–Hubbard ladders,” *Nature* **606**, 484 (2022).
- [14] A. Nag, A. Nocera, S. Agrestini, M. Garcia-Fernandez, C. Walters, S.-W. Cheong, S. Johnston, and K.-J. Zhou, “Quadrupolar magnetic excitations in an isotropic spin-1 antiferromagnet,” *Nat. Commun.* **13**, 2327 (2022).
- [15] P. Jelínek, “Quantum spin chains go organic,” *Nat. Chem.* **15**, 12 (2023).
- [16] E. G. Dalla Torre, E. Berg, and E. Altman, “Hidden order in 1d bose insulators,” *Phys. Rev. Lett.* **97**, 260401 (2006).
- [17] E. Berg, E. G. Dalla Torre, T. Giamarchi, and E. Altman, “Rise and fall of hidden string order of lattice bosons,” *Phys. Rev. B* **77**, 245119 (2008).
- [18] O. V. Maximova, S. V. Streltsov, and A. N. Vasiliev, “Long range ordered, dimerized, large-D and Haldane phases in spin 1 chain compounds,” *Crit. Rev. Solid State Mater. Sci.* **46**, 371 (2021).
- [19] H. Onishi and T. Hotta, “Orbital-controlled magnetic transition between gapful and gapless phases in the Haldane system with t_{2g} -orbital degeneracy,” *Phys. Rev. B* **70**, 100402 (2004).
- [20] L. de’ Medici, J. Mravlje, and A. Georges, “Janus-Faced Influence of Hund’s Rule Coupling in Strongly Correlated Materials,” *Phys. Rev. Lett.* **107**, 256401 (2011).
- [21] S. R. White, “Density matrix renormalization group algorithms with a single center site,” *Phys. Rev. B* **72**, 180403 (2005).
- [22] U. Schollwöck, “The density-matrix renormalization group,” *Rev. Mod. Phys.* **77**, 259 (2005).
- [23] See supplementary materials.
- [24] G. Muller, H. Thomas, M. W. Puga, and H. Beck, “Quantum spin dynamics of the one-dimensional planar antiferromagnet,” *J. Phys. C: Solid State Phys* **14**, 3399 (1981).
- [25] P. Laurell, A. Scheie, D. A. Tennant, S. Okamoto, G. Alvarez, and E. Dagotto, “Magnetic excitations, nonclassicality, and quantum wake spin dynamics in the Hubbard chain,” *Phys. Rev. B* **106**, 085110 (2022).
- [26] S. R. White and I. Affleck, “Spectral function for the $S = 1$ Heisenberg antiferromagnetic chain,” *Phys. Rev. B* **77**, 134437 (2008).
- [27] J. Becker, T. Köhler, A. C. Tiegel, S. R. Manmana, S. Wessel, and A. Honecker, “Finite-temperature dynamics and thermal intraband magnon scattering in Haldane spin-one chains,” *Phys. Rev. B* **96**, 060403 (2017).
- [28] E. Jeckelmann, “Dynamical density-matrix renormalization-group method,” *Phys. Rev. B* **66**, 045114 (2002).
- [29] A. Nocera and G. Alvarez, “Spectral functions with the density matrix renormalization group: Krylov-space approach for correction vectors,” *Phys. Rev. E* **94**, 053308 (2016).
- [30] I. Affleck and E. H. Lieb, “A proof of part of Haldane’s conjecture on spin chains,” *Lett. Math. Phys.* **12**, 57 (1986).
- [31] T. Kennedy and H. Tasaki, “Hidden symmetry breaking and the Haldane phase in $S = 1$ quantum spin chains,” *Phys. Rev. B* **147**, 431 (1992).
- [32] J. Fraxanet, D. González-Cuadra, T. Pfau, M. Lewenstein, T. Langen, and L. Barbiero, “Topological Quantum Critical Points in the Extended Bose-Hubbard Model,” *Phys. Rev. Lett.* **128**, 043402 (2022).
- [33] S. Qin, T.-K. Ng, and Z.-B. Su, “Edge states in open antiferromagnetic Heisenberg chains,” *Phys. Rev. B* **52**, 12844 (1995).
- [34] S. Yamamoto and S. Miyashita, “Low-lying excitations in the $S = 1$ antiferromagnetic Heisenberg chain,” *Phys. Lett. A* **235**, 545 (1997).
- [35] H. Li and F. D. M. Haldane, “Entanglement Spectrum as a Generalization of Entanglement Entropy: Identification of Topological Order in Non-Abelian Fractional Quantum Hall Effect States,” *Phys. Rev. Lett.* **101**, 010504 (2008).
- [36] F. Pollmann, A. M. Turner, E. Berg, and M. Oshikawa, “Entanglement spectrum of a topological phase in one dimension,” *Phys. Rev. B* **81**, 064439 (2010).
- [37] M. den Nijs and K. Rommelse, “Preroughening transitions in crystal surfaces and valence-bond phases in quan-

- tum spin chains,” *Phys. Rev. B* **40**, 4709 (1989).
- [38] T. Kennedy and H. Tasaki, “Hidden $Z_2 \times Z_2$ symmetry breaking in Haldane-gap antiferromagnets,” *Phys. Rev. B* **45**, 304 (1992).
- [39] M. Oshikawa, “Hidden $Z_2 \times Z_2$ symmetry in quantum spin chains with arbitrary integer spin,” *J. Phys.: Condens. Matter* **4**, 7469 (1992).
- [40] K. Totsuka and M. Suzuki, “Matrix formalism for the VBS-type models and hidden order,” *J. Phys.: Condens. Matter* **7**, 1639 (1995).
- [41] S. Qin, J. Lou, L. Sun, and C. Chen, “Nonlocal Topological Order in Antiferromagnetic Heisenberg Chains,” *Phys. Rev. Lett.* **90**, 067202 (2003).
- [42] F. Pollmann, E. Berg, A. M. Turner, and M. Oshikawa, “Symmetry protection of topological phases in one-dimensional quantum spin systems,” *Phys. Rev. B* **85**, 075125 (2012).
- [43] J. Lou, S. Qin, and C. Chen, “String Order in Half-Integer-Spin Antiferromagnetic Heisenberg Chains,” *Phys. Rev. Lett.* **91**, 087204 (2003).
- [44] N. D. Patel, N. Kaushal, A. Nocera, G. Alvarez, and E. Dagotto, “Emergence of superconductivity in doped multiorbital Hubbard chains,” *npj Quantum Mater.* **5**, 27 (2020).
- [45] J. Herbrych, “Data for ”Transition to the Haldane phase driven by electron-electron correlations”,” Zenodo (2023), <https://doi.org/10.5281/zenodo.7854617> and <https://bitbucket.org/herbrychjacek/corrwro>.
- [46] G. Alvarez, “Source code for ”Transition to the Haldane phase driven by electron-electron correlations”,” Oak Ridge National Laboratory (2023), <https://code.ornl.gov/gonzalo.3/dmrgpp>.

**METHODS for
Transition to the Haldane phase driven by electron-electron correlations**

by A. Jażdżewska, M. Mierzejewski, M. Środa, A. Nocera, G. Alvarez, E. Dagotto, and J. Herbrych

DMRG METHOD.

The Hamiltonians and observables discussed here were studied using the zero-temperature density matrix renormalization group (DMRG) method [4, 22] within the single center site approach [21], where the dynamical correlation functions are evaluated via the dynamical-DMRG [28, 29], i.e., calculating spectral functions directly in frequency space with the correction-vector method using the Krylov decomposition [29]. We have kept up to $M = 3072$ states, performed at least 15 sweeps, and used $A = 0.001$ vector-offset in the single-site DMRG approach, allowing to accurately simulate system sizes up to $L \lesssim 140$ sites of the two-orbital Hubbard model. We have used the DMRG++ computer program developed at Oak Ridge National Laboratory (https://code.ornl.gov/gonzalo_3/dmrgpp). The input scripts for the DMRG++ package to reproduce our results can be found at <https://bitbucket.org/herbrychjacek/corrwro/> and on the DMRG++ webpage.

DYNAMICAL SPIN STRUCTURE FACTOR.

The dynamical spin structure factors are evaluated as

$$S(q, \omega) = \frac{2}{L+1} \sum_{\ell=1}^L \cos[(\ell - L/2)q] \langle \langle \mathbf{T}_\ell \mathbf{T}_{L/2} \rangle \rangle_\omega, \quad (\text{S1})$$

where $q = n\pi/(L+1)$, $n = 0, \dots, L$, and non-local Green's function is given by

$$\langle \langle \mathbf{T}_m \mathbf{T}_n \rangle \rangle_\omega = -\frac{1}{\pi} \text{Im} \langle \text{gs} | \mathbf{T}_m \frac{1}{\omega + i\eta - H + \epsilon_0} \mathbf{T}_n | \text{gs} \rangle. \quad (\text{S2})$$

Here $|\text{gs}\rangle$ represents the ground-state with energy ϵ_0 . The $S(q, \omega)$ spectra presented in Fig. 1A of the main text were calculated with the frequency resolution $\delta\omega/J \simeq 0.03$ and broadening $\eta = 2\delta\omega$ [note the U -dependence of the spin exchange $J = 2t^2/(U + J_H)$].

LARGEST GAP IN THE ENTANGLEMENT SPECTRUM.

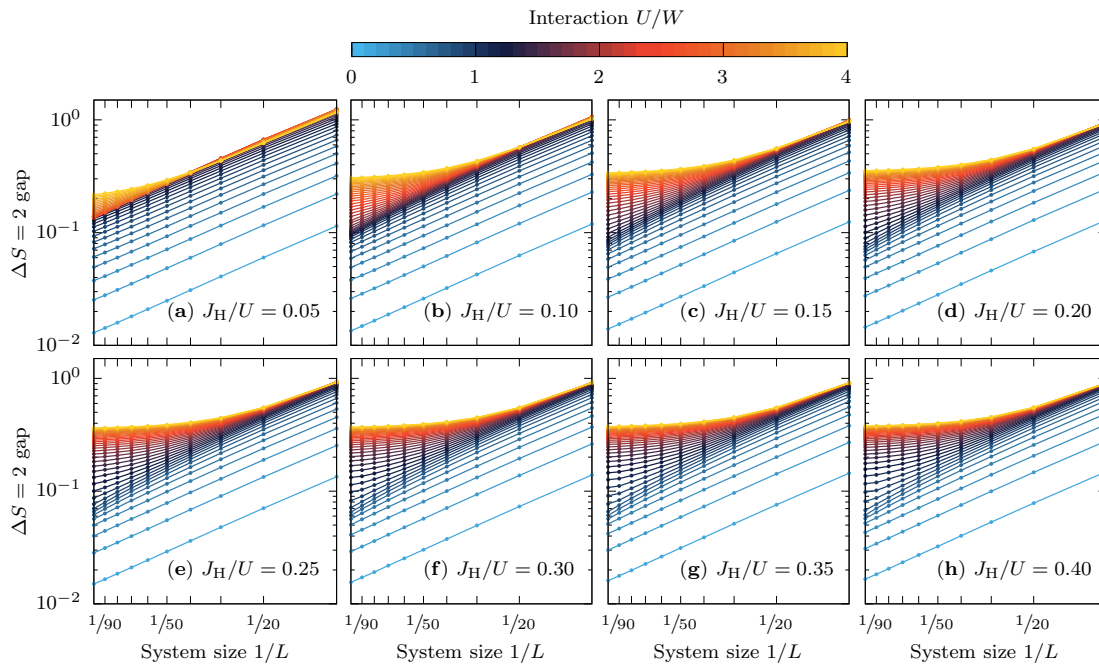
In order to find the largest gap in the entanglement spectrum, first we have calculated consecutive gaps $\delta_n = \min(\ln \lambda_n - \ln \lambda_{n-1}; \ln \lambda_{n+1} - \ln \lambda_n)$. The largest gap is then obtained from $\max(\delta_1, \delta_2, \dots)$.

**SUPPLEMENTAL MATERIAL for
Transition to the Haldane phase driven by electron-electron correlations**

by A. Jazdzewska, M. Mierzejewski, M. Środa, A. Nocera, G. Alvarez, E. Dagotto, and J. Herbrych

GAP ANALYSIS.

In Fig. S1, we present the finite-size $1/L$ and interaction U dependence of the $\Delta S = 2$ gap (the magnon gap Δ_S/J) for various values of the Hund exchange $J_H/U = 0.05, 0.10, \dots, 0.40$. The main text displays the results of $1/L$ extrapolations of this data in Fig. 2B.

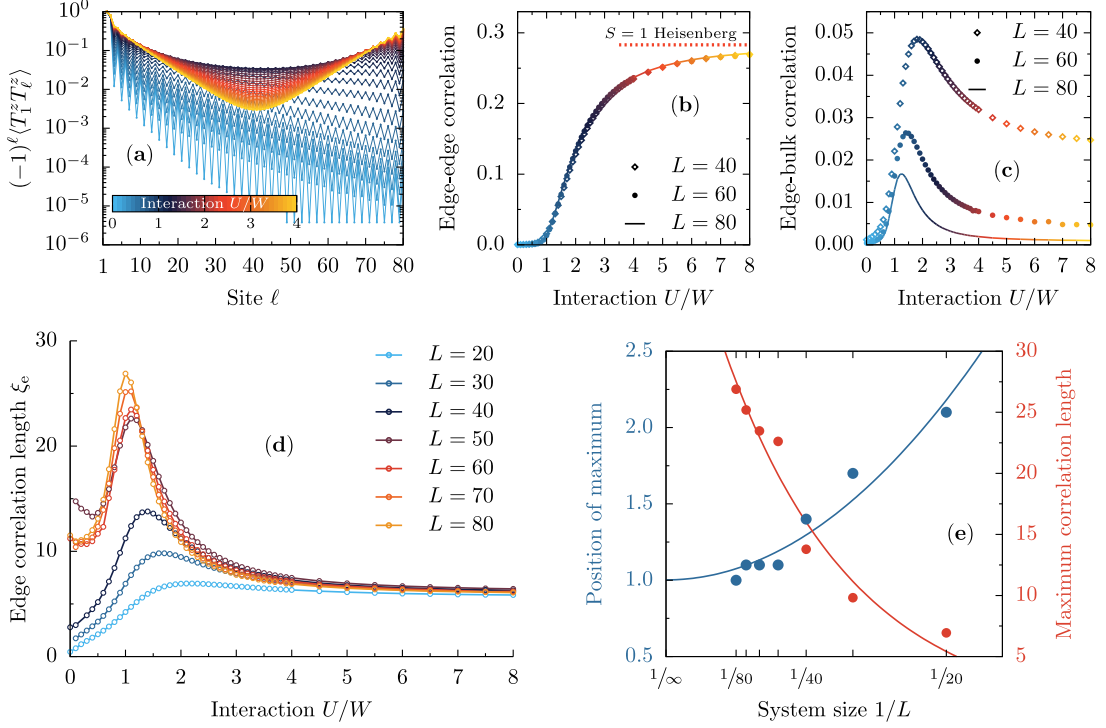


Supplementary Figure S1. **Spin gaps.** Finite-size scaling of $\Delta S = 2$ excitations (magnon gaps) for $J_H/U = 0.05, 0.10, \dots, 0.40$ and $L \in \{10, 20, \dots, 100\}$. Line color-code represents the value of interaction U . All data in units of spin exchange $J = 2t^2/(U + J_H)$. The saturation to the finite value (to the Haldane gap $\Delta_S/J \simeq 0.41$) is clearly visible in all panels.

STATIC AND DYNAMIC SPIN CORRELATIONS.

In the main text, we have described how the dynamical spin-spin correlation, i.e., the non-local Green's function $\langle\langle T_1^z T_\ell^z \rangle\rangle_{\omega=0}$, behave vs. distance ℓ and strength of the interaction U . Here, we present additional results for the static spin correlations, $\langle T_1^z T_\ell^z \rangle = \langle \text{gs} | T_1^z T_\ell^z | \text{gs} \rangle$.

In Fig. S2, we present the analysis of the static $\langle T_1^z T_\ell^z \rangle$, similar to the one presented in Fig. 3 of the main text. As evident from panels (a-d), the overall behaviour of $\langle T_1^z T_\ell^z \rangle$ is almost identical to the zero-frequency $\omega = 0$ data. The main difference between the static and the dynamic correlation function can be observed in the extracted edge correlation length ξ_e close to the transition $U \sim U_c$ [compare Fig. 3C of the main text and Fig. S2(d)]. I.e., the edge correlation length extracted from $\langle\langle T_1^z T_\ell^z \rangle\rangle_{\omega=0}$ data is much sharper than the one extracted from the static $\langle T_1^z T_\ell^z \rangle$.



Supplementary Figure S2. **Static spin correlations.** (a) Distance ℓ dependence of static spin-spin correlations $(-1)^\ell \langle T_1^z T_\ell^z \rangle$ for various values of interaction U (denoted by color code). The results are normalized by the $\ell = 1$ value of the correlation function. (b) Edge-edge $|\langle T_1^z T_{L/2}^z \rangle|$ and (c) edge-bulk $|\langle T_1^z T_{L/2}^z \rangle|$ spin correlations vs. interaction strength U/W . At U_c , one observes the appearance of finite edge-edge correlations, saturating at $U \gg W$ to the value given by the $S = 1$ Heisenberg model (red dashed line). (d) Edge correlation length ξ_e vs. interaction U strength, extracted from $(-1)^\ell \langle T_1^z T_\ell^z \rangle = a \exp(-\ell/\xi_e)$ for $\ell < L/2$. (e) System-size dependence of the position of (blue points, left y-axis) and the value (red points, right y-axis) of the maximum edge correlation length. All data calculated for $J_H/U = 0.25$.

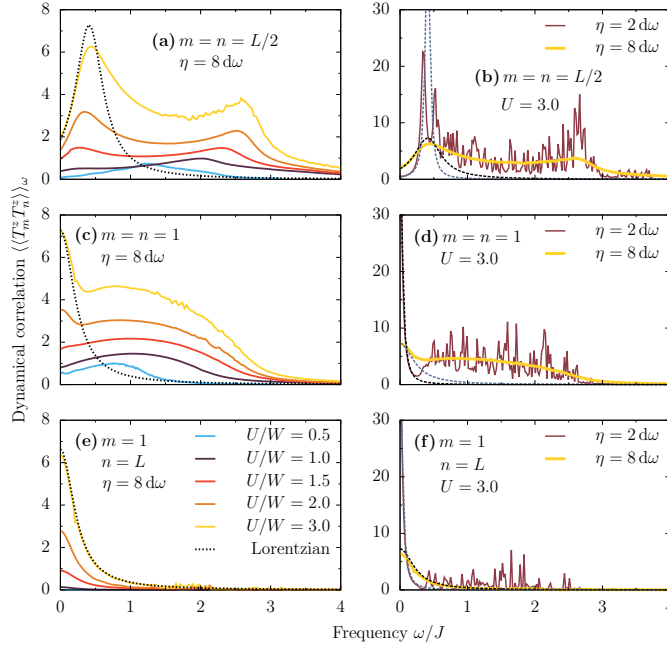
Nevertheless, the scaling with the system size [see Fig. S2(e)] of the position of the maximum of ξ_e as well as the value itself indicate a transition at U_c .

To understand the difference between static and dynamic results, consider the sum rule relating (at zero temperature) both of these quantities, i.e.,

$$\langle T_m^z T_n^z \rangle = \int_0^\infty d\omega \langle \langle T_m^z T_n^z \rangle \rangle_\omega. \quad (\text{S3})$$

It is evident that both approaches would yield the same behaviour if $\langle \langle T_m^z T_n^z \rangle \rangle_\omega = \delta(\omega)$. However, our analysis presented in Fig. S3 indicates that the behaviour of the non-local Green's function $\langle \langle T_m^z T_n^z \rangle \rangle_\omega$ strongly depends on the pair of sites (m, n) considered. Note that, in the presented analysis, we have used finite broadening η [see Eq. (S2)]. Consequently, all sharp features of the spectrum are broadened by a Lorentzian.

Within the fermionic Haldane phase, $U > U_c$, the spectrum of the bulk of the system, $m \sim n \sim L/2$, has only the incoherent part $\omega > 0$, and it is gapped; see Fig. S3(a,b). Such behaviour is expected because (m, n) elements contribute (via the Fourier transform) to the overall dispersion relation presented in Fig. 1 of the main text. On the other hand, the correlation between the edge $m = 1$ and the rest of the system needs more attention: (i) consistent with the phenomenology of zero-energy edge modes, the edge-edge $(m, n) = (1, L)$ dynamical correlations contain only the $\omega = 0$ δ -function (broaden by the Lorentzian in our numerical investigation), see Fig. S3(c,d). Consequently



Supplementary Figure S3. **Dynamical spin correlations** $\langle\langle T_m^z T_n^z \rangle\rangle_\omega$. Shown are the frequency ω dependence of the local Green's function in (a,b) the bulk of the system $m = n = L/2$ and in (b,c) at the edge $m = n = 1$. (d,e) The non-local Green function between edges of the system ($m = 1, n = L$). In all plots, color solid curves represent data for various values of interaction $U/W = 0.5, 1.0, \dots, 3.0$, $J_H/U = 0.25$, and $\eta = 8d\omega$ (left column) and $\eta = 2d\omega$ (right column). The dashed line represents the Lorentzian.

$\langle T_1^z T_\ell^z \rangle \simeq \langle\langle T_1^z T_\ell^z \rangle\rangle_{\omega=0}$. (ii) Edge-bulk correlation ($1, \sim L/2$) vanishes, again, consistent with the presence of the edge states (not shown). (iii) However, in the proximity of the edges (for $m \sim n \sim 1$), the dynamical correlations contain both coherent $\omega \sim 0$ (edge mode) and incoherent $\omega > 0$ parts [see Fig. S3(e,f)], and $\langle T_1^z T_{m \sim 1}^z \rangle \neq \langle\langle T_1^z T_{m \sim 1}^z \rangle\rangle_{\omega=0}$.

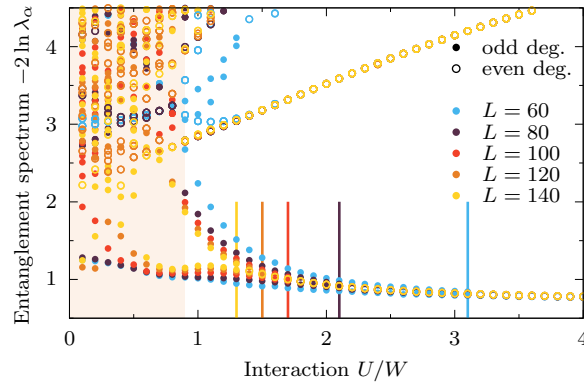
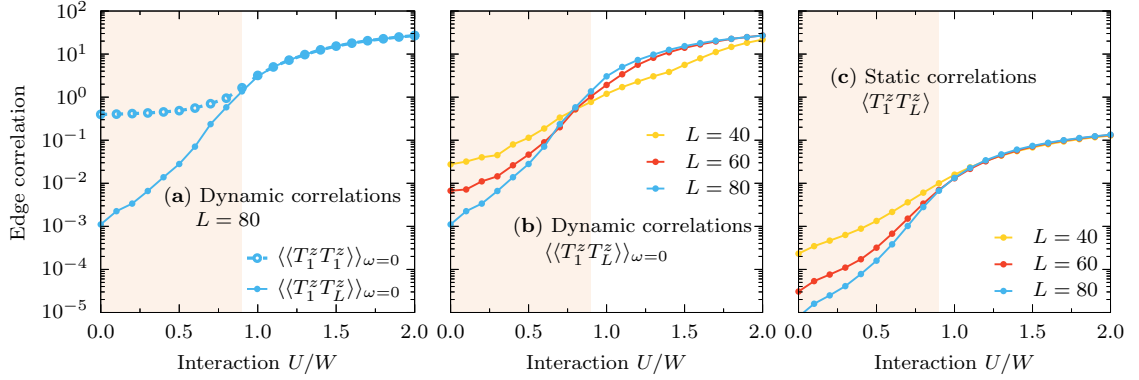
Finally, in Fig. S4, we present additional evidence for the topological phase transition at $U = U_c \simeq 0.9W$ (for $J_H/U = 0.25$) from spin correlation data.

(1) In panel (a), we compare the local Green's function $n = m = 1$ and non-local edge-edge correlations $n = 1, m = L$ at zero-frequency $\omega = 0$. The change in the local value is related to the development of the magnetic moment \mathcal{S} . On the other hand, the non-local (edge-edge) probes only the appearance of edge zero-modes (as discussed in the main text). It is evident from the presented results that both quantities merge at $U = U_c$, consistent with the presence of the zero frequency edge modes for $U > U_c$.

(2) In panels (b) and (c), we present the same data as in Fig. 3B of the main text and Fig. S2(b), respectively, in a log- y scale. Evidently, for $U > U_c$, the non-zero correlation functions do not originate from finite-size effects. On the other hand, for $U < U_c$, the values of edge-edge correlations (both static and dynamic) decay exponentially with system size.

ENTANGLEMENT SPECTRUM.

Figure S5 depicts additional results for the entanglement spectrum $-2 \ln \lambda_\alpha$. Consistent with the discussion presented in the main text, the value of the interaction U for which the spectrum is evenly degenerate moves to U_c with increasing system size L (see also Fig. 4 of the main text). Furthermore, it is evident from the presented results that the λ_α spectrum does not contain any apparent structure for $U < U_c$, and the condition [i.e., $\ln \lambda_{i+1} - \ln \lambda_i \leq 0.01$] of evenly degenerate entanglement spectrum is not fulfilled.



Supplementary Figure S5. **Entanglement entropy spectrum.** Interaction U/W dependence of the entanglement spectrum $-2 \ln \lambda_\alpha$, obtained for $J_H/U = 0.25$ and $L = 60, 80, \dots, 140$ site systems divided in half. The vertical lines depict the value of interaction at which the lowest 50 eigenvalues λ_α are evenly degenerate. The shaded region depicts the topologically trivial phase.

HUND BANDS IN SPECTRA OF MULTIORBITAL SYSTEMS

The investigation of Majorana modes two chapters ago, in Chap. 4, focused on studying the spectral functions near the Fermi level. However, a closer examination of the higher energy spectrum unveils an unexpected feature—an additional dispersive band that emerges alongside the well-known Hubbard bands. This particular band had been underestimated in the existing literature, thus prompting further investigation. The work [O4] presented in this chapter is devoted to a detailed exploration of this finding.

The most important result here is recognizing that this additional band, henceforth called *Hund band*, is a generic spectral feature of multiorbital systems that occurs at energies given only by the Hund's coupling J_H . This is markedly different from the Hubbard satellites, which also follow the interaction U . To establish this conclusion, I conducted extensive calculations of spectral functions using the density-matrix renormalization group method for two multiorbital models: the generalized Kondo-Heisenberg model and the three-orbital Hubbard model. Through this analysis, it became evident that the Hund bands emerge whenever the single-particle removal or addition processes arrive at higher multiplets of the dominant valence subspace. This is possible provided that the following conditions are met: (i) the higher multiplets exist, (ii) these multiplets are allowed by the selection rules for particle addition or removal, and (iii) the charge fluctuations are substantial. All of these prerequisites are satisfied in what are commonly referred to as Hund's metals (see below). Furthermore, it should be noted that the emergence of Hund bands does not depend on the presence of the orbital-selective Mott phase, nor on the system's dimensionality. This is supported by the dynamical mean-field theory results for an orbitally-symmetric model in infinite-dimensional and quasi-two-dimensional settings. Hence, the findings of the present chapter go beyond the context of the 123 ladders, but should apply to any multiorbital system with appreciable Hund coupling. Accordingly, the simpler chain geometry is preferred here in the density-matrix renormalization group calculations. To assist the reader, a concise discussion on Hund's metals and related concepts will follow.

The presence of sizable Hund's coupling in multiorbital models gives rise to a new perspective on strong correlations. Within this context, significant attention has been devoted to studying the *Hund's metals* (see, e.g., [165,168] for reviews), a term introduced in [167]. Roughly speaking, a Hund's metal is a correlated (bad) metallic state induced by substantial Hund's coupling J_H at a moderate Coulomb interaction U , characterized by strong correlation effects but not in immediate proximity to a Mott insulator. This state was argued to be relevant for various materials, e.g., ruthenates [165,278–281] and, particularly, the iron-based systems [165,168]. Despite its importance, a precise definition of the Hund's metal has proven to be elusive [37,168].

One approach to more precisely define the Hund's metals is phenomenological in nature and points to the specific features that arise consistently in realistic simulations and in experimental data [168]. The three crucial features are: (i) enhanced electron correlations and masses, (ii) the prevalence of high-spin atomic multiplets leading to large local magnetic moments, and (iii) orbital selectivity. These characteristics become more prominent as the system undergoes a crossover from a “normal” metal to the Hund's metal, which occurs with an increase in the strength of the interaction or the proximity to half-filling [168]. Moreover, these features are quite robust and general as they arise from local many-body physics, making the details of the bare band structure less important [168]. Note that if the orbital selectivity is enhanced via a significant lifting of the orbital symmetry, the orbital-selective Mott phase (see Sec. 2.6) may emerge from the Hund's metal [282].

The alternative characterization of the Hund's metal aims to zoom in on its microscopic origin [283–285]. It is motivated by the unexpected observation that, at any integer filling different from half filling, a finite J_H actually increases the critical U necessary for Mott localization. This is peculiar as one would naturally expect that both these interactions restrict the motion of electrons. The persistence of the metallic solution can be attributed to the competition between two incompatible insulator states: the conventional Mott insulator ($U \gg J_H$) and the Hund's insulator ($J_H \gg U$) [283]. While the former wants to minimize double occupancies, the latter favors predominantly high-spin local configurations. Consider, for example, a three-orbital system. When there are three electrons in three orbitals per site (half filling), both requirements are satisfied by a uniform charge distribution, such as $|\dots, \uparrow\uparrow\uparrow, \uparrow\uparrow\uparrow, \uparrow\uparrow\uparrow, \dots\rangle$. This configuration simultaneously minimizes double occupancies and maximizes the on-site magnetic moment, $S = 3/2$. However, for two electrons in three orbitals¹, the Mott insulator still favors a uniform charge distribution $|\dots, \uparrow\uparrow, \uparrow\uparrow, \uparrow\uparrow, \dots\rangle$, while the Hund's insulator seeks to maintain $S = 3/2$ by distributing the charge as $|\dots, \uparrow\uparrow\uparrow, 0, \uparrow\uparrow\uparrow, \dots\rangle$. When these two insulating solutions are nearly degenerate, large fluctuations between the atomic configurations characterizing each state result in persistent metallicity, giving rise to the Hund's metal behavior. In the case of the Kanamori interaction (Sec. 2.5.1), this occurs around the experimentally relevant ratio $J_H/U \simeq 1/3$ [283].

In the context of the original findings presented in this chapter, the relevance of Hund's metals lies precisely in the significant charge fluctuations associated with them. These charge fluctuations are the culprit behind the possibility of the U -independent excitations, as the reader shall learn below.

¹Analogous situation should occur for any integer filling away from half filling.

Hund bands in spectra of multiorbital systems

M. Środa,¹ J. Mravlje,² G. Alvarez,³ E. Dagotto,^{4,5} and J. Herbrych¹

¹*Institute of Theoretical Physics, Faculty of Fundamental Problems of Technology,
Wrocław University of Science and Technology, 50-370 Wrocław, Poland*

²*Jožef Stefan Institute, SI-1000 Ljubljana, Slovenia*

³*Computational Sciences and Engineering Division, Oak Ridge National Laboratory, Oak Ridge, Tennessee 37831, USA*

⁴*Department of Physics and Astronomy, University of Tennessee, Knoxville, Tennessee 37996, USA*

⁵*Materials Science and Technology Division, Oak Ridge National Laboratory, Oak Ridge, Tennessee 37831, USA*

(Dated: June 23, 2023)

Spectroscopy experiments are routinely used to characterize the behavior of strongly correlated systems. An in-depth understanding of the different spectral features is thus essential. Here, we show that the spectrum of the multiorbital Hubbard model exhibits unique Hund bands that occur at energies given only by the Hund coupling J_H , as distinct from the Hubbard satellites following the interaction U . We focus on experimentally relevant single-particle and optical spectra that we calculate for a model related to iron chalcogenide ladders. The calculations are performed via the density-matrix renormalization group and Lanczos methods. The generality of the implications is verified by considering a generic multiorbital model within dynamical mean-field theory.

Introduction. Strongly correlated systems are at the heart of modern condensed matter physics. The celebrated single-band Hubbard model, describing (doped) Mott insulators, is still extensively studied in the context of Cu-based high-temperature superconductivity [1–3]. Equally exciting case is that of iron-based superconductors where the presence of several active orbitals leads to novel effects beyond the “standard” Mott physics [4–6]. A nontrivial example is the orbital-selective Mott phase (OSMP) [5, 7–10], where Mott-localized and itinerant electrons coexist.

A key probe of electronic excitations is the single-particle spectral function $A(k, \omega)$, characterizing the excitations’ dispersion. It is experimentally accessible by angle-resolved photoemission spectroscopy (ARPES) [11, 12]. To understand the origin of different spectral features, it is convenient to consider idealized models that can be studied theoretically and monitor how the signatures of correlations (e.g., the Hubbard bands) evolve with increasing Coulomb interaction U . This is especially true for quantum systems of reduced dimensionality, for which quasixact numerical methods [13, 14], or even closed analytical solutions [15], provide unbiased information on the elementary excitations. However, even in reduced dimensionality obtaining accurate results for the multiorbital Hubbard model remains challenging. The difficulty lies in the exceptionally large Hilbert space. Because of that, the spectral functions are often calculated using the dynamical mean-field theory (DMFT) [16–19]. This approach, that strictly applies at large dimensionality, avoids the finite-size limitation, but often relies on solvers in Matsubara frequencies and hence the resulting spectral functions are blurred due to analytical continuation (see Ref. [20] that discusses this and introduces a method to alleviate the problem).

In this Letter, we numerically investigate the spectral functions of several multiorbital models. Our main result is summarized in Fig. 1(a). The electronic spectrum of a single-

orbital model (without the Hund coupling $J_H \rightarrow 0$) consists of the usual upper and lower Hubbard bands (UHB and LHB, respectively) that develop with U . In multiorbital systems, the finite J_H gives rise to additional excitations. Some of these states can appear at energies between UHB and LHB that depend exclusively on J_H (i.e., are independent of U), paving the way to measure J_H directly. Since such excitations occur due to the Hund coupling and have a robust dispersion [see Fig. 1(b,c) and [21] for the full spectrum of $A(k, \omega)$], we call them *Hund bands*. We recognize that the Hund bands arise whenever single-particle removal/addition processes yield a higher multiplet of the dominant valence subspace. This can occur provided: (i) the higher multiplets exist, (ii) these multiplets are allowed by the selection rules upon adding/removing a particle, and (iii) the charge fluctuations are significant. All these requirements are met for Hund’s metals. Earlier work documented multiplet splittings in the Hubbard bands [20, 22, 23], in the fully occupied orbital [24], found additional “holon-doublon” peaks [25–30], and analyzed the energy-level structure, revealing multiplets that violate the Hund’s rules [31]. Here, we stress that charge excitations independent of U are a *generic* consequence of the multiorbital systems.

To reach these conclusions, we use the density-matrix renormalization group method (DMRG) [32–37] and Lanczos diagonalization [2, 38]. To show that our findings are generic, we study both the two- and three-orbital Hubbard model. Furthermore, we supplement our analysis with the effective model of the OSMP - the generalized Kondo-Heisenberg Hamiltonian. Finally, we confirm our findings with DMFT calculations. Our results apply to many experiments investigating the spectral properties of multiorbital materials, particularly iron-based compounds [39, 40], ruthenates [24, 41–43], iridates [44, 45], and nickel oxides [46–50].

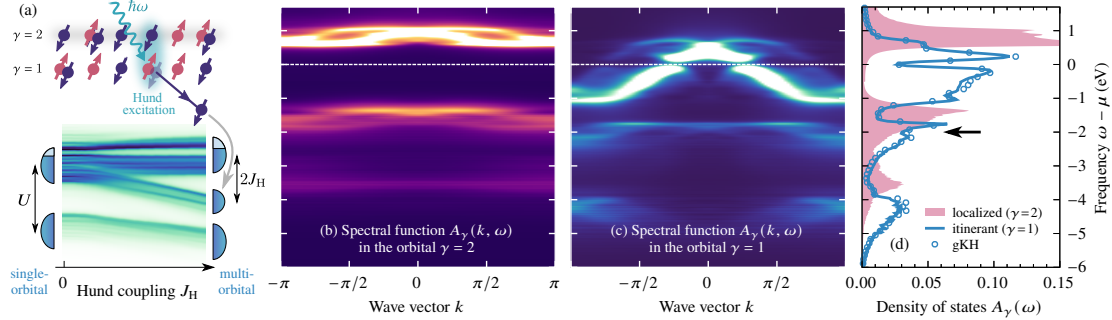


Figure 1. (a) Sketch of the Hund band accompanying the standard Hubbard bands. (b), (c) Orbital- and momentum-resolved spectral function $A_\gamma(k, \omega)$ in the two-orbital Hubbard model for $n = 2.5$, $U/W = 1.3$, $J_H/U = 0.25$, $L = 48$ sites, and orbitals (b) $\gamma = 2$ and (c) $\gamma = 1$. The horizontal line marks the chemical potential μ . (d) Orbital-resolved density-of-states $A_\gamma(\omega)$. Points depict the corresponding effective generalized Kondo-Heisenberg model (gKH); see the text for details. The arrow points at the Hund band in the itinerant orbital. Results obtained with DMRG using broadening $\eta = 0.04$.

Model. We focus on the SU(2)-symmetric multiorbital Hubbard-Kanamori chain,

$$\begin{aligned}
 H_H = & - \sum_{\gamma\gamma'\ell\sigma} t_{\gamma\gamma'} \left(c_{\gamma\ell\sigma}^\dagger c_{\gamma'\ell+1\sigma} + \text{H.c.} \right) + \sum_{\gamma\ell} \Delta_\gamma n_{\gamma\ell} \\
 & + U \sum_{\gamma\ell} n_{\gamma\ell\uparrow} n_{\gamma\ell\downarrow} + (U - 5J_H/2) \sum_{\gamma < \gamma', \ell} n_{\gamma\ell} n_{\gamma'\ell} \\
 & - 2J_H \sum_{\gamma < \gamma', \ell} \mathbf{S}_{\gamma\ell} \cdot \mathbf{S}_{\gamma'\ell} + J_H \sum_{\gamma < \gamma', \ell} \left(P_{\gamma\ell}^\dagger P_{\gamma'\ell} + \text{H.c.} \right). \quad (1)
 \end{aligned}$$

Here, $c_{\gamma\ell\sigma}^\dagger$ creates an electron with spin σ at orbital γ of site ℓ . $t_{\gamma\gamma'}$ is the symmetric hopping matrix in orbital space. Δ_γ denotes the crystal-field splitting. $n_{\gamma\ell} = \sum_\sigma n_{\gamma\ell\sigma}$ represents the total density of electrons. U is the standard repulsive Hubbard interaction. J_H is the Hund coupling between spins $\mathbf{S}_{\gamma\ell}$ at different orbitals γ . The last term $P_{\gamma\ell}^\dagger P_{\gamma'\ell}$ denotes interorbital pair hopping, $P_{\gamma\ell} = c_{\gamma\ell\uparrow} c_{\gamma\ell\downarrow}$. We assume open boundary conditions, as required by DMRG. For the two-orbital model, $\gamma \in \{1, 2\}$, we used (in eV): $t_{11} = -0.5$, $t_{22} = -0.15$, $t_{12} = t_{21} = 0$, $\Delta_1 = 0$, $\Delta_2 = 0.8$; whereas for the three-orbital model: $\gamma \in \{0, 1, 2\}$, $t_{00} = t_{11} = -0.5$, $t_{22} = -0.15$, $t_{02} = t_{12} = 0.1$, $t_{01} = 0$, $\Delta_0 = -0.1$, $\Delta_1 = 0$, $\Delta_2 = 0.8$. These values were previously used to study the iron-based ladders of 123 family [9, 10, 51–54]. The bandwidth of the two-orbital model, $W = 2.1$, is used as the energy unit [55]. All energy labels given throughout the text are independent of the J_H/U ratio.

We also study the minimal model of the OSMP: the generalized Kondo-Heisenberg model (gKH). This model was derived [10, 53, 54] to capture the static and dynamic properties of BaFe₂Se₃ iron-based ladder [56–58]. It describes interacting itinerant electrons (with spin s_i) coupled via Hund cou-

pling to the localized spins \mathbf{S}_i ,

$$\begin{aligned}
 H_K = & - t_i \sum_{\ell\sigma} \left(c_{\ell\sigma}^\dagger c_{\ell+1\sigma} + \text{H.c.} \right) + U \sum_{\ell} n_{\ell\uparrow} n_{\ell\downarrow} \\
 & + K \sum_{\ell} \mathbf{S}_{i\ell} \cdot \mathbf{S}_{i\ell+1} - 2J_H \sum_{\ell} s_{i\ell} \cdot \mathbf{S}_{i\ell}. \quad (2)
 \end{aligned}$$

For the gKH model: $t_i = -0.5$, $K = 4t_1^2/U$, $t_1 = -0.15$, matching the OSMP of our two-orbital Hubbard model [10].

Hund bands. Let us study the orbital-resolved single-particle spectral function $A_\gamma(k, \omega)$ and the density-of-states (DOS) $A_\gamma(\omega) \propto \sum_\sigma \langle \langle c_{\gamma,L/2,\sigma}^\dagger; c_{\gamma,L/2,\sigma} \rangle \rangle_\omega^h + \langle \langle c_{\gamma,L/2,\sigma}; c_{\gamma,L/2,\sigma}^\dagger \rangle \rangle_\omega^e$ [21]. Here, k is the momentum, ω the energy, and $\langle \langle \dots \rangle \rangle_\omega^{h,e}$ represent the hole and electron components.

The origin of the Hund bands can be clearly illustrated in an OSMP system. Figure 1(b)-(d) presents data for the two-orbital Hubbard model (2oH) at electron filling $n = 2.5$ and interaction $U \simeq W$. Clearly, the narrow orbital $\gamma = 2$ [Fig. 1(b)] has a gap at the Fermi level μ , while the orbital $\gamma = 1$ [Fig. 1(c)] is metallic with a finite DOS at μ . This behavior is consistent with the OSMP [10], the narrow orbital is Mott-localized with the electron density equal to 1. However, instead of two excitation bands (UHB and LHB), expected from the Mott physics, we observe a prominent three-peak structure [see also the DOS in Fig. 1(d)]. This structure is also visible in the itinerant orbital ($\gamma = 1$), Fig. 1(c), with an electron density equal to 1.5. Note that the itinerant orbital's spectrum is accurately reproduced by the effective gKH model.

Let us take a closer look at how the three-peak spectrum develops with the interaction U . Figure 2(a) shows $A_1(\omega)$ for the gKH model at noninteger filling $n = 1.5$. In the $U \rightarrow 0$ limit, we recover the noninteracting behavior: a single metallic band. However, already at $U/W \simeq 0.8$, i.e., close to the OSMP transition [9, 10], the three-peak structure is visible in

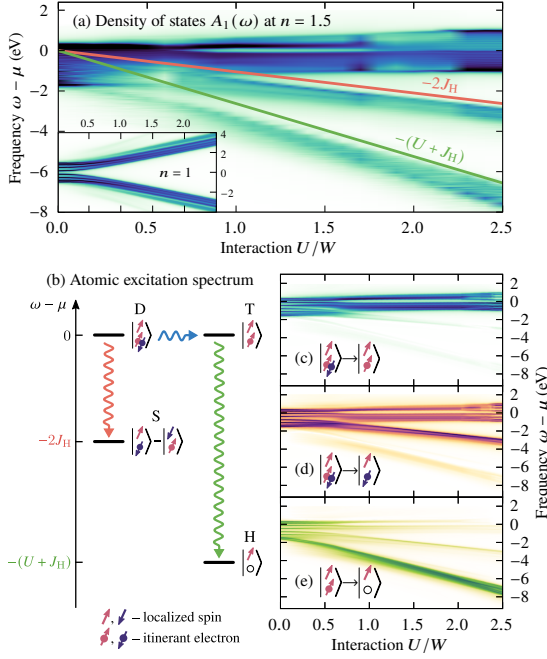


Figure 2. (a) Interaction U dependence of the itinerant orbital's density-of-states (DOS) $A_1(\omega)$ obtained for the gKH model with $L = 48$ sites, $J_H/U = 0.25$, and $n = 1.5$. Results obtained with DMRG using $\eta = 0.04$ broadening. The solid lines represent the atomic-limit transitions. Inset depicts the results for half electron filling $n = 1$. (b) Atomic excitation spectrum. For clarity, we mark only the hole-like (electron removal) excitations and show only one spin projection. D, T, S, H labels stand for doublon, triplet, singlet, and holon, respectively. (c)-(e) DOS $A_1(\omega)$ projected on the specific final configurations: (c) parallel spins, (d) antiparallel spins, and (e) on the holon; see the text for details. Results obtained with Lanczos diagonalization of $L = 8$ lattice with broadening $\eta = 0.05$.

$A_1(\omega)$, and becomes clearer the larger the interaction U becomes. Since the three-peak structure is most pronounced for $U \gg W$, it is instructive to examine the atomic limit $U, J_H \rightarrow \infty$ of the gKH model; see Fig. 2(b). The atom realizes the noninteger filling $n = 1.5$ provided the ground states (gs) of the 1- and 2-electron sectors are degenerate, which is achieved at $\mu = U + J_H/2$. Then, the gs consists of a local interorbital triplet, denoted as $|T\rangle$, which is degenerate with an itinerant doublon with localized spin, denoted as $|D\rangle$. By removing an electron from the triplet, one creates a holon in the itinerant orbital ($|T\rangle \rightarrow |H\rangle$), with the cost of energy $U + J_H$. Interestingly, from the doubly occupied state, one can remove an electron in two different ways. Depending on the spin projection of the removed electron, one can arrive at a local triplet or singlet, $|D\rangle \rightarrow |T\rangle$ or $|D\rangle \rightarrow |S\rangle$, respectively. The former is a zero-energy transition between degenerate states of the gs, while the latter costs an energy $2J_H$ as it breaks the Hund's rule. In Fig. 2(a), we plot the relevant energy scales of the

atomic limit ($U + J_H$ and $2J_H$) and find good agreement with the full many-body calculations of the gKH chain.

Projections on the atomic configurations. To make a stronger case for the atomic-limit interpretation of the three-peak spectrum, we decompose the spectral function of the full many-body calculation into individual transitions [29]. To this end, we use the projector \mathcal{P} onto specific configurations of the on-site Ising basis $|\gamma = 1, \gamma = 2\rangle$, i.e., $\langle\langle c_{\gamma,L/2,\sigma}^\dagger; \mathcal{P}c_{\gamma,L/2,\sigma} \rangle\rangle_\omega^h$ [21]. For clarity, we discuss only the hole part (below μ), as the electron part can be described analogously. Upon removing an electron from the itinerant orbital, we distinguish three contributions. (i) In Fig. 2(c), we project onto the parallel-spin configuration, $\mathcal{P} = |\uparrow, \uparrow\rangle\langle\uparrow, \uparrow| + |\downarrow, \downarrow\rangle\langle\downarrow, \downarrow|$. The resulting weight forms a band of excitations close to the Fermi level $\omega \simeq \mu$. This transition is responsible for the metallic properties of the lattice. (ii) In Fig. 2(d), we instead project onto the antiparallel configuration, $\mathcal{P} = |\uparrow, \downarrow\rangle\langle\uparrow, \downarrow| + |\downarrow, \uparrow\rangle\langle\downarrow, \uparrow|$. We observe large weight in the middle band and some smaller weight at $\omega \simeq \mu$. The middle band represents the interorbital singlet which breaks the Hund's rule: this is the $2J_H$ Hund excitation. The band at $\omega \simeq \mu$ represents the $S^z = 0$ component of the triplet ($|\uparrow, \downarrow\rangle + |\downarrow, \uparrow\rangle$), costing zero energy to excite. (iii) Finally, in Fig. 2(e), we project onto the holon configuration, $\mathcal{P} = |0, \uparrow\rangle\langle 0, \uparrow| + |0, \downarrow\rangle\langle 0, \downarrow|$. This gives the energetically lowest band of excitations, which we recognize as the LHB, arising from triplet to holon transitions. The starting state needs to be a triplet because singlets are excluded from the gs by the Hund's rule.

Noninteger vs integer filling. As shown above, for non-integer filling (doped system), the atomic limit is enough to explain the Hund bands. When the atomic gs of adjacent particle-number subspaces, say n and $n - 1$, are degenerate, there is no cost U for the transition from the gs of subspace n to the gs of subspace $n - 1$. The excitation cost is zero; it is compensated by μ which is tuned to cause the degeneracy. However, if the $n - 1$ subspace contains not only the gs but also higher multiplets, these multiplets can be accessed in the photoemission process $n \rightarrow n - 1$ with just the energy $\propto J_H$. Analogous reasoning applies to inverse transitions $n - 1 \rightarrow n$. Thus, remarkably, this results in U -independent Hund bands.

Consider now this behavior in a more general system, hosting more atomic configurations with different n . In Fig. 3 we present the three-orbital Hubbard model (3oH) results [59] for various electron fillings. For $n = 4.5$, the atomic limit of our setup [21] predicts one Hund excitation (between states with 5 and 4 electrons) with energy $2J_H$ [60], along with several U -dependent Hubbard excitations. We pinpoint the Hund band using the projector analysis, shown in Fig. 3(b). We differentiate transitions arriving at $|\uparrow\downarrow, \uparrow, \uparrow\rangle$ and $|\uparrow\downarrow, \downarrow, \uparrow\rangle$. Similarly, for the $n = 3.5$ filling, the atomic limit implies Hund bands in photoemission at $3J_H$ and $5J_H$. They are shown in Fig. 3(c). The $3J_H$ band is a transition to a low-spin $S = 1/2$ state [\mathcal{P} onto $|\uparrow, \downarrow, \uparrow\rangle$; see Fig. 3(a)]. The $5J_H$ band originates in states of the form $|\uparrow\downarrow, 0, \uparrow\rangle \pm |0, \uparrow\downarrow, \uparrow\rangle$, where “-” is degenerate with the $3J_H$ excitation while “+” forms the $5J_H$ peak. The

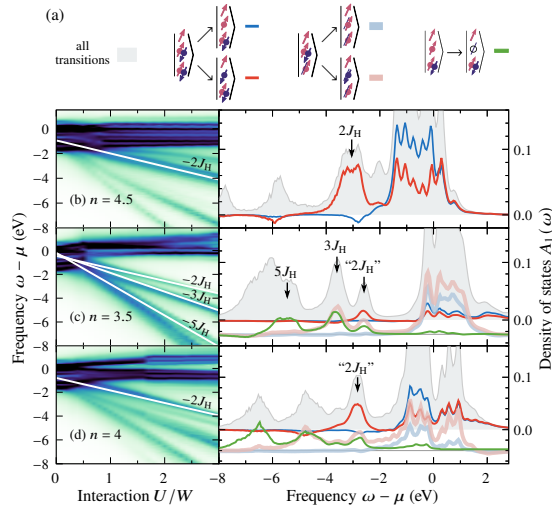


Figure 3. (a) Sketch of the transitions to final configurations that contribute to the Hund bands of the three-orbital Hubbard model (3oH). For clarity, we present only the representative configurations (while the results are summed over several configurations of the same type). The labeling of the arrows follows Fig. 2. (b)-(d) DOS $A_1(\omega)$ of the itinerant orbital ($\gamma = 1$) of 3oH with $J_H/U = 0.25$. Left panels depict $A_1(\omega)$ as function of the interaction U , while right panels show detailed spectra with projections for $U/W = 2$. (b), (c), and (d) depict results for $n = 4.5$, $n = 3.5$, and $n = 4$, respectively. The arrows on the right panels point at the Hund bands [60], with “...” denoting the peaks observable only on a lattice. The solid lines in the left column mark the $-2J_H$, $-3J_H$, and $-5J_H$ slopes. The unlabeled peaks are Hubbard bands which have a U dependence [21]. Results obtained with DMRG on an $L = 8$ lattice with broadening $\eta = 0.1$.

latter are the holon-doublon states [25–30]. Their origin was discussed in [25, 27] but without realizing they are a particular example of the generic physics of Hund bands revealed here. Surprisingly, the $2J_H$ band persists even for $n = 3.5$ (as implied by the smaller but nonvanishing weight of $|\uparrow\downarrow, \downarrow, \uparrow\rangle$), inducing a third Hund peak, absent in the atomic spectrum. The intensity of this mode decreases with U .

By contrast, for *integer* filling $n \in \{1, 2, 3, \dots\}$, the atomic limit alone does not predict the Hund bands. The atom lacks the necessary charge fluctuations as its gs does not span adjacent particle-number subspaces. Thus, only the “standard” Hubbard bands should be observed [5, 61]. However, in the lattice, the charge fluctuations are possible provided the interaction U is not too large at a given filling n . For half filling, the fluctuations vanish already for $U \sim W$ and the Hubbard bands are well developed [see, e.g., the inset of Fig. 2(a)]. Away from half filling, $U \sim W$ does not suppress the fluctuations. They are significant even at integer n , and vanish only at elevated $U \sim 10W$ [5, 52, 62]. Consequently, the many-body gs has significant contribution of states with neighboring local occupations, $|n-1\rangle$ and $|n+1\rangle$. Adding/removing

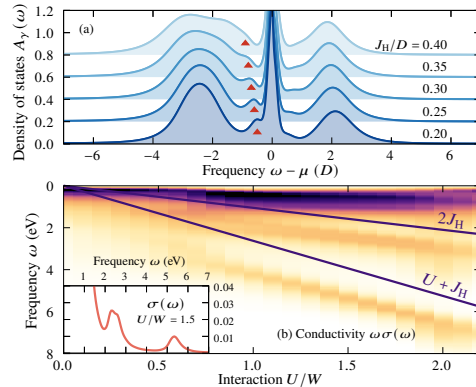


Figure 4. (a) $A_\gamma(\omega)$ calculated with the DMFT method for an orbitally degenerate three-orbital Hubbard model with semicircular DOS, integer filling $n = 4$, $U/D = 3.8$, and $J_H/D = 0.20, \dots, 0.40$. The half bandwidth $D = 1$ is used as the energy unit; see [21] for details. Triangles mark $\omega = -2J_H$ with a constant shift of -0.1 [60]. (b) Optical conductivity $\omega\sigma(\omega)$ vs. the interaction U . The lines mark the atomic-limit energy scales. Notice the $2J_H$ peak appearing for $U/W > 0.8$. Inset: data for $U/W = 1.5$. Results obtained via DMRG for the gKH model with $n = 1.5$, $J_H/U = 0.25$, $L = 24$ sites, and broadening $\eta = 0.1$.

particles in these states allows reaching the higher multiplets of the atomic ground-state subspace $|n\rangle$, and the Hund bands emerge.

Consider the $n = 4$ case, i.e., one electron above half-filling for 3oH. In the atom, the gs has only 4-electron configurations, but in the lattice we find significant on-site fluctuations to 5- and 3-electron states [4, 63]. In Fig. 3(d), we project onto the same configurations as for $n = 4.5$ and again find the $2J_H$ Hund band (originating in the $n = 5 \rightarrow 4$ transitions). We should notice only half of the peak is exhausted by the projection onto $|\uparrow\downarrow, \downarrow, \uparrow\rangle$ and our results also indicate a weak U dependence. We could not discern Hund bands corresponding to electron addition processes from 3-electron states: For a high-spin initial configuration $n = 3$, $S = 3/2$ the selection rules forbid reaching the low-spin $n = 4$, $S = 0$ state [64].

Conclusions. We showed that the charge fluctuations and finite Hund exchange present in the multiorbital Hubbard model cause the formation of unique bands of excitations. These Hund bands are formed by the energetically costly low-angular-momentum states (i.e., on-site configurations which break the Hund’s rules) and they do not depend on Hubbard U . The latter makes them distinct from the Hubbard-band multiplet splittings. Among the Hund bands the canonical spin-singlet mode ($\omega \simeq 2J_H$) is especially prevalent.

Our results are a generic consequence of multiorbital systems. They originate in the existence of higher multiplets, hence they do not depend on the presence of the orbital-selective Mott phase (see [21] for additional discussion), nor on the system’s dimensionality. To confirm this, in Fig. 4(a), we present DMFT calculations in infinite dimensions. We

focus on generic rather than material-specific features and consider a semicircular density of states and orbital degeneracy [21]. The DMFT results clearly show the $2J_H$ mode. In Supplemental Material [21], we repeat the calculations for a typical t_{2g} DOS and also find the Hund band.

Our findings are relevant for ARPES, resonant inelastic x-ray scattering [65], Raman spectroscopy [66, 67], nonequilibrium investigations [68–70], and reflectivity/transmission measurements [71–74]. Figure 4(b) demonstrates the last: it presents how the optical conductivity [21] evolves with U for the gKH model at $n = 1.5$. Crucially, we observe the Hund band at $\omega \simeq 2J_H$. Often, such additional spectral features are attributed to the interband transitions. Here, we showed that additional modes can also originate in the Hund exchange and, consequently, can be used to estimate the value of J_H .

M.Ś. and J.H. acknowledge grant support by the Polish National Agency of Academic Exchange (NAWA) under contract PPN/PPO/2018/1/00035 and by the National Science Centre (NCN), Poland via project 2019/35/B/ST3/01207. J.M. acknowledges support by Slovenian research agency under Program No. P1-0044, J1-2458, J1-2456, J1-2463. G.A. was supported in part by the Scientific Discovery through Advanced Computing (SciDAC) program funded by the U.S. DOE, Office of Science, Advanced Scientific Computing Research and BES, Division of Materials Sciences and Engineering. E.D. was supported by the US Department of Energy, Office of Science, Basic Energy Sciences, Materials Sciences and Engineering Division. Part of the calculations has been carried out using resources provided by Wroclaw Centre for Networking and Supercomputing (<http://wcss.pl>).

- [1] D. J. Scalapino, “A common thread: The pairing interaction for unconventional superconductors,” *Rev. Mod. Phys.* **84**, 1383 (2012).
- [2] E. Dagotto, “Correlated electrons in high-temperature superconductors,” *Rev. Mod. Phys.* **66**, 763 (1994).
- [3] S. M. O’Mahony, W. Ren, W. Chen, Y. X. Chong, X. Liu, H. Eisaki, S. Uchida, M. H. Hamidian, and J. C. S. Davis, “On the electron pairing mechanism of copper-oxide high temperature superconductivity,” *Proc. Natl. Acad. Sci. U.S.A.* **119**, e2207449119 (2022).
- [4] Z. Yin, K. Haule, and G. Kotliar, “Kinetic frustration and the nature of the magnetic and paramagnetic states in iron pnictides and iron chalcogenides,” *Nat. Matter.* **10**, 932 (2011).
- [5] A. Georges, L. Medici, and J. Mravlje, “Strong Correlations from Hund’s Coupling,” *Annu. Rev. Condens. Matter Phys.* **4**, 137 (2013).
- [6] M. Yi, Y. Zhang, Z.-X. Shen, and D. Lu, “Role of the orbital degree of freedom in iron-based superconductors,” *npj Quantum Mater.* **2**, 57 (2017).
- [7] A. Koga, N. Kawakami, T. M. Rice, and M. Sigrist, “Orbital-Selective Mott Transitions in the Degenerate Hubbard Model,” *Phys. Rev. Lett.* **92**, 216402 (2004).
- [8] L. de’Medici, A. Georges, and S. Biermann, “Orbital-selective mott transition in multiband systems: Slave-spin representation and dynamical mean-field theory,” *Phys. Rev. B* **72**, 205124 (2005).
- [9] J. Rincón, A. Moreo, G. Alvarez, and E. Dagotto, “Exotic magnetic order in the orbital-selective mott regime of multiorbital systems,” *Phys. Rev. Lett.* **112**, 106405 (2014).
- [10] J. Herbrych, J. Heverhagen, N. D. Patel, G. Alvarez, M. Daghofer, A. Moreo, and E. Dagotto, “Novel magnetic block states in low-dimensional iron-based superconductors,” *Phys. Rev. Lett.* **123**, 027203 (2019).
- [11] A. Damascelli, Z. Hussain, and Z.-X. Shen, “Angle-resolved photoemission studies of the cuprate superconductors,” *Rev. Mod. Phys.* **75**, 473 (2003).
- [12] Y. Wang, Y. He, K. Wohlfeld, M. Hashimoto, E. W. Huang, D. Lu, S.-K. Mo, S. Komiya, C. Jia, B. Moritz, Z.-X. Shen, and T. P. Devereaux, “Emergence of quasiparticles in a doped Mott insulator,” *Commun. Phys.* **3**, 210 (2020).
- [13] H. Benthien, F. Gebhard, and E. Jeckelmann, “Spectral function of the one-dimensional hubbard model away from half filling,” *Phys. Rev. Lett.* **92**, 256401 (2004).
- [14] A. E. Feiguin and G. A. Fiete, “Spin-incoherent behavior in the ground state of strongly correlated systems,” *Phys. Rev. Lett.* **106**, 146401 (2011).
- [15] F. Essler, H. Frahm, F. Göhmann, A. Klümper, and V. E. Korepin, *The One-Dimensional Hubbard Model* (Cambridge University Press, Cambridge, England, 2010).
- [16] A. Georges, G. Kotliar, W. Krauth, and M. J. Rozenberg, “Dynamical mean-field theory of strongly correlated fermion systems and the limit of infinite dimensions,” *Rev. Mod. Phys.* **68**, 13 (1996).
- [17] E. Jakobi, N. Blümer, and P. van Dongen, “Orbital-selective mott transitions in a doped two-band hubbard model with crystal field splitting,” *Phys. Rev. B* **87**, 205135 (2013).
- [18] A. van Roekeghem, P. Richard, H. Ding, and S. Biermann, “Spectral properties of transition metal pnictides and chalcogenides: Angle-resolved photoemission spectroscopy and dynamical mean-field theory,” *C. R. Phys.* **17**, 140 (2016).
- [19] A. Tamai, M. Zingl, E. Rozbicki, E. Cappelli, S. Riccò, A. de la Torre, S. McKeown Walker, F. Y. Bruno, P. D. C. King, W. Meevasana, M. Shi, M. Radović, N. C. Plumb, A. S. Gibbs, A. P. Mackenzie, C. Berthod, H. U. R. Strand, M. Kim, A. Georges, and F. Baumberger, “High-resolution photoemission on Sr_2RuO_4 reveals correlation-enhanced effective spin-orbit coupling and dominantly local self-energies,” *Phys. Rev. X* **9**, 021048 (2019).
- [20] D. Bauernfeind, M. Zingl, R. Triebl, M. Aichhorn, and H. G. Evertz, “Fork tensor-product states: Efficient multiorbital real-time dmft solver,” *Phys. Rev. X* **7**, 031013 (2017).
- [21] See Supplemental Material for: (1) Refs. [75–83], not cited in the main text, (2) definition of the single-particle spectral function, (3) three-orbital results for the momentum dependence of the spectral function, (4) two- and three-orbital results for fixed J_H (showing that Hund bands are U independent whereas Hubbard bands are not), (5) derivation of the atomic-limit energies for the three-orbital model, (6) Hund bands in an orbitally degenerate three-orbital system, (7) Hund bands for orbital-dependent interactions, (8) details of the DMFT calculations, (9) DMFT calculations for a realistic t_{2g} density of states, and (10) definition of the optical conductivity $\sigma(\omega)$.
- [22] K. Hallberg, D. J. García, Pablo S. Cornaglia, Jorge I. Facio, and Y. Núñez-Fernández, “State-of-the-art techniques for calculating spectral functions in models for correlated materials,” *Europhysics Letters (EPL)* **112**, 17001 (2015).
- [23] K.M. Stadler, G. Kotliar, A. Weichselbaum, and J. von Delft, “Hundness versus Mottness in a three-band Hubbard–Hund model: On the origin of strong correlations in Hund metals,”

- Ann. Phys.* **405**, 365 (2019).
- [24] D. Sutter, C. G. Fatuzzo, S. Moser, M. Kim, R. Fittipaldi, A. Vecchione, V. Granata, Y. Sassa, F. Cossalter, G. Gatti, M. Grioni, H. M. Rønnow, N. C. Plumb, C. E. Matt, M. Shi, M. Hoesch, T. K. Kim, T-R Chang, H-T Jeng, C. Jozwiak, A. Bostwick, E. Rotenberg, A. Georges, T. Neupert, and J. Chang, “Hallmarks of Hund’s coupling in the Mott insulator Ca_2RuO_4 ,” *Nat. Commun.* **8**, 15176 (2017).
- [25] Y. Núñez Fernández, G. Kotliar, and K. Hallberg, “Emergent low-energy bound states in the two-orbital Hubbard model,” *Phys. Rev. B* **97**, 121113(R) (2018).
- [26] Y. Niu, J. Sun, Y. Ni, J. Liu, Y. Song, and S. Feng, “Doublon-holon excitations split by Hund’s rule coupling within the orbital-selective Mott phase,” *Phys. Rev. B* **100**, 075158 (2019).
- [27] F. B. Kugler, Seung-Sup B. Lee, A. Weichselbaum, G. Kotliar, and J. von Delft, “Orbital differentiation in Hund metals,” *Phys. Rev. B* **100**, 115159 (2019).
- [28] Y. Komijani, K. Hallberg, and G. Kotliar, “Renormalized dispersing multiplets in the spectrum of nearly mott localized systems,” *Phys. Rev. B* **99**, 125150 (2019).
- [29] K. Hallberg and Y. Núñez-Fernández, “Subbands in the doped two-orbital kanamori-hubbard model,” *Phys. Rev. B* **102**, 245138 (2020).
- [30] N. Aucar Boidi, H. Fernández García, Y. Núñez Fernández, and K. Hallberg, “In-gap band in the one-dimensional two-orbital Kanamori-Hubbard model with interorbital Coulomb interaction,” *Phys. Rev. Research* **3**, 043213 (2021).
- [31] A. Richaud, M. Ferraretto, and M. Capone, “Interaction-resistant metals in multicomponent fermi systems,” *Phys. Rev. B* **103**, 205132 (2021).
- [32] S. R. White, “Density matrix formulation for quantum renormalization groups,” *Phys. Rev. Lett.* **69**, 2863 (1992).
- [33] U. Schollwöck, “The density-matrix renormalization group,” *Rev. Mod. Phys.* **77**, 259 (2005).
- [34] S. R. White, “Density matrix renormalization group algorithms with a single center site,” *Phys. Rev. B* **72**, 180403(R) (2005).
- [35] G. Alvarez, “The density matrix renormalization group for strongly correlated electron systems: A generic implementation,” *Comput. Phys. Commun.* **180**, 1572 (2009).
- [36] A. Nocera and G. Alvarez, “Spectral functions with the density matrix renormalization group: Krylov-space approach for correction vectors,” *Phys. Rev. E* **94**, 053308 (2016).
- [37] We use the DMRG++ computer program developed at Oak Ridge National Laboratory (see <https://github.io/dmrgPlusPlus>). We run DMRG within the single-center site approach and keep up to $M = 1200$ states during ~ 11 finite-size sweeps. The truncation error for the ground state is $\lesssim 10^{-6}$. The spectral functions are calculated directly in frequency space using the Krylov-space approach for correction vectors. For the calculation of the optical conductivity $\sigma(\omega)$, we use up to $M = 2000$ states during 15 sweeps.
- [38] P. Prelovšek and J. Bonča, “Ground state and finite temperature lanczos methods,” in *Strongly Correlated Systems - Numerical Methods*, edited by A. Avella and F. Mancini (Springer, Berlin, 2013).
- [39] M. D. Watson, S. Backes, A. A. Haghighirad, M. Hoesch, Timur K. Kim, A. I. Coldea, and R. Valentí, “Formation of Hubbard-like bands as a fingerprint of strong electron-electron interactions in FeSe ,” *Phys. Rev. B* **95**, 081106(R) (2017).
- [40] D. V. Evtushinsky, M. Aichhorn, Y. Sassa, Z.-H. Liu, J. Maletz, T. Wolf, A. N. Yaresko, S. Biermann, S. V. Borisenko, and B. Büchner, “Direct observation of dispersive lower Hubbard band in iron-based superconductor FeSe ,” [arXiv:1612.02313](https://arxiv.org/abs/1612.02313).
- [41] T. Hotta and E. Dagotto, “Prediction of orbital ordering in single-layered ruthenates,” *Phys. Rev. Lett.* **88**, 017201 (2001).
- [42] D. Sutter, M. Kim, C. E. Matt, M. Horio, R. Fittipaldi, A. Vecchione, V. Granata, K. Hauser, Y. Sassa, G. Gatti, M. Grioni, M. Hoesch, T. K. Kim, E. Rienks, N. C. Plumb, M. Shi, T. Neupert, A. Georges, and J. Chang, “Orbitally selective breakdown of Fermi liquid quasiparticles in $\text{Ca}_{1.8}\text{Sr}_{0.2}\text{RuO}_4$,” *Phys. Rev. B* **99**, 121115(R) (2019).
- [43] H. Gretarsson, H. Suzuki, Hoon Kim, K. Ueda, M. Krautloher, B. J. Kim, H. Yavaş, G. Khaliullin, and B. Keimer, “Observation of spin-orbit excitations and Hund’s multiplets in Ca_2RuO_4 ,” *Phys. Rev. B* **100**, 045123 (2019).
- [44] B. Yuan, J. P. Clancy, A. M. Cook, C. M. Thompson, J. Greedan, G. Cao, B. C. Jeon, T. W. Noh, M. H. Upton, D. Casa, T. Gog, A. Paramekanti, and Young-June Kim, “Determination of Hund’s coupling in $5d$ oxides using resonant inelastic x-ray scattering,” *Phys. Rev. B* **95**, 235114 (2017).
- [45] E. M. Pärshcke and R. Ray, “Influence of the multiplet structure on the photoemission spectra of spin-orbit driven Mott insulators: Application to Sr_2IrO_4 ,” *Phys. Rev. B* **98**, 064422 (2018).
- [46] V. I. Anisimov, D. Bukhvalov, and T. M. Rice, “Electronic structure of possible nickelate analogs to the cuprates,” *Phys. Rev. B* **59**, 7901 (1999).
- [47] J. Zhang, A. S. Botana, J. W. Freeland, D. Phelan, H. Zheng, V. Pardo, M. R. Norman, and J. F. Mitchell, “Large orbital polarization in a metallic square-planar nickelate,” *Nat. Phys.* **13**, 864 (2017).
- [48] D. Li, K. Lee, B. Y. Wang, M. Osada, S. Crossley, H. R. Lee, Y. Cui, Y. Hikita, and H. Y. Hwang, “Superconductivity in an infinite-layer nickelate,” *Nature* **572**, 624 (2019).
- [49] X. Wan, V. Ivanov, G. Resta, I. Leonov, and S. Y. Savrasov, “Exchange interactions and sensitivity of the Ni two-hole spin state to Hund’s coupling in doped NdNiO_2 ,” *Phys. Rev. B* **103**, 075123 (2021).
- [50] Q. Gu, and H.-H. Wen, “Superconductivity in nickel-based 112 systems,” *Innovation* **3**, 100202 (2021).
- [51] J. Herbrych, N. Kaushal, A. Nocera, G. Alvarez, A. Moreo, and E. Dagotto, “Spin dynamics of the block orbital-selective mott phase,” *Nat. Commun.* **9**, 3736 (2018).
- [52] J. Rincón, A. Moreo, G. Alvarez, and E. Dagotto, “Quantum phase transition between orbital-selective Mott states in Hund’s metals,” *Phys. Rev. B* **90**, 241105(R) (2014).
- [53] M. Środa, E. Dagotto, and J. Herbrych, “Quantum magnetism of iron-based ladders: Blocks, spirals, and spin flux,” *Phys. Rev. B* **104**, 045128 (2021).
- [54] J. Herbrych, G. Alvarez, A. Moreo, and E. Dagotto, “Block orbital-selective mott insulators: A spin excitation analysis,” *Phys. Rev. B* **102**, 115134 (2020).
- [55] For the three-orbital model, the actual kinetic-energy span equals 2.45 eV. However, we use $W = 2.1$ eV as the energy unit. This facilitates easier comparison with other models.
- [56] M. Mourigal, S. Wu, M. B. Stone, J. R. Neilson, J. M. Caron, T. M. McQueen, and C. L. Broholm, “Block Magnetic Excitations in the Orbitally Selective Mott Insulator BaFe_2Se_3 ,” *Phys. Rev. Lett.* **115**, 047401 (2015).
- [57] Y. Nambu, K. Ohgushi, S. Suzuki, F. Du, M. Avdeev, Y. Uwatoko, K. Munakata, H. Fukazawa, S. Chi, Y. Ueda, and T. J. Sato, “Block magnetism coupled with local distortion in the iron-based spin-ladder compound BaFe_2Se_3 ,” *Phys. Rev. B* **85**, 064413 (2012).
- [58] S. Wu, J. Yin, T. Smart, A. Acharya, C. L. Bull, N. P. Funnell, T. R. Forrest, G. Simutis, R. Khasanov, S. K. Lewin, M. Wang, B. A. Frandsen, R. Jeanloz, and R. J. Birgeneau, “Robust block magnetism in the spin ladder compound BaFe_2Se_3 under hydrostatic pressure,” *Phys. Rev. B* **100**, 214511 (2019).

- [59] For our parameters, the three-orbital model is in the OSMP (with $\gamma = 2$ localized) for $U/W \gtrsim 0.9$.
- [60] We mark each Hund band by its J_H dependence. The J_H dependence agrees between the lattice and the atom very well, even though the exact values of the excitation energies may differ. Such a situation is clearly observed in Fig. 2(a). In subsequent figures, we often shift the atomic energy scales by a constant so as to match the evolution of the lattice peaks.
- [61] L. de' Medici, J. Mravlje, and A. Georges, "Janus-faced influence of Hund's rule coupling in strongly correlated materials," *Phys. Rev. Lett.* **107**, 256401 (2011).
- [62] K. Haule and G. Kotliar, "Coherence-incoherence crossover in the normal state of iron oxypnictides and importance of Hund's rule coupling," *New J. Phys.* **11**, 025021 (2009).
- [63] J. Karp, M. Bramberger, M. Grundner, U. Schollwöck, A. J. Millis, and M. Zingl, "Sr₂MoO₄ and Sr₂RuO₄: Disentangling the Roles of Hund's and van Hove Physics," *Phys. Rev. Lett.* **125**, 166401 (2020).
- [64] The same selection rules apply at $n = 3.5$, where the $2J_H$ and $5J_H$ Hund bands of $n = 4$ subspace are not observed in electron addition processes (i.e., above μ).
- [65] P. Werner, S. Johnston, and M. Eckstein, "Nonequilibrium-DMFT based RIXS investigation of the two-orbital Hubbard model," *EPL* **133**, 57005 (2021).
- [66] T. Tohyama, J. Inoue, and S. Maekawa, "Raman scattering in the two-dimensional Hubbard model," *Physica B Condens. Matter* **186**, 968 (1992).
- [67] H.-Y. Lu, D. Wang, S. Chen, W. Wang, and P.-F. Gong, "Electronic Raman spectra in iron-based superconductors with two-orbital model," *Physica C Supercond.* **471**, 453 (2011).
- [68] H. U. R. Strand, D. Golež, M. Eckstein, and P. Werner, "Hund's coupling driven photocarrier relaxation in the two-band Mott insulator," *Phys. Rev. B* **96**, 165104 (2017).
- [69] F. Petocchi, S. Beck, C. Ederer, and P. Werner, "Hund excitations and the efficiency of Mott solar cells," *Phys. Rev. B* **100**, 075147 (2019).
- [70] K. Gillmeister, D. Golež, C.-T. Chiang, N. Bittner, Y. Pavlyukh, J. Berakdar, P. Werner, and W. Widdra, "Ultrafast coupled charge and spin dynamics in strongly correlated NiO," *Nat. Commun.* **11**, 4095 (2020).
- [71] A. A. Schafgans, S. J. Moon, B. C. Pursley, A. D. LaForge, M. M. Qazilbash, A. S. Sefat, D. Mandrus, K. Haule, G. Kotliar, and D. N. Basov, "Electronic Correlations and Unconventional Spectral Weight Transfer in the High-Temperature Pnictide BaFe_{2-x}Co_xAs₂ Superconductor Using Infrared Spectroscopy," *Phys. Rev. Lett.* **108**, 147002 (2012).
- [72] A. Chamukha, "Optical conductivity of iron-based superconductors," *J. Phys.: Condens. Matter* **26**, 253203 (2014).
- [73] M. Nakajima, K. Yanase, F. Nabeshima, Y. Imai, A. Maeda, and S. Tajima, "Gradual Fermi-surface modification in orbitally ordered state of FeSe revealed by optical spectroscopy," *Phys. Rev. B* **95**, 184502 (2017).
- [74] A. Pal, M. Chinotti, J.-H. Chu, H.-H. Kuo, I. R. Fisher, and L. Degiorgi, "Optical conductivity of iron-based superconductors," *npj Quant. Mater.* **4**, 3 (2019).
- [75] E. Jeckelmann, "Dynamical density-matrix renormalization-group method," *Phys. Rev. B* **66**, 045114 (2002).
- [76] W. Stephan and K. Penc, "Dynamical density-density correlations in one-dimensional Mott insulators," *Phys. Rev. B* **54**, R17269 (1996).
- [77] R. Žitko and T. Pruschke, "Energy resolution and discretization artifacts in the numerical renormalization group," *Phys. Rev. B* **79**, 085106 (2009).
- [78] R. Žitko, "NRG Ljubljana," (2021).
- [79] H. Wadati, J. Mravlje, K. Yoshimatsu, H. Kumigashira, M. Oshima, T. Sugiyama, E. Ikenaga, A. Fujimori, A. Georges, A. Radeinac, K. S. Takahashi, M. Kawasaki, and Y. Tokura, "Photoemission and DMFT study of electronic correlations in SrMoO₃: Effects of Hund's rule coupling and possible plasmonic sideband," *Phys. Rev. B* **90**, 205131 (2014).
- [80] D. Stricker, J. Mravlje, C. Berthod, R. Fittipaldi, A. Vecchione, A. Georges, and D. van der Marel, "Optical Response of Sr₂RuO₄ Reveals Universal Fermi-Liquid Scaling and Quasiparticles Beyond Landau Theory," *Phys. Rev. Lett.* **113**, 087404 (2014).
- [81] K. M. Stadler, Z. P. Yin, J. von Delft, G. Kotliar, and A. Weichselbaum, "Dynamical mean-field theory plus numerical renormalization-group study of spin-orbital separation in a three-band Hund metal," *Phys. Rev. Lett.* **115**, 136401 (2015).
- [82] A. Horvat, R. Žitko, and J. Mravlje, "Non-Fermi-liquid fixed point in multi-orbital Kondo impurity model relevant for Hund's metals," [arXiv:1907.07100](https://arxiv.org/abs/1907.07100).
- [83] E. Walter, K. M. Stadler, S. S. B. Lee, Y. Wang, G. Kotliar, A. Weichselbaum, and J. von Delft, "Uncovering Non-Fermi-Liquid Behavior in Hund Metals: Conformal Field Theory Analysis of an SU(2) × SU(3) Spin-Orbital Kondo Model," *Phys. Rev. X* **10**, 031052 (2020).

**SUPPLEMENTAL MATERIAL for
Hund bands in spectra of multiorbital systems**

by M. Środa, J. Mravlje, G. Alvarez, E. Dagotto, and J. Herbrych

**Supplemental Note 1
Definition of the single-particle spectral function**

The orbital-resolved single-particle spectral function is defined as

$$A_\gamma(k, \omega) = \frac{1}{\sqrt{L}} \sum_{\ell\sigma} e^{ik(\ell-c)} \left(\langle \langle c_{\gamma\ell\sigma}^\dagger; c_{\gamma c\sigma} \rangle \rangle_\omega^h + \langle \langle c_{\gamma\ell\sigma}; c_{\gamma c\sigma}^\dagger \rangle \rangle_\omega^e \right),$$

$$\langle \langle A; B \rangle \rangle_\omega^{h,e} = -\frac{1}{\pi} \text{Im} \langle \text{gs} | A \frac{1}{\omega^\pm \pm (H - \epsilon_{\text{gs}})} B | \text{gs} \rangle. \quad (\text{S1})$$

Here, k denotes the momentum, the $+$ and $-$ signs correspond to the hole $\langle \langle \dots \rangle \rangle_\omega^h$ and electron $\langle \langle \dots \rangle \rangle_\omega^e$ components, respectively, $\omega^\pm = \omega + i\eta$ with ω being the energy, $c = L/2$, and $|\text{gs}\rangle$ is the ground state (gs) with energy ϵ_{gs} . The density of states (DOS) is obtained as $A_\gamma(\omega) = (1/L) \sum_k A_\gamma(k, \omega)$.

The origin of $c = L/2$ is the so-called central-site trick. In the Fourier transform, Eq. (S1), we replace the expensive double sum over two sites with a single sum over just one site. In other words, the distances are measured w.r.t. the center of the lattice. This trick is exact for periodic boundary conditions (where each site c is equivalent) and introduces only minor quantitative corrections in the open boundary case.

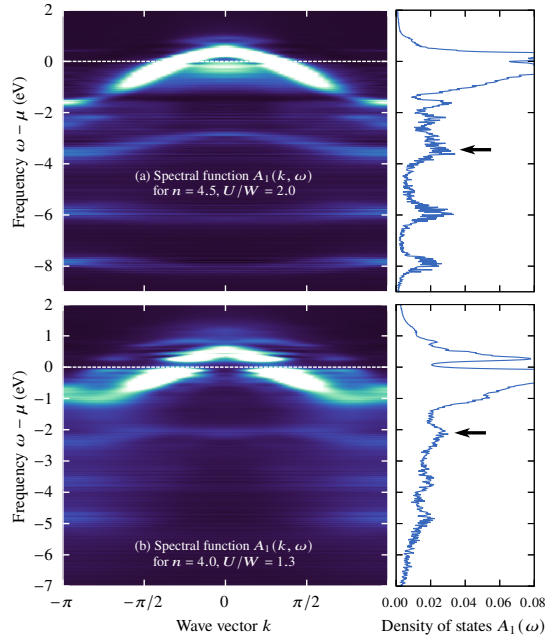
**Supplemental Note 2
Three-orbital results for the momentum-dependence of the spectral function**

In the main text, we used the two-orbital Hubbard model (2oH) to show that the Hund excitations form robust dispersive bands. Here, we show that the same holds true for the three-orbital Hubbard model (3oH).

Figure S1 presents the momentum-resolved single-particle spectral function $A_\gamma(k, \omega)$ in the itinerant orbital $\gamma = 1$ of the 3oH. Panels (a) and (b) show the fillings $n = 4.5$ and $n = 4.0$, respectively. Clearly, in the momentum-resolved function $A_\gamma(k, \omega)$ the spectral features are much better separated than in the density of states $A_\gamma(\omega)$. In particular, one observes that the Hund excitations (arrows) have robust dispersion and indeed form individual bands. This is particularly interesting for the integer filling $n = 4.0$ [Fig. S1(b)], where the Hund excitation is not a consequence of the atomic limit but is still possible due to intersite particle fluctuations.

**Supplemental Note 3
Two- and three-orbital results for fixed J_H**

In this Supplemental Note, we show that the Hund bands are U independent. To this end, we fix $J_H = W/2$ and vary



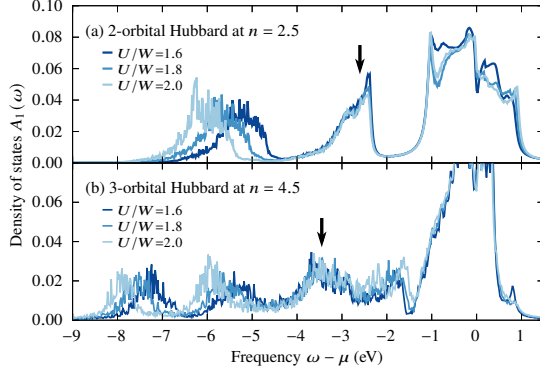
Supplemental Figure S1. Momentum-resolved single-particle spectral function $A_\gamma(k, \omega)$ of the itinerant orbital $\gamma = 1$ of the three-orbital Hubbard model for (a) $n = 4.5$, $U/W = 2.0$ and (b) $n = 4.0$, $U/W = 1.3$. The Hund coupling is $J_H/U = 0.25$. The right column shows the corresponding momentum-integrated spectra, i.e., the densities of states $A_\gamma(\omega)$. The arrows point at the Hund bands, as identified in the main text. Results obtained with DMRG on a $L = 32$ lattice with broadening $\eta = 0.04$.

only U . The remaining parameters of the models are kept the same as in the main text.

Figure S2(a) presents the density of states $A_1(\omega)$ of the itinerant orbital of the two-orbital Hubbard model (2oH) at $n = 2.5$. Unlike the leftmost peak, which has a clear U dependence, the middle peak does not shift when the interaction U is varied. This is the Hund-singlet excitation with the atomic energy $2J_H$, identified in Fig. 1(d) and Fig. 2 of the main text. Here, it can be clearly seen that its energy is fully independent of the J_H/U ratio.

Similar behavior is observed in the three-orbital Hubbard model (3oH). Figure S2(b) shows the data for the filling $n = 4.5$, where one expects the same Hund-singlet excitation as above. Among several U -dependent excitations (Hubbard excitations), one observes a prominent peak whose position and shape are not affected by the change in U . Again, this is

the Hund-singlet excitation identified in Fig. 3(b) of the main text.



Supplemental Figure S2. (a) $A_\gamma(\omega)$ of the itinerant orbital ($\gamma = 1$) for the two-orbital Hubbard model ($n = 2.5$, $L = 48$) with fixed $J_H = W/2$ and varying U . Clearly, the Hund band depends only on J_H and is U independent. (b) The same as in (a) but for the three-orbital Hubbard model with $n = 4.5$ and $L = 32$ sites. The arrows point at the Hund bands, as identified in the main text. The unlabeled peaks are Hubbard bands which clearly have a U dependence. Results obtained with DMRG using broadening $\eta = 0.04$.

Supplemental Note 4

Atomic-limit excitation energies for the three-orbital model

In the orbitally degenerate case of the 3oH, $t_{\gamma\gamma'} \propto \delta_{\gamma\gamma'}$, $\Delta_\gamma = 0$, and for an atom, the Hubbard-Kanamori model [Eq. (1) of the main text] can be brought to a simple form [5]

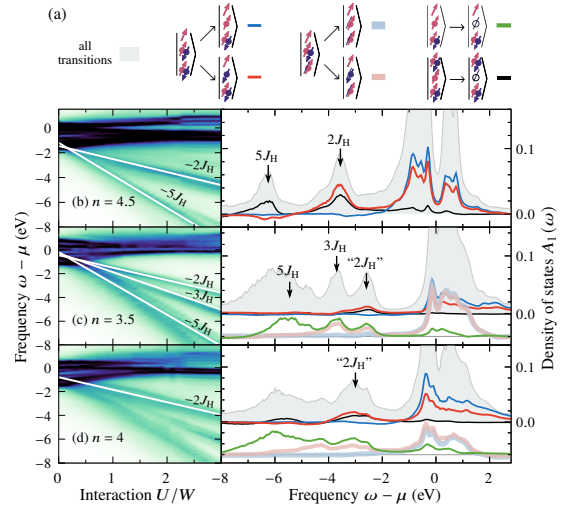
$$H = (U - 3J_H) \frac{\hat{N}(\hat{N} - 1)}{2} - 2J_H \mathbf{S}^2 - \frac{J_H}{2} \mathbf{L}^2 + \frac{5}{2} J_H \hat{N}, \quad (\text{S2})$$

where \hat{N} is the total particle number operator, \mathbf{S} the total spin operator, \mathbf{L} the total orbital angular momentum operator. In this form the rotational symmetry is readily apparent. Moreover, this form allows us to classify all eigenstates (and their energies) in terms of the quantum numbers N , S , L . This is shown in Table SI, where we show both ‘bare’ energies and also energies w.r.t. the atomic gs for fillings $n = 4.5, 4.0, 3.5, 3.0$. To obtain the energies of the excitations, we need to subtract the energies of the gs and the target state with a sign appropriate for the electron- or hole-like single-particle excitation.

To conduct the projector analysis, we also need to know how the eigenstates appear in the Ising-configuration basis $|\Gamma_{\gamma=0}, \Gamma_{\gamma=1}, \Gamma_{\gamma=2}\rangle$, where $\Gamma \in \{|0\rangle, |\uparrow\rangle, |\downarrow\rangle, |\uparrow\downarrow\rangle\}$. Since the eigenstate superpositions are rather lengthy, in Table SI we list only up to two example eigenstates per each N , S , L subspace.

Naturally, a finite crystal field ($\Delta_\gamma \neq 0$) modifies the spectrum shown in Table SI. The effect of the crystal field is

twofold: (i) it modifies the energies and (ii) it may exclude certain configurations from the gs (more generally, it induces splittings in the spectrum). Regarding (i), if $J_H, U \gg \Delta_\gamma$, the change in energies is marginal and one can still use Table SI to investigate the excitations. This is the case for the 3oH parameters of the itinerant orbitals, which we used in the main text. Namely, the slopes of the unlabeled excitations in Fig. 3 of the main text (left column) are accurately reproduced by Table SI. The example of effect (ii) is that in Fig. 3(b), showing $n = 4.5$, one cannot observe the Hund excitation with energy $5J_H$ ($N, S, L = 4, 0, 0$). To see it, the configuration $|\uparrow\downarrow, \uparrow, \uparrow\downarrow\rangle$ would need to be present in the gs, so that the photoemission from $\gamma = 1$ could reach $|\uparrow\downarrow, 0, \uparrow\downarrow\rangle$. However, the former configuration is excluded from the gs by $\Delta_2 = 0.8$ (and/or OSMP), as it has a doublon in the orbital $\gamma = 2$. In contrast, such a configuration is present for the orbitally degenerate system, where the $5J_H$ excitation becomes observable (see the next Supplemental Note).



Supplemental Figure S3. (a) Sketch of the transitions to final configurations that contribute to the Hund bands of the three-orbital Hubbard model (3oH). For clarity, we present only the representative configurations (while the results are summed over several configurations of the same type). (b)-(d) DOS $A_1(\omega)$ of the orbitally degenerate 3oH (see the text for details) with $J_H/U = 0.25$. Left panels depict $A_1(\omega)$ as a function of the interaction U , while right panels show detailed spectra with projections for $U/W = 2$. (b), (c), and (d) depict results for $n = 4.5$, $n = 3.5$, and $n = 4$, respectively. The arrows on the right panels point at the Hund bands [60], with “...” denoting the peaks observable only in the lattice. The solid lines in the left column mark the $-2J_H$, $-3J_H$, and $-5J_H$ slopes. The U and J_H dependence of the unlabeled peaks follows Table SI. Results obtained with DMRG on an $L = 8$ lattice with broadening $\eta = 0.1$.

Table SI. Eigenstates and eigenvalues of the Hamiltonian (S2). For brevity, in the column ‘Ising basis’ we show only up to two representative eigenstates from a given N, S, L subspace, whereas the remaining eigenstates consist of similar Ising configurations. The shown energies are independent of the J_H/U ratio. In the last four columns, we show the energies w.r.t. the gs for fillings $n = 4.5, 4.0, 3.5, 3.0$ and we restrict ourselves only to the states with $N_{gs} \pm 1$, where N_{gs} is the number of particles in the gs. The chemical potentials corresponding to the latter fillings are $\mu_{n=4.5} = 4U - 7J_H$, $\mu_{n=4.0} = \frac{1}{2}(7U - 11J_H)$, $\mu_{n=3.5} = 3U - 4J_H$, $\mu_{n=3.0} = \frac{5}{2}U - 5J_H$, respectively. The gs of each fixed N sector is given in the first row of that sector.

N, S, L	Degeneracy	Ising basis	Energy $\epsilon_{N,S,L}$	Energy $(\epsilon_{N,S,L} - \mu N) - (\epsilon_{gs} - \mu N_{gs})$			
				$n = 4.5$	$n = 4.0$	$n = 3.5$	$n = 3.0$
0, 0, 0	1	$ 0, 0, 0\rangle$	0				
$1, \frac{1}{2}, 1$	6	$ \uparrow, 0, 0\rangle$	0				
2, 1, 1	9	$ \uparrow, \uparrow, 0\rangle,$ $\frac{1}{\sqrt{2}} \uparrow, \downarrow, 0\rangle + \frac{1}{\sqrt{2}} \downarrow, \uparrow, 0\rangle$	$U - 3J_H$			$U + 2J_H$	$\frac{1}{2}(U + 2J_H)$
2, 0, 2	5	$\frac{1}{\sqrt{2}} \uparrow, \downarrow, 0\rangle - \frac{1}{\sqrt{2}} \downarrow, \uparrow, 0\rangle,$ $\frac{1}{\sqrt{6}} \uparrow\downarrow, 0, 0\rangle + \frac{1}{\sqrt{6}} 0, \uparrow\downarrow, 0\rangle - \sqrt{\frac{2}{3}} 0, 0, \uparrow\downarrow\rangle$	$U - J_H$			$U + 4J_H$	$\frac{1}{2}(U + 6J_H)$
2, 0, 0	1	$\frac{1}{\sqrt{3}} \uparrow\downarrow, 0, 0\rangle + \frac{1}{\sqrt{3}} 0, \uparrow\downarrow, 0\rangle + \frac{1}{\sqrt{3}} 0, 0, \uparrow\downarrow\rangle$	$U + 2J_H$			$U + 7J_H$	$\frac{1}{2}(U + 12J_H)$
$3, \frac{3}{2}, 0$	4	$ \uparrow, \uparrow, \uparrow\rangle,$ $\frac{1}{\sqrt{3}} \uparrow, \uparrow, \downarrow\rangle + \frac{1}{\sqrt{3}} \uparrow, \downarrow, \uparrow\rangle + \frac{1}{\sqrt{3}} \downarrow, \uparrow, \uparrow\rangle$	$3U - 9J_H$	$U - 3J_H$	$\frac{1}{2}(U - 3J_H)$	0	0
$3, \frac{1}{2}, 2$	10	$\frac{1}{\sqrt{6}} \uparrow, \uparrow, \downarrow\rangle + \frac{1}{\sqrt{6}} \uparrow, \downarrow, \uparrow\rangle - \sqrt{\frac{2}{3}} \downarrow, \uparrow, \uparrow\rangle,$ $\frac{1}{\sqrt{2}} \uparrow\downarrow, 0, \uparrow\rangle - \frac{1}{\sqrt{2}} 0, \uparrow\downarrow, \uparrow\rangle$	$3U - 6J_H$	U	$\frac{1}{2}(U + 3J_H)$	$3J_H$	$3J_H$
$3, \frac{1}{2}, 1$	6	$\frac{1}{\sqrt{2}} \uparrow\downarrow, 0, \uparrow\rangle + \frac{1}{\sqrt{2}} 0, \uparrow\downarrow, \uparrow\rangle$	$3U - 4J_H$	$U + 2J_H$	$\frac{1}{2}(U + 7J_H)$	$5J_H$	$5J_H$
4, 1, 1	9	$ \uparrow\downarrow, \uparrow, \uparrow\rangle,$ $\frac{1}{\sqrt{2}} \uparrow\downarrow, \uparrow, \downarrow\rangle + \frac{1}{\sqrt{2}} \uparrow\downarrow, \downarrow, \uparrow\rangle$	$6U - 13J_H$	0	0	0	$\frac{1}{2}(U + 2J_H)$
4, 0, 2	5	$\frac{1}{\sqrt{2}} \uparrow\downarrow, \uparrow, \downarrow\rangle - \frac{1}{\sqrt{2}} \uparrow\downarrow, \downarrow, \uparrow\rangle,$ $\frac{1}{\sqrt{6}} \uparrow\downarrow, \uparrow\downarrow, 0\rangle + \frac{1}{\sqrt{6}} \uparrow\downarrow, 0, \uparrow\downarrow\rangle - \sqrt{\frac{2}{3}} 0, \uparrow\downarrow, \uparrow\downarrow\rangle$	$6U - 11J_H$	$2J_H$	$2J_H$	$2J_H$	$\frac{1}{2}(U + 6J_H)$
4, 0, 0	1	$\frac{1}{\sqrt{3}} \uparrow\downarrow, \uparrow\downarrow, 0\rangle + \frac{1}{\sqrt{3}} \uparrow\downarrow, 0, \uparrow\downarrow\rangle + \frac{1}{\sqrt{3}} 0, \uparrow\downarrow, \uparrow\downarrow\rangle$	$6U - 8J_H$	$5J_H$	$5J_H$	$5J_H$	$\frac{1}{2}(U + 12J_H)$
$5, \frac{1}{2}, 1$	6	$ \uparrow\downarrow, \uparrow\downarrow, \uparrow\rangle$	$10U - 20J_H$	0	$\frac{1}{2}(U - 3J_H)$	$U - 3J_H$	
6, 0, 0	1	$ \uparrow\downarrow, \uparrow\downarrow, \uparrow\downarrow\rangle$	$15U - 30J_H$	$U - 3J_H$			

Supplemental Note 5

Hund bands in an orbitally degenerate three-orbital system

In this Supplemental Note, we study an orbitally degenerate 3oH ($t_{\gamma\gamma'} = -0.5\delta_{\gamma\gamma'}$, $\Delta_\gamma = 0$ and other parameters the same as in the main text) via the same projector analysis as in Fig. 3 of the main text. Our main conclusion is that the Hund bands emerge also without the OSMP.

In Fig. S3(b), we show the results for filling $n = 4.5$. According to Table SI, we expect two Hund excitations with energy costs $2J_H$, $5J_H$ and we detect both of these using appropriate projections. Surprisingly, two Hubbard excitations with energy costs $U - 3J_H$ and $U + 2J_H$, which were visible in Fig. 3 of the main text, are not visible here. There is also an additional weak gap forming at the chemical potential. These two features could be related to the fact that without the OSMP the system is further away from the Mott-insulating state, where the atomic limit should work best. The spectrum of the orbitally degenerate system is thus more strongly renormalized. Nonetheless, the crucial Hund excitations are clearly visible.

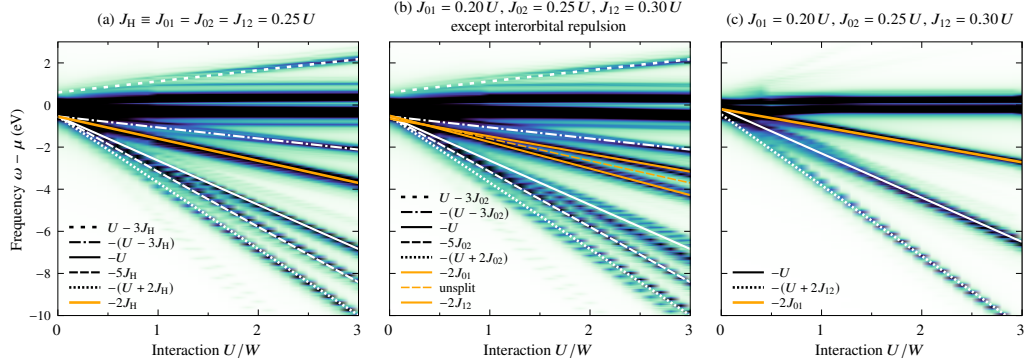
Figures S3(c),(d) display the data for fillings $n = 3.5$

and $n = 4.0$, respectively. Here, apart from the peaks being broader, the spectra closely resemble Fig. 3(c),(d) of the main text and the same conclusions follow. Note that for $n = 3.5, 4.0$, the energy of the $2J_H$ Hund excitation agrees with Table SI only if one treats the fluctuating 5-electron configuration as being part of the gs (i.e., as having energy ϵ_{gs}). For $n = 4.0$ [Fig. S3(d)], we also observe a small weight of the fluctuating $n = 5 \rightarrow 4$ Hund excitation with energy $5J_H$, but for our choice of $J_H/U = 0.25$, it overlaps with the Hubbard excitation $\frac{1}{2}(U + 7J_H)$ (the slopes are very similar).

Supplemental Note 6

Hund bands for orbital-dependent interactions

In many materials the interactions of the Hamiltonian (1) of the main text can be orbital-differentiated. To give a comprehensive answer on the fate of the Hund bands in such a case, we present additional result for the spectral functions $A_{\gamma=1}(\omega)$. We study a system where the Hund coupling depends on the orbitals involved, i.e., $J_H \equiv J_{\gamma\gamma'}$. In summary, two scenarios are possible: (i) the Hund band can be simply



Supplemental Figure S4. Density of states $A_{\gamma=1}(\omega)$ of the $\gamma = 1$ orbital in the three-orbital Hubbard model. The system is orbitally degenerate and close to the atomic limit: $t_{\gamma\gamma'} = 0.2\delta_{\gamma\gamma'}$, $\Delta_\gamma = 0$, and $L = 4$, with $n = 4.5$. (a) Symmetric, orbitally independent Hund couplings. (b) Orbitally dependent Hund couplings, but with the interorbital repulsion kept independent. The dashed orange line corresponds to “unsplit” $2J_H$ excitation of panel (a). (c) All interactions orbitally dependent. The lines in panels (a)-(c) correspond to excitation energies from Table SI. Results obtained with DMRG for broadening $\eta = 0.05$.

split (if the orbital occupancies remain symmetric) or (ii) the spectrum can be more strongly modified (if the occupancies become orbital-dependent).

In Fig. S4, we show the density of states $A_{\gamma=1}(\omega)$ of the $\gamma = 1$ orbital in the three-orbital Hubbard model. For the sake of clarity, we choose a simple orbital-degenerate system close to the atomic limit: $t_{\gamma\gamma'} = 0.2\delta_{\gamma\gamma'}$, $\Delta_\gamma = 0$, and $L = 4$, at the $n = 4.5$ filling. In Fig. S4(a), we show the symmetric (orbital-independent) case, where all Hund couplings are the same, $J_H = 0.25 U$. This case serves as a reference to the results in the main text (e.g., Fig. 3) and the Supplemental Material (Fig. S3). Table SI accounts for all observed excitations: there is one $2J_H$ line (in orange).

Next, we differentiate only the pair hopping and the direct Hund exchange: $J_H \equiv J_{\gamma\gamma'}$ with $\gamma = 0, 1, 2$ denoting the orbitals. We choose $J_{01} = 0.20 U$, $J_{02} = 0.25 U$ and $J_{12} = 0.30 U$. In Fig. S4(b), we show the scenario (i), where the $2J_H$ band splits into two bands $2J_{01}$ and $2J_{12}$ (solid orange lines). The $2J_{02}$ band is not visible, because we remove an electron only from the $\gamma = 1$ orbital. Thus, there are only two possible transitions giving $2J_{\gamma\gamma'}$ bands, schematically shown as

$$\begin{aligned} & \xrightarrow{2J_{01}} |\uparrow, \uparrow\downarrow, \uparrow\downarrow\rangle \rightarrow |\uparrow, \downarrow, \uparrow\downarrow\rangle, \\ & \xrightarrow{2J_{12}} |\uparrow\downarrow, \uparrow\downarrow, \uparrow\rangle \rightarrow |\uparrow\downarrow, \downarrow, \uparrow\rangle. \end{aligned}$$

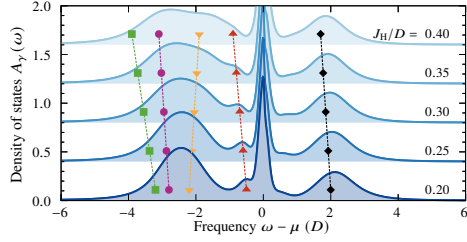
Besides the $2J_{01}$ and $2J_{12}$ excitations, the remaining part of the spectrum still follows Table SI, albeit with small splittings in its lower part. Crucially, although above we made the pair hopping and exchange interactions orbital-dependent, we still kept the interorbital repulsion orbital-independent. The rationale was to keep the on-site orbital occupancies intact, $\langle n_0 \rangle = \langle n_1 \rangle = \langle n_2 \rangle = 1.5$, thus keeping both on-site states $|\uparrow, \uparrow\downarrow, \uparrow\downarrow\rangle, |\uparrow\downarrow, \uparrow\downarrow, \uparrow\rangle$ in the ground state.

In Fig. S4(c), on the other hand, all interaction terms are orbital-dependent. Due to the now asymmetric interorbital repulsion, the system lowers its energy by unequal orbital occupancies: $\langle n_0 \rangle = 1$, $\langle n_1 \rangle = 1.5$, and $\langle n_2 \rangle = 2$. Thus, the ground state keeps only the $|\uparrow, \uparrow\downarrow, \uparrow\downarrow\rangle$ configuration from the two possibilities discussed above. As a result, only the $2J_{01}$ band is observable in photoemission from $\gamma = 1$ orbital, whereas $2J_{12}$ is absent. Similarly, a few other bands, which were visible in Fig. S4(a) and Fig. S4(b), are not present in Fig. S4(c). Their initial configurations are now excluded from the ground state. This is scenario (ii): the spectrum of a *single* orbital does not include splittings and is more strongly modified due to the orbital-dependent $J_{\gamma\gamma'}$. Still, if one would remove an electron from $\gamma = 2$, it should be possible to observe the $2J_{02}$ band. Therefore, experimentally, when one looks at the combined spectrum of all orbitals, the splitting should be observable also in scenario (ii).

Supplemental Note 7 Details of the DMFT results for the semicircular DOS

We also considered the three-orbital problem within the DMFT method, where we used the numerical renormalization group (NRG) method [77, 78] to solve the impurity problem. We used $\Lambda = 4$, averaged over 4 different realizations of Z and kept up to 4000 states in the diagonalization. We checked that the results remain consistent if these technical parameters are varied.

In Fig. 4(a) of the main text and Fig. S5, we show the calculated spectral functions for several J_H . Due to the logarithmic discretization of NRG, which leads to larger broadening of the high-energy features, the Hund excitation at energy $2J_H$ is best visible when it lies between the quasiparticle peak and the inner edge of the Hubbard band. This occurs for



Supplemental Figure S5. DMFT-NRG results for $A_\gamma(\omega)$ for an orbitally degenerate three-orbital Hubbard model with semicircular DOS of half bandwidth $D = 1$ and $U/D = 3.8$, $n = 4$. The values of J_H in units of D are indicated on the plot. The curves are given a vertical offset for clarity. Symbols \blacksquare , \bullet , \blacktriangledown , \blacklozenge mark the atomic-limit excitations $-\frac{1}{2}(U + 7J_H) - \delta$, $-\frac{1}{2}(U + 3J_H) - \delta$, $-\frac{1}{2}(U - 3J_H) - \delta$, and $\frac{1}{2}(U - 3J_H) + \delta$, respectively. Atomic-limit excitations are shifted by $\delta = D/2$; see the text for details. Symbol \blacktriangle marks the Hund excitation $-2J_H$. Finally, all symbols are also shifted by -0.1 .

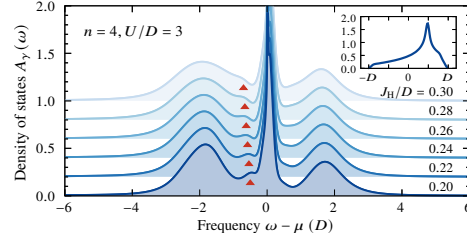
$J_H/D = 0.2 - 0.3$, where $D = 1$ is the half bandwidth, used as the unit of energy. In the plot, we also indicate the values of the atomic and Hund excitations. For the atomic excitations, we additionally introduce an outward shift of $\delta = D/2$. The rationale for this shift is that the lower Hubbard band predominantly consists of the occupied states that have momenta below the Fermi surface (band energies in the window $[-D, \epsilon_F]$) whereas the upper Hubbard band consists of the empty states with energies above the Fermi energy. Note that we could not discern the $5J_H$ Hund band in the DMFT data, possibly due to a combination of its small weight (it is represented by only one multiplet) and the large broadening.

Let us also stress here that the Hund-band excitation energy grows with J_H and is hence distinct from the side-peak *within* the quasiparticle spectrum [79–83] that is also characteristic of multiorbital physics. The energy of the latter feature, present in the quasiparticle peak in Hund’s metals, is lower and drops with increasing J_H .

Supplemental Note 8 DMFT results for a typical t_{2g} DOS

It is of interest to investigate whether the Hund bands can be resolved also for realistic DOS. For this reason, we repeat DMFT-NRG calculations for the case of a typical t_{2g} DOS (the same that was used in calculations of Ref. [5]), shown in Fig. S6. One finds that the Hund bands indeed occur: the $2J_H$ band is clearly present.

Similarly as in the main text, it is advantageous to look at quite small values of J_H so that the peak occurs where there is no other DOS. Notice that NRG is based on logarithmic discretization, and spectra at the energies corresponding to Hubbard bands are overbroadened. If one used a solver with better resolution at higher frequencies, such as the approach of



Supplemental Figure S6. DMFT-NRG results for $A_\gamma(\omega)$ for an orbitally degenerate three-orbital Hubbard model with typical t_{2g} DOS (inset) of half bandwidth $D = 1$. The interaction and filling are $U/D = 3$, $n = 4$, respectively. The values of J_H in units of D are indicated on the plot. The curves are given a vertical offset for clarity. Symbol \blacktriangle marks the energy of the Hund band $-2J_H + \delta$ with the constant shift $\delta = -0.1$.

Ref. [20], the Hund bands should be visible also when overlapping with the Hubbard bands.

Supplemental Note 9 Definition of the optical conductivity

The calculation of the optical conductivity $\sigma(\omega)$ proved to be the most computationally demanding part of our effort. To calculate dynamical correlation functions with DMRG, we used the Krylov-space approach for correction vectors [36]. With this method and for our system, we achieved the best results by calculating $\sigma(\omega)$ indirectly, i.e., from the limit of density-density correlations.

The (complex) dynamical density-density correlation function is defined as

$$C_N(k, \omega^+) = -\frac{1}{\pi} \langle \text{gs} | n_{\gamma k} \frac{1}{\omega^+ - (H - \epsilon_{\text{gs}})} n_{\gamma k} | \text{gs} \rangle, \quad (\text{S3})$$

where $\omega^+ = \omega + i\eta$, $n_{\gamma k} = \sqrt{\frac{2}{L+1}} \sum_\ell \sin(k\ell) (n_{\gamma\ell} - \langle n_{\gamma\ell} \rangle)$ with $\langle n_{\gamma\ell} \rangle$ being the average local electron density and $k = Z \frac{\pi}{L+1}$ ($Z = 1, \dots, L$), as appropriate for open boundary conditions. The imaginary part of Eq. (S3) is the dynamical density structure factor $N(k, \omega) = \text{Im} C_N$, which can be measured experimentally.

Using the continuity equation, we obtain $\sigma(\omega)$ from the long-wavelength part of the density structure factor $N(k, \omega)$ [76]

$$\sigma(\omega) = \lim_{k \rightarrow 0} \frac{\pi}{4 \sin^2(k/2)} \omega N(k, \omega). \quad (\text{S4})$$

Since in our DMRG procedure we compute both real and imaginary parts of C_N , we make use of both [75] and calculate the optical conductivity as

$$\sigma(\omega) = \lim_{k \rightarrow 0} \frac{\pi}{4 \sin^2(k/2)} \text{Im} (\omega^+ C_N(k, \omega^+)). \quad (\text{S5})$$

The $k \rightarrow 0$ limit is achieved by performing the calculation for the smallest possible k , i.e., by calculating $C_N(k = \frac{\pi}{L+1}, \omega^+)$.

Note that for a given system size, the above method may show larger finite-size effects than calculating $\sigma(\omega)$ directly from the current-current correlations. Still, we found it to be more computationally efficient, even though we needed a

much larger bond dimension to converge $\sigma(\omega)$ than to converge the density of states $A_\gamma(\omega)$. Therefore, although our DMRG results for $\sigma(\omega)$ are qualitatively correct (they were compared to Lanczos diagonalization in small lattices), their quantitative accuracy could be further improved in future efforts.

SUMMARY AND CONCLUSIONS

In this thesis, I aimed to establish the static and dynamic properties of the multiorbital Hubbard model in low dimensions (the ladder or chain geometry). This objective was strongly inspired by the 123 family of iron-based ladders, which defined a starting point for exploring the realistic parameter regimes of the model. However, my intention was not to replicate the properties of specific compounds in an *ab initio* manner. Rather, I adopted a broader perspective, aiming to provide a global view on the fascinating properties displayed not only by the 123 family but potentially by other low-dimensional multiorbital compounds with strong correlations.

I am confident that this thesis satisfactorily achieved the above goal by unveiling four distinct properties of the low-dimensional Hubbard model. Specifically, this thesis revealed: (i) rich magnetism of the ladder geometry, (ii) topological Majorana zero modes, (iii) topological Haldane state, and (iv) prominent Hund bands in the electronic spectra. These properties were presented in the form of four articles [O1–O4], to which I actively contributed as a coauthor. The primary approach I used to characterize these properties involved extensive numerical calculations via the density-matrix renormalization group method. A short summary of the discovered properties is in order. It is followed by a discussion of conclusions and future directions.

The first property I investigated in this thesis was the magnetism of the orbital-selective Mott phase (Chap. 3). While previous studies of magnetism of the 123 family focused mainly on the simpler chain configuration, I extended the analysis to the ladder setup, bringing the theory closer to experiment. My main achievement was charting the doping n vs interaction U magnetic phase diagram. This phase diagram demonstrated surprising robustness of rich magnetic patterns observed first in the chain, such as blocks and block spirals, as the dimensionality was increased to the ladder. Additionally, I revealed that the ladder geometry hosts new phases absent in the chain counterpart, including incommensurate antiferromagnetism, phase separation, and a novel quantum spin-flux state.

Building upon the discovery of rich magnetism, I explored the interplay between the block-spiral order and superconductivity (Chap. 4). This investigation revealed that

placing a low-dimensional multiorbital system within the OSMP in proximity to an s -wave superconductor facilitates the emergence of topological Majorana zero modes. These modes emerge in an interaction-induced topological phase transition, driven by the change of the magnetic properties. That is, above a critical value of the interaction U the system simultaneously develops spiral spin order, spin-triplet pairing amplitudes, and robust peaks in the local density of states at the edges of the system. In this work, I independently cross-checked the analytical derivations for the nonlocal spectral functions. The latter results provided strong evidence for the edge modes being indeed of Majorana character. These findings suggest that the 123 iron ladders could potentially serve as a novel platform for experimentally realizing the Majorana modes.

I continued the investigation of topological properties in Chap. 5, focusing on a different parameter regime of the multiorbital models. Specifically, I explored the behavior of the two-orbital Hubbard chain at half filling. The results revealed that this system can be driven into the Haldane phase through another sharp and interaction-driven topological phase transition. Remarkably, the transition occurred at relatively modest values of the Hubbard repulsion U , before the system reached the fully formed magnetic moments characteristic of the spin-1 Heisenberg chain. While the Haldane phase and its associated spin-1/2 edge states are well-known in the latter system, the original findings presented here extended the concept of Haldane phases to the realm of delocalized electrons. To further validate the Haldane nature of this topological phase, I conducted benchmark calculations of the string order parameter within the density-matrix renormalization group method.

To finish my exploration of the multiorbital Hubbard model, I delved into the investigation of its spectral properties (Chap. 6). My central finding in this regard is the identification of a generic spectral feature in multiorbital systems, referred to as the Hund band. Unlike the Hubbard satellites, the energy of the Hund band is exclusively determined by the Hund coupling J_H and remains independent of the interaction strength U . To demonstrate this, I performed extensive calculations of the spectral functions across various multiorbital models. Importantly, these findings transcend the specific context of the 123 ladders. They are generic and applicable to any multiorbital system with significant Hund's coupling and charge fluctuations, regardless of the presence of the orbital-selective Mott phase or the system's dimensionality.

Allow me to share two intriguing conclusions that can be drawn from my findings. First and foremost, it is evident that low-dimensional multiorbital systems harbor a remarkable wealth of exotic phenomena. Most likely, the results presented in this thesis merely scratch the surface of what may lie beneath. This observation should serve as strong motivation for crystal growers and experimentalists to dedicate more attention to investigating multiorbital chains and ladders. Taking another perspective, a complementary conclusion arises, highlighting the broader applicability of my findings. While the specific details of the properties I uncovered are unquestionably tied to the low-dimensional geometry, there are indications of general tendencies towards these properties even in high-dimensional systems. For instance, nontrivial magnetic tendencies were observed in some higher-dimensional pnictides and chalcogenides (see the introduction to Chap. 3). Furthermore, there are experimental observations consistent with the emergence of Majorana zero modes in the vortex cores of $\text{FeTe}_{1-x}\text{Se}_x$

compounds (see the introduction to Chap. 4). Finally, the Hund bands are expected to be a generic feature in a multiorbital system regardless of dimensionality. The only property that seems to be constrained to the low dimensionality is the Haldane phase. My thesis thus leads to the interesting conclusion that low-dimensional multiorbital models are not only useful for describing compounds with a low-dimensional crystal structure but also shed light on higher-dimensional physics. While this conclusion may seem like an obvious conjecture, providing actual evidence to support it is a challenging endeavor. In this thesis, I presented such evidence through an intensive computational effort.

Looking ahead, there are several future directions to explore. One avenue involves refining the properties discovered in this work to a specific compound. This could be accomplished by utilizing an *ab initio* approach, such as density functional theory, to determine the parameters of the multiorbital Hubbard model, which would then be solved for the ground state using the density-matrix renormalization group. By following this approach, it becomes possible to offer more precise guidance to crystal growers and experimentalists. A more exciting future direction involves investigating nonequilibrium problems. While significant progress was made for higher-dimensional systems using the nonequilibrium dynamical mean-field theory, this method does not allow for the tracking of time-dependent dynamics with spatial resolution. To achieve spatial resolution, the density-matrix renormalization group can be used, shifting the focus to the complementary limit of low dimensions. Drawing upon the findings of my thesis, an intriguing investigation would involve exploring how the propagation of photocarriers disrupts the magnetic background and gives rise to Hund excitations in both time and space.



DENSITY-MATRIX RENORMALIZATION GROUP

Although very simple in its formulation, the Hubbard model is notoriously difficult to solve. Due to the strong correlations, the most reliable methods to solve it are numerical. In the single-orbital case, much was uncovered by applying the brute-force methods of exact and Lanczos diagonalization [16,62]. However, the complexity of these methods scales exponentially in system size. This limits the attainable system sizes to ~ 16 sites, which arranged into a two-dimensional lattice result in a 4×4 cluster. Such a cluster cannot escape strong finite-size effects, prohibiting the study of long-distance correlations and the access to the thermodynamic limit. Fortunately, there exist superconducting cuprates, whose dimensionality is lower than that of planes, for example, the $(\text{La, Sr, Ca})_{14}\text{Cu}_{24}\text{O}_{41}$ family [120–123]. Their main structural motif are two coupled chains, often called *two-leg ladders*. Such a geometry is much more forgiving for brute-force numerics. For instance, the Lanczos method was successful in predicting superconductivity in such ladders [286] and in studying their spin excitation spectrum [287]. The materials motivating this thesis are also ladders, but their multiorbital degrees of freedom inflate the size of the Hilbert space, restricting the applicability of exact and Lanczos diagonalization. A more powerful method is thus necessary.

Today, it is the *density-matrix renormalization group* (DMRG) method [7,8] that takes the central place in the numerical study of the Hubbard model. DMRG does not suffer from the sign problem, the bane of quantum Monte Carlo, and its accuracy, at least in one dimension, is on par with exact diagonalization. At the same time, it beats exact diagonalization by orders of magnitude regarding the accessible system sizes. The method's first big triumph was the calculation of the Haldane excitation gap in the $S = 1$ Heisenberg chain to an unprecedented accuracy [288]. Since then, DMRG has been successfully applied to various interacting systems and has become a crucial addition to the numerical toolbox of a condensed-matter physicist. Due to its accuracy, high performance in low-dimensional systems, and reliable treatment of electronic correlations, DMRG is also the method of choice for the present thesis. A short

discussion of its concepts is thus beneficial. For in-depth reviews, see, e.g., [289,290], which, however, go beyond what is necessary to follow the results of this thesis.

Matrix-product states

DMRG was first formulated in the renormalization-group language and this is where it got its name. In this context, the key insight made by S. White was to keep D most probable eigenstates of the (reduced) density matrix during the renormalization-group scheme, instead of D lowest-energy eigenstates as done in Wilson's numerical renormalization group [8]. While Wilson's scheme relied on the energy scale separation of impurity problems, White's new scheme could be applied to general many-body problems. Later, it was realized that the wave function produced by DMRG has the particular form of the so-called *matrix-product state* [291,292]. This led to the reformulation of the algorithm by explicitly taking advantage of this form [290,293]. In modern understanding, DMRG is viewed as a variational method in the space of matrix-product states.

A matrix-product state (MPS) is the following parametrization of the many-body wave function

$$\begin{aligned} |\psi\rangle &= \sum_{\sigma_1, \dots, \sigma_L} \psi^{\sigma_1, \dots, \sigma_L} |\sigma_1, \dots, \sigma_L\rangle \\ &= \sum_{\sigma_1, \dots, \sigma_L} \sum_{m_1, \dots, m_{L-1}} M_{m_0, m_1}^{\sigma_1} M_{m_1, m_2}^{\sigma_2} \cdots M_{m_{L-1}, m_L}^{\sigma_L} |\sigma_1, \dots, \sigma_L\rangle. \end{aligned} \quad (\text{A.1})$$

The first line is the standard expression for the many-body wave function in the tensor-product basis. Here, $|\psi\rangle$ is a general quantum state, $\psi^{\sigma_1, \dots, \sigma_L}$ is its wave function, and $|\sigma_i\rangle$ are the basis states of the d -dimensional local Hilbert spaces attributed to each site $i = 1, \dots, L$ of the lattice. For example, $|\sigma_i\rangle \in \{|\uparrow\rangle, |\downarrow\rangle\}$ for the Heisenberg model. The second line is the MPS parametrization. For each site and each local state σ_i , there is a matrix M^{σ_i} with elements $M_{m_{i-1}, m_i}^{\sigma_i}$, so that each M is actually a rank-3 tensor¹. The indices m_i are called virtual or bond indices, whereas σ_i are physical indices which correspond to the on-site configuration. Although each bond can have a different number of indices, $m_i = 1, \dots, D_i$, the name bond dimension² usually refers to the maximal dimension across all bonds $D = \max_i D_i$. By performing the matrix multiplication (the so-called contraction) represented by the sum $\sum_{m_1, \dots, m_{L-1}}$, one recovers the wave-function coefficient³ $\psi^{\sigma_1, \dots, \sigma_L}$. Figure A.1 shows a graphical representation of Eq. (A.1).

The number of parameters specifying an MPS scales linearly in system size, LD^2d . This is better than the exponential (d^L) scaling of the number of coefficients $\psi^{\sigma_1, \dots, \sigma_L}$. However, the decomposition of $\psi^{\sigma_1, \dots, \sigma_L}$ into an MPS is exact only if one lets D grow exponentially [290]. Hence, although the MPS parametrization achieves linearity in L , it is still exponential in D , which seems to be of little benefit. The usefulness of the MPS ansatz relies on *truncation*. One restricts D to a modest number $D \sim 10^2 - 10^4$, making

¹It has three indices: σ_i, m_{i-1}, m_i .

²The bond dimension is called "the number of states kept" in the old DMRG language.

³The matrix product evaluates to a scalar provided that the boundary matrices $M^{\sigma_1}, M^{\sigma_L}$ are actually vectors, i.e., the indices m_0, m_L are trivial, $m_0 = m_L = 1$.

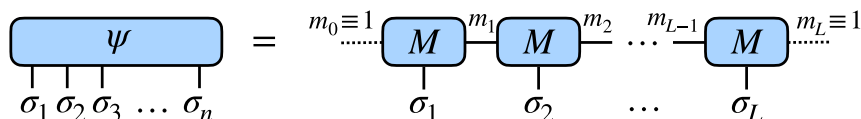


Figure A.1: Graphical representation of the decomposition into a matrix-product state.

INSPIRED BY A FIGURE FROM [294].

the MPS decomposition approximate, but requiring much less information than specifying all $\psi^{\sigma_1, \dots, \sigma_L}$. This does not mean discarding any of the $|\sigma_1, \dots, \sigma_L\rangle$ configurations. An approximate MPS is still a linear combination of all basis states, only the form of the superposition is restricted [290]. Instead, fixing D_i of a particular bond amounts to keeping only the D_i largest eigenvalues (and eigenstates) of a reduced density matrix obtained by bipartitioning the system at this bond [290,294]. This will control the amount of entanglement an MPS can capture. For instance, $D = 1$ corresponds to an unentangled product state, i.e., the reduced density matrix at each bond keeps only one eigenvalue. If a state is weakly entangled, then only a few eigenstates of the reduced density matrix contribute appreciably and are needed for a faithful representation. One can then safely truncate with a small loss of accuracy. The latter loss is conveniently quantified by the sum of the discarded eigenvalues, the so-called truncation error.

The success of the MPS ansatz rests on the fact that the *ground states* of physical Hamiltonians *are* weakly entangled. This has been rigorously quantified for the ground

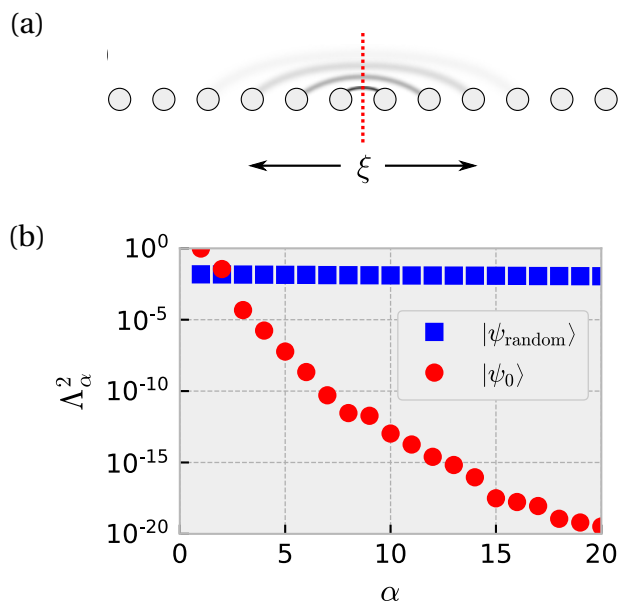


Figure A.2: (a) Sketch showing that in gapped ground states the entanglement involves only a few states within the correlation length ξ near the bipartition boundary. (b) The eigenspectrum of the reduced density matrix obtained by bipartitioning the ground state of the transverse-field Ising model ($g = 1.5$) and a random state. The Hamiltonian reads $H = -\sum_i \sigma_i^z \sigma_{i+1}^z + g \sum_i \sigma_i^x$, where $\sigma_i^{z,x}$ are Pauli matrices and the system consists of $L = 16$ spins. The index α enumerates the eigenvalues. ADAPTED FROM [294].

states of gapped one-dimensional (1D) Hamiltonians [295–298] and is connected to the so-called area laws for the entanglement entropy (see [299] for a review). In the ground state of a gapped system, the entanglement entropy between a subsystem and its complement grows only as the area of the boundary enclosing that subsystem. Since the entanglement does not depend on the volume of the subsystem, it should be concentrated only in a few sites located close to the boundary [see Fig. A.2(a)].

In 1D, the area of the boundary is constant for any subsystem and the MPS description becomes extremely efficient. Figure A.2(b) shows a typical behavior of the eigenspectrum of a reduced density matrix for a ground state in 1D. The eigenvalues decay exponentially and a modest D is enough to guarantee an accurate description of this state via an MPS. In fact, for a gapped 1D system, the bond dimension guaranteeing accurate results is constant in the system size L [290], whereas it is only polynomial in L for a gapless one [296]. In the two-dimensional (2D) case, the bond dimension must grow exponentially to capture the entanglement properties given by the area law [290,300]. This is why the DMRG method is mostly restricted to the 1D geometry, i.e., to chains and narrow ladders. Still, accurate calculations in finite 2D systems are possible, e.g., by assuming cylindrical geometry [300] or by extending the MPS ansatz [297].

The DMRG algorithm

The DMRG algorithm aims to find the ground state of the Hamiltonian H within the space of MPS by varying the matrix elements $M_{m_{i-1}, m_i}^{\sigma_i}$. Starting with an initial MPS $|\psi\rangle$ of a fixed bond dimension D , DMRG aims to solve the minimization problem

$$E = \min_{|\psi\rangle} \frac{\langle \psi | H | \psi \rangle}{\langle \psi | \psi \rangle}, \quad (\text{A.2})$$

where E is the energy. This is equivalent to minimizing $\langle \psi | H | \psi \rangle$ under the constraint $\langle \psi | \psi \rangle = 1$. In the simplest case, the initial MPS is random or is a product state. Instead of an unfeasible global update of all M^{σ_i} matrices, the optimization problem is decomposed into a set of local problems. Two neighboring matrices are updated at a time, while the others are kept fixed⁴. This needs to be done in a sequence, called a *sweep*⁵, starting from one end of the lattice and progressing towards the other. Each local update minimizes $\langle \psi | H | \psi \rangle$ by solving a local eigenvalue problem given by an effective two-site Hamiltonian H_{eff} [294], i.e., the full eigenvalue problem is projected to the local MPS environment. Solving the local eigenproblem is the most computationally expensive part of the algorithm. The dimension of the effective Hamiltonian is $D^2 d^2 \times D^2 d^2$, which is usually too large for full diagonalization [290], especially in the multiorbital setting. Fortunately, since one aims to minimize the energy, only the lowest eigenvalue and eigenstate is needed. To find it, one can use an iterative solver, e.g., the Lanczos or Jacobi-Davidson method. The eigenvector found by, say, the Lanczos

⁴Here, for the purpose of the presentation, the most basic two-site version of DMRG is assumed. The calculations in this thesis were actually performed using a one-site approach [301], which reduced the computational cost. Nonetheless, both schemes proceed very similarly and there are only small technical differences.

⁵Usually one sweep is composed of two half sweeps, so that it involves traversing the system from left to right and back.

method is split by a singular value decomposition, the result is truncated to a fixed D and used to update the M^{σ_i} matrices. The sweeping continues until the energy does not decrease anymore (or some other convergence criterion is satisfied). Importantly, the variational search should not be performed in only one class of MPS with a predetermined bond dimension D . One should increase D progressively during sweeping, so that it is possible to find the maximal D beyond which the ground state stops improving. Naturally, the larger D , the more costly the calculation, so that there is a trade-off between accessible system sizes L , bond dimensions D , the local Hilbert-space dimensions d , and the complexity of the Hamiltonian terms. After finding the ground state, one can use efficient MPS algorithms to calculate virtually any observable, including but not limited to local expectation values, correlation functions, and spectral functions.

Although DMRG is variational, its ansatz is very general and its efficiency relies only on general entanglement properties [290]. The ansatz is not tailored to a particular physical situation. Moreover, due to the existence of the well-defined accuracy parameter (the bond dimension) and the error measure (truncation error), DMRG is often referred to as a quasi-exact method. In principle, an MPS ansatz with unlimited resources $D \rightarrow \infty$ allows for an exact, even if inefficient, representation for the ground state of any Hamiltonian. As a result, DMRG is capable of faithfully capturing *all* correlation effects present within the ground state, both local and nonlocal. However, being variational, DMRG still suffers from the possibility to get stuck in local minima. This is especially true for gapless systems and/or beyond 1D. One thus needs to be careful when judging the convergence of the calculations. One well known issue is that DMRG can spontaneously break a symmetry, resulting in, e.g., non-zero magnetization in a finite system. A detailed discussion of this problem can be found in the Supplementary Material of Ref. [76].

Finally, a comment on the choice of boundary conditions is in order. Most numerical studies on finite-size systems use the periodic boundary conditions (PBC), with the aim to avoid edge effects. By contrast, in DMRG, open boundary conditions (OBC) are often the most convenient. There are several reasons for that, one being that the standard MPS definition, Eq. (A.1), is actually specialized to OBC. When this definition is used for PBC, the entanglement between the first and last sites is encoded across all inner bonds, increasing the complexity as $D \rightarrow D^2$ [290,297]. Although one can redefine an MPS to better capture PBC [293], one then needs to deal with generalized eigenvalue problems [290,297], and other inconveniences in defining the algorithms (e.g., the lack of a so-called mixed canonical form [294,297]). Because DMRG often facilitates the study of systems large enough for edge effects to become unimportant, it is usually most convenient to simply use OBC.

BIBLIOGRAPHY

- [1] P. W. Anderson, *Science* **177**, 393 (1972).
- [2] J. Spałek, *Wstęp do fizyki materii skondensowanej* (Wydawnictwo Naukowe PWN, Warszawa, 2015).
- [3] J. Spałek, *Eur. J. Phys.* **21**, 511 (2000).
- [4] G. R. Stewart, *Rev. Mod. Phys.* **56**, 755 (1984).
- [5] P. Coleman, *Introduction to Many-Body Physics* (Cambridge University Press, Cambridge, 2015).
- [6] R. B. Laughlin, *Phys. Rev. Lett.* **50**, 1395 (1983).
- [7] S. R. White, *Phys. Rev. Lett.* **69**, 2863 (1992).
- [8] S. R. White, *Phys. Rev. B* **48**, 10345 (1993).
- [9] A. Georges and G. Kotliar, *Phys. Rev. B* **45**, 6479 (1992).
- [10] A. Georges, G. Kotliar, W. Krauth, and M. J. Rozenberg, *Rev. Mod. Phys.* **68**, 13 (1996).
- [11] R. Blankenbecler, D. J. Scalapino, and R. L. Sugar, *Phys. Rev. D* **24**, 2278 (1981).
- [12] N. V. Prokof'ev and B. V. Svistunov, *Phys. Rev. Lett.* **81**, 2514 (1998).
- [13] W. M. C. Foulkes, L. Mitas, R. J. Needs, and G. Rajagopal, *Rev. Mod. Phys.* **73**, 33 (2001).
- [14] J. Spałek, *Philos. Mag.* **95**, 661 (2015).
- [15] J. Spałek, *Acta Phys. Pol. A* **143**, 169 (2023).
- [16] E. Dagotto, *Rev. Mod. Phys.* **66**, 763 (1994).
- [17] A. Damascelli, Z. Hussain, and Z.-X. Shen, *Rev. Mod. Phys.* **75**, 473 (2003).
- [18] P. A. Lee, N. Nagaosa, and X.-G. Wen, *Rev. Mod. Phys.* **78**, 17 (2006).
- [19] P. A. Lee, *Rep. Prog. Phys.* **71**, 012501 (2007).
- [20] D. J. Scalapino, *Rev. Mod. Phys.* **84**, 1383 (2012).
- [21] A. Jordan, *Inference* **5**, (2019).
- [22] A. J. Leggett, "Lecture notes on Superconductivity, Ancient and Modern (University of Illinois Urbana-Champaign)," <https://courses.physics.illinois.edu/phys598sc2/fa2015/>, accessed: 2023-01-25.
- [23] J. G. Bednorz and K. A. Müller, *Z. Phys. B: Condens. Matter* **64**, 189 (1986).
- [24] J. R. Gavaler, *Appl. Phys. Lett.* **23**, 480 (1973).
- [25] L. R. Testardi, J. H. Wernick, and W. A. Royer, *Solid State Commun.* **15**, 1 (1974).
- [26] V. L. Ginzburg, *Rev. Mod. Phys.* **76**, 981 (2004).
- [27] E. Tretkoff, "Reliving the Good Old Days," <http://www.aps.org/publications/apsnews/200705/woodstock.cfm>, accessed: 2023-01-26.

- [28] Wikipedia, “Woodstock of physics,” https://en.wikipedia.org/wiki/Woodstock_of_physics, accessed: 2023-01-26.
- [29] M. K. Wu, J. R. Ashburn, C. J. Torng, P. H. Hor, R. L. Meng, L. Gao, Z. J. Huang, Y. Q. Wang, and C. W. Chu, *Phys. Rev. Lett.* **58**, 908 (1987).
- [30] A. Schilling, M. Cantoni, J. D. Guo, and H. R. Ott, *Nature* **363**, 56 (1993).
- [31] M. S. Colclough, C. E. Gough, M. Keene, C. M. Muirhead, N. Thomas, J. S. Abell, and S. Sutton, *Nature* **328**, 47 (1987).
- [32] L. P. Lee, K. Char, M. S. Colclough, and G. Zaharchuk, *Appl. Phys. Lett.* **59**, 3051 (1991).
- [33] P. W. Anderson, “Theory of Superconductivity in Oxides, Grant Report,” <https://apps.dtic.mil/sti/citations/ADA244726>, accessed: 2023-01-27.
- [34] P. W. Anderson, “The Theory of High T_c Superconductivity,” in *High-Temperature Superconductivity: Physical Properties, Microscopic Theory, and Mechanisms*, edited by J. Ashkenazi, S. E. Barnes, F. Zuo, G. C. Vezzoli, and B. M. Klein (Springer US, Boston, MA, 1991).
- [35] L. Lu, J. N. Hancock, G. Chabot-Couture, K. Ishii, O. P. Vajk, G. Yu, J. Mizuki, D. Casa, T. Gog, and M. Greven, *Phys. Rev. B* **74**, 224509 (2006).
- [36] M. Imada, A. Fujimori, and Y. Tokura, *Rev. Mod. Phys.* **70**, 1039 (1998).
- [37] L. de’ Medici and M. Capone, “Modeling Many-Body Physics with Slave-Spin Mean-Field: Mott and Hund’s Physics in Fe-Superconductors,” in *The Iron Pnictide Superconductors: An Introduction and Overview*, Springer Series in Solid-State Sciences, edited by F. Mancini and R. Citro (Springer International Publishing, Cham, 2017).
- [38] G. Aeppli, S. M. Hayden, H. A. Mook, Z. Fisk, S.-W. Cheong, D. Rytz, J. P. Remeika, G. P. Espinosa, and A. S. Cooper, *Phys. Rev. Lett.* **62**, 2052 (1989).
- [39] N. S. Headings, S. M. Hayden, R. Coldea, and T. G. Perring, *Phys. Rev. Lett.* **105**, 247001 (2010).
- [40] J. M. Tranquada, G. Xu, and I. A. Zaliznyak, *J. Magn. Magn. Mater.* **350**, 148 (2014).
- [41] J. R. Schrieffer and J. S. Brooks, eds., *Handbook of High-Temperature Superconductivity* (Springer, New York, NY, 2007).
- [42] D. A. Wollman, D. J. Van Harlingen, W. C. Lee, D. M. Ginsberg, and A. J. Leggett, *Phys. Rev. Lett.* **71**, 2134 (1993).
- [43] C. C. Tsuei and J. R. Kirtley, *Rev. Mod. Phys.* **72**, 969 (2000).
- [44] H. Motzkau, “Schematic doping phase diagram of cuprate high-temperature superconductors,” https://commons.wikimedia.org/wiki/File:Cuprates_phasedigagram_en.svg, accessed: 2023-01-30.
- [45] S. I. Mirzaei, D. Stricker, J. N. Hancock, C. Berthod, A. Georges, E. van Heumen, M. K. Chan, X. Zhao, Y. Li, M. Greven, N. Barišić, and D. van der Marel, *Proc. Natl. Acad. Sci. U.S.A.* **110**, 5774 (2013).
- [46] M. K. Chan, M. J. Veit, C. J. Dorow, Y. Ge, Y. Li, W. Tabis, Y. Tang, X. Zhao, N. Barišić, and M. Greven, *Phys. Rev. Lett.* **113**, 177005 (2014).

-
- [47] J. Meng, G. Liu, W. Zhang, L. Zhao, H. Liu, X. Jia, D. Mu, S. Liu, X. Dong, J. Zhang, W. Lu, G. Wang, Y. Zhou, Y. Zhu, X. Wang, Z. Xu, C. Chen, and X. J. Zhou, *Nature* **462**, 335 (2009).
- [48] B. Keimer, S. A. Kivelson, M. R. Norman, S. Uchida, and J. Zaanen, *Nature* **518**, 179 (2015).
- [49] E. Fradkin, S. A. Kivelson, and J. M. Tranquada, *Rev. Mod. Phys.* **87**, 457 (2015).
- [50] T. R. Chien, Z. Z. Wang, and N. P. Ong, *Phys. Rev. Lett.* **67**, 2088 (1991).
- [51] C. M. Varma, *Rev. Mod. Phys.* **92**, 031001 (2020).
- [52] D. N. Basov and A. V. Chubukov, *Nat. Phys.* **7**, 272 (2011).
- [53] J. Zaanen, [arXiv:1012.5461](https://arxiv.org/abs/1012.5461) (2011).
- [54] P. W. Anderson, *Proc. Natl. Acad. Sci. U.S.A.* **92**, 6668 (1995).
- [55] P. W. Anderson, *Science* **316**, 1705 (2007).
- [56] P. W. Anderson, *Science* **235**, 1196 (1987).
- [57] P. W. Anderson, P. A. Lee, M. Randeria, T. M. Rice, N. Trivedi, and F. C. Zhang, *J. Phys. Condens. Matter* **16**, R755 (2004).
- [58] S. M. O'Mahony, W. Ren, W. Chen, Y. X. Chong, X. Liu, H. Eisaki, S. Uchida, M. H. Hamidian, and J. C. S. Davis, *Proc. Natl. Acad. Sci. U.S.A.* **119**, e2207449119 (2022).
- [59] M. Hirayama, Y. Yamaji, T. Misawa, and M. Imada, *Phys. Rev. B* **98**, 134501 (2018).
- [60] W. Zhang, *Photoemission Spectroscopy on High Temperature Superconductor: A Study of $Bi_2Sr_2CaCu_2O_8$ by Laser-Based Angle-Resolved Photoemission*, Springer Theses (Springer, Berlin, Heidelberg, 2013).
- [61] J. Fink, N. Nucker, H. A. Romberg, and J. C. Fuggle, *IBM J. Res. Dev.* **33**, 372 (1989).
- [62] J. Jaklič and P. Prelovšek, *Adv. Phys.* **49**, 1 (2000).
- [63] A.-M. S. Tremblay, B. Kyung, and D. Sénéchal, *Low Temp. Phys.* **32**, 424 (2006).
- [64] M. Qin, T. Schäfer, S. Andergassen, P. Corboz, and E. Gull, *Annu. Rev. Condens. Matter Phys.* **13**, 275 (2022).
- [65] A. V. Chubukov and J. P. Lu, *Phys. Rev. B* **46**, 11163 (1992).
- [66] A. V. Chubukov, *Phys. Rev. B* **48**, 1097 (1993).
- [67] M. Jarrell, T. Maier, M. H. Hettler, and A. N. Tahvildarzadeh, *Europhys. Lett.* **56**, 563 (2001).
- [68] S. Raghu, S. A. Kivelson, and D. J. Scalapino, *Phys. Rev. B* **81**, 224505 (2010).
- [69] B.-X. Zheng, C.-M. Chung, P. Corboz, G. Ehlers, M.-P. Qin, R. M. Noack, H. Shi, S. R. White, S. Zhang, and G. K.-L. Chan, *Science* **358**, 1155 (2017).
- [70] Simons Collaboration on the Many-Electron Problem, M. Qin, C.-M. Chung, H. Shi, E. Vitali, C. Hubig, U. Schollwöck, S. R. White, and S. Zhang, *Phys. Rev. X* **10**, 031016 (2020).
- [71] J. F. Annett and R. M. Martin, *Phys. Rev. B* **42**, 3929 (1990).
- [72] H.-C. Jiang and T. P. Devereaux, *Science* **365**, 1424 (2019).
- [73] Y.-F. Jiang, J. Zaanen, T. P. Devereaux, and H.-C. Jiang, *Phys. Rev. Res.* **2**, 033073 (2020).
- [74] S. Gong, W. Zhu, and D. N. Sheng, *Phys. Rev. Lett.* **127**, 097003 (2021).
- [75] H.-C. Jiang, *npj Quant. Mater.* **6**, 1 (2021).

- [76] S. Jiang, D. J. Scalapino, and S. R. White, *Proc. Natl. Acad. Sci. U.S.A.* **118**, e2109978118 (2021).
- [77] H.-C. Jiang and S. A. Kivelson, *Phys. Rev. Lett.* **127**, 097002 (2021).
- [78] K. A. Chao, J. Spałek, and A. M. Oles, *J. Phys. C: Solid State Phys.* **10**, L271 (1977).
- [79] K. A. Chao, J. Spałek, and A. M. Oleś, *Phys. Rev. B* **18**, 3453 (1978).
- [80] J. Spałek, *Acta Phys. Pol. A* **111**, 409 (2007).
- [81] H. Takahashi, A. Sugimoto, Y. Nambu, T. Yamauchi, Y. Hirata, T. Kawakami, M. Avdeev, K. Matsubayashi, F. Du, C. Kawashima, H. Soeda, S. Nakano, Y. Uwatoko, Y. Ueda, T. J. Sato, and K. Ohgushi, *Nat. Mater.* **14**, 1008 (2015).
- [82] T. Yamauchi, Y. Hirata, Y. Ueda, and K. Ohgushi, *Phys. Rev. Lett.* **115**, 246402 (2015).
- [83] J. Ying, H. Lei, C. Petrovic, Y. Xiao, and V. V. Struzhkin, *Phys. Rev. B* **95**, 241109 (2017).
- [84] Y. Zhang, L.-F. Lin, J.-J. Zhang, E. Dagotto, and S. Dong, *Phys. Rev. B* **97**, 045119 (2018).
- [85] M. Mourigal, S. Wu, M. B. Stone, J. R. Neilson, J. M. Caron, T. M. McQueen, and C. L. Broholm, *Phys. Rev. Lett.* **115**, 047401 (2015).
- [86] S. Wu, J. Yin, T. Smart, A. Acharya, C. L. Bull, N. P. Funnell, T. R. Forrest, G. Simutis, R. Khasanov, S. K. Lewin, M. Wang, B. A. Frandsen, R. Jeanloz, and R. J. Birge-neau, *Phys. Rev. B* **100**, 214511 (2019).
- [87] J. M. Caron, J. R. Neilson, D. C. Miller, A. Llobet, and T. M. McQueen, *Phys. Rev. B* **84**, 180409 (2011).
- [88] Y. Nambu, K. Ohgushi, S. Suzuki, F. Du, M. Avdeev, Y. Uwatoko, K. Munakata, H. Fukazawa, S. Chi, Y. Ueda, and T. J. Sato, *Phys. Rev. B* **85**, 064413 (2012).
- [89] J. M. Caron, J. R. Neilson, D. C. Miller, K. Arpino, A. Llobet, and T. M. McQueen, *Phys. Rev. B* **85**, 180405 (2012).
- [90] S. Chi, Y. Uwatoko, H. Cao, Y. Hirata, K. Hashizume, T. Aoyama, and K. Ohgushi, *Phys. Rev. Lett.* **117**, 047003 (2016).
- [91] L. Craco and S. Leoni, *Phys. Rev. B* **101**, 245133 (2020).
- [92] Z. Seidov, H.-A. Krug von Nidda, J. Hemberger, A. Loidl, G. Sultanov, E. Kerimova, and A. Panfilov, *Phys. Rev. B* **65**, 014433 (2001).
- [93] B. Pandey, L.-F. Lin, R. Soni, N. Kaushal, J. Herbrych, G. Alvarez, and E. Dagotto, *Phys. Rev. B* **102**, 035149 (2020).
- [94] P. Stüble, S. Peschke, D. Johrendt, and C. Röhr, *J. Solid State Chem.* **258**, 416 (2018).
- [95] W. Bronger, A. Kvas, and P. Müller, *J. Solid State Chem.* **70**, 262 (1987).
- [96] L.-F. Lin, Y. Zhang, G. Alvarez, J. Herbrych, A. Moreo, and E. Dagotto, *Phys. Rev. B* **105**, 075119 (2022).
- [97] X. Liu, K. M. Taddei, S. Li, W. Liu, N. Dhale, R. Kadado, D. Berman, C. D. Cruz, and B. Lv, *Phys. Rev. B* **102**, 180403 (2020).
- [98] Y. J. Fan, J. J. Feng, J. Y. Zhang, W. Zhou, B. Qian, and Z. X. Shi, *J. Supercond. Nov. Magn.* **34**, 1113 (2021).
- [99] S. K. Tiwary and S. Vasudevan, *Phys. Rev. B* **56**, 7812 (1997).

-
- [100] Z. Seidov, H.-A. Krug von Nidda, V. Tsurkan, I. G. Filippova, A. Günther, T. P. Gavrilova, F. G. Vagizov, A. G. Kiiamov, L. R. Tagirov, and A. Loidl, *Phys. Rev. B* **94**, 134414 (2016).
- [101] Y. Zhang, L.-F. Lin, G. Alvarez, A. Moreo, and E. Dagotto, *Phys. Rev. B* **104**, 125122 (2021).
- [102] L.-F. Lin, Y. Zhang, G. Alvarez, A. Moreo, and E. Dagotto, *Phys. Rev. Lett.* **127**, 077204 (2021).
- [103] Q. Luo, K. Foyevtsova, G. D. Samolyuk, F. Reberdo, and E. Dagotto, *Phys. Rev. B* **90**, 035128 (2014).
- [104] G. R. Stewart, *Rev. Mod. Phys.* **83**, 1589 (2011).
- [105] Y. Kamihara, H. Hiramatsu, M. Hirano, R. Kawamura, H. Yanagi, T. Kamiya, and H. Hosono, *J. Am. Chem. Soc.* **128**, 10012 (2006).
- [106] Y. Kamihara, T. Watanabe, M. Hirano, and H. Hosono, *J. Am. Chem. Soc.* **130**, 3296 (2008).
- [107] C. Q. Choi, “A New Iron Age,” <https://www.scientificamerican.com/article/iron-exposed-as-high-temp-superconductor/>, accessed: 2023-05-02.
- [108] C. Day, *Phys. Today* **62**, 36 (2009).
- [109] H. Takahashi, K. Igawa, K. Arii, Y. Kamihara, M. Hirano, and H. Hosono, *Nature* **453**, 376 (2008).
- [110] M. Rotter, M. Tegel, and D. Johrendt, *Phys. Rev. Lett.* **101**, 107006 (2008).
- [111] X. C. Wang, Q. Q. Liu, Y. X. Lv, W. B. Gao, L. X. Yang, R. C. Yu, F. Y. Li, and C. Q. Jin, *Solid State Commun.* **148**, 538 (2008).
- [112] F.-C. Hsu, J.-Y. Luo, K.-W. Yeh, T.-K. Chen, T.-W. Huang, P. M. Wu, Y.-C. Lee, Y.-L. Huang, Y.-Y. Chu, D.-C. Yan, and M.-K. Wu, *Proc. Natl. Acad. Sci. U.S.A.* **105**, 14262 (2008).
- [113] Z.-A. Ren, G.-C. Che, X.-L. Dong, J. Yang, W. Lu, W. Yi, X.-L. Shen, Z.-C. Li, L.-L. Sun, F. Zhou, and Z.-X. Zhao, *Europhys. Lett.* **83**, 17002 (2008).
- [114] G. Wu, Y. L. Xie, H. Chen, M. Zhong, R. H. Liu, B. C. Shi, Q. J. Li, X. F. Wang, T. Wu, Y. J. Yan, J. J. Ying, and X. H. Chen, *J. Phys. Condens. Matter* **21**, 142203 (2009).
- [115] J.-F. Ge, Z.-L. Liu, C. Liu, C.-L. Gao, D. Qian, Q.-K. Xue, Y. Liu, and J.-F. Jia, *Nat. Mater.* **14**, 285 (2015).
- [116] D. Huang and J. E. Hoffman, *Annu. Rev. Condens. Matter Phys.* **8**, 311 (2017).
- [117] H. Sun, M. Huo, X. Hu, J. Li, Y. Han, L. Tang, Z. Mao, P. Yang, B. Wang, J. Cheng, D.-X. Yao, G.-M. Zhang, and M. Wang, [arXiv:2305.09586](https://arxiv.org/abs/2305.09586) (2023).
- [118] R. M. Fernandes, A. I. Coldea, H. Ding, I. R. Fisher, P. J. Hirschfeld, and G. Kotliar, *Nature* **601**, 35 (2022).
- [119] E. Dagotto, *Rev. Mod. Phys.* **85**, 849 (2013).
- [120] K. M. Kojima, N. Motoyama, H. Eisaki, and S. Uchida, *J. Electron Spectrosc. Relat. Phenom.* **117–118**, 237 (2001).
- [121] M. Uehara, T. Nagata, J. Akimitsu, H. Takahashi, N. Môri, and K. Kinoshita, *J. Phys. Soc. Jpn.* **65**, 2764 (1996).
- [122] N. Motoyama, H. Eisaki, S. Uchida, N. Takeshita, N. Môri, T. Nakanishi, and H. Takahashi, *Europhys. Lett.* **58**, 758 (2002).

- [123] S. Maekawa, *Science* **273**, 1515 (1996).
- [124] E. Dagotto, *Rep. Prog. Phys.* **62**, 1525 (1999).
- [125] K. O. Klepp, W. Sparlinek, and H. Boller, *J. Alloys Compd.* **238**, 1 (1996).
- [126] T. Balić-Žunić, L. Karanović, and D. Poleti, *Acta Chim. Slov.* **55**, 801 (2008).
- [127] G. Amthauer and K. Bente, *Sci. Nat.* **70**, 146 (1983).
- [128] R. H. Mitchell, K. C. Ross, and E. G. Potter, *J. Solid State Chem.* **177**, 1867 (2004).
- [129] F. Du, K. Ohgushi, Y. Nambu, T. Kawakami, M. Avdeev, Y. Hirata, Y. Watanabe, T. J. Sato, and Y. Ueda, *Phys. Rev. B* **85**, 214436 (2012).
- [130] Y. Zhang, L.-F. Lin, A. Moreo, S. Dong, and E. Dagotto, *Phys. Rev. B* **100**, 184419 (2019).
- [131] Y. Zhang, L.-F. Lin, A. Moreo, S. Dong, and E. Dagotto, *Phys. Rev. B* **101**, 144417 (2020).
- [132] S. Imaizumi, T. Aoyama, R. Kimura, K. Sasaki, Y. Nambu, M. Avdeev, Y. Hirata, Y. Ikemoto, T. Moriwaki, Y. Imai, and K. Ohgushi, *Phys. Rev. B* **102**, 035104 (2020).
- [133] X. Chen, P. Dai, D. Feng, T. Xiang, and F.-C. Zhang, *Natl. Sci. Rev.* **1**, 371 (2014).
- [134] B. Saparov, S. Calder, B. Sipos, H. Cao, S. Chi, D. J. Singh, A. D. Christianson, M. D. Lumsden, and A. S. Sefat, *Phys. Rev. B* **84**, 245132 (2011).
- [135] S. Wu, B. A. Frandsen, M. Wang, M. Yi, and R. Birgeneau, *J. Supercond. Nov. Magn.* **33**, 143 (2020).
- [136] T. Aoyama, S. Imaizumi, T. Togashi, Y. Sato, K. Hashizume, Y. Nambu, Y. Hirata, M. Matsubara, and K. Ohgushi, *Phys. Rev. B* **99**, 241109 (2019).
- [137] W. Zheng, V. Balédent, M. B. Lepetit, P. Retailleau, E. V. Elslande, C. R. Pasquier, P. Auban-Senzier, A. Forget, D. Colson, and P. Foury-Leylekian, *Phys. Rev. B* **101**, 020101 (2020).
- [138] V. Svitlyk, D. Chernyshov, E. Pomjakushina, A. Krzton-Maziopa, K. Conder, V. Pomjakushin, R. Pöttgen, and V. Dmitriev, *J. Phys. Condens. Matter* **25**, 315403 (2013).
- [139] V. Svitlyk, G. Garbarino, A. D. Rosa, E. Pomjakushina, A. Krzton-Maziopa, K. Conder, M. Nunez-Regueiro, and M. Mezouar, *J. Phys. Condens. Matter* **31**, 085401 (2019).
- [140] J. Paglione and R. L. Greene, *Nat. Phys.* **6**, 645 (2010).
- [141] M. Rotter, M. Tegel, D. Johrendt, I. Schellenberg, W. Hermes, and R. Pöttgen, *Phys. Rev. B* **78**, 020503 (2008).
- [142] H. Hosono, A. Yamamoto, H. Hiramatsu, and Y. Ma, *Mater. Today* **21**, 278 (2018).
- [143] U. Karahasanovic, R. M. Fernandes, and J. Schmalian, “Nematic Order and Fluctuations in Iron-Based Superconductors,” in *The Iron Pnictide Superconductors: An Introduction and Overview*, Springer Series in Solid-State Sciences, edited by F. Mancini and R. Citro (Springer International Publishing, Cham, 2017).
- [144] M. Yi, Y. Zhang, Z.-X. Shen, and D. Lu, *npj Quant. Mater.* **2**, 1 (2017).
- [145] F. Wang and D.-H. Lee, *Science* **332**, 200 (2011).
- [146] S. Jiang, H. Xing, G. Xuan, C. Wang, Z. Ren, C. Feng, J. Dai, Z. Xu, and G. Cao, *J. Phys. Condens. Matter* **21**, 382203 (2009).

-
- [147] P. Materne, W. Bi, J. Zhao, M. Y. Hu, M. L. Amigó, S. Seiro, S. Aswartham, B. Büchner, and E. E. Alp, *Phys. Rev. B* **99**, 020505 (2019).
- [148] Y. Zhang, L. Lin, J.-J. Zhang, E. Dagotto, and S. Dong, *Phys. Rev. B* **95**, 115154 (2017).
- [149] N. D. Patel, A. Nocera, G. Alvarez, R. Arita, A. Moreo, and E. Dagotto, *Phys. Rev. B* **94**, 075119 (2016).
- [150] B. Pandey, R. Soni, L.-F. Lin, G. Alvarez, and E. Dagotto, *Phys. Rev. B* **103**, 214513 (2021).
- [151] W.-G. Zheng, V. Balédent, C. V. Colin, F. Damay, J.-P. Rueff, A. Forget, D. Colson, and P. Foury-Leylekian, *Commun. Phys.* **5**, 1 (2022).
- [152] W. Malaeb, T. Yoshida, T. Kataoka, A. Fujimori, M. Kubota, K. Ono, H. Usui, K. Kuroki, R. Arita, H. Aoki, Y. Kamihara, M. Hirano, and H. Hosono, *J. Phys. Soc. Jpn.* **77**, 093714 (2008).
- [153] S. Lebègue, *Phys. Rev. B* **75**, 035110 (2007).
- [154] C. Cao, P. J. Hirschfeld, and H.-P. Cheng, *Phys. Rev. B* **77**, 220506 (2008).
- [155] D. J. Singh and M.-H. Du, *Phys. Rev. Lett.* **100**, 237003 (2008).
- [156] M. Daghofer, A. Nicholson, A. Moreo, and E. Dagotto, *Phys. Rev. B* **81**, 014511 (2010).
- [157] Y. Zhang, F. Chen, C. He, B. Zhou, B. P. Xie, C. Fang, W. F. Tsai, X. H. Chen, H. Hayashi, J. Jiang, H. Iwasawa, K. Shimada, H. Namatame, M. Taniguchi, J. P. Hu, and D. L. Feng, *Phys. Rev. B* **83**, 054510 (2011).
- [158] M. Yi, Z.-K. Liu, Y. Zhang, R. Yu, J.-X. Zhu, J. J. Lee, R. G. Moore, F. T. Schmitt, W. Li, S. C. Riggs, J.-H. Chu, B. Lv, J. Hu, M. Hashimoto, S.-K. Mo, Z. Hussain, Z. Q. Mao, C. W. Chu, I. R. Fisher, Q. Si, Z.-X. Shen, and D. H. Lu, *Nat. Commun.* **6**, 7777 (2015).
- [159] R. Arita, H. Ikeda, S. Sakai, and M.-T. Suzuki, *Phys. Rev. B* **92**, 054515 (2015).
- [160] Benjah-bmm27, “Tetrahedron-3D-balls,” <https://commons.wikimedia.org/wiki/File:Tetrahedral-3D-balls.png>, accessed: 2023-05-15.
- [161] YanA, “Crystal field splitting pattern of atomic d-orbitals for a tetrahedral metal complex,” https://commons.wikimedia.org/wiki/File:Tetrahedral_splitting_diagram.svg, accessed: 2023-05-15, modified.
- [162] A. Oberoi and J. Nuckles, “High Spin and Low Spin Complexes (Chemistry LibreTexts),” [https://chem.libretexts.org/Courses/Douglas_College/DC%3A_Chem_2330_\(0%27Connor\)/4%3A_Crystal_Field_Theory/4.3%3A_High_Spin_and_Low_Spin_Complexes](https://chem.libretexts.org/Courses/Douglas_College/DC%3A_Chem_2330_(0%27Connor)/4%3A_Crystal_Field_Theory/4.3%3A_High_Spin_and_Low_Spin_Complexes), accessed: 2023-05-15.
- [163] S. S. Zumdahl, *Chemical Principles* (Houghton Mifflin Company, Boston, New York, 2005).
- [164] P. Fazekas, *Lecture Notes on Electron Correlation and Magnetism* (World Scientific, Singapore, 1999).
- [165] A. Georges, L. de’ Medici, and J. Mravlje, *Annu. Rev. Condens. Matter Phys.* **4**, 137 (2013).
- [166] K. M. Stadler, G. Kotliar, A. Weichselbaum, and J. von Delft, *Ann. Phys.* **405**, 365 (2019).
- [167] Z. P. Yin, K. Haule, and G. Kotliar, *Nat. Mater.* **10**, 932 (2011).

- [168] L. de' Medici, "Hund's Metals Explained," in *The Physics of Correlated Insulators, Metals, and Superconductors Modeling and Simulation Vol. 7*, Lecture Notes of the Autumn School on Correlated Electrons 2017, edited by E. Pavarini, E. Koch, R. Scalettar, and R. Martin (Forschungszentrum Jülich, Germany, 2017).
- [169] Q. Luo, A. Nicholson, J. Riera, D.-X. Yao, A. Moreo, and E. Dagotto, *Phys. Rev. B* **84**, 140506 (2011).
- [170] Q. Luo, A. Nicholson, J. Rincón, S. Liang, J. Riera, G. Alvarez, L. Wang, W. Ku, G. D. Samolyuk, A. Moreo, and E. Dagotto, *Phys. Rev. B* **87**, 024404 (2013).
- [171] Q. Luo and E. Dagotto, *Phys. Rev. B* **89**, 045115 (2014).
- [172] W.-G. Yin, C.-H. Lin, and W. Ku, *Phys. Rev. B* **86**, 081106 (2012).
- [173] S. Dong, J.-M. Liu, and E. Dagotto, *Phys. Rev. Lett.* **113**, 187204 (2014).
- [174] L. de' Medici, G. Giovannetti, and M. Capone, *Phys. Rev. Lett.* **112**, 177001 (2014).
- [175] L. de' Medici, "Weak and Strong Correlations in Fe Superconductors," in *Iron-Based Superconductivity*, Springer Series in Materials Science, edited by P. D. Johnson, G. Xu, and W.-G. Yin (Springer International Publishing, Cham, 2015).
- [176] Q. Luo, G. Martins, D.-X. Yao, M. Daghofer, R. Yu, A. Moreo, and E. Dagotto, *Phys. Rev. B* **82**, 104508 (2010).
- [177] S.-L. Yu, J. Kang, and J.-X. Li, *Phys. Rev. B* **79**, 064517 (2009).
- [178] J. Rincón, A. Moreo, G. Alvarez, and E. Dagotto, *Phys. Rev. Lett.* **112**, 106405 (2014).
- [179] J. Herbrych, N. Kaushal, A. Nocera, G. Alvarez, A. Moreo, and E. Dagotto, *Nat. Commun.* **9**, 3736 (2018).
- [180] N. D. Patel, A. Nocera, G. Alvarez, A. Moreo, S. Johnston, and E. Dagotto, *Commun. Phys.* **2**, 1 (2019).
- [181] J. Kanamori, *Prog. Theor. Phys.* **30**, 275 (1963).
- [182] A. M. Oleś, *Phys. Rev. B* **28**, 327 (1983).
- [183] E. Dagotto, T. Hotta, and A. Moreo, *Phys. Rep.* **344**, 1 (2001).
- [184] M. Berović, *Exploring Hund's Correlated Metals: Charge Instabilities and Effect of Selective Interactions*, Ph.D. thesis, International School for Advanced Studies (SISSA), Trieste, Italy (2018).
- [185] K. Haule and G. Kotliar, *New J. Phys.* **11**, 025021 (2009).
- [186] P. Dai, J. Hu, and E. Dagotto, *Nat. Phys.* **8**, 709 (2012).
- [187] J. Rincón, A. Moreo, G. Alvarez, and E. Dagotto, *Phys. Rev. B* **90**, 241105 (2014).
- [188] A. Kostin, P. O. Sprau, A. Kreisel, Y. X. Chong, A. E. Böhmer, P. C. Canfield, P. J. Hirschfeld, B. M. Andersen, and J. C. S. Davis, *Nat. Mater.* **17**, 869 (2018).
- [189] P. O. Sprau, A. Kostin, A. Kreisel, A. E. Böhmer, V. Taufour, P. C. Canfield, S. Mukherjee, P. J. Hirschfeld, B. M. Andersen, and J. C. S. Davis, *Science* **357**, 75 (2017).
- [190] L. de' Medici, S. R. Hassan, M. Capone, and X. Dai, *Phys. Rev. Lett.* **102**, 126401 (2009).
- [191] L. de' Medici, *Phys. Rev. B* **83**, 205112 (2011).
- [192] L. Fanfarillo and E. Bascones, *Phys. Rev. B* **92**, 075136 (2015).

-
- [193] V. Anisimov, I. Nekrasov, D. Kondakov, T. Rice, and M. Sigrist, *Eur. Phys. J. B* **25**, 191 (2002).
- [194] A. Koga, N. Kawakami, T. M. Rice, and M. Sigrist, *Phys. Rev. Lett.* **92**, 216402 (2004).
- [195] L. de' Medici, A. Georges, and S. Biermann, *Phys. Rev. B* **72**, 205124 (2005).
- [196] J. Herbrych, J. Heverhagen, N. D. Patel, G. Alvarez, M. Daghofer, A. Moreo, and E. Dagotto, *Phys. Rev. Lett.* **123**, 027203 (2019).
- [197] R. Yu and Q. Si, *Phys. Rev. B* **96**, 125110 (2017).
- [198] H. Hu, L. Chen, J.-X. Zhu, R. Yu, and Q. Si, [arXiv:2203.06140](https://arxiv.org/abs/2203.06140) (2022).
- [199] F. B. Kugler and G. Kotliar, *Phys. Rev. Lett.* **129**, 096403 (2022).
- [200] E. A. Stepanov, *Phys. Rev. Lett.* **129**, 096404 (2022).
- [201] D. Ootsuki, N. L. Saini, F. Du, Y. Hirata, K. Ohgushi, Y. Ueda, and T. Mizokawa, *Phys. Rev. B* **91**, 014505 (2015).
- [202] C. Monney, A. Uldry, K. J. Zhou, A. Krzton-Maziopa, E. Pomjakushina, V. N. Strocov, B. Delley, and T. Schmitt, *Phys. Rev. B* **88**, 165103 (2013).
- [203] K. Takubo, Y. Yokoyama, H. Wadati, S. Iwasaki, T. Mizokawa, T. Boyko, R. Sutarto, F. He, K. Hashizume, S. Imaizumi, T. Aoyama, Y. Imai, and K. Ohgushi, *Phys. Rev. B* **96**, 115157 (2017).
- [204] L. Craco and S. Leoni, *Phys. Rev. B* **98**, 195107 (2018).
- [205] H. Lei, H. Ryu, A. I. Frenkel, and C. Petrovic, *Phys. Rev. B* **84**, 214511 (2011).
- [206] J. Herbrych, G. Alvarez, A. Moreo, and E. Dagotto, *Phys. Rev. B* **102**, 115134 (2020).
- [207] J. Herbrych, J. Heverhagen, G. Alvarez, M. Daghofer, A. Moreo, and E. Dagotto, *Proc. Natl. Acad. Sci. U.S.A.* **117**, 16226 (2020).
- [208] J. R. Schrieffer and P. A. Wolff, *Phys. Rev.* **149**, 491 (1966).
- [209] M. Chatzieftheriou, A. Kowalski, M. Berović, A. Amaricci, M. Capone, L. De Leo, G. Sangiovanni, and L. de' Medici, *Phys. Rev. Lett.* **130**, 066401 (2023).
- [210] M. Crispino, M. Chatzieftheriou, T. Gorni, and L. de' Medici, *Phys. Rev. B* **107**, 155149 (2023).
- [211] M. Murase, K. Okada, Y. Kobayashi, Y. Hirata, K. Hashizume, T. Aoyama, K. Ohgushi, and M. Itoh, *Phys. Rev. B* **102**, 014433 (2020).
- [212] D. K. Pratt, M. G. Kim, A. Kreyssig, Y. B. Lee, G. S. Tucker, A. Thaler, W. Tian, J. L. Zarestky, S. L. Bud'ko, P. C. Canfield, B. N. Harmon, A. I. Goldman, and R. J. McQueeney, *Phys. Rev. Lett.* **106**, 257001 (2011).
- [213] J. M. Allred, K. M. Taddei, D. E. Bugaris, M. J. Krogstad, S. H. Lapidus, D. Y. Chung, H. Claus, M. G. Kanatzidis, D. E. Brown, J. Kang, R. M. Fernandes, I. Eremin, S. Rosenkranz, O. Chmaissem, and R. Osborn, *Nat. Phys.* **12**, 493 (2016).
- [214] R. M. Fernandes, S. A. Kivelson, and E. Berg, *Phys. Rev. B* **93**, 014511 (2016).
- [215] W. R. Meier, Q.-P. Ding, A. Kreyssig, S. L. Bud'ko, A. Sapkota, K. Kothapalli, V. Borisov, R. Valentí, C. D. Batista, P. P. Orth, R. M. Fernandes, A. I. Goldman, Y. Furukawa, A. E. Böhmer, and P. C. Canfield, *npj Quant. Mater.* **3**, 1 (2018).
- [216] W. Bao, Y. Qiu, Q. Huang, M. A. Green, P. Zajdel, M. R. Fitzsimmons, M. Zhernenkov, S. Chang, M. Fang, B. Qian, E. K. Vehstedt, J. Yang, H. M. Pham, L. Spinu, and Z. Q. Mao, *Phys. Rev. Lett.* **102**, 247001 (2009).

- [217] S. Li, C. De La Cruz, Q. Huang, Y. Chen, J. W. Lynn, J. Hu, Y.-L. Huang, F.-C. Hsu, K.-W. Yeh, M.-K. Wu, and P. Dai, *Phys. Rev. B* **79**, 054503 (2009).
- [218] J. K. Glasbrenner, I. I. Mazin, H. O. Jeschke, P. J. Hirschfeld, R. M. Fernandes, and R. Valentí, *Nat. Phys.* **11**, 953 (2015).
- [219] E. E. Rodriguez, C. Stock, P. Zajdel, K. L. Krycka, C. F. Majkrzak, P. Zavalij, and M. A. Green, *Phys. Rev. B* **84**, 064403 (2011).
- [220] B. Wei, Q.-Z. Huang, G.-F. Chen, D.-M. Wang, J.-B. He, and Y.-M. Qiu, *Chin. Phys. Lett.* **28**, 086104 (2011).
- [221] F. Ye, S. Chi, W. Bao, X. F. Wang, J. J. Ying, X. H. Chen, H. D. Wang, C. H. Dong, and M. Fang, *Phys. Rev. Lett.* **107**, 137003 (2011).
- [222] M. Wang, C. Fang, D.-X. Yao, G. Tan, L. W. Harriger, Y. Song, T. Netherton, C. Zhang, M. Wang, M. B. Stone, W. Tian, J. Hu, and P. Dai, *Nat. Commun.* **2**, 580 (2011).
- [223] Y.-Z. You, H. Yao, and D.-H. Lee, *Phys. Rev. B* **84**, 020406 (2011).
- [224] R. Yu, P. Goswami, and Q. Si, *Phys. Rev. B* **84**, 094451 (2011).
- [225] E. Majorana, *Nuovo Cimento* **14**, 171 (1937).
- [226] A. Y. Kitaev, *Phys. Usp.* **44**, 131 (2001).
- [227] A. Y. Kitaev, *Ann. Phys.* **303**, 2 (2003).
- [228] J. Alicea, *Rep. Prog. Phys.* **75**, 076501 (2012).
- [229] A. Więckowski, *Mody Majorany w jednowymiarowych układach z oddziaływaniami wielociałowymi*, Ph.D. thesis, Wrocław University of Science and Technology, Wrocław, Poland (2020).
- [230] S. R. Elliott and M. Franz, *Rev. Mod. Phys.* **87**, 137 (2015).
- [231] C. Nayak, S. H. Simon, A. Stern, M. Freedman, and S. Das Sarma, *Rev. Mod. Phys.* **80**, 1083 (2008).
- [232] J. Alicea, Y. Oreg, G. Refael, F. von Oppen, and M. P. A. Fisher, *Nat. Phys.* **7**, 412 (2011).
- [233] R. M. Lutchyn, J. D. Sau, and S. Das Sarma, *Phys. Rev. Lett.* **105**, 077001 (2010).
- [234] Y. Oreg, G. Refael, and F. Von Oppen, *Phys. Rev. Lett.* **105**, 177002 (2010).
- [235] T.-P. Choy, J. M. Edge, A. R. Akhmerov, and C. W. J. Beenakker, *Phys. Rev. B* **84**, 195442 (2011).
- [236] S. Nadj-Perge, I. K. Drozdov, B. A. Bernevig, and A. Yazdani, *Phys. Rev. B* **88**, 020407 (2013).
- [237] I. Reis, D. J. J. Marchand, and M. Franz, *Phys. Rev. B* **90**, 085124 (2014).
- [238] M. Schechter, K. Flensberg, M. H. Christensen, B. M. Andersen, and J. Paaske, *Phys. Rev. B* **93**, 140503 (2016).
- [239] B. Braunecker and P. Simon, *Phys. Rev. Lett.* **111**, 147202 (2013).
- [240] J. Klinovaja, P. Stano, A. Yazdani, and D. Loss, *Phys. Rev. Lett.* **111**, 186805 (2013).
- [241] M. M. Vazifeh and M. Franz, *Phys. Rev. Lett.* **111**, 206802 (2013).
- [242] A. Gorczyca-Goraj, T. Domański, and M. M. Maška, *Phys. Rev. B* **99**, 235430 (2019).
- [243] M. M. Maška, N. Sedlmayr, A. Kobiałka, and T. Domański, *Phys. Rev. B* **103**, 235419 (2021).

-
- [244] B. Braunecker, G. I. Japaridze, J. Klinovaja, and D. Loss, *Phys. Rev. B* **82**, 045127 (2010).
- [245] V. Mourik, K. Zuo, S. M. Frolov, S. R. Plissard, E. P. A. M. Bakkers, and L. P. Kouwenhoven, *Science* **336**, 1003 (2012).
- [246] A. Das, Y. Ronen, Y. Most, Y. Oreg, M. Heiblum, and H. Shtrikman, *Nat. Phys.* **8**, 887 (2012).
- [247] M. T. Deng, C. L. Yu, G. Y. Huang, M. Larsson, P. Caroff, and H. Q. Xu, *Nano Lett.* **12**, 6414 (2012).
- [248] A. D. K. Finck, D. J. Van Harlingen, P. K. Mohseni, K. Jung, and X. Li, *Phys. Rev. Lett.* **110**, 126406 (2013).
- [249] Ö. Gül, H. Zhang, J. D. S. Bommer, M. W. A. de Moor, D. Car, S. R. Plissard, E. P. A. M. Bakkers, A. Geresdi, K. Watanabe, T. Taniguchi, and L. P. Kouwenhoven, *Nat. Nanotechnol.* **13**, 192 (2018).
- [250] F. Nichele, A. C. C. Drachmann, A. M. Whiticar, E. C. T. O'Farrell, H. J. Suominen, A. Fornieri, T. Wang, G. C. Gardner, C. Thomas, A. T. Hatke, P. Krogstrup, M. J. Manfra, K. Flensberg, and C. M. Marcus, *Phys. Rev. Lett.* **119**, 136803 (2017).
- [251] M. T. Deng, S. Vaitiekėnas, E. B. Hansen, J. Danon, M. Leijnse, K. Flensberg, J. Nygård, P. Krogstrup, and C. M. Marcus, *Science* **354**, 1557 (2016).
- [252] M.-T. Deng, S. Vaitiekėnas, E. Prada, P. San-Jose, J. Nygård, P. Krogstrup, R. Aguado, and C. M. Marcus, *Phys. Rev. B* **98**, 085125 (2018).
- [253] S. Nadj-Perge, I. K. Drozdov, J. Li, H. Chen, S. Jeon, J. Seo, A. H. MacDonald, B. A. Bernevig, and A. Yazdani, *Science* **346**, 602 (2014).
- [254] R. Pawlak, M. Kisiel, J. Klinovaja, T. Meier, S. Kawai, T. Glatzel, D. Loss, and E. Meyer, *npj Quant. Inf.* **2**, 1 (2016).
- [255] M. Ruby, B. W. Heinrich, Y. Peng, F. von Oppen, and K. J. Franke, *Nano Lett.* **17**, 4473 (2017).
- [256] S. Jeon, Y. Xie, J. Li, Z. Wang, B. A. Bernevig, and A. Yazdani, *Science* **358**, 772 (2017).
- [257] B. E. Feldman, M. T. Randeria, J. Li, S. Jeon, Y. Xie, Z. Wang, I. K. Drozdov, B. Andrei Bernevig, and A. Yazdani, *Nat. Phys.* **13**, 286 (2017).
- [258] H. Kim, A. Palacio-Morales, T. Posske, L. Rózsa, K. Palotás, L. Szunyogh, M. Thorwart, and R. Wiesendanger, *Sci. Adv.* **4**, eaar5251 (2018).
- [259] L. Schneider, S. Brinker, M. Steinbrecher, J. Hermenau, T. Posske, M. dos Santos Dias, S. Lounis, R. Wiesendanger, and J. Wiebe, *Nat. Commun.* **11**, 4707 (2020).
- [260] D. Wang, L. Kong, P. Fan, H. Chen, S. Zhu, W. Liu, L. Cao, Y. Sun, S. Du, J. Schneeloch, R. Zhong, G. Gu, L. Fu, H. Ding, and H.-J. Gao, *Science* **362**, 333 (2018).
- [261] P. Zhang, K. Yaji, T. Hashimoto, Y. Ota, T. Kondo, K. Okazaki, Z. Wang, J. Wen, G. D. Gu, H. Ding, and S. Shin, *Science* **360**, 182 (2018).
- [262] T. Machida, Y. Sun, S. Pyon, S. Takeda, Y. Kohsaka, T. Hanaguri, T. Sasagawa, and T. Tamegai, *Nat. Mater.* **18**, 811 (2019).
- [263] L. Kong, S. Zhu, M. Papaj, H. Chen, L. Cao, H. Isobe, Y. Xing, W. Liu, D. Wang, P. Fan, Y. Sun, S. Du, J. Schneeloch, R. Zhong, G. Gu, L. Fu, H.-J. Gao, and H. Ding, *Nat. Phys.* **15**, 1181 (2019).

- [264] Z. Wang, J. O. Rodriguez, L. Jiao, S. Howard, M. Graham, G. D. Gu, T. L. Hughes, D. K. Morr, and V. Madhavan, *Science* **367**, 104 (2020).
- [265] C. Chen, K. Jiang, Y. Zhang, C. Liu, Y. Liu, Z. Wang, and J. Wang, *Nat. Phys.* **16**, 536 (2020).
- [266] J. Li, H. Chen, I. K. Drozdov, A. Yazdani, B. A. Bernevig, and A. H. MacDonald, *Phys. Rev. B* **90**, 235433 (2014).
- [267] F. D. M. Haldane, *Phys. Lett. A* **93**, 464 (1983).
- [268] F. D. M. Haldane, *Phys. Rev. Lett.* **50**, 1153 (1983).
- [269] “The Nobel Prize in Physics 2016,” <https://www.nobelprize.org/prizes/physics/2016/summary/>, accessed: 2023-06-17.
- [270] M. den Nijs and K. Rommelse, *Phys. Rev. B* **40**, 4709 (1989).
- [271] T. Kennedy and H. Tasaki, *Phys. Rev. B* **45**, 304 (1992).
- [272] T. Kennedy and H. Tasaki, *Commun. Math. Phys.* **147**, 431 (1992).
- [273] F. Pollmann, E. Berg, A. M. Turner, and M. Oshikawa, *Phys. Rev. B* **85**, 075125 (2012).
- [274] I. Affleck, T. Kennedy, E. H. Lieb, and H. Tasaki, *Phys. Rev. Lett.* **59**, 799 (1987).
- [275] I. Affleck, T. Kennedy, E. H. Lieb, and H. Tasaki, *Commun. Math. Phys.* **115**, 477 (1988).
- [276] U. Schollwöck, O. Golinelli, and T. Jolicœur, *Phys. Rev. B* **54**, 4038 (1996).
- [277] J. Kim, M. Kim, N. Kawashima, J. H. Han, and H.-Y. Lee, *Phys. Rev. B* **102**, 085117 (2020).
- [278] J. Mravlje and A. Georges, *Phys. Rev. Lett.* **117**, 036401 (2016).
- [279] J. Mravlje, M. Aichhorn, T. Miyake, K. Haule, G. Kotliar, and A. Georges, *Phys. Rev. Lett.* **106**, 096401 (2011).
- [280] X. Deng, K. Haule, and G. Kotliar, *Phys. Rev. Lett.* **116**, 256401 (2016).
- [281] T. Kondo, M. Ochi, M. Nakayama, H. Taniguchi, S. Akebi, K. Kuroda, M. Arita, S. Sakai, H. Namatame, M. Taniguchi, Y. Maeno, R. Arita, and S. Shin, *Phys. Rev. Lett.* **117**, 247001 (2016).
- [282] J. I. Facio and P. S. Cornaglia, *J. Phys. Condens. Matter* **31**, 245602 (2019).
- [283] A. Isidori, M. Berović, L. Fanfarillo, L. de’ Medici, M. Fabrizio, and M. Capone, *Phys. Rev. Lett.* **122**, 186401 (2019).
- [284] A. Richaud, M. Ferraretto, and M. Capone, *Phys. Rev. B* **103**, 205132 (2021).
- [285] A. Richaud, M. Ferraretto, and M. Capone, *Condens. Matter* **7**, 18 (2022).
- [286] E. Dagotto, J. Riera, and D. Scalapino, *Phys. Rev. B* **45**, 5744 (1992).
- [287] T. Barnes, E. Dagotto, J. Riera, and E. S. Swanson, *Phys. Rev. B* **47**, 3196 (1993).
- [288] S. R. White and D. A. Huse, *Phys. Rev. B* **48**, 3844 (1993).
- [289] U. Schollwöck, *Rev. Mod. Phys.* **77**, 259 (2005).
- [290] U. Schollwöck, *Ann. Phys.* **326**, 96 (2011).
- [291] S. Östlund and S. Rommer, *Phys. Rev. Lett.* **75**, 3537 (1995).
- [292] J. Dukelsky, M. A. Martín-Delgado, T. Nishino, and G. Sierra, *Europhys. Lett.* **43**, 457 (1998).
- [293] F. Verstraete, D. Porras, and J. I. Cirac, *Phys. Rev. Lett.* **93**, 227205 (2004).
- [294] J. Hauschild and F. Pollmann, *SciPost Phys. Lect. Notes* **5**, (2018).

-
- [295] M. B. Hastings, *J. Stat. Mech.* **2007**, P08024 (2007).
- [296] F. Verstraete and J. I. Cirac, *Phys. Rev. B* **73**, 094423 (2006).
- [297] F. Verstraete, V. Murg, and J. Cirac, *Adv. Phys.* **57**, 143 (2008).
- [298] N. Schuch, M. M. Wolf, F. Verstraete, and J. I. Cirac, *Phys. Rev. Lett.* **100**, 030504 (2008).
- [299] J. Eisert, M. Cramer, and M. B. Plenio, *Rev. Mod. Phys.* **82**, 277 (2010).
- [300] E. Stoudenmire and S. R. White, *Annu. Rev. Condens. Matter Phys.* **3**, 111 (2012).
- [301] S. R. White, *Phys. Rev. B* **72**, 180403 (2005)

ACKNOWLEDGMENTS

I would like to express my heartfelt appreciation to the following individuals who have been instrumental in bringing this thesis to fruition.

First and foremost, I am deeply grateful to my supervisor, Jacek Herbrych, for his continuous guidance, steadfast support, and profound dedication to shaping my scientific career and future success. His meticulous proofreadings, insightful comments, and commitment to completing projects in a timely manner have significantly influenced the direction and enhanced the quality of my work. I would also like to extend my gratitude to my other mentor, Marcin Mierzejewski, for always being available and providing valuable scientific guidance and support whenever I needed it.

My sincere appreciation goes to all my collaborators on the papers prepared during my Ph.D. program, including Elbio Dagotto, Jernej Mravlje, Gonzalo Alvarez, Peter Prelovšek, Agnieszka Jażdżewska, Alberto Nocera, and other friends I had the pleasure of meeting during conferences and the early stages of my scientific career.

Special thanks are extended to all those who participated in our daily lunches in Wrocław, creating a supportive and enjoyable working environment. I would like to give a special mention to Maciej M. Maśka, whose delightful company and lighthearted antics added an extra dose of joy to our interactions. Furthermore, I would like to express my deepest appreciation to all my Ph.D. colleagues, especially those who shared the office 503 with me. Your camaraderie, support, and shared experiences have fostered a vibrant academic community, constantly inspiring growth and making this journey all the more rewarding.

Last but certainly not least, I would like to extend my deepest gratitude to my wife, Edyta, whose unwavering support, counsel, and empathy have been the cornerstone of my personal and professional development. Her patience and understanding during long working hours and her steadfast belief in my scientific career goals have been instrumental in overcoming challenges and pursuing excellence.



The research in this thesis was financially supported by the Polish National Agency of Academic Exchange (NAWA) under contract PPN/PPO/2018/1/00035 and the National Science Centre (NCN), Poland, through project 2019/35/B/ST3/01207. A major part of the numerical calculations was carried out using resources provided by Wrocław Centre for Networking and Supercomputing.